UC Berkeley
UC Berkeley Electronic Theses and Dissertations

Title

Organic Ligands and Colloidal Nanocrystal Surface Thermodynamics

Permalink

https://escholarship.org/uc/item/57m44008

Author

Calvin, Jason John

Publication Date

2022

Peer reviewed|Thesis/dissertation

eScholarship.org Powered by the California Digital Library
University of California

Organic Ligands and Colloidal Nanocrystal Surface Thermodynamics

by

Jason J. Calvin

A dissertation submitted in partial satisfaction of the

requirements for the degree of

Doctor of Philosophy

in

Chemistry

in the

Graduate Division

of the

University of California, Berkeley

Committee in charge:

Professor A. Paul Alivisatos, Chair
Professor Stephen R. Leone
Professor Frances Hellman

Spring 2022

Organic Ligands and Colloidal Nanocrystal Surface Thermodynamics

Copyright 2022
by
Jason J. Calvin

Abstract

Organic Ligands and Colloidal Nanocrystal Surface Thermodynamics

by

Jason J. Calvin

Doctor of Philosophy in Chemistry

University of California, Berkeley

Professor A. Paul Alivisatos, Chair

As materials approach the nanoscale, they begin to exhibit size dependent properties. In particular, a larger fraction of atoms that make up the whole of the material are located on the material's surface. Colloidal nanocrystals are commonly synthesized where their surfaces are terminated by organic molecules, often referred to as ligands. Calorimetric techniques such as isothermal titration calorimetry have been applied to colloidal nanocrystals to study reactions at their surfaces over the past several years, but modeling these reactions has proven challenging. In this work, isothermal titration calorimetry was used to understand reaction mechanisms that increase the luminescence in semiconductor nanocrystals, or quantum dots. Furthermore, the collective effects of the aliphatic carbon chains that make up much of the organic component of colloidal nanocrystals were examined and insights from simulations using a local environment dependent model, the Ising model, will be discussed. With these insights, the structure of the organic ligand shell surrounding the nanocrystal was further probed using traditional X-ray diffraction techniques, which showed ordering of ligands in the organic ligand shell, both as dried powders and in a liquid environment. Finally, dissolution calorimetry experiments measuring negative surface energies of colloidal nanocrystals will be discussed as well as their implications for understanding the thermodynamics of colloidal nanocrystals.

Chapters 1 and 2 will lay the ground work for understanding the structure of colloidal nanocrystals and the main techniques used to study reactions at nanocrystal's surface. Chapter 3 will discuss measurements of reactions at the nanocrystal surface that impact their luminescence, while Chapter 4 will delve into parameters that influence the strength of collective effects between organic ligands bound to nanocrystal surfaces. Chapter 5 will focus on X-ray diffraction measurements of the structure of the organic ligand shell, while Chapter 6 will be devoted to studying negative surface and interface energies of colloidal nanocrystals. Chapter 7 will discuss the future of thermodynamic studies on the surfaces of colloidal nanocrystals.

To the readers

Often while writing I wondered the purpose of this text, especially as the advice I received was to simply, "staple my papers together and call it a Ph.D." If that were the case, I feel this whole effort would have been a colossal waste of my time, although tempting. However, I have often found supporting information in papers as well as theses and dissertations to give the most useful insights, although I had once been told that, "putting something in the supporting information only ensures that it will never be read." It is my hope that my more candid insights into my research than I could provide in published articles (particularly in the appendices) as well as how I perceive them working together will prove themselves useful to future students.

Contents

Contents **ii**

List of Figures **v**

List of Tables **viii**

1 Colloidal Nanocrystals as Inorganic and Organic Composites **1**
1.1 An Introduction to Colloidal Semiconductor Nanocrystals, or Quantum Dots 1
1.2 The Organic Ligand Shell 3
1.3 An Ideal Platform for Studying Surface Chemistry Thermodynamics 5

2 Studying Reactions at Colloidal Nanocrystal Surfaces **6**
2.1 Isothermal Titration Calorimetry 6
2.2 ^{1}H Nuclear Magnetic Resonance 11
2.3 Ising Model Simulations 12

3 Improving Optical Properties via Ligands and Surface Equilibrium **14**
3.1 Improving Indium Phosphide Quantum Dot Luminescence 14
3.2 Treatment of Indium Phosphide Quantum Dots with Metal Halide Salts . . . 16
3.3 Ising Models to Test Hypothesis of Reaction Mechanism 24
3.4 A Hypothesis Regarding the Improved Luminescence 27
3.5 Challenges Regarding Absolute Ligand Adsorption Enthalpies 30
3.6 The Adsorption of Cadmium Oleate to Cadmium Sulfide Quantum Dots . . 31
3.7 An Ising Model to Estimate Absolute Thermodynamic Parameters 35
3.8 Computational Calculations of Thermodynamic Parameters 38
3.9 The Impact of a Dynamic Ligand Shell on Luminescence 41

4 Parameters Influencing Inter-Ligand Interactions **46**
4.1 Investigating the Impact of Ligand Length 46
4.2 An Ising Model to Investigate the Effect of Ligand Length 54
4.3 Phosphonic Acid Ligand Exchanges 59
4.4 Potential Reaction Mechanism for Phosphonic Acid Exchanges 62
4.5 The Role of Nanocrystal Size on Inter-Ligand Interactions 65

4.6 Measurements Varying Nanocrystal Size 67
4.7 A More Complex Ising Model with a Phase Transition 67

5 Direct Diffraction Measurements of Organic Ligand Shell Structure 75
5.1 Structure of Ligands on Colloidal Nanocrystals 75
5.2 Assignment of the Peculiar Powder X-ray Diffraction Peak 76
5.3 Evidence Supporting the Ligand Peak Hypothesis 78
5.4 Modulating the Ligand Peak 81
5.5 Observing Ordered Ligands in Solution 90
5.6 Implications for Nanocrystal Characterization 93

6 Surface and Interface Energies of Colloidal Nanocrystals 95
6.1 Surface Energy and Nanocrystals 95
6.2 Dissolution Calorimetry of Colloidal Quantum Dots 97
6.3 Origins of a Negative Surface Energy 101
6.4 Interfacial Energy of Indium Phosphide/Zinc Sulfide Core/Shell Nanocrystals 103
6.5 Implications of Negative Surface and Interfacial Energies 105

7 Future Perspectives on Colloidal Nanocrystal Surface Thermodynamics 107

Bibliography 110

A Chemicals, Synthesis, and Characterization of Studied Materials 123
A.1 Chemicals 123
A.2 Indium Phosphide Quantum Dots 124
A.3 Cadmium Sulfide Quantum Dots 130
A.4 Cadmium Selenide Quantum Dots 134
A.5 Zinc Sulfide Quantum Dots 137
A.6 Indium Phosphide/Zinc Sulfide Core/Shell Quantum Dots 139
A.7 Lead Sulfide Quantum Dots 142
A.8 Cadmium Oxide Nanocrystals 144
A.9 Washing Procedures 145
A.10 Indium Myristate 148
A.11 Cadmium Oleate 150

B Experimental Methods and Data 153
B.1 Isothermal Titration Calorimetry 153
B.2 ^{1}H Nuclear Magnetic Resonance 155
B.3 Solid State Nuclear Magnetic Resonance 157
B.4 Optical Measurements 158
B.5 X-ray Photoelectron Spectroscopy 159
B.6 Inductively Coupled Plasma Optical Emission Spectroscopy 160
B.7 X-ray Diffraction 160

B.8 Drop Solution Calorimetry 162
B.9 Electron Microscopy 164
B.10 Sizing Image Analysis for Surface Energy Calculations 166
B.11 CHNS Elemental Analysis 168
B.12 Other Ligand Exchanges 168

C On the Use of Nanocrystal Size and Extinction Coefficient Calculators 172
C.1 Size and Extinction Coefficient Calculation Background 172
C.2 Indium Phosphide Size Calculators 173
C.3 Cadmium Sulfide Concentration Calculators 176

D Theoretical and Computational Chemistry Methods 179
D.1 Ising Model Simulations 179
D.2 Restriction of Internal Rotations of Aliphatic Chains 182
D.3 Powder X-ray Diffraction Simulations 184
D.4 Molecular Dynamics Simulations of Aliphatic Chains 185
D.5 Thermodynamics of Cadmium Complexes 185

E Ising Model Simulation Code 188
E.1 On the Ising Model Simulation 188
E.2 Python Script 191
E.3 Ising Model Generated Graphs 201

List of Figures

1.1 Illustration of band gap changing with quantum dot size 2
1.2 Cartoon of the organic ligand shell of colloidal nanocrystals 4

2.1 Schematic of an isothermal titration calorimeter 6
2.2 Example of ^{1}H NMR data showing bound and unbound ligands 10

3.1 Optical measurements of InP quantum dots before and after metal halide treatment 17
3.2 NMR measurements of InP quantum dots before and after metal halide treatment 18
3.3 ITC data of titrations of InP quantum dots with metal halide salts 19
3.4 Extended indium chloride treatment to InP quantum dots. 20
3.5 Schemes of the reaction mechanisms with metal halides 22
3.6 XPS spectra of InP quantum dots before and after metal halide treatment . . . 23
3.7 Simulated enthalpy and bound ligand fraction compared to experimental data . 25
3.8 Additional optical measurements of metal halide salt treated InP quantum dots 28
3.9 Absorption and luminescence of washed CdS quantum dots 32
3.10 Enthalpy of addition of cadmium oleate to washed CdS quantum dots 33
3.11 Number of adsorbed ligands per CdS quantum dot as a function of mole ratio . 34
3.12 CdS Ising model simulated data compared to the experimental results 36
3.13 Luminescence increase upon adding solid cadmium oleate 42
3.14 Histograms of the number of bound ligands of the Ising model simulations . . . 44

4.1 Optical measurements of InP quantum dots capped with carboxylic acids 47
4.2 Isothermal titration calorimetry data of oleic acid titrations of InP quantum dots 48
4.3 ^{1}H NMR of coverage of oleate ligands and native ligands 50
4.4 Binding enthalpy per exchange from ITC and ^{1}H NMR 51
4.5 Langmuir modeling of ^{1}H NMR and ITC data 52
4.6 Ising model data from carboxylic acid exchanges on InP quantum dots 54
4.7 Composition maps of carboxylic acid exchange Ising models 56
4.8 ITC data of phosphonic acids titrations of InP quantum dots 60
4.9 NMR plots of ligand coverages during reactions of with octadecylphosphonic acid 61
4.10 ITC measurements of zinc chloride reacting with a size series of InP quantum dots 66
4.11 ^{1}H NMR of zinc chloride reacting with a size series of InP quantum dots 68
4.12 Example Ising model simulations of InP size models 70

4.13 Predicted and experimental values generated from the modified Ising models . . 71
4.14 Thermodynamic Ising model fit parameters plotted against nanocrystal curvature 72

5.1 PXRD spectra of InP quantum dots 77
5.2 PXRD spectra of synthesized indium myristate 78
5.3 ^{1}H NMR of InP quantum dots 79
5.4 Fitted PXRD spectra of InP quantum dots 80
5.5 Simulated PXRD spectra of InP quantum dots 81
5.6 Fitted PXRD spectra of CdSe quantum dots 82
5.7 Experimental PXRD spectra of inorganic ligand exchanged InP quantum dots . 83
5.8 Experimental and simulated PXRD spectra of InP quantum dot size series . . . 85
5.9 Experimental and simulated PXRD spectra of $RCOO^{-}$ capped InP quantum dots 86
5.10 Experimental PXRD spectra of organic ligand exchanged InP quantum dots . . 87
5.11 Simulated variable temperature PXRD spectra of InP quantum dots 88
5.12 Experimental variable temperature PXRD spectra of InP quantum dots 89
5.13 Raw XRD spectra of solutions sealed in polyimide capillary tubes 90
5.14 Fit XRD spectrum of myristate capped InP quantum dots in toluene 91
5.15 XRD spectra of solvated InP quantum dots 92

6.1 Experimental procedure and raw results of dissolution calorimetry experiments . 96
6.2 ^{1}H NMR spectra of oleic acid 98
6.3 Measurements of the dissolution enthalpy of differently sized InP quantum dots 99
6.4 Measurements of the dissolution enthalpy of size series of different quantum dots 100
6.5 Models of surfaces and measurements of CdO nanocrystal surface energy 102
6.6 Measurements of the interfacial energy of InP/ZnS quantum dots 104

A.1 TEM images of InP quantum dots synthesized under argon 125
A.2 ^{1}H NMR of InP quantum dots 127
A.3 Powder X-ray diffraction pattern from indium phosphide quantum dots 128
A.4 Solid state NMR spectra of InP quantum dots 129
A.5 Characterization of size series of InP quantum dots 131
A.6 TEM image of CdS quantum dots 132
A.7 ^{1}H NMR of cadmium sulfide quantum dots washed in tetrahydrofuran 134
A.8 ^{1}H NMR of cadmium sulfide quantum dots washed in hexane 135
A.9 Powder X-ray diffraction of cadmium sulfide quantum dots 136
A.10 Characterization of size series of CdS quantum dots 137
A.11 Characterization of CdSe quantum dots 138
A.12 Characterization of size series of ZnS quantum dots 139
A.13 HAADF-STEM images of InP/ZnS with EDS mapping 141
A.14 Characterization of indium phosphide/zinc sulfide core/shell nanocrystals 143
A.15 Characterization of lead sulfide quantum dots 145
A.16 Characterization of cadmium oxide nanocrystals 146

A.17 ^{1}H NMR of indium myristate 149
A.18 FTIR spectra of indium myristate 150
A.19 ^{1}H NMR of cadmium oleate 151
A.20 FTIR spectra of synthesized cadmium oleate 152

B.1 ^{1}H NMR spectrum showing impurity of the methyl group 156
B.2 ^{1}H NMR evidence of pipette contamination. 157
B.3 Schematic of Setaram C80 calorimeter. 163
B.4 ^{1}H NMR of indium phosphide quantum dots treated with oleylamine 170

C.1 InP quantum dot sizing data 175
C.2 CdS extinction coefficient data 178

D.1 Gaussian 16 images of indium myristate 183

E.1 Ising model simulation generated graph example 201
E.2 Ising model simulation generated map example 202

List of Tables

3.1 Parameters (in kJ/mol) for the Ising model of the metal halide reactions 26
3.2 Parameters (in kJ/mol) for the Ising model of the cadmium oleate reaction . . . 37
3.3 Thermodynamic quantities calculated for cadmium carboxylate reactions 39

4.1 Parameters for the Ising model of the carboxylic acid exchanges 55
4.2 Ligand coverages for InP quantum dot size series 68
4.3 Ising model parameters for InP quantum dot size series 69

5.1 List of references where ligand peak is observed 76

A.1 Elemental analysis of indium myristate 149

B.1 ITC concentrations for InP quantum dot size series 154
B.2 Fitting parameters for fluorescent lifetimes of InP quantum dots 158
B.3 ICP-OES measurements on metal halide treated InP quantum dots 160
B.4 Elemental ratios of samples used in dissolution calorimetry experiments 161
B.5 Calorimetry data for the nanocrystal samples 164
B.6 Extra calorimetry data for the nanocrystal samples 165
B.7 Calorimetry data for bulk materials measured and reference data used 165
B.8 Size characterization of samples used in dissolution calorimetry experiments . . 167
B.9 Elemental analysis of samples used in dissolution calorimetry experiments 169

C.1 Comparison of Ising model parameters for different nanocrystal calculators . . . 176

D.1 Raw CCSD(T) energy calculations 186
D.2 Calculated entropies of metal complexes and tetrahydrofuran 187

Acknowledgments

First and foremost, I must acknowledge Dr. Paul Alivisatos for giving me the opportunity to join his lab and to take a chance on some unorthodox calorimetry measurements. The freedom that I enjoyed while in his group will almost certainly be the only time in my professional life where I could do almost whatever I pleased and pursue what I wanted to pursue. I am also grateful that he found what I was doing to be interesting, and that he always wanted to hear me talk about my research. I have to also acknowledge the great advice that I received as his student, and that he was always willing to support whatever applications I wanted to apply to and that he helped me in finding my next steps beyond my Ph.D.

Of course I would like to acknowledge my funding sources, which included the National Science Foundation's Graduate Research Fellowship (Grant DGE 1752814), the U.S. Department of Energy, Office of Science, Office of Basic Energy Sciences, Materials Sciences and Engineering Division, under Contract No. DE-AC02-05-CH11231 (Physical Chemistry of Inorganic Nanostructures Program (KC3103)), a grant from Samsung (044369), and the Philomathia Graduate Student Fellowship from the Kavli NanoScience Institute, University of California, Berkeley.

Beyond the funding sources, I have to acknowledge several professors, staff, and students on campus, at Lawrence Berkeley National Lab, and elsewhere that helped me complete this work, including Dr. Hasan Celik, Dr. Wei-Chih Lao, and Dr. Alicia Lund from the NMR facility (funded by NIH S10OD024998), Dr. Elena Kreimer who assisted with the ICP-OES work and especially for running countless CHNS elemental analysis samples, Dr. Yi-Hsien Lu and and Dr. Henry Li for assistance in doing XPS, Dr. Liana Klivansky for assistance with temperature-dependent powder X-ray diffraction measurements, Dr. Dave Small, Dr. Kathleen Durkin, and Diptarka Hait for help and advice using the Molecular Graphics Computational Facility (funded by NIH S10OD023532), Dr. Eran Rabani, Dipti Jasrasaria, and Kaiyue Peng for discussing the surface energy results, Dr. David Limmer for teaching me about the Ising model and discussing my modifications, Douglas Scudder from the machine shop for assistance in fabrication of parts, and James Breen and Laurel Wong for fabrication of glassware. I'd like to thank Dr. Alexandra Navrotsky for not only being a stellar scientist whose work I am constantly referencing, but also for giving me great and completely selfless advice. I would also like to acknowledge our lab manager, Negest Williams, who has always been in my corner and wanting only the best for me.

I was lucky enough to have some truly excellent lab members in our group during my time, and in particular I would like to acknowledge Dr. Brent Koscher, Dr. Justin Ondry, Ethan Curling, Priscilla Pieters, and Han Le for being not only great lab mates but also good friends. Beyond just being good friends, Dr. David Nenon and Dr. Joseph Swabeck helped me in learning how to do my first syntheses and working with me on my first projects, and Dr. Assaf Ben-Moshe for being willing to work on a surprisingly frustrating project together. I also would be remiss to not acknowledge Dr. Erin O'Brien who first showed me the lab's isothermal titration calorimeter and who worked tirelessly with me to publish our paper

together. I'd like to acknowledge another good friend, Jakob Dahl, for always being willing to discuss projects and help me with my code. A huge thanks goes out to Michelle Crook for being willing to image so many samples for me over the past couple of years, the surface energy project would definitely have not been completed without her help. I want to give a special shout-out to Dr. Matthew Hauwiller for being my best friend in lab during my first year and the excellent early mornings that we had together.

I would like to acknowledge Adam Sedlak and Tierni Kaufman, the best undergraduate students that I could have hoped to work with. Amazingly, Adam was willing to do late-night NMR measurements with me for some reason, and Tierni was willing to measure the sizes of thousands of particles. Some of the best times that I had in my Ph.D. was when we got together for our sub-group meeting to discuss the projects and the science that we were all doing. Thanks so much for being willing to read papers and get back to me quickly as we tried to do as much work as we could in the time that we had together.

I would also like to acknowledge Dr. Steve Leone. Not only did he give me an opportunity to teach Chem 125 twice, which gave me some of my favorite teaching moments, but he was always available for me to get advice from. He was more than willing to discuss potential postdoctoral positions, he gave me advice on graduating early, he helping me prepare for my qualifying exam, and he of course sat on my qualifying exam. He's also been very helpful in getting this dissertation written. I couldn't have asked for a better faculty member (other than Dr. Alivisatos) to help me on my way.

Perhaps, at least academically, I owe no greater thanks than to Dr. Brian Woodfield, my research advisor from when I was at Brigham Young University. A funny fact of life is that we rarely know what few comments we will make that will get stuck in someone's mind, and we just better hope that the ones that do are the one's we'd like. I certain that Dr. Woodfield doesn't remember most, or any, of the conversations that we had, but I remember quite a few of them, and they've made me a better scientist. If it weren't for him I certainly wouldn't have come down this path, come to this university, or be pursuing the path that I am, and I'll be forever grateful for the impact that he's had on me.

To Amanda Brewer, the person that this dissertation should probably be dedicated to as I'm certain she'll be the only one who will read it (unless required). Against all odds, you've become my best friend that I've had here. The late nights doing NMR or coding or just discussing life have turned into my happiest memories from my Ph.D. Your willingness to do the work when it isn't fun, to not give up, to learn, and to help has been unmatched, and this past year and a half wouldn't have come together without you. While I will miss many things after I graduate, leaving our friendship and work together is truly tragic. I couldn't have hoped for a better friend.

To my parents, Carolee and John, I owe the most to you. If only I could express in this short acknowledgment section how much I love and appreciate you. Fortunately we talk at least once a week, so I don't need to get it all out right here. Suffice it to say, without your love and support through all my years of education I wouldn't be where I am now. You've always believed in me, and without you I wouldn't be the man I am today. I am eternally grateful to you both.

Finally, the greatest acknowledgment goes to my wife, Angela Teuscher. After five years of marriage, you aren't sick of me (mostly) and you've supported me both emotionally and financially for this trip. I am so grateful that I got to do this California adventure with you, and that we're moving on to new adventures soon. Of course, I couldn't have made the Ising model without all of your coding knowledge and help, and you've made this time so enjoyable. Thanks for always taking care of our three cats, if you can believe it, and for being my partner. This wouldn't have happened without you. I love you.

Chapter 1

Colloidal Nanocrystals as Inorganic and Organic Composites

Reproduced in part with permission from Calvin, J. C.; Brewer, A. S.; Alivisatos, A. P. "The Role of Organic Ligand Shell Structures in Colloidal Nanocrystal Synthesis" *Nat. Synth.* **2022**, *1*, 127–137. Copyright 2022 Springer Nature Limited.[1]

1.1 An Introduction to Colloidal Semiconductor Nanocrystals, or Quantum Dots

Generally, intrinsic material properties do not change with the size of the material. For example, if one takes a copper rod and divides it in two, extrinsic properties, such as mass or volume, change, but the density, an intrinsic value, does not change. Considering the size of the atoms that constitute the material, changing the volume from a cubic centimeter to half a cubic centimeter matters very little to the the chemical environment that determines the structure and properties of the material. This generality remains true until materials reach the nanoscale, where length scales may range from 10's to 100's of atoms. At the nanoscale, two important phenomena occur. First, quantum confinement effects begin to manifest.[2,3] Second, a significant number of atoms that make up the material are in different chemical environments, specifically, as size decreases, the number of atoms of the surface of the material increases relative to the atoms that make up the interior.

The effect of having a large constituency of atoms on the surface has many practical applications. Probably the most obvious is in terms of heterogenous catalysis, where chemical catalysis happens at the surface of a material. Having a large amount of solid catalyst does not help if only a tiny fraction of the material can perform catalysis at the surface. By reducing the catalyst to micron or nanoscale sizes means that the fraction of atoms on the surface has significantly increased, and the same amount of material can perform much more

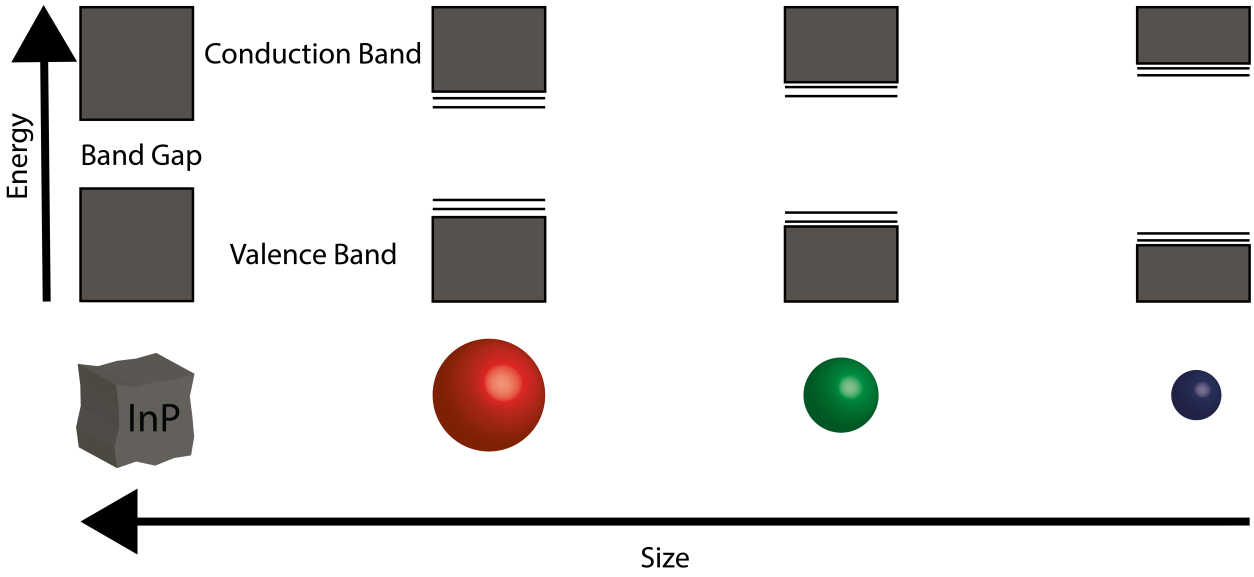


Figure 1.1: Illustration of band gap changing with quantum dot size. As nanocrystals become smaller their band gaps become larger, resulting in blue shifts to their absorption and luminescence spectra.

catalysis.[4,5] If the catalyst is expensive, like platinum group metals, maximizing catalysis with less material is always the goal.

The other most well known effect of going to the nanoscale involves semiconductor nanocrystals. Normal semiconductors have a band gap, or the absence of electron levels, between their highest filled electron levels and their lowest unfilled electron levels. To excite electrons from those highest filled electron levels, or the valence band, to the lowest unfilled electron levels, or the conduction band, semiconductors can absorb a photon of light with an energy that is equal to or greater than the energy gap between the conduction and valence band.[6] This band gap is exploited in most applications of semiconductors, and it is critical in understanding device applications such as solar cells and diodes.[7–9]

The band gap is another intrinsic property of a semiconductor, and it can be manipulated by changing aspects of the material like the amount of impurities in the semiconductor (known as doping).[6] However, it can also be changed when the size of the semiconductor crystal becomes small enough, where smaller nanocrystals have larger band gaps, meaning the energy of a photon needed to excite electrons in the crystal becomes higher and shifted to "bluer" wavelengths (see Figure 1.1).[2,3] In a direct band gap semiconductor, where the material can more easily emit photons after they have been absorbed, the wavelength of light emitted changes with the size of the material and can be tuned to cover the entire visible color spectrum. In the regime where the band gap changes with the size of the crystal, we refer to these semiconductor nanocrystals as quantum dots.[2,3]

There are many ways to synthesize nanocrystals, but one of the cheapest ways that

results in high quality, well-defined, and size controlled nanocrystals is through a colloidal synthesis, where the surfaces of the nanocrystal are terminated by capping groups, such as long, aliphatic chains of carbons that help control the size and prevent fusion of nanocrystals during growth.[2] The resulting materials are generally synthesized and are stable in organic solvents, which allows for convenient solution processing. The organic groups on the surface of the nanocrystal are often referred to as the organic ligand shell, and this structure and its influence on material properties are the primary focus of this work.

Nanocrystals present an interesting and often unexplored aspect of statistical thermodynamics. In rigorous statistical mechanics and thermodynamic derivations, very large numbers of particles are often assumed.[10] However, in nanocrystals, these assumptions begin to break down. For example, in colloidal nanocrystals, there may only be hundreds of organic ligands on the surface of a nanocrystal, and if there is a phase transition in the organic ligand shell, ideas of first order or second order phase transitions, including the sharpness of the transition, likely no longer apply. Thus, in studying the thermodynamics of small systems,[11] nanocrystals provide a platform to also study more theoretical aspects of thermodynamics. This work helps provide the experimental foundation for theoretical understanding of the limits of statistical thermodynamics.

1.2 The Organic Ligand Shell

Fundamentally, most colloidal nanocrystals are composites consisting of an inorganic core and an organic ligand shell. This organic ligand shell enables colloidal stability in solvents,[12,13] prevents inorganic cores from fusing,[14,15] passivates undercoordinated atoms that lead to exciton traps in quantum dots,[16–18] acts as soft matter in artificial solids assembly,[14,19–21] and provides a platform for modification of inorganic cores (see Figure 1.2).[17,22] Beyond contributing to colloidal nanocrystals properties, they are essential in synthesis.

Organic ligands mediate growth by binding to growing nanocrystal surfaces as a surfactant. The group that binds to the nanocrystal surface is referred to as the head group, while the rest of capping ligand is referred to as the tail group.[21,23,24] Typically, in hydrophobic environments, when growth is terminated by exhaustion of precursors or reaction quenching, these ligands form an organic shell around each nanocrystal, with head groups facing into the nanocrystal and organic tail groups facing outward. The nature of the ligands dictates the inorganic nanocrystal surface structure,[12,24,25] and ligands have been designed to promote surfaces that minimize surface defects in quantum dots.[17,26,27] A variety of head groups have been used to terminate colloidal nanocrystal surfaces, such as carboxylates, amines, phosphonates, thiols, and halides, and often a mixture of capping groups is used.[17,18,22,28–32] The amount, type, and impurities of ligands used in nanocrystal synthesis has implications for nanocrystal size, shape, crystal structure, and stability as well as their optical and electronic properties.[33,34]

Head groups play a critical role in controlling colloidal nanocrystal growth, and different nanocrystal shapes can be formed by manipulating head group binding. Using combina-

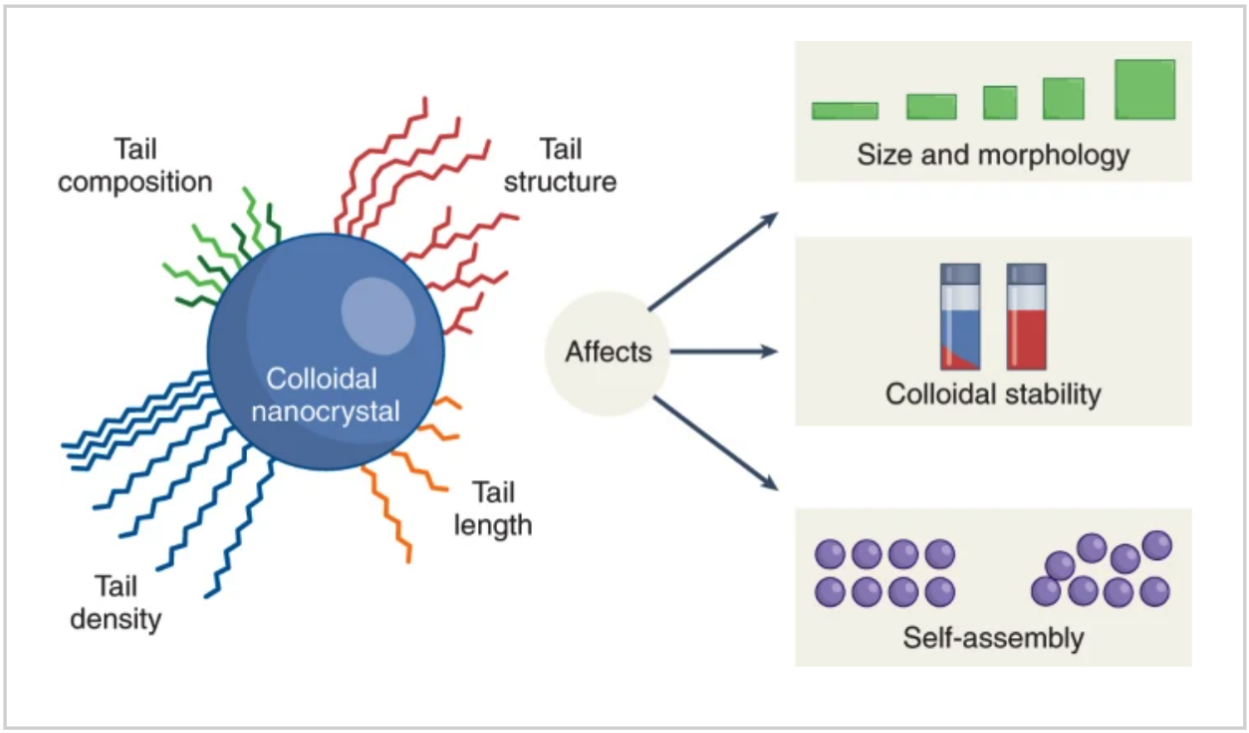


Figure 1.2: Cartoon of the organic ligand shell of colloidal nanocrystals and how it affects size, morphology, colloidal stability, and self-assembly of nanoparticles.

tions of carboxylate and thiol capping ligands in lead sulfide nanocrystal syntheses result in cubes or octahedrons, or shapes in between.[35] This is attributed to the variable surface energy of different nanocrystal facets, which can be manipulated by using different capping ligands.[20,25,29,32,36] As a result, shape control has mostly been the result of mixed ligand syntheses. In addition, it has been reported that growth temperature and ligand concentration can also lead to faceting by controlling the kinetics of head groups adsorbing and desorbing to nanocrystal surfaces during growth.[36–38]

While significant research has been done on the influence of organic ligand head groups in this regard,[21] less attention has been devoted to tail groups and organic ligand shell structure.[39–41] The ligand shell structure has a remarkable influence on their properties. For example, colloidal quantum dot photoluminescence can be impacted by order or disorder in the ligand shell.[42–46] The steric bulkiness of aliphatic chains can make it difficult for ligands to adequately passivate inorganic surfaces, leading to undercoordinated atoms and potential electronic defects.[17,26] The impact of ligand ordering has also been observed in the catalytic response of hybrid palladium nanoparticles and in the electron transfer of cadmium sulfide nanorods.[4,47]

Both the head group and the tail group of the capping ligands can be varied to achieve distinct goals. Head groups are more strongly coupled with the nanocrystal and are often

chosen based on the desired growth temperature, and as they are in direct contact with the inorganic nanocrystal surface atoms, they are also chosen for their influence on electronic properties. In contrast, tail groups utilize many weak interactions and entropic effects to offer tremendous power in controlling the colloidal stability and assembly. This contrast between strong and weak interactions is characteristic of work on the nanoscale in general. Strong head group interactions offer design control on the most local scale, while many weak tail group interactions allow for design control on a larger scale. These different inter-ligand interactions and collective effects of the organic ligand shell have surprising implications and impacts on colloidal nanocrystal properties and will likely prove meaningful to further advancing the field to create more tailored and specific nanocrystals with a wide range of properties.

1.3 An Ideal Platform for Studying Surface Chemistry Thermodynamics

As previously mentioned, once materials reach the nanoscale, a significant proportion of their atoms reside on the surface of the material. This, coupled with the solution nature of colloidal nanocrystals, makes it much easier to probe the fundamental surface chemistry more traditional solution based chemistry methods.[18,28,48–52] For example, the organic ligands and reactions of their surfaces can be studied using techniques such as NMR in organic solvents,[28,48–50] traditional techniques such as luminescence and absorption are easy to measure,[18,51,52] and crucially, calorimetric measurements of surface thermodynamic properties become convenient to do.[30,31,53,54]

Unlike spectroscopic measurements, calorimetric measurements need significantly more material to work with, as heats smaller than microjoules become difficult to measure. While calorimetric measurements have been called "spectroscopy without selection rules,"[55] the other major downside to these measurements is that unlike spectroscopy, where one can look in different regimes of the electromagnetic spectrum and hopefully features do not overlap, in calorimetry, heat is heat, wherever it comes from. Thus, designing control reactions and ensuring only the reaction of interest is being observed calls for significant creativity. Although challenges in calorimetry of surfaces exist, nanoparticles are likely the ideal platform to overcome them.

Chapter 2

Studying Reactions at Colloidal Nanocrystal Surfaces

2.1 Isothermal Titration Calorimetry

While there are many different classes of calorimeters, the two most common are the adiabatic calorimeter and the isothermal calorimeter. In an adiabatic calorimeter, no heat is allowed to flow in or out of the system, so as heat is generated or absorbed in the reaction, the temperature of the reaction mixture will change. If the heat capacity of the system is known, then the heat of the reaction can be determined from the temperature change and the heat capacity.[56,57] However, for studying the heat of reactions, this type of calorimeter is less than ideal. In the most rigorous definition, the enthalpy of the reaction (the thermodynamic quantity being calculated in these reactions) is the heat of the reaction at a constant temperature and pressure. In an adiabatic calorimeter, technically the temperature is not

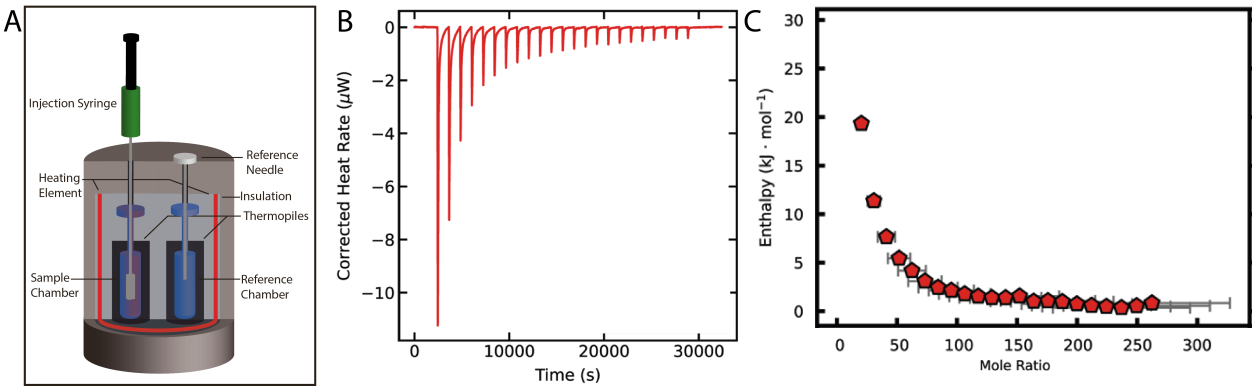


Figure 2.1: Schematic of an isothermal titration calorimeter (A) and example raw (B) and integrated heat flow data (C).

constant (although typical temperature changes are not large as reaction heats are small and the heat capacity is large). A more rigorous technique is to use an isothermal calorimeter. In an isothermal calorimeter, the temperature is kept constant during the reaction because heat flow is allowed, typically using some type of heater, and so instead of the temperature being monitored during the reaction, the heat flow into the sample cell to maintain a constant temperature is measured.[58,59] Once the reaction has finished and the system returns to equilibrium, the heat flow (typically measured in Watts) can be integrated over time to calculate the total heat of the reaction, and this is rigorously defined as the enthalpy, assuming the reaction occurs at constant pressure. In general, the differential heat flow is recorded, where both a reference cell and a sample cell are present, but the reaction only occurs in the sample cell, and the differential heat flow is the difference in heat flow between the sample cell and and reference cell.

Isothermal titration calorimetry measures the heat of small reactions that occur as one solution is titrated into another (Figure 2.1). Similar to acid-base titrations, in general, a reaction occurs between the analyte and titrant, and as more and more titrant is added to the solution, eventually the analyte is consumed, and there ceases to be a reaction between the species. As the reaction happens, heat is either generated in an exothermic reaction or absorbed in a endothermic reaction, and when no reaction is happening, there is no heat change. As many reactions are in equilibrium, by adding small amounts of the titrant to the solution, a plot of the heat of the reaction against the amount of titrant added can be constructed, and from this data, information about the thermodynamics and equilibrium can be deduced. Isothermal titration calorimetry is not a new technique, and it has been particularly instrumental in the field of biology for quite some time to study the thermodynamics of enzyme or protein binding.[60–63]

A key piece of information to keep in mind is that the enthalpy of the reaction is actually not the fundamental driving force of a reaction. A reaction can occur with a positive or negative enthalpy, but rather the change in the Gibbs free energy determines if a reaction occurs, where the change in Gibbs free energy must be negative (an exercise is left to the reader to show that a negative change in the Gibbs free energy of the system corresponds to an increase in the entropy of the universe, or the entropy of the system plus the surroundings). While this may be seen as a down side for calorimetry as generally enthalpies of reactions are measured, this is actually a strength, especially when applied to isothermal titration calorimetry. From the heat titration curve the equilibrium constant of the reaction can be calculated as well as the enthalpy of the reaction, and with this knowledge both the enthalpy, entropy, and Gibbs free energy of the reaction can be calculated, thus revealing the most important thermodynamic properties.[30,31] This contrasts with something like a Langmuir isotherm, where the equilibrium constant and the Gibbs free energy of reaction can be calculated, but the interplay between enthalpy and entropy cannot.[64–66]

While this seems like a simple enough system, there are some technical aspects to isothermal titration calorimetry that complicate understanding the thermodynamics of the reaction. As one solution is titrated into another, there are a few thermal effects that must be accounted for. First, there is a heat of friction generated by moving a liquid through the

syringe. While this may seem like a negligible source of heat, it generates (in this author's experience) on average approximately 20 μJ of heat, which is detectable by commercial isothermal titration calorimeters. This can be measured by injecting neat solvent into itself. This also raises an important point. For these sensitive calorimeters, the solvent of the titrant and the analyte must be the same. If they are not, the enthalpy of mixing of solvents will be the only detectable signal, and will generally be larger than the dynamic range of the instrument, which is on the order of 5000 μJ. Technically, there is a dynamic heat flow limit of the instrument, perhaps around 150 μW. However, considering that the instrument must return to baseline between injections, and this will take longer with a larger total heat measurement, it is this author's experience that around 2000 μJ should be targeted for the first injection. Almost invariably, the user will need to adjust concentrations, by trial and error, of the analyte and titrant as well as the titrant injection volume (typically between 10 and 2.5 μL) before an ideal titration curve can be constructed.

Second, there are heat of dilution effects for both the analyte and the titrant. This effect is typically most significant in the titrant, as it is generally more concentrated than the analyte, but these effects should be considered. In general, titrating the titrant into a solution that contains no analyte (*i.e.* a neat solution) determines the heat of dilution of the titrant as well as the frictional heat of the injection, and so subtracting this effect from the measured signal is an absolute necessity, especially with concentrated solutions of titrant and when dealing with small heats of reaction. Additionally, by injecting neat solvent into the analyte, the heat of dilution of the analyte can be determined, although with colloidal nanocrystals there is an additional complication to be discussed below.

When discussing technical details of isothermal titration calorimetry, the idea of an effective volume is important to note. Suppose the sample cell and the reference cell each hold 0.5 mL of solution, and thus the heat capacity of the two solutions are the same, then in an ideal situation the same amount of heat is required to keep both solutions at 25 °C. As a side note, for these instruments, the jacket of the cells is actually kept slightly lower than the desired temperature so that heat must always be input to the system and the heaters do not turn on and off trying to maintain the temperature, rather a constant supply of heat is required. However, if 10 μL of titrant is added to the sample cell, the new volume will be 0.51 mL, and the heat capacity of the solution will change. This then introduces a new baseline thermal input, and drawing a baseline to integrate the signal will be challenging. To account for this, the sample and the reference cell are filled such that the total volume overflows both cells into a reservoir that is not coupled to the heating system but rather is insulated. Thus, when additional volume is added, the volume where the heat of the reaction occurs does not change, and the heat capacity change of the system should be negligible. However, this means that with subsequent injections the moles of analyte being titrated not only changes in terms of concentration, but also in actual moles of analyte being measured in the cell. Commercial software accounts for this inconvenience, but if additional data processing is needed, this aspect cannot be neglected.

In addition to the concentration of the analyte and titrant, as well as the volume of titrant injected, other variables can be modified for experiments. This includes temperature

control (although 25 °C is probably the desired temperature for reporting standard state thermodynamic values), stirring speed, and time between injections. Typically, 250 RPM stirring speed is adequate, and faster stirring may introduce more baseline noise. However, stirring is needed to ensure that the reaction returns to equilibrium in a reasonable time (and increases the heat flow signal). It was found by this author that 40 minutes between injections was manageable, and with a 250 μL syringe (where only 230 μL was injected, detailed below) this resulted in 23 injections of 10 μL, and took about 18 hours, considering equilibration time and final baseline measurements. As these commercial calorimeters are generally designed to work with high surface tension aqueous solutions, they expect that the user will not be able to get all of the air out of the syringe, and so an air bubble must be included in the syringe. Generally, only 230 μL of solution is injected to avoid injecting any of the air bubble.

Other difficulties in doing isothermal titration calorimetery measurements have to do with preparing the syringe. The syringe is first filled with solution, including the air bubble, to greater than 250 μL. Then, the syringe is screwed into the buret handle. This pushes out some excess solution and ensures a consistent starting volume for every injection. The excess solution must be carefully wiped off of the tip of the syringe. If the very tip of the syringe is wiped, capillary action can draw solution out of the syringe, which messes up the volume inside the syringe. To obtain reliable results, this must be carefully avoided. Finally, when performing the experiment, it is this author's experience, which has also been reported by others, that the first injection typically does not track with the other injections. Generally, the first injection will have a lower signal than subsequent injections. This is attributed to two potential causes. First, if any solution has come out of the tip of the syringe, the injection volume will be lower than the subsequent injections. Second, while ideally there would be no mixing between the tip of the syringe and the analyte solution, during the equilibration period (which can take some time), there may be some diffusion of the the titrant into the analyte. Care should be taken to minimize the time between injections because if too much time is allowed there may be leaching from the syringe tip in the cells.

Before discussing the technical details with nanocrystal reactions, the final note on general isothermal titration calorimetry measurements involves the baseline of the reaction and the shape of the heat injections. This should be carefully observed by the user, and there are a few things to note. First, as mentioned above, the first data point is usually not reliable, and should not be used in analysis. However, it has been observed in many reactions that the first few titration points do not follow the trend of the rest of the reactions. If this is the case, it generally means that there are multiple reactions happening, and for the case of nanocrystal reactions this has been observed and attributed to ligands filling empty sites before undergoing a ligand exchange, and this will be discussed in Chapter 4. Second, the baseline should be relatively flat. If the baseline becomes excessively noisy or drifts in one direction, this typically is indicative of nanocrystal aggregation, and this means that these data points should not be trusted. Finally, if the differential heat flow does not come back to the original baseline before the next injection, the time between injections should be longer.

For the measurements of nanocrystals, there are a few main technical aspects that must

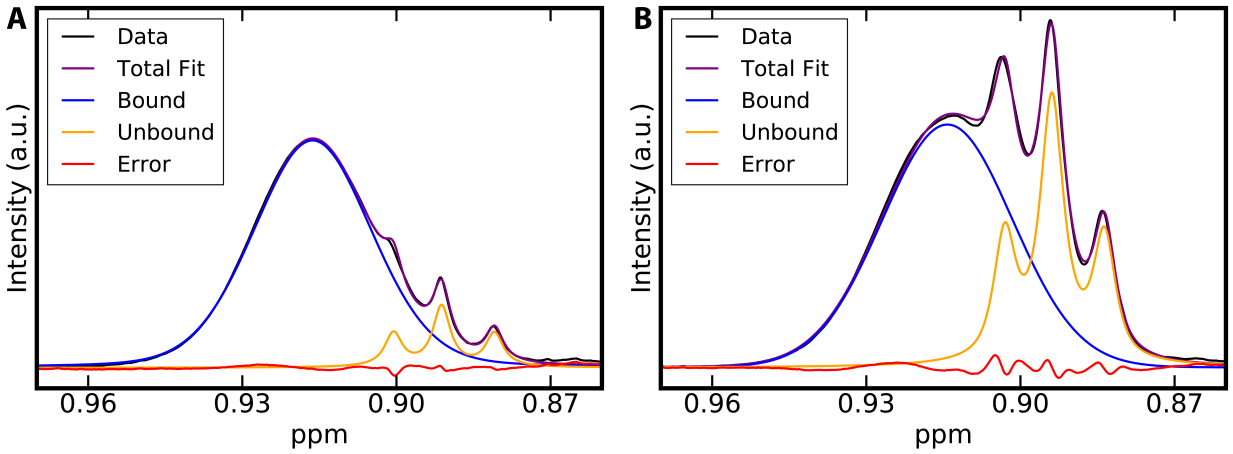


Figure 2.2: Example of ^{1}H NMR data showing bound and unbound ligands. (A) An example of the vinyl protons of oleate with little unbound ligand. (B) An example of the vinyl protons of oleate with significant unbound ligand. Spectra taken in tetrahydrofuran-d_8 .

be discussed. First, it is generally agreed upon that the nanocrystals should be the analyte, and some ligand or reaction species the titrant. Second, depending on the solvent used, the ligands may be dynamically bound to the surface (Chapter 3). If this is the case, dilution measurements are convoluted with the enthalpy of dilution of the nanocrystals as well as the enthalpy of shifting the equilibrium of the ligands off of the surface of the nanocrystal. These effects are very hard to correct, but in general they should be small, and in these studies they were negected. Third, and most importantly, commercial software models for isothermal titration curves should probably be avoided. There are two main reasons for this. First, many commercial models do not allow for the number of sites of an analyte to be very large, like the number of ligands on the surface of a nanocrystal. This can be worked around by fitting custom models, but doing so requires knowledge of the effective volume as discussed above, or instead of treating nanocrystals as the analyte one could treat the ligands as the analyte, only having one site rather than many. However, the biggest pitfall with this (or traditional fitting methods) is that these models assume that there is no relationship between neighboring sites. As will be seen in the subsequent chapters, this is a critical error that most thermodynamic analyses of isothermal titration calorimetry measurements neglect, and because of this, ^{1}H NMR and an Ising model are critical for understanding reactions at nanocrystal surfaces.

2.2 ^{1}H Nuclear Magnetic Resonance

While isothermal titration calorimetry measurements have become more common place for studying reactions at the surfaces of nanocrystals over the past several years, more traditionally these reactions have been studied by NMR measurements. As the nanocrystals are colloidal, they can be suspended in solvents, which allows solution NMR measurements to be performed quite easily. The reason that NMR is an ideal technique for studying reactions at nanocrystal surfaces is because ligands that are bound to the surface of the nanocrystal appear different in the spectra than ligands that are free in solution (Figure 2.2).[18,28,48,49,67] There are two causes for this phenomena. First, ligands that are free in solution are in a different chemical environment than ligands that are bound to the surface of the nanocrystal, so the chemical shift is slightly different. Second, the tumbling speed of the ligands that are free are much faster than those that are bound to the nanocrystal, the variety of chemical environments for ligands bound to the nanocrystal are more broad, and the relaxation time is faster on the nanocrystal, which all corresponds to a more broad peak in the NMR spectra for ligands that are bound to the surface of the nanocrystal. Because of these factors, an NMR spectra can be used to figure out the fraction of ligands bound to the surface and ligands that are free in solution (Figure 2.2).

Traditionally, NMR measurements are not considered to be quantitative when a spectra is collected. Often the peaks are integrated to get relative areas of protons in different chemical environments, but with molecules, it is well known that rounding to the nearest whole number is generally correct, and significant deviations from whole numbers can occur. However, this can be mitigated for quantitative NMR purposes. The reason that these deviations occur is differing relaxation times of protons in different chemical environments, and if the system does not reach equilibrium and another pulse is performed, the signal will change. However, if sufficient time between NMR pulses is allowed, then all the spins, regardless of chemical environment, should be at thermal equilibrium, and the signal should be uniform across the protons. Thus, while measurements can take significantly longer, this is valuable to get quantitative measurements. Generally a minimum of 20 seconds between pulses is sufficient.

With an internal standard such as mesitylene of a known concentration, the concentration of the ligands in the sample and relative fractions of ligands bound and unbound can be determined by analysis of the NMR spectra. If the concentration of the nanocrystals is known, the number of ligands per nanocrystal can be determined, and if the size of the nanocrystal is known, ligand coverages can also be computed. If a ligand exchange is performed and the ligands have different NMR signals, then as the ligand exchange occurs, or as more exchange ligand is titrated into the sample, the fractional coverage of the ligands can be determined. This type of analysis is the traditional way of studying ligand exchanges on nanocrystals, and it can be quite informative. It is a nice way of looking at the data, because the extent of the ligand exchange is determined by the change in the Gibbs free energy, and as mentioned above, in the very simplest models, a Langmuir isotherm can be used to determine these thermodynamic parameters and equilibrium constants. However, it

is commonly observed that these models do not adequately fit the data (similarly for the isothermal titration calorimetry measurements) and thus two-site models are used. However, based on the measurements that will be described in Chapters 3 and 4, it is likely that inter-ligand interactions are more likely to be the cause of these discrepancies rather than different sites on nanocrystals, at least to a first-order approximation.

2.3 Ising Model Simulations

To account for these inter-ligand interactions, an Ising model is the simplest approximation. Ising models were originally used to study thermodynamics and phase transitions in magnetic materials, as the spins in the atoms that must align to create a permanent magnet not only are influenced by some external magnetic field (where alignment with the field is in a lower energy state) but also their alignment with their neighboring spins. Being aligned with neighboring spins also lowers the energy.[10] However, having random orientations of spins is more favorable entropically, and thus this becomes an interesting thermodynamic problem. It turns out that there is no phase transition in one-dimensional chains of spins, determined by Ising, although there is one and the solution can be solved in two-dimensions and was done so by Onsager.[10] While solving the model in two-dimensions is possible, it is much easier to use a Monte-Carlo simulation of a two dimensional Ising model, and all of the Ising models presented herein were done with simulations.

The beauty of the Ising model is in its simplicity as well as its use in many other fields than just magnets.[12,42,68–70] Rather, if there are local influences on the thermodynamics of a system, an Ising model can likely be used to model the system. In the case of inter-ligand interactions on the surface of nanocrystals, a spin up state can be considered a native ligand, while a spin down state can be considered an exchange ligand. The external magnetic field can be translated to representing the the binding energy of the head groups, and the influence of neighboring spins can be translated to represent the van der Waals interactions between organic ligands (see Chapter 3). Further, we can have a representation of ligands that are free in solution and ligands that are bound to the nanocrystal, and we can randomly select ligands from both populations and attempt to swap them. The probability of swapping ligands is given as

$$P = \mathrm{e}^{-\Delta G/k_{\mathrm{B}}T}$$

and if ΔG is negative the swap will occur, while if it is positive then there is some probability that diminishes as ΔG becomes larger or if $k_{\mathrm{B}}T$ becomes smaller. Determining the values for ΔG is the main goal of the Ising model simulations, which can depend on several factors that will be described in Chapters 3 and 4. The other nice feature of these models is that both the isothermal titration calorimetry data and the ^{1}H NMR data can be modeled together, further constraining the realistic thermodynamic values. More details on the Ising model simulations are given in Appendices D and E as well as the code used to run the simulations.

With these techniques in mind, Chapters 3 and 4 will delve into the thermodynamics of ligand exchanges on the surface of colloidal quantum dots.

Chapter 3

Improving Optical Properties via Ligands and Surface Equilibrium

Reproduced in part with permission from Calvin, J. C.; Swabeck J. K.; Sedlak, A. B.; Kim, Y.; Jang, E.; Alivisatos, A. P. "Thermodynamic Investigation of Increased Luminescence in Indium Phosphide Quantum Dots by Treatment with Metal Halide Salts" *J. Am. Chem. Soc.* **2020**, *142*(44), 18897–18906. Copyright 2020 American Chemical Society.[71]

This chapter will have two main parts; part one will discuss the thermodynamics and in increase in luminescence of indium phosphide quantum dots by treatment with metal halide salts while part two will discuss the thermodynamics and luminescence impacts of a dynamic ligand shell on cadmium sulfide quantum dots.

3.1 Improving Indium Phosphide Quantum Dot Luminescence

Indium phosphide based quantum dots are the material most favored for new quantum dot displays, as cadmium containing quantum dots are currently being phased out due to cadmium's toxicity and carcinogenic effects.[72–74] Advances in quantum dot chemistry of type III-V semiconductors have typically lagged behind their type II-VI counterparts, with II-VI quantum dots—such as in cadmium selenide/cadmium sulfide core/shell quantum dots—achieving a greater than 99% quantum yield.[3,75–77] Even without an inorganic shell, type II-VI quantum dots tend to have higher quantum yields and narrower emission linewidths than type III-V quantum dots. Therefore, improving the optoelectronic properties of indium phosphide based quantum dots is critical to incentivizing the transition to less toxic quantum dot materials.[78]

Improvements to the optoelectronic properties of indium phosphide quantum dots using typical approaches such as organic ligand capping or a hydrofluoric acid etching have various limitations. Organic capping ligands used during synthesis have been shown to positively

affect the quantum yields of indium phosphide quantum dots, but not to levels viable for commercial display applications.[79–81] A post-synthetic treatment using a hydrofluoric acid etch has also proven to successfully increase quantum yields.[22,82,83] The most widespread and effective method for creating indium phosphide based quantum dot luminophores of sufficient efficiency for consumer displays—with luminescence quantum yield as high as 95%[77,84–86]—is to grow an inorganic shell, such as zinc sulfide, around the core quantum dot. However, the quality of the core in core shell quantum dots, as well as the nature of the surface of the core before growth of the inorganic shell, likely influences the quality of the final product. This further creates the need to understand how post-synthetic treatments optimize the properties of the core material and provide ideal platforms for shell growth.

One post-synthetic surface treatment that has seen some success is the addition of metal halide salts to quantum dots.[17,22,87–89] A proposed mechanism[87,88] for the reaction with the metal halides is similar to the mechanism for a post-synthetic treatment of quantum dots using reactive silyl chloride derivatives, wherein the silyl chloride bond is cleaved, the silyl group binds with a displaced carboxylate, and the surface is subsequently chlorinated.[67,90–92] Support for this hypothesis, in which some of the original organic ligand is replaced by chlorides, has been shown through CHN elemental analysis, FTIR, and ^{1}H NMR, all of which indicate the loss of organic ligands.[87,92,93]

Alternatively, experimental work has provided evidence that the metal halide salts are attached as a unit, via a Z-type ligand binding motif, to the surface of both type II-VI and type III-V quantum dots.[17,22,89,92] The origin of the increased luminescence under this reaction mechanism has been supported by recent theoretical calculations on type II-VI quantum dots attributing the origin of the hole trap sites to undercoordinated chalcogenides on the surface of the quantum dot. Small metal halide salts should fill these vacancies on the surface, passivating the hole traps.[94] Under this mechanism, where the carboxylate group directly coordinates to the cation and the metal halide salts bind only to the undercoordinated anions, little to no loss of organic ligands would be expected. An additional complication in understanding the proposed mechanism is the effect of the polarity of the solvent in which the treatment is given. More polar solvents, such as acetone, can dissociate the metal from the halide resulting in direct halogenation and loss of organic ligand,[92,93,95] whereas less polar solvents, such as toluene, deliver the halide salt to the quantum dot surface as a single unit with the assistance of a soluble coordinating amine.[17,89]

In light of the importance in understanding the mechanism by which trap passivation occurs and the need for optimizing indium phosphide as a core material, we chose to study the treatment of quantum dots with metal halide salts. We elected to investigate the reaction of zinc chloride, zinc bromide, and indium chloride with indium phosphide quantum dots capped with a single ligand, myristate, in tetrahydrofuran, a solvent with enough polarity to solubilize both the quantum dots and the inorganic ligands, but not so polar as to dissociate the metal halide complex. These reaction conditions were chosen to simplify confounding reactions that could have occurred with mixed ligands or solvents and to give the clearest insight to the reaction mechanism. We used quantitative ^{1}H NMR and isothermal titration calorimetry to study the thermodynamics of ligands binding to the surface of the quantum

dots.[30,54,96,97]

3.2 Treatment of Indium Phosphide Quantum Dots with Metal Halide Salts

Optical measurements of the reaction of indium phosphide quantum dots and the metal halide salts are shown in Figure 3.1. The absorption spectrum (Fig. 3.1A) is almost identical before and after the reactions with only a slight redshift in the spectrum. This is likely caused by electrons in the conduction band minimum being more delocalized, reducing the band gap, as shown by theoretical calculations previously and observed when treating indium phosphide quantum dots with hydrofluoric acid.[22] A significant improvement in the luminescence quantum yield is observed after treatment, particularly with zinc chloride. This improvement is also manifest in luminescence lifetimes becoming more mono-exponential with treatment (Fig. 3.1B). Additionally, quantum yield titration measurements show an increase in luminescence over the extent of the reaction with zinc chloride (Fig. 3.1C).

^{1}H NMR was performed before and after ligand treatment.[42] Myristate is the capping ligand for these indium phosphide quantum dots—coordinating to excess indium atoms on the surface[98]—and the easiest peak to observe in ^{1}H NMR is the methyl group around 0.90 ppm (Fig. 3.2A). The broad peak corresponds to ligands bound to the nanocrystal, while the narrower triplet represents ligands that are free in solution.[18,42,49,67] Quantitative NMR measurements were made by fitting and integrating peaks to yield the fractions of the bound and unbound organic group. For the untreated sample, 189 $\pm$ 49 indium myristate ligands/nanocrystal were observed through ^{1}H NMR, resulting in a ligand coverage of 4.1 $\pm$ 1.1 indium myristates/nm^2, as determined by sizing and concentration calculations derived from UV-vis absorption data (see Appendix C.2 for a discussion on errors with this concentration and size calculator).[99] After treatment with the metal halide salts the fraction of bound ligand decreased significantly (Fig. 3.2B). Upon allowing a solution of indium phosphide quantum dots that had been treated with zinc chloride to stand for a day, the solution became cloudy and a white precipitate appeared. The precipitate was isolated and shown to be indium myristate through ^{1}H NMR, FTIR, and elemental analysis when compared with synthesized indium myristate (Appendix A.10).

The precipitate observed with the reaction with the metal halides was formed to a lesser extent when zinc bromide is used and was not observed when the quantum dots were treated with indium chloride, although the ^{1}H NMR measurements indicate that the concentration of free ligand in solution should be greater after treatment with indium chloride. The indium myristate that was synthesized to help confirm identification of the precipitate was soluble in tetrahydrofuran to a greater extent than was present in the quantum dot reactions. A potential explanation for this phenomenon is the ability for metal carboxylates to form "polymers" of metal centers bridged by carboxylate ligands.[100] Zinc halides may promote this reaction, increasing molecular weight and decreasing solubility, although this is just

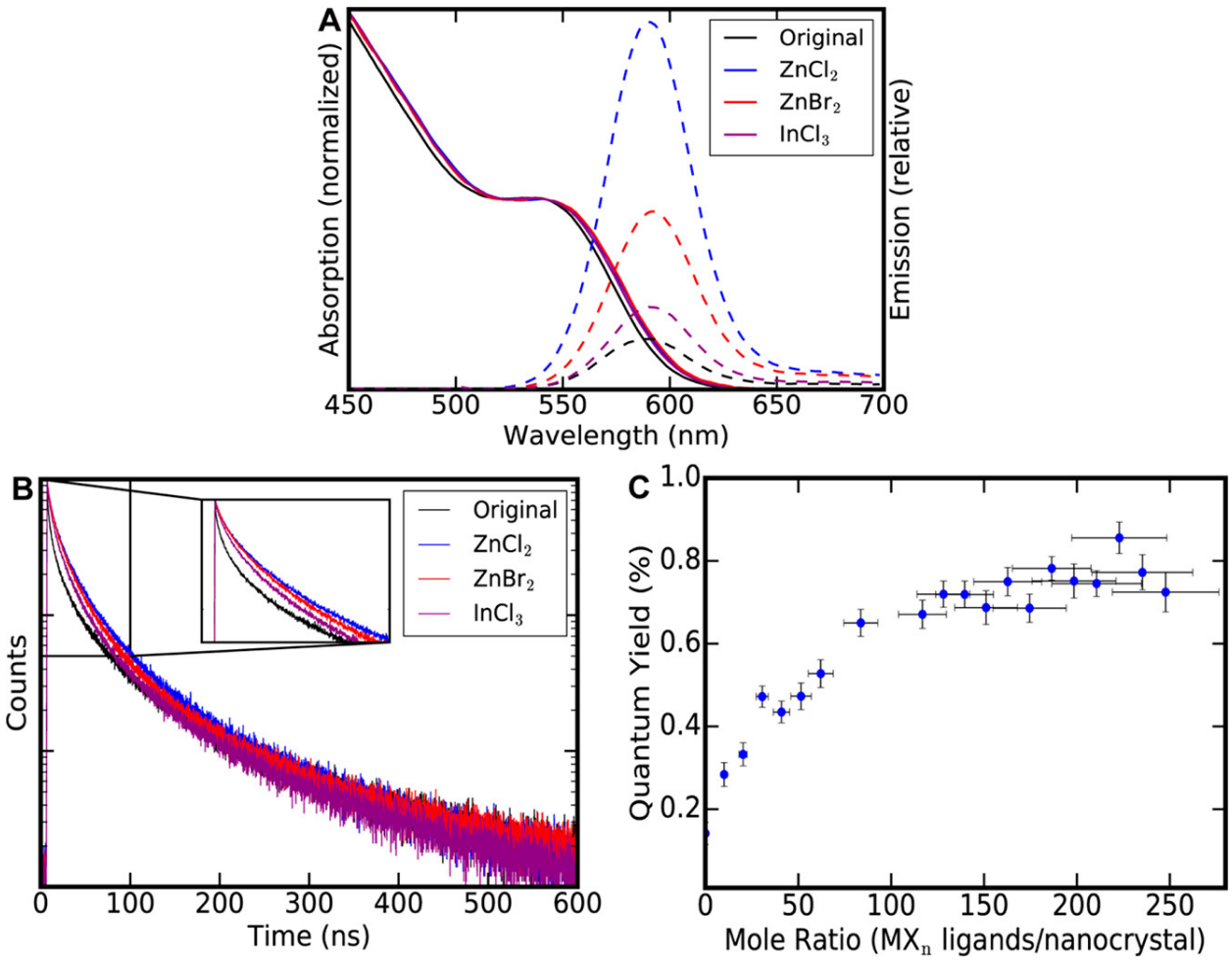


Figure 3.1: Optical measurements of InP quantum dots before and after metal halide treatment. (A) Normalized absorption measurements on as synthesized and treated indium phosphide quantum dots (solid lines) and relative luminescence measurements corrected for concentration (dashed lines). (B) Normalized luminescence lifetime measurements on as synthesized and treated indium phosphide quantum dots. Inset depicts luminescence between 0 and 100 nanoseconds. (C) Quantum yield measurements as a function of mole ratio for indium phosphide quantum dots treated with zinc chloride. The standard errors in the mole ratio and quantum yield are depicted by error bars. For all plots zinc chloride treatments are colored blue, zinc bromide treatments are red, and indium chloride treatments are purple.

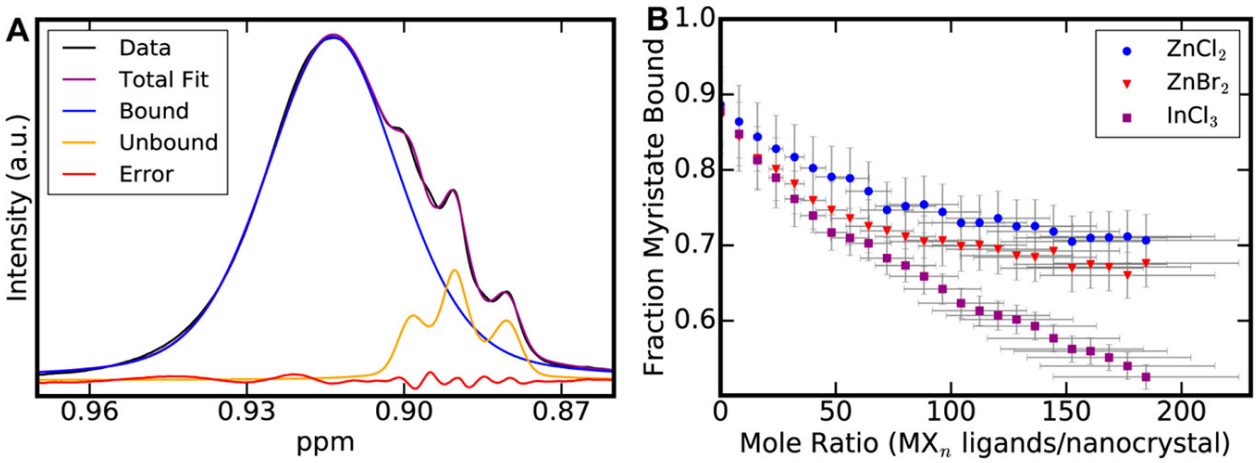


Figure 3.2: NMR measurements of InP quantum dots before and after metal halide treatment. Note that this effect is much more pronounced after treatment with indium chloride as opposed to the zinc halide salts. (A) Example ^{1}H NMR spectrum of the methyl group of myristate and the deconvolution of the bound and unbound peaks that make up the spectrum. The spectrum shown is for as-synthesized indium phosphide quantum dots. The raw spectrum is colored black, total fit is purple, bound peak is blue, unbound peak is yellow, and residual error is red. (B) Zinc chloride additions (blue), zinc bromide additions (red), and indium chloride additions (purple). indium phosphide nanocrystals were diluted in THF to a concentration of 0.032 mM and were titrated with metal halide salts dissolved in THF at a concentration of 31 mM. The standard errors in mole ratio and fraction unbound are depicted by error bars.

speculation.

Isothermal titration calorimetry measurements of the reaction with an identical set of indium phosphide quantum dots in tetrahydrofuran yielded markedly different results, suggesting several key differences in reaction mechanisms between the zinc halides and indium chloride. First, although the greatest enhancements to the luminescence of the indium phosphide quantum dots resulted from treatments with zinc chloride, both the treatments with zinc chloride and zinc bromide were endothermic whereas those with indium chloride were exothermic (Figure 3.3). Second, the reaction with indium chloride is much more extensive than with the zinc halides, and isothermal titration calorimetry reactions described above end before the reaction with indium chloride has reached completion. To obtain the cleanest thermodynamic reactions, dilute titrants are needed, and concentrations of quantum dots and metal halide salts are optimized to provide adequate signal that does not oversaturate the instrument. However, this leads to the indium chloride reaction not being finished after the titrant in the syringe is consumed. Figure 3.4 depicts the reaction of indium chloride with a different series of indium phosphide quantum dots capped with myristate at a concentration of 32 μM quantum dots and 93 mM indium chloride in tetrahydrofuran with 2.5

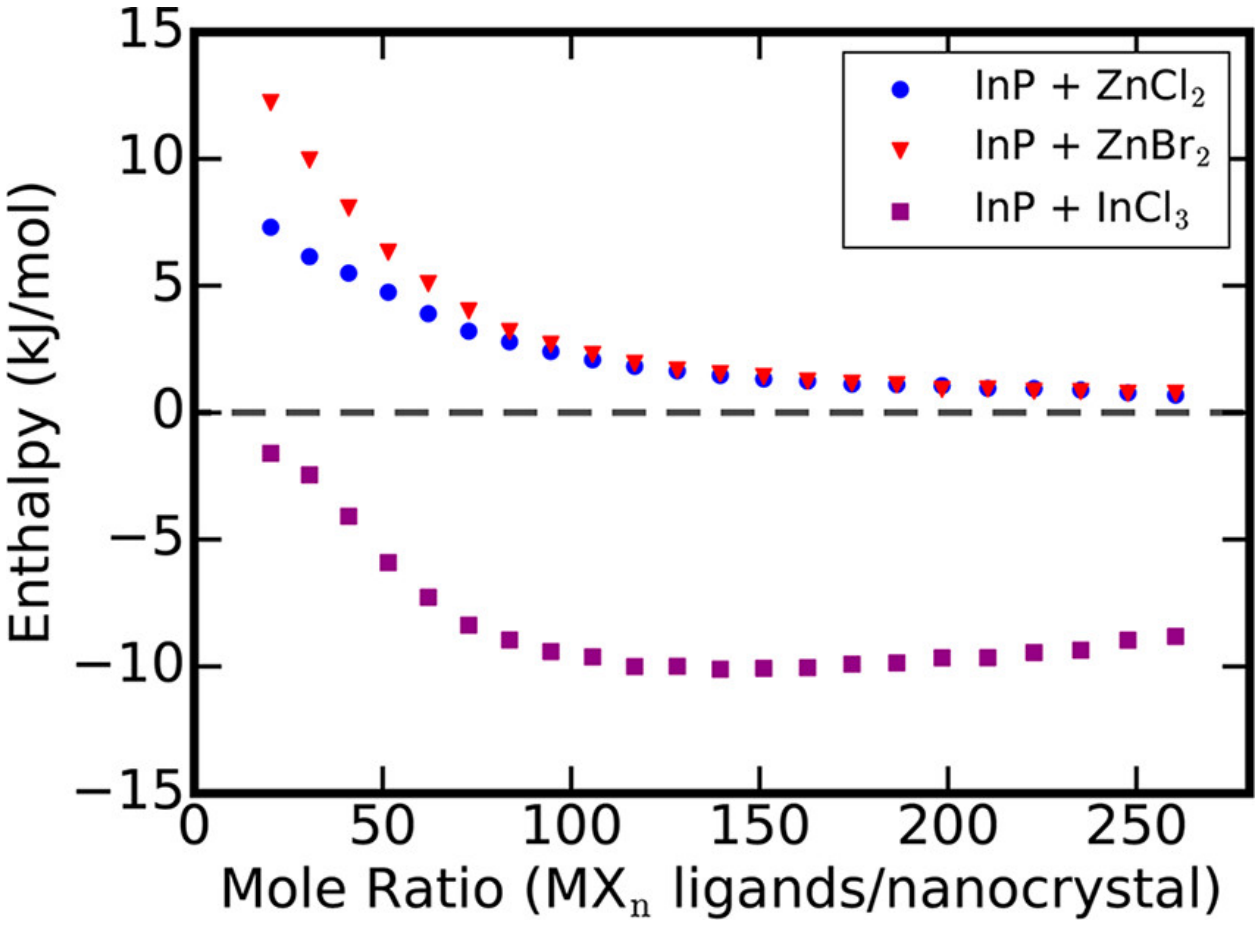


Figure 3.3: Isothermal titration calorimetry data of titrations of InP quantum dots with metal halide salts. Zinc chloride additions (blue), zinc bromide additions (red), and indium chloride additions (purple). indium phosphide nanocrystals were diluted in THF to a concentration of 0.032 mM and were titrated with metal halide salts dissolved in THF at a concentration of 31 mM. The standard error in the mole ratio increases from 10% to 20% as titrations progress, and the standard error in enthalpy is 2% for all points and is depicted by error bars.

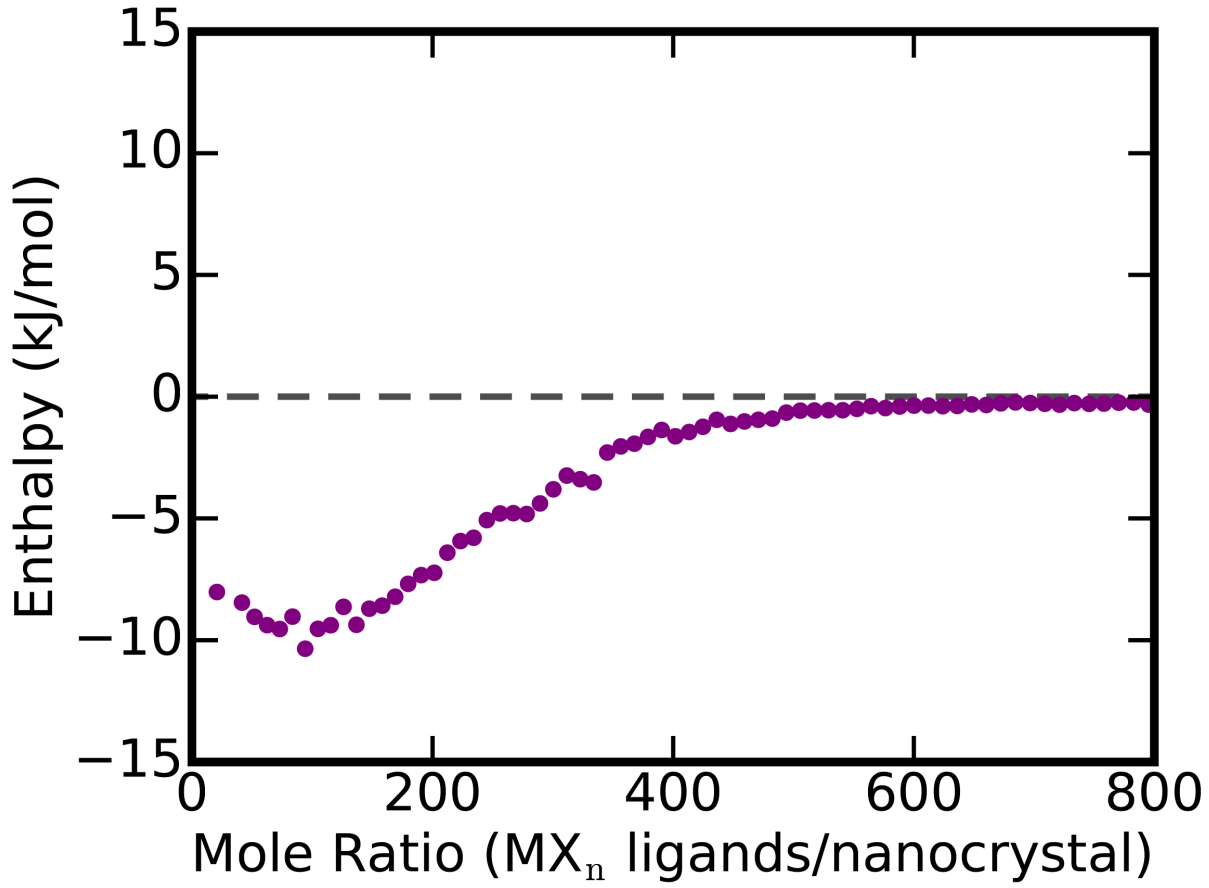


Figure 3.4: Extended indium chloride treatment to InP quantum dots.

μL injections. Lastly, the reaction with indium chloride exhibited unusual behavior, initially becoming more exothermic as the reaction progressed but later becoming less exothermic as the reaction approached completion.

The most interesting feature from the thermodynamic measurements is the unusual calorimetric titration curve of the reaction of indium phosphide quantum dots with indium chloride (Figure 3.3). For simple reactions, such as a ligand adding to an empty surface site on a nanocrystal, the measured enthalpy should progress monotonically, where the reaction is most vigorous at the beginning of the reaction as the greatest number of empty sites are available, and as the reaction progresses the measured enthalpy should approach a baseline. However, this reaction becomes more exothermic as the reaction progresses before eventually reaching completion (Figure 3.4). This unusual titration curve is critical in understanding the reaction mechanism, and illustrates that isothermal titration calorimetry is a foundational companion measurement along with ^{1}H NMR in understanding the reaction chemistry at

the surface of colloidal quantum dots. During the reactions of the myristate capped indium phosphide quantum dots with zinc chloride, zinc bromide, and indium chloride, ^{1}H NMR data show that the fraction of bound myristates is decreasing (Figure 3.2), suggesting that ligands are exchanging during the reaction. With the evidence from these two measurement techniques, we hypothesize that this unusual titration curve with indium chloride can be attributed to the additional energy needed to break inter-ligand interactions of the organic ligands on the surface of the quantum dot during the ligand exchange when ligand coverage is high, and this makes the reaction more endothermic; however, as ligands are removed from the surface, the remaining ligands will have, on average, fewer inter-ligand interactions and should be easier to remove from the surface, and this makes the reaction more exothermic.

The precipitation of indium myristate from the reaction also shows that myristate is being removed from the surface of the quantum dot in the form of indium myristate. Previously Anderson *et al.* have shown that tetrahydrofuran assists in displacing metal carboxylates from the surface of quantum dots,[16] and we suggest that coordinating tetrahydrofuran not only solubilizes the metal halide salts but also assists in removing indium myristate from the surface, and we see a significant fraction of myristate that is unbound before the reaction begins. Anderson *et al.* have also shown that amines are quite potent in displacing metal carboxylates from the surface of quantum dots.[16] Because amines are used to solubilize the metal halide salts in the reaction performed by Kirkwood *et al.*,[17] we postulate that our proposed reaction mechanism of a ligand exchange may also be applicable in their system. However, we do not dispute computational findings by Kirkwood *et al.*[17] that undercoordinated anions on the surface of colloidal quantum dots contribute to lowering of the quantum yield, as has been seen experimentally elsewhere.[16] Thus, our hypothesis of the reaction mechanism is that indium myristate is in dynamic equilibrium with the surface of the quantum dots, leaving undercoordinated phosphorus at the surface that the metal halides can bind to as a unit in a Z-type ligand fashion (Figure 3.5).

In the system studied by Kirkwood *et al.*,[17] reactions were performed at elevated temperatures and used oleylamine to solubilize the metal halide salts in toluene, whereas in this series of experiments treatments were performed at room temperature and tetrahydrofuran was used to both solubilize the metal halide salts and suspend the quantum dots. Due to this significant change in the system being studied, we performed extensive X-ray photoelectron spectroscopy, which show the presence of zinc and halides after the addition of the zinc halides, as well as the presence of chlorine after the addition of indium chloride (Figure 3.6), even after extensive washing to remove excess ligands. These measurements show that both the metal and the halide are present on the surface after treatment. Similar findings were found by Kirkwood *et al.* by using energy-dispersive X-ray measurements for elemental analysis.[17] Regarding the ^{1}H NMR analysis, this analysis could not be used in the system described by Kirkwood *et al.* as the tetradecylphosphonate methyl peak is obscured by the oleylamine used to solubilize the metal halide salts.[17]

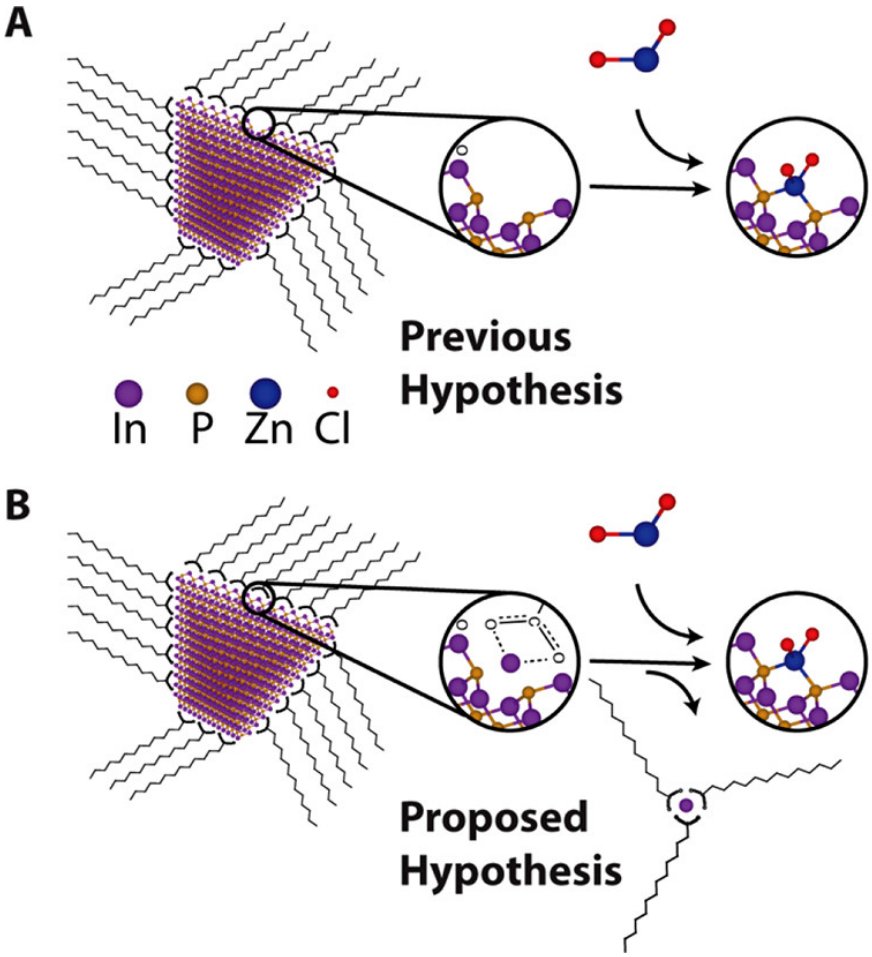


Figure 3.5: Schemes of the reaction mechanisms with metal halides. Schemes of the previously proposed reaction mechanism (A) and the newly proposed reaction mechanism (B) for the reaction of metal halide salts with colloidal quantum dots. The previously proposed reaction mechanism suggests a ligand addition, where metal halide salts passivated undercoordinated anions, while the new mechanism proposes a ligand exchange between the native indium myristates and the metal halides.

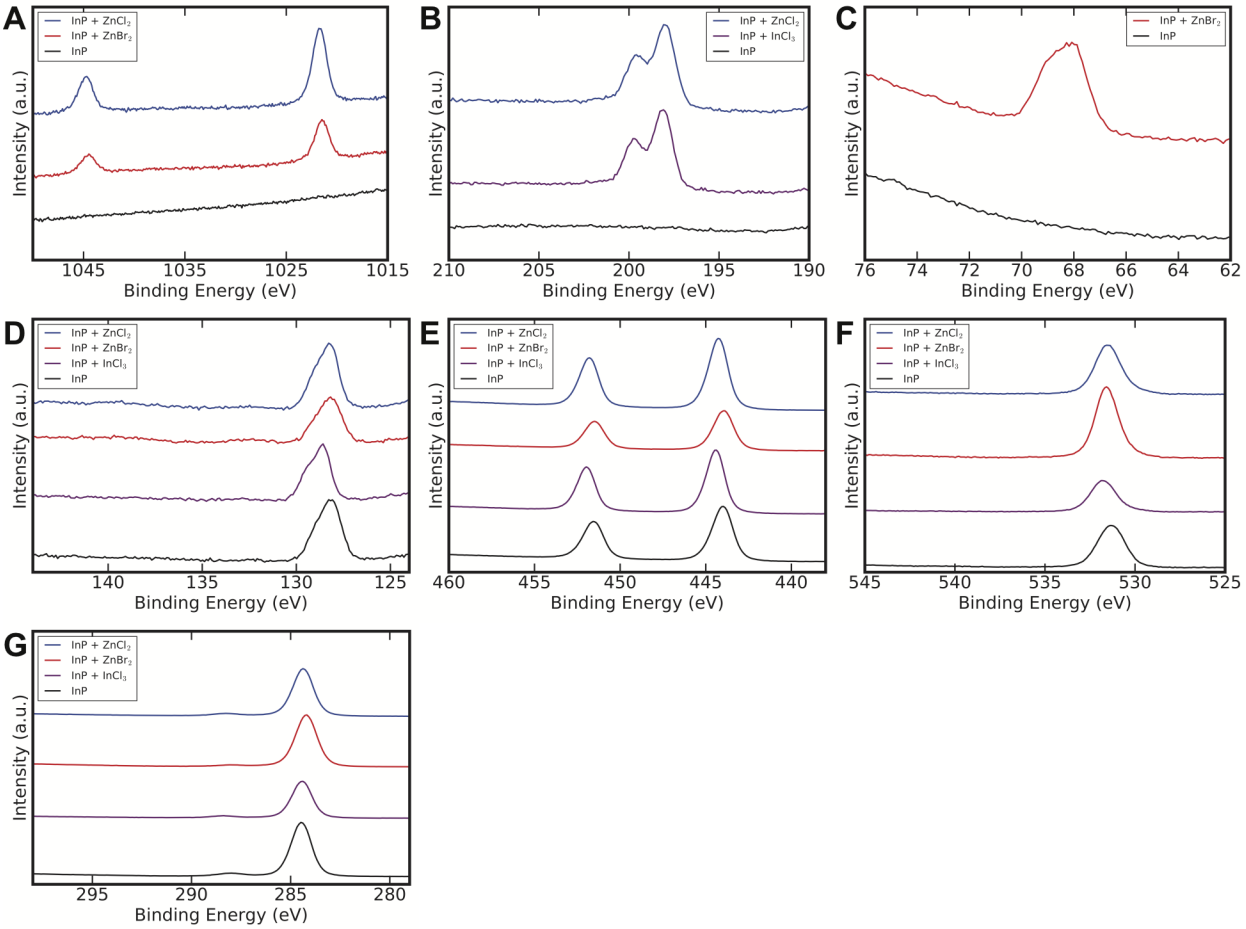


Figure 3.6: X-ray photoelectron spectroscopy spectra of InP quantum dots before and after metal halide treatment. (A) Zn 2p (B) Cl 2p (C) Br 3d (D) P 2d (E) In 3d (F) O 1s and (G) C 1s spectra of as synthesized indium phosphide quantum dots (black), zinc chloride treated quantum dots (blue), zinc bromide treated quantum dots (red), and indium chloride treated quantum dots (purple). After treatment, the quantum dots were washed with acetone and resuspended in hexanes twice to remove excess metal halide salts and free indium myristate.

3.3 Ising Models to Test Hypothesis of Reaction Mechanism

Tight ligand packing on the surface of the indium phosphide quantum dots leads to relatively strong van der Waals interactions of the organic ligands, which can be observed by thermodynamic measurements.[30,101] These inter-ligand interactions lead to the initial increase in the exothermic signal for indium chloride titrations. As more organic ligands are removed from the surface, there are, on average, fewer van der Waals interactions that must be broken during the ligand exchange, and thus there is an increase in the exothermic signal. As the titration proceeds, the surface reaches an equilibrium balance between organic and inorganic ligands, but due to the exothermic nature of the ligand exchange, the exchange occurs to a greater extent than with the zinc halides.

Beyond the enthalpy contributions to the reaction from the exchange of head groups attached to the quantum dot and the inter-ligand interactions, it is reasonable to expect that there should be a significant entropic driving force in the ligand exchange. The myristate capping ligand is a straight-chain carboxylate, and it has been shown previously that these straight-chain ligands can order on the surface of the nanocrystal.[42] By removing these ligands from the surface, both the entropy of the now less constrained displaced organic ligands and the ligands left behind at lower packing density should increase. Finally, there are likely both enthalpic and entropic contributions to the exchange due to solvating effects of both ligand species and coordination of tetrahydrofuran.

With all of these interactions occurring, simulations of the reaction are an invaluable aid to see if the proposed reaction mechanism is plausible and understand the extent of each of these contributions. The complex interplay between the binding energies of the ligands, inter-ligand interactions, and entropy changes due to organic ligands being removed from the surface during the reaction can all be investigated in a modified Ising model simulation, and a similar model has previously been used to model the nanocrystal surfaces.[42]

Self-consistent parameters for a basic model can be derived from the ^{1}H NMR data and isothermal titration calorimetry data for these reactions (Figure 3.7), and values for each parameter can be found in Table 1. There are several limitations of this Ising model, the most significant being that only nearest neighbor interactions are accounted for. While van der Waals interactions contributing to the enthalpy are likely to be short range, ordering of ligands and the entropy associated may have long range effects. Additionally, there are no empty sites on the lattice, although there are free indium myristates in solution, implying empty sites. While the modified Ising model does not perfectly fit the experimental data, and the exact values from the model should not be taken at face value, several interesting insights can be gained from the fits.

First, the difference in head binding energies between indium myristate and the metal halide salts (represented in Table 3.1 as ΔH_{head}) are exothermic in every case. However, the overall reaction with the zinc halides is endothermic as breaking inter-ligand interactions, between the native organic ligands, contributes more to the overall enthalpy as compared to

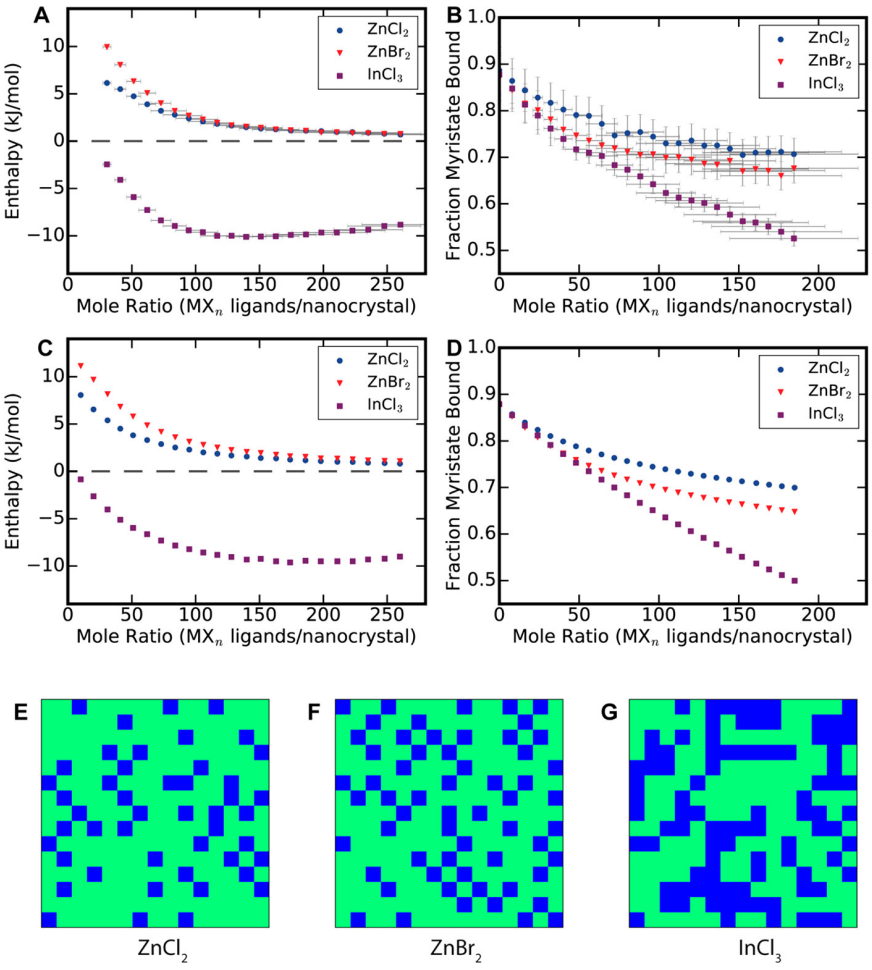


Figure 3.7: Simulated enthalpy and bound ligand fraction compared to experimental data. (A) Enthalpy of reactions derived from isothermal titration calorimetry measurements of ligand exchange. (B) ^{1}H NMR data of ligand exchange. (C) Results of a modified Ising model simulation of isothermal titration calorimetry reactions. (D) Fraction of unbound ligand as a function of mole ratio from simulations. (E) Coverage map for zinc chloride simulation. (F) Coverage map for zinc bromide simulation. (G) Coverage map for indium chloride. Green squares represent organic indium myristates while blue squares represent inorganic metal halides. The coverage maps are representative of the surface of the nanocrystal where each individual square represents a binding site on the nanocrystal.

	ΔH_{head}	$\Delta H_{tail}AB$	$\Delta H_{tail}BB$	$T\Delta S_{head}$	$T\Delta S_{tail}AB$	$T\Delta S_{tail}BB$
$ZnCl_2$	-40.18	13.06	22.78	-25.86	8.90	7.39
$ZnBr_2$	-40.56	13.49	22.81	-25.86	9.84	7.51
$InCl_3$	-55.65	13.96	13.63	-31.98	7.61	2.06

Table 3.1: Parameters (in kJ/mol) for the Ising model of the metal halide reactions. Each parameter is relative to the original lattice, which was populated with organic ligands. $\Delta H_{tail}AB$ represents the change in interaction energy from two organic ligands and an organic ligand and an inorganic ligand, while $\Delta H_{tail}BB$ represents the change in interaction energy from two organic ligands to that between two inorganic ligands, and the same system is used for $T\Delta S_{tail}AB$ and $T\Delta S_{tail}BB$

the reaction with indium chloride. This exothermic head binding energy could be caused by several factors, including changes in the coordination of myristates and tetrahydrofurans as well as solvation energy or differences in electrostatic interactions. Unfortunately, isothermal titration calorimetry and Ising model simulations can only yield composites of all of these effects and teasing them out would require several much more in depth calorimetric and computational simulations. However, it is interesting to note that the more tightly binding ligand does not necessarily result in a higher quantum yield. One of the more striking features of the reaction is the negative entropy of moving a ligand from the surface to solution, although the inter-ligand entropy does follow as predicted. This is attributed to the differences in solvation entropy between the ligands, as indium myristate is much larger than the metal halide salts and would require a much larger solvation shell.[39] Finally, there are also differences between the parameters of the zinc halide species and the indium halide species other than the binding energy. This is attributed to the additional chloride in indium chloride, which appears to affect nearest neighbor interactions differently than the zinc chloride.

One final consideration of the model is the arrangements of the ligands on the surface of the quantum dots. As mentioned above, the inter-ligand interactions from the organic ligands contribute significantly to the thermodynamics, and without these interactions the isothermal titration calorimetry data cannot be modelled. By including these interactions, the shape of the isothermal titration calorimetry measurements can be recreated. When inter-ligand interactions are included, a further consequence is that the exchanged ligands on the surface are not randomly distributed, but instead cluster together in patches as seen in the simulated maps of the ligands in Figure 3.7E–G.[42,102,103]

3.4 A Hypothesis Regarding the Improved Luminescence

The combination of reaction calorimetry and NMR studies show that metal halide reactions with the surface of indium phosphide quantum dots cannot be described accurately as a relatively simple passivation of undercoordinated anions. Any such explanation for the increase in luminescence of the quantum dots by reduction of trap sites is also called into question, although it is feasible to consider that the average number of undercoordinated phosphorus sites may be decreasing due to these treatments. However, in comparing Figure 3.1C with Figure 3.2B, improvement in luminescence appears to track with the displacement of myristates. If passivation of undercoordinated sites was the main cause of increased luminescence, we would expect a drastic improvement of luminescence at the start of the reaction as undercoordinated sites are passivated, followed by a somewhat constant luminescence with the subsequent ligand exchange.

Previously, treatments of the surface of indium phosphide quantum dots with indium carboxylates has not been shown to drastically improve quantum yield.[26,27] In the framework of passivation of undercoordinated sites, this observation has been attributed to the steric hinderance of carboxylate ligands implying that the small size of the metal halides is able to better overcome these steric effect to reach undercoordinated sites.[17] While reduction in the number of hole trap sites from undercoordinated anions is well understood to increase quantum yield,[16] the ligand exchange here appears to be a one-to-one exchange and not a simple addition, supported by comparisons of the ^{1}H NMR and isothermal titration calorimetry data as well as the simulations, meaning this explanation for increased luminescence may no longer be relevant. Work performed by Stein *et al.* and Hughes *et al.* suggest that a ligand exchange, from indium carboxylates to zinc or cadmium carboxylates, passivates the surface with divalent cations and increases the quantum yield by reducing electron trapping from undercoordinated trivalent indiums, due to steric hinderance of the three carboxylates needed for coordination.[26,27] Additionally, they claim that binding fluoride anions to indium has the same effect, as fluoride anions are small enough to bind to indium atoms on the surface without significant steric hinderance.[26]

To investigate this explanation, indium phosphide quantum dots were treated with a range of zinc and indium metal halides and the absorbance and luminescence were recorded (Figure 3.8). For a given halide, zinc salts outperform their indium counterparts, and in some cases the addition of a metal halide salt actually decreases luminescence. This observation further suggests that a simple site passivation model for the reaction is insufficient. Additionally, a pronounced red shift of the luminescence peak and absorbance spectra can be observed which increases with halide size. This phenomenon is also ascribed to the electrons in the conduction band being more delocalized, as mentioned above, and increasing halide size appears to increase this effect.[22] Treatment with fluoride salts was not included as their solubility in tetrahydrofuran was significantly less than the other salts, but addition of a saturated solution of fluoride salts improved luminescence over the chloride salts although it

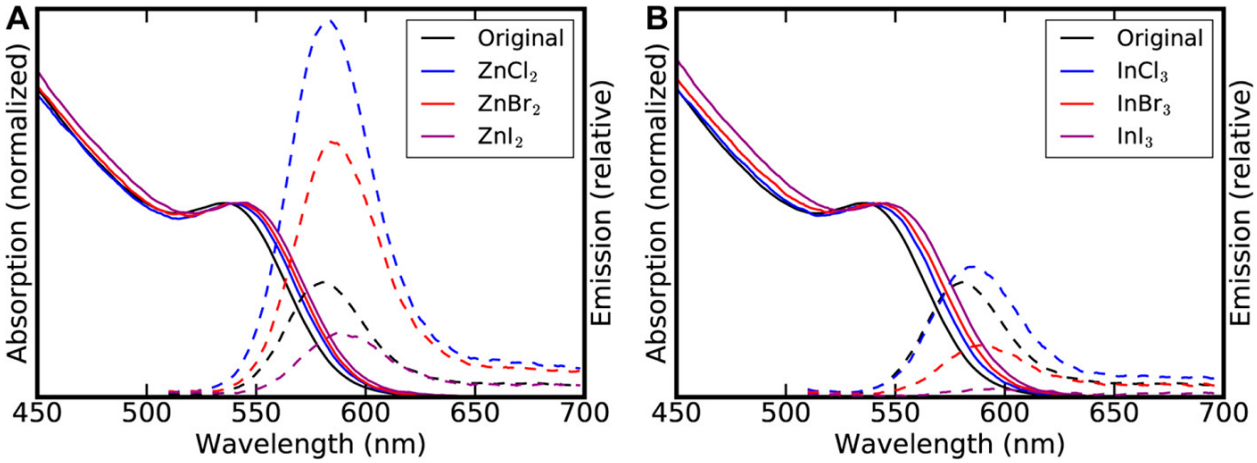


Figure 3.8: Additional optical measurements of metal halide salt treated InP quantum dots. Normalized absorption measurements on as-synthesized and treated indium phosphide quantum dots (solid lines) and relative luminescence measurements corrected for concentration (dashed lines). Note that as electronegativity of the halide decreases, luminescence decreases. (A) Reaction with zinc halides. (B) Reaction with indium halides. Additionally, note that optical measurements differ slightly from those in Figure 3.1A because of variations between synthesized samples.

was at an unknown, lower concentration. Previously, this trend where chloride salts passivate better than bromide salts has been attributed to the smaller size of the chloride cation, allowing the metal halide to better passivate the undercoordinated anions.[17]

While these measurements do not rule out the electron trapping explanation proposed by Hughes *et al.* regarding zinc and cadmium carboxylates, this trend suggests that a more complicated explanation may be in order. The evidence presented above and in the literature suggests that that the electronegativity of the coordinating ligand influences trap states, and by replacing less electronegative coordinating ligands (such as carboxylates) with more electronegative ligands (like chlorides), trapping of excitons is reduced. If less electronegative ligands (like iodides) replace the carboxylates, the quantum yield decreases. We suggest that this influences hole trap states as these electronegative anions withdraw negative charge from the surface of the quantum dot. This would explain the increase in luminescence of both type II-VI quantum dots and III-V quantum dots that has been observed, as it has recently been suggested that only hole-trap sites influence quantum yield in type II-VI quantum dots.[17,89,94] By replacing the carboxylate ligands with more electronegative halides such as chloride, more negative charge is removed from the surface and the luminescence improves. The difference observed between zinc and indium halides is attributed to the lower charge on the zinc, allowing the halides to more easily withdraw excess negative charge.

The higher energy shift of the phosphorous peak in the X-ray photoelectron spectroscopy

data (Figure 3.6D) after the addition of indium chloride as compared to the zinc chloride also supports the conclusion that the phosphorous atoms bind to the added metal. This would suggest that indium chloride has a stronger electron withdrawing effect than zinc chloride when considering a Z-type ligand scheme. However, while indium chloride appeared to have the strongest withdrawing effect, more charge may be localized at the anions in zinc chloride rather than the metal due to zinc being in a 2+ oxidation state compared to the 3+ oxidation state of indium.

Our hypothesis also agrees with the findings by Stein *et al.* and Hughes *et al.* where an exchange from indium carboxylates to divalent metal carboxylates with indium phosphide quantum dots improves photoluminescence,[26,27] suggesting that the carboxylates are able to more easily withdraw excess negative charge from divalent cations. This appears to contradict studies conducted by Kirkwood *et al.* in which the greatest improvements to luminescence occurred after treatments with indium chloride, although treatments of cadmium telluride quantum dots with cadmium chloride did significantly improve luminescence.[17] However, the extent of passivation or potential ligand exchange in this study was not rigorously characterized, obscuring more definite conclusions. We find that in our treatment with metal halide salts indium chloride exchanges with the native ligands to a much greater extent, which could be the cause of greater luminescence improvements with the treatments of cadmium telluride quantum dots. Additionally, II-VI and III-V quantum dots should be compared with care, as it is possible that there is an ideal amount of charge modulation on the surface that may be different from material to material. This concept of modulating the charge on the surface of nanoscale materials has found success in monolayer semiconductors such as MoS_2 by applying a voltage across the material to move the Fermi level.[104] Parallels between these effects and the electronic properties of ligands on the surface is under current investigation; however, significantly more work should be done from an experimental and theoretical standpoint before any firm conclusions could be reached.

Indeed, results by Hughes *et al.* suggest the ligand exchange to divalent carboxylates improves quantum yield by reducing electron trapping, in contrast with our findings and those of Kirkwood *et al.* that improvements correlate with reduced hole trapping.[17,26] These hypotheses should be studied further, perhaps by treatments of these metal halide salts using trioctylphosphine or oleylamine as a carrier ligand or through computational methods. Better understanding of these treatments and the origins of improvements in quantum yield may benefit from an in-depth, quantitative study of such treatments with metal halide and metal carboxylates with a variety of both II-VI and III-V quantum dots using techniques outlined here such as ^{1}H NMR and isothermal titration calorimetry. In the next sections, thermodynamics of ligand adsorption and impacts on luminescence properties of cadmium sulfide quantum dots will be discussed.

3.5 Challenges Regarding Absolute Ligand Adsorption Enthalpies

From the measurements on these indium phosphide quantum dots, it is evident that the combination of isothermal titration calorimetry and ^{1}H NMR can provide valuable insight into the reaction mechanism. Unfortunately, in terms of a ligand exchange, the parameters extracted from the Ising model only provide the relative binding energies of the head groups. Knowledge of the absolute adsorption energy of these species, as well as their propensity to desorb from the surface, is critical for maximizing the density of ligands on the surface in order to fully passivate trap states to improve luminescence. It is well known that undercoordinated chalcogenides are the main source of deep hole traps in type II-VI quantum dots such as cadmium selenide and cadmium sulfide, and that Z-type ligands like metal carboxylates or metal halides can passivate these traps.[16,17,94] While the organic ligands are often instrumental in the synthesis of quantum dots, they are sterically bulky and can limit the complete passivation of a quantum dot's surface. This is particularly problematic in type III-V quantum dots such as indium phosphide, where aliphatic carboxylates cannot effectively passivate higher charged terminating surfaces due to their steric bulkiness, which results in electron traps.[26,72] Understanding the surface chemistry of these metal carboxylates (as well as the thermodynamics of their adsorption) not only can be used to better describe these environments, but may also yield insights into the ligand exchange reaction equilibrium between adsorbed surface ligands and ligands free in solution.[16,18,49,98,101]

Previous attempts have been made to calculate the adsorption energies of metal carboxylate complexes.[64,65,105] However, large discrepancies still exist between studies as to the exact energies and adsorption mechanism. ^{1}H NMR spectroscopy can be used to monitor the displacement of metal carboxylates from the quantum dot surface via by L-type ligands that coordinate to the metal. Utilizing ^{1}H NMR measurements, studies carried out by Drijvers *et al.* and Singh *et al.* suggest that the surface of cadmium chalcogenide quantum dots may have multiple adsorption sites for cadmium carboxylates.[64,65] Similarly, Kessler *et al.* modeled the displacement of lead oleate species from lead sulfide with one and two-site models where the nanocrystal faceting changed as a function of size.[66] However, a previous study by Li *et al.* indicates that there is only one adsorption energy of carboxylates to cadmium selenide surfaces.[106] Since it has been challenging to directly measure the adsorption energy of the metal carboxylates to the surface, computational chemistry methods have been employed. For example, Drijvers *et al.* used DFT to calculate the adsorption energy of cadmium chloride to the surface of a faceted cadmium selenide quantum dot. They found that the adsorption energy for cadmium chloride varied from -106.8 to -256.6 kJ/mol. This was supported by their ^{1}H NMR measurements, which indicated the existence of at least two different adsorption sites on the surface of the quantum dots. However, from their ^{1}H NMR measurements and fitting of adsorption constants, they determined that this difference in the free energy of the two sites should be in the range of 12–16 kJ/mol.[64] Singh *et al.* found that the adsorption energy for cadmium chloride to the surface of a cadmium sulfide

quantum dot varied from -132.4 to -298.3 kJ/mol using similar calculations.[65] In a separate study, Tamukong *et al.* used DFT to calculate the adsorption of acetate, cadmium acetate, and the ionic cadmium acetate^{+1} acetate^{-1} pair to the surface of cadmium selenide clusters, and found that the range of adsorption energies for cadmium acetate or the ionic pair ranged from -84.9 kJ/mol to -503 kJ/mol.[105] From these calculations, the adsorption energies of the ionic pair were found to be greater than those of the neutral cadmium acetate ligands. However, it has been shown that there exists a variety of carboxylate coordination structures on the surface of quantum dots, suggesting that both types of structures are likely present.[25,98] Additionally, it should be expected that for faceted particles, the adsorption energies of metal carboxylates would be facet dependent.

While evidence for multiple adsorption sites of carboxylates has been found, less work has considered the effects of the carboxylate's aliphatic chain. From the observations discussed previously, it is evident that interactions of ligands with the surface of a nanocrystal are dependent on neighboring ligands. Therefore, as the local conditions experienced by a ligand change with ligand coverage, associated thermodynamic constants can also change in a complex manner. To further study the binding energy of metal carboxylates to the surface of colloidal quantum dots, we elected to study the adsorption of cadmium oleate to the surface of cadmium sulfide quantum dots via isothermal titration calorimetry and ^{1}H NMR. Tetrahydrofuran (a weak L-type ligand that can displace metal carboxylates) was used as the solvent to create a dynamic ligand environment. Cadmium sulfide was selected as the quantum dot of study because it is the main material used to shell cadmium selenide quantum dots, which have reached some of the highest reported quantum yields.[76]

3.6 The Adsorption of Cadmium Oleate to Cadmium Sulfide Quantum Dots

Zinc blende cadmium sulfide quantum dots capped exclusively with oleates were synthesized using typical hot-injection methods. The crude quantum dots were then purified through multiple washing cycles using tetrahydrofuran as the solvent and acetone as the anti-solvent. The evolution of the optical properties during sequential washing steps is depicted in Figure 3.9A. TEM characterization (Appendix A.3) reveals monodisperse, spherical quantum dots with an average diameter of 4.3 nm $\pm$ 0.4 nm. Washing the quantum dots in tetrahydrofuran and acetone decreases the luminescence of both the band-edge emission and the trap state emission, which has been attributed to the removal of cadmium oleate from the surface of the quantum dots.[16] Through sequential washing steps, cadmium oleate ligands can thus be gently removed from the surface creating ligand-deficient quantum dots. This hypothesis is further supported by the increased luminescence shown in Figure 3.9B, where the addition of cadmium oleate to the ligand-deficient quantum dots greatly increased the luminescence, indicating that the added cadmium oleate adsorbed to the surface of the quantum dots. Additionally, the cadmium sulfide peak emission shifts from 435 nm to 440

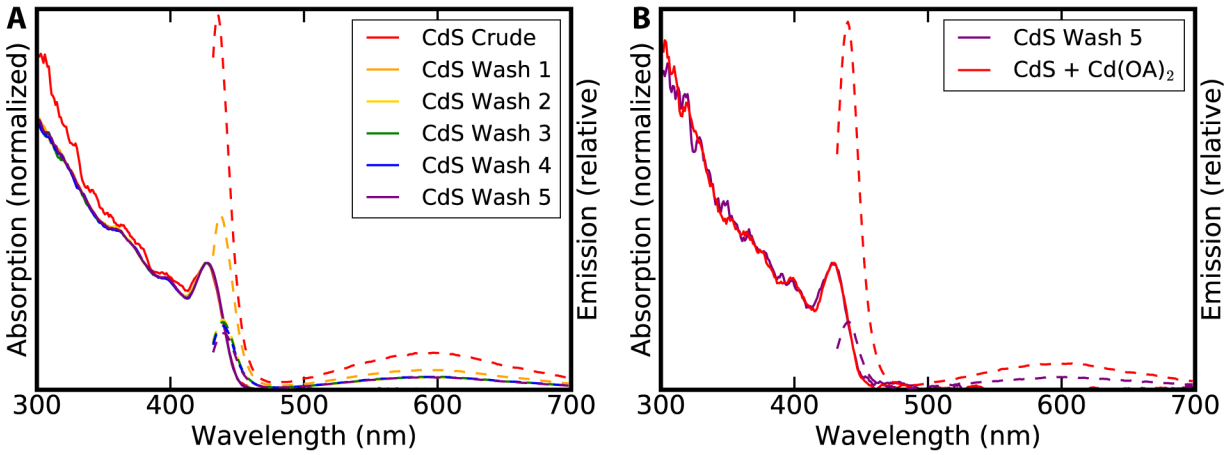


Figure 3.9: Absorption and luminescence of washed CdS quantum dots (A) Absorption (solid lines) and luminescence (dashed lines) spectra of cadmium sulfide quantum dots during washing cycles using tetrahydrofuran and acetone. As the washing cycle progresses, the relative luminescence of the quantum dots decreases, both from the band-edge emission and the trap state emission. This is attributed to cadmium oleates being removed from the surface by tetrahydrofuran, leaving undercoordinated sulfurs and hole-trapping. (B) Absorption and luminescence spectra of the thoroughly washed cadmium sulfide quantum dots before and after treatment with excess cadmium oleate. The addition of cadmium oleate reverses the drop in luminescence for both band-edge emission and trap state emission, supporting the hypothesis that during the washing steps cadmium oleate is being displaced from the surface. Note that the concentration of the nanocrystals in solution in panel (B) were taken from solutions before and after the isothermal titration calorimetry measurements and are at lower concentrations than the nanocrystals in solution in panel (A), which were taken during the washing steps, thus the spectra are slightly different and the absorption spectra in (B) are slightly noisier.

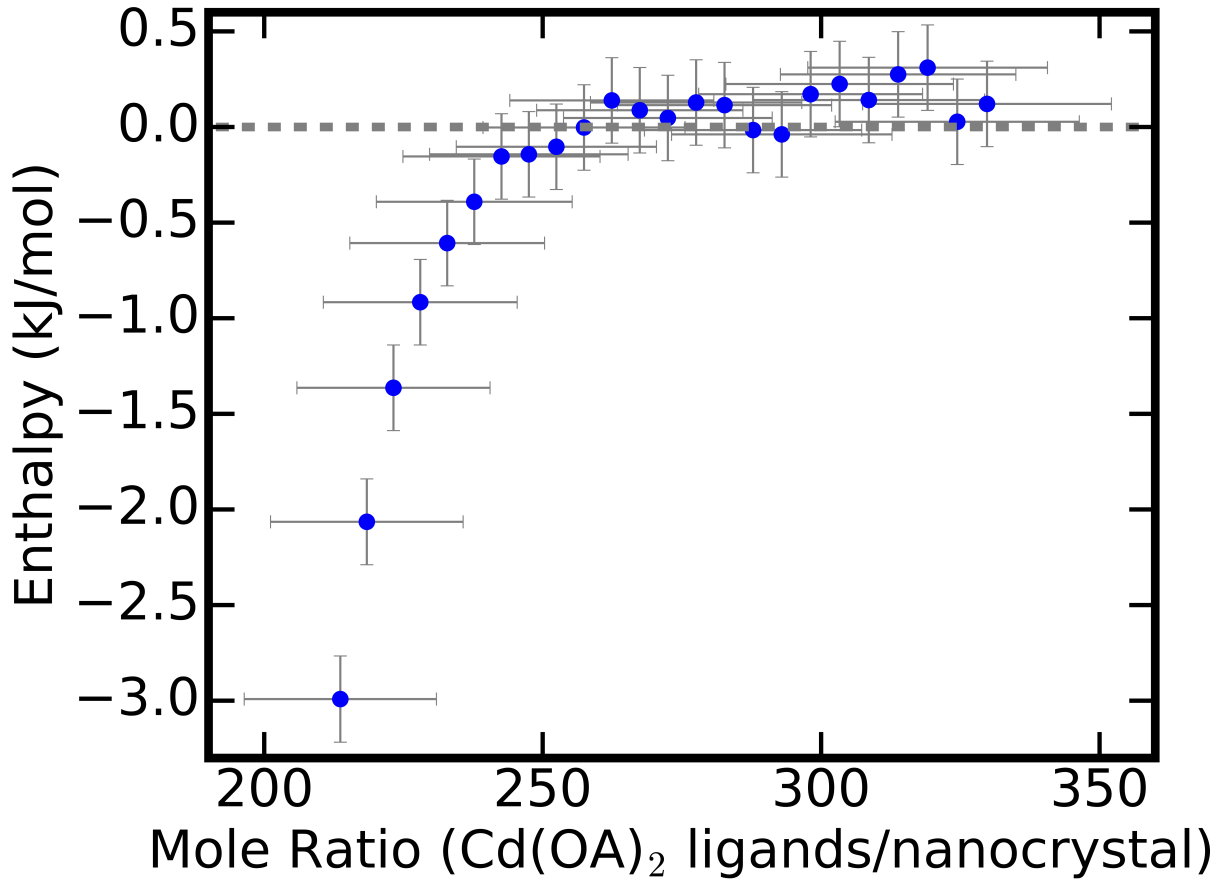


Figure 3.10: Enthalpy of addition of cadmium oleate to washed CdS quantum dots. The enthalpy of adsorption of cadmium oleate to the surface of the cadmium sulfide quantum dots is quite small, attributed to breaking tetrahydrofuran dative bonds to cadmium oleate during the process. Cadmium oleate was added past the saturation point to ensure that the surfaces of the quantum dots have nearly full-coverage at the reaction endpoint. Note that the titration reaction begins at a relatively high mole ratio due to the presence of cadmium oleates, on the surfaces of quantum dots and free in solution, before any addition.

nm during the washing process. While the emission intensity recovers after the addition of cadmium oleate, the peak position remains at 440 nm. This is attributed to size selection during washing, where the smallest cadmium sulfide quantum dots, which have higher frequency emissions, are lost to the supernatant. This loss of smaller particles is also supported by the observation that the first exciton peak narrows after the first washing step.

To measure the adsorption energy of cadmium oleate to the surface of the cadmium

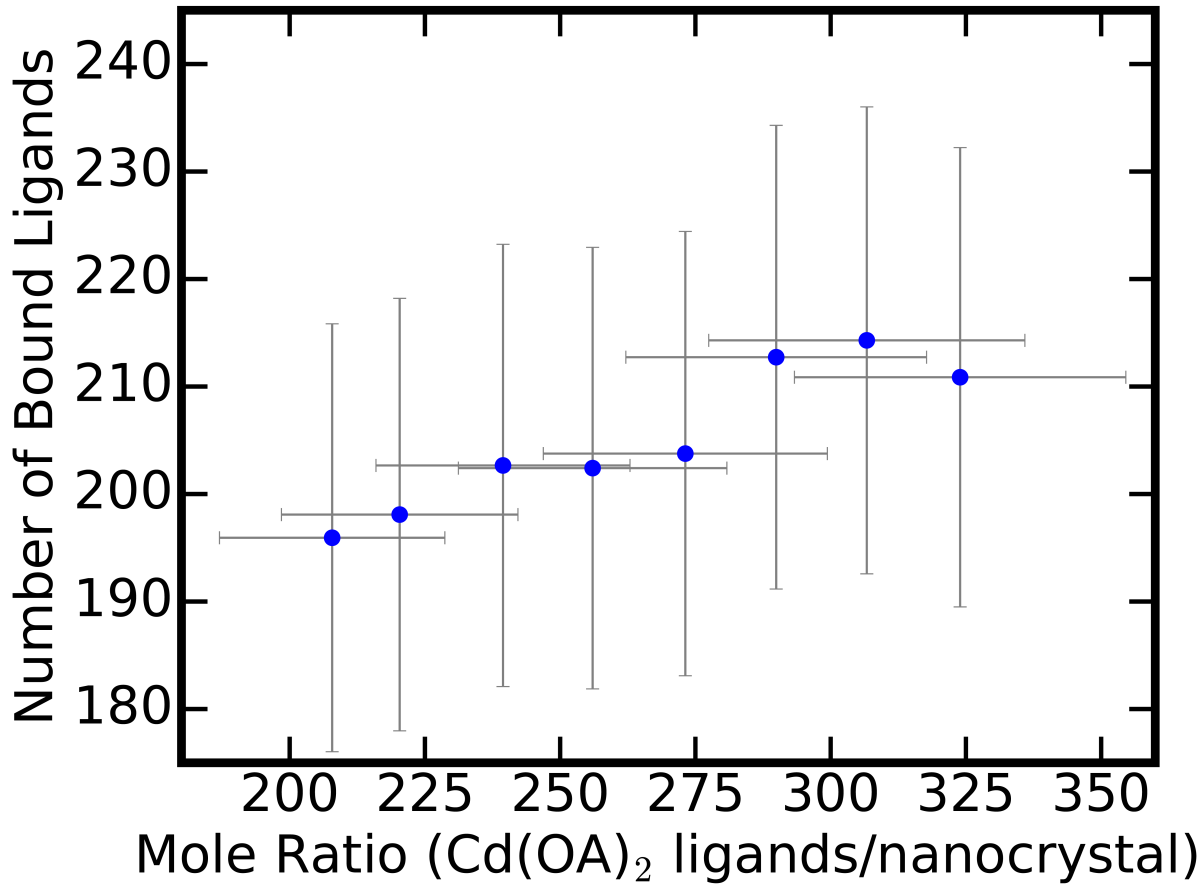


Figure 3.11: Number of adsorbed ligands per CdS quantum dot as a function of mole ratio.

sulfide quantum dots, isothermal titration calorimetry and ^{1}H NMR measurements were performed. The thoroughly washed quantum dots were titrated with a solution of cadmium oleate, and the resulting heats of reaction are recorded in Figure 3.10. Measurements were replicated and averaged due to the low net signal, and the uncertainty is higher than many other isothermal titration calorimetry measurements. The addition of cadmium oleate to the quantum dots is exothermic, indicating that cadmium oleate is adsorbing to the quantum dots. As more cadmium oleate is added, subsequent injections become less exothermic as the surface of the quantum dots becomes saturated. This can be observed as a plateau at 0 kJ/mol that begins at a mole ratio of 260 cadmium oleates nanocrystal (Figure 3.10).

This is further supported by quantitative ^{1}H NMR measurements, taken in tetrahydrofuran-d_8, of the oleate methyl group peak during the titration with cadmium oleate, depicted in Figure 3.11. Paralleling the isothermal titration calorimetry measurements in Figure 2, the

number of bound ligands measured by NMR plateaus at 210 ligands per nanocrystal. Based on the integration of the methyl resonance in the ^{1}H NMR data and utilizing known extinction coefficients to determine the concentration of quantum dots in solution, the average cadmium oleate coverage of the ligand-deficient quantum dots was determined to be 196 $\pm$ 20 ligands adsorbed per nanoparticle, corresponding to a ligand density of 3.26 $\pm$ 0.73 ligands/nm^2. After the addition of cadmium oleate, the ligand coverage increased to 211 $\pm$ 21 ligands adsorbed per nanoparticle, corresponding of 3.51 $\pm$ 0.79 ligands/nm^2. The ligand coverage of nanoparticles isolated in hexanes was found to be 3.43 $\pm$ 0.79 ligands/nm^2. These calculations are consistent with measurements by Singh *et al.*[65] Although the ligand coverage increased with the addition of cadmium oleate, the increase in ligand coverage is small. Meanwhile, the errors in quantifying such a small increase in ligand coverage using ^{1}H NMR are relatively large (Figure 3.11). In this sense, the isothermal titration calorimetry measurements are superior to the ^{1}H NMR measurements as they are more sensitive to the addition of ligands to the surface of the nanoparticles. From the isothermal titration calorimetry measurements in combination with the ^{1}H NMR data, we estimate that the average binding enthalpy of cadmium oleate to the surface of the quantum dots is approximately -3 kJ/mol.

The use of L-type ligands, such as tetrahydrofuran, has previously been shown to displace metal carboxylates from the surface of a nanocrystal, although among L-type ligands, tetrahydrofuran is a somewhat weak displacer.[16,64] Using tetrahydrofuran as the solvent for the nanocrystals transforms the static ligand shell into a dynamic one, where an equilibrium between the ligands on the surface of the quantum dot and ligands free in solution is established. This dynamic equilibrium can be utilized to disassociate ligands from the surface of the quantum dot through multiple washing steps to create a ligand-deficient quantum dot.

By adding additional free ligand to the solution, an equilibrium can be re-established in which more metal carboxylate ligands are adsorbed to the surface due to the high free ligand concentrations, thus restoring the luminescence of the cadmium sulfide quantum dots (Figure 3.9B). The enthalpy of this reaction can be measured by isothermal titration calorimetry. To our knowledge, this is the first direct measurement of the adsorption thermodynamics of metal carboxylates to the surface of colloidal quantum dots, although several attempts have been made to determine these types of values indirectly or through computations.[64,65,105]

3.7 An Ising Model to Estimate Absolute Thermodynamic Parameters

Ideally, an equilibrium constant could be calculated from the ^{1}H NMR measurements to determine the Gibbs free energy of the reaction. By combining this with the isothermal titration calorimetry results, the entropy of the reaction could also be calculated. However, there are two main complications with this approach. First, the change in adsorbed ligands over the course of this reaction is fairly small while the error in quantitative ^{1}H NMR

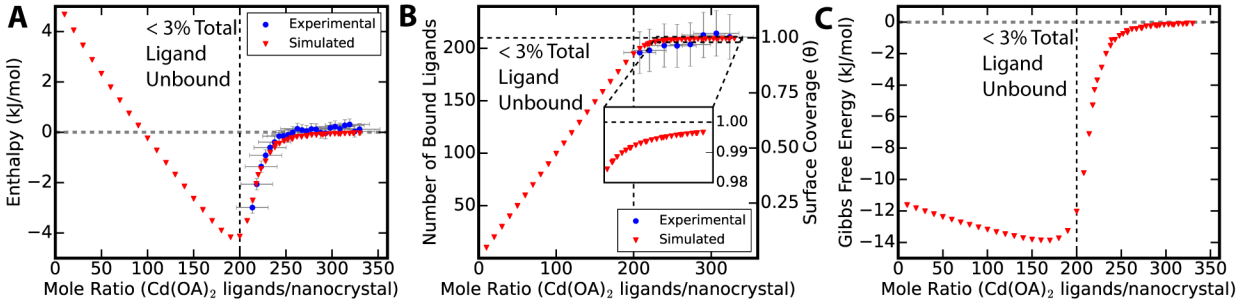


Figure 3.12: CdS Ising model simulated data compared to the experimental results. Experimental results are represented by blue circles and simulated results are represented by red triangles. Error in experimental results is depicted by gray error bars. (A) isothermal titration calorimetry experimental results of the titration reactions and simulated enthalpy from the Ising model. (B) Total number of adsorbed ligands from ^{1}H NMR and Ising model simulations. (C) Simulated Gibbs free energy of the titration reaction.

is fairly large, making this method insufficient for accurate calculations of an equilibrium constant. Second, the simplest isotherm model that can fit the data for adsorption of ligands to the surface of a nanocrystal, the Langmuir isotherm,[48,106,107] neglects interactions between adsorbates. As discussed previously, inter-ligand interactions between the long aliphatic chains have been shown to be non-negligible, particularly when dealing with such small enthalpies of adsorption. While isotherms such as the Fowler-Guggenheim isotherm can account for inter-ligand interactions,[108] without a more complete isotherm across a range of ligand concentrations, these methods fail as well. L-type ligands that bind to the metal carboxylates more strongly, such as tetramethylethylenediamine (TMEDA),[64] could strip the ligands more efficiently. However, this introduces additional reactions on the surface of the nanocrystal that would make studying the thermodynamics significantly more complex, negating the advantages of using tetrahydrofuran as the solvent to simply enable a dynamic ligand shell.

Rather than use an isotherm, we elected to again use a modified Ising model simulation.[12,42,68–70] Due to the limited data set, ensuring a unique fit for the Ising model parameters is challenging. However, assuming that inter-ligand interaction parameters and entropy of ligand binding parameters are similar in magnitude to those found in the previous experiment with complete reaction datasets and using those as a starting point for the optimization, the Ising model simulation optimization was able to find consistent fitting parameters.

The results of the Ising model are depicted in Figure 3.12, while the parameters used for the optimized fit are found in Table 3.2. While the simulated enthalpy, depicted in Figure 3.12A, is consistent with the experimental data within the experimental range, the behavior appears more unique at mole ratios below the experimental range. The simulated behavior

ΔH_{head}	ΔH_{tail}	$T\Delta S_{head}$	$T\Delta S_{tail}$
4.98	-2.85	16.53	-1.88

Table 3.2: Parameters (in kJ/mol) for the Ising model of the cadmium oleate reaction. The parameters are relative to the empty space, which had zero head interaction energy and zero nearest-neighbor interaction energy.

of the reaction enthalpy in this lower range is, however, expected from a reaction involving Van der Waals forces of inter-ligand interactions. As ligand coverage increases, the average number of nearest neighbors increases, causing the reaction to become more exothermic before becoming less exothermic. As the surface of the nanocrystal then becomes saturated, fewer ligands are added to the surface, and the enthalpy returns to zero. These results indicate that the enthalpic contribution of inter-ligand interactions plays an important role in dictating the addition of cadmium oleate to cadmium sulfide quantum dots.

While inter-ligand interactions on the surface of a nanocrystal influence the thermodynamics of reactions, they are much weaker than inter-ligand interactions observed in self-assembled monolayers of alkanes, which reportedly have an estimated enthalpy between -0.8 and -1.7 kJ/mol for each CH_2 unit.[109,110] This can be attributed to three factors. First and foremost, these enthalpies are relative to the solvated cadmium oleate ligand, not to the ligand in vacuum. Second, the bent chain nature of oleate contributes to significantly weaker van der Waals forces between the chains. Finally, the curved nature of the ligand shell would also spread the ligands out more than they would be on a flat surface, further decreasing their inter-ligand interactions.

In addition to the enthalpy, entropy also plays a role in the addition of cadmium oleate the surface of cadmium sulfide quantum dots. There is a significant gain in entropy when ligands bind as the solvation shell around the ligand is disrupted. Beyond the Van der Waals interactions between the ligands, there is also an entropy loss when the ligands adsorb to a quantum dot surface that has dense ligand coverage. Internal rotations of the long aliphatic chains become restricted by neighboring ligands, resulting in a loss of vibrational entropy. From the Ising model simulations, the inter-ligand van der Waals interactions appear to be stronger than the inter-ligand entropic effects. From these measurements, we find further evidence that the entropy of ligands adsorbing and desorbing from the surface plays a critical role in governing the thermodynamics of ligands on quantum dot surfaces.

From the Ising model simulations, there is approximately one empty site per nanocrystal, on average, at the saturated ligand densities calculated (a difference which could not be quantified by ^{1}H NMR due to instrument limitations and error in the spectra analysis) and increasing cadmium oleate concentrations in the feasible range does not appreciably increase the average number of adsorbed ligands to 100% coverage (Figure 3.12B inset). Additionally, from these Ising model simulations of the ^{1}H NMR data (Figure 3.12B), it becomes clear that reaching low ligand coverages is inaccessible by this method of gently stripping ligands off with tetrahydrofuran as the solvent. Below a total ligand density of 200 cadmium oleates

per cadmium sulfide quantum dot, the amount of free ligand that could be washed away in subsequent washing steps is less than 3% of the total ligand density, as determined from the Ising model. This explains why subsequent washing steps are less impactful on the luminescence of the quantum dots.

Combining the enthalpic and entropic contributions determined from the Ising model simulations, an overall Gibbs free energy for the adsorption of cadmium oleate to the quantum dot surface can be determined. Because the enthalpy and entropy change over the course of the titration, the Gibbs free energy also changes accordingly. The calculated Gibbs free energy for adsorption of a ligand ranges from -15.43 kJ/mol to -11.55 kJ/mol depending on the local adsorption environment. This corresponds to a variable equilibrium constant ranging between $5.0 \cdot 10^2$ M^{-1} to $1.1 \cdot 10^2$ M^{-1}, or a factor of about 5. Thus, it is difficult to assign a general, fixed equilibrium constant for the ligand addition when it is explicitly determined by ligand density, i.e., the binding of ligands to neighboring sites cannot be considered independently due to interactions. When considering the Gibbs free energy of the reaction, the titration curve looks more traditional with a negative Gibbs free energy of adsorption, further indicating that this reaction is driven mainly by entropic considerations (Figure 3.12C).

3.8 Computational Calculations of Thermodynamic Parameters

From the Ising model, the adsorption enthalpy of cadmium oleate to the surface of cadmium sulfide quantum dots is calculated to be at most -6.42 kJ/mol, depending on nearest neighbor interactions. At face value, one of the more surprising results is how weakly cadmium oleate adsorbs to the surface of the cadmium sulfide quantum dots. However, this is easily explained if tetrahydrofuran is dissociating from the cadmium oleate complex as it is added to the surface, resulting in a positive enthalpic contribution that would counteract the negative contribution of cadmium oleate being added to the surface.[111–113] Additionally, the organic ligands likely reorient around the metal center when moving from the liquid phase to the surface of the quantum dots, which may also contribute to the adsorption energy on the surface of quantum dots.[100]

To assess whether the dissociation of tetrahydrofuran from cadmium oleate is a reasonable explanation for the low adsorption enthalpy, coupled cluster single-double and perturbative triple, or CCSD(T), computational chemistry calculations were employed. To estimate the energy lost when breaking the cadmium oleate tetrahydrofuran complex, calculations were performed on cadmium acetate molecules with zero, two, and four coordinating tetrahydrofuran molecules (further referred to as $Cd(OAc)_2$, $Cd(OAc)_2 \cdot 2THF$, and $Cd(OAc)_2 \cdot 4THF$, respectively). It has previously been reported that two L-type ligands will readily form a complex with the cadmium carboxylate.[64] However, in the present system, tetrahydrofuran acts as the solvent and is therefore present in significant excess, and it becomes less clear

Reaction	ΔH	TΔS	ΔG
$Cd(OAc)_2$ + 2THF → $Cd(OAc)_2$·2THF	-194.6	-117(-55)	-78(-140)
$Cd(OAc)_2$ + 4THF → $Cd(OAc)_2$·4THF	-326	-258(-135)	-68(-191)
$Cd(OAc)_2$·2THF + 2THF → $Cd(OAc)_2$·4THF	-131.4	-141(-80)	10(-51)
$2Cd(OAc)_2$ + 4THF → $2Cd(OAc)_2$·2THF	-389	-234(-110)	-155(-279)
$2Cd(OAc)_2$ + 4THF → $Cd(OAc)_2$·4THF + $Cd(OAc)_2$	-326	-258(-135)	-68(-191)
$2Cd(OAc)_2$ + 8THF → $2Cd(OAc)_2$·4THF	-652	-516(-270)	-136(-382)
CdS_{NC} + $Cd(OA)_2$·4THF → CdS_{NC}·$Cd(OA)_2$ + 4THF	-4.98 to -6.42	16.53 to 9.01	-11.55 to -15.43
CdS_{NC} + $Cd(OA)_2$ → CdS_{NC}·$Cd(OA)_2$	-321 to -332	-118 to -126	-203 t0 -206

Table 3.3: Thermodynamic quantities calculated for cadmium carboxylate reactions through computational methods and isothermal titration calorimetry in kJ/mol at T = 298.15 K. Note that the coordination calculations for cadmium acetate and cadmium oleate were assumed to be roughly equivalent. Values in paratheses are corrected from the gas phase calculations. CdS_{NC} refers to a cadmium sulfide nanocrystal.

what the complex in solution will be, so both $Cd(OAc)_2$·2THF, and $Cd(OAc)_2$·4THF were evaluated. The values from the computations and combined computational and calorimetric measurements are tabulated in Table 3.3, while the raw computational results can be found in Appendix D.5.

From these calculations, the coordination energy of $Cd(OAc)_2$·2THF from cadmium acetate and two tetrahydrofuran molecules was found to be -194.6 ± 8.4 kJ/mol (-97.3 kJ/mol THF), while the coordination energy to $Cd(OAc)_2$·4THF from cadmium acetate and four tetrahydrofuran molecules was found to be -326 ± 10 kJ/mol (-82 kJ/mol THF). Forming the additional two bonds when moving from $Cd(OAc)_2$·2THF to $Cd(OAc)_2$·4THF has a change in energy of -131.4 ± 8.4 kJ/mol (-65.7 kJ/mol THF). Beyond coordination energy, the entropy loss due to coordination and solvation should also be considered, as $T\Delta S_{head}$ has the largest contribution in the Ising model. The solvation contribution was also been found to be significant in the previous Ising model-simulation. In the gas phase, the loss in entropy from coordinating tetrahydrofuran molecules to cadmium acetate can be calculated by quantum calculations, and results of these calculations can be found in Appendix D.5. The change in the quantity defined as temperature multiplied by entropy (TS) for the coordination of two tetrahydrofuran molecules to cadmium acetate at 298.15 K is -117 kJ/mol (-58 kJ/mol THF) and -258 kJ/mol (-65 kJ/mol THF) for the coordination of four tetrahydrofuran molecules to cadmium acetate. Coordinating the additional two tetrahydrofuran molecules when moving from $Cd(OAc)_2$·2THF to $Cd(OAc)_2$·4THF has a change in TS of -141 kJ/mol. However, these calculations significantly overestimate the entropy of molecules in the liquid state.[113] Fortunately, estimations for losses in entropy due to coordination in the liquid state have previously been determined,[114] and we can estimate that the gas to liquid phase correction for tetrahydrofuran is 31.01 kJ/mol in terms of TS (see Appendix D.5 for details and calculations). Thus, coordinating two tetrahydrofuran molecules to cadmium acetate in the liquid state actually has a TS loss of only -55 kJ/mol (47% of the gas phase TS), and coordinating four tetrahydrofuran molecules to cadmium acetate in the liquid state has a TS loss of only

-135 kJ/mol (55% of the gas phase entropy). When compared with the calculated bond energy of coordinating the THF molecules, this indicates that $Cd(OAc)_2{\cdot}4THF$ would be the most stable complex in an excess of tetrahydrofuran in the liquid phase. However, it would be much more favorable to form two $Cd(OAc)_2{\cdot}2THF$ complexes (ΔG = -279 kJ/mol) rather than one $Cd(OAc)_2{\cdot}4THF$ complex (ΔG=-191 kJ/mol) if tetrahydrofuran is the limiting reagent, hence why other researchers have found a molar ratio of 2:1 for L-type ligands to metal carboxylate complexes when titrating with L-type ligands.[16,64] These results suggest that the formation of $Cd(OAc)_2{\cdot}4THF$ is favored in excess tetrahydrofuran. With these computational results we can estimate the thermodynamics of binding of cadmium oleate to the surface of cadmium sulfide quantum dots.

The adsorption energy of cadmium oleate to the surface of cadmium sulfide nanocrystals in a nonpolar solvent can be corrected by combining the binding energy of tetrahydrofuran with the adsorption energy found from the Ising model. When surface coverage is high, this results in an adsorption enthalpy of -332 kJ/mol assuming that the coordination energies of tetrahydrofuran calculated for cadmium acetate are similar to those for cadmium oleate. Although direct thermochemical data is not available for cadmium oleate (which would allow the calculation of the coordination entropy of cadmium oleate to the surface of a cadmium sulfide quantum dot, as was performed for the coordination of tetrahydrofuran to cadmium oleate), the coordination entropy of cadmium oleate to the surface of a cadmium sulfide quantum dot can be calculated from the Ising model. The Ising model calculates that the total TS change of coordinating cadmium oleate to the surface of the quantum dot in a solution of tetrahydrofuran is 16.53 kJ/mol at 298.15 K. As mentioned above, the calculated change in TS for the release of four tetrahydrofuran molecules from a cadmium acetate complex is 135 kJ/mol. Thus, the calculated change in TS of coordination of cadmium oleate to the surface of a cadmium sulfide quantum dot at 298.15 K is found to be -118 kJ/mol in a noncoordinating solvent.

From the Ising model simulations and correcting for the coordination of tetrahydrofuran, the adsorption enthalpy of cadmium oleate to the surface of cadmium sulfide quantum dots in a noncoordinating solvent is calculated to be between -321 and -332 kJ/mol depending on surface coverage. A corrected Gibbs free energy of adsorption of cadmium oleate to the surface of a cadmium sulfide quantum dot in a noncoordinating solvent can be calculated to be in the range of -203 to -206 kJ/mol by using the change in TS calculated above (-118 kJ/mol) and the dependence on surface coverage from the Ising model. The calculated equilibrium constant in a noncoordinating solvent is calculated to be between $3.66{\cdot}10^{35}$ M^{-1} and $1.23{\cdot}10^{36}$ M^{-1}. Such strong adsorption energies of the metal carboxylate could not be measured without the assistance of the coordinating tetrahydrofuran to create the ligand deficient quantum dots. From the perspective of cadmium sulfide quantum dots in a noncoordinating solvent, such as hexanes or toluene, these ligands will not desorb from the surface, and the ligand shell can be considered static. Alongside the hypotheses on the role of multiple adsorption sites,[64–66] this shift in the thermodynamics of coordination based on ligand coverage further supports the hypothesis that coverage dependence can play a significant role and may explain some conclusions that single-site binding models do not fit

observed isotherms.

3.9 The Impact of a Dynamic Ligand Shell on Luminescence

The use of tetrahydrofuran as the solvent for colloidal cadmium sulfide quantum dots transforms the traditionally static ligand shell into a dynamic one, where ligands freely desorb and adsorb to the surface. The surface coverage of quantum dots in this dynamic equilibrium is determined by the concentration of ligands in solution. This system draws parallels to colloidal lead halide perovskite nanocrystals, where ligands are generally much more weakly adsorbed to the nanocrystal even in non-coordinating solvents such a hexanes or toluene.[18,29] Much like the type II-VI and III-V semiconducting nanocrystals, ligands can help passivate surface traps and removing ligands is generally deleterious to the quantum dot optical properties.[18] Diluting a system in dynamic equilibrium between adsorbed and free ligands has previously been observed in lead halide perovskite nanocrystals to decrease quantum yields.[18] After isolation, a small excess of added ligands has proven to be effective at increasing the quantum yield, and significant work has been done to find ligands that adsorb more tightly to their surface to prevent this effect.[18,29]

As has previously been observed, the removal of metal carboxylates from the surface of cadmium sulfide quantum dots significantly decreases luminescence (Figure 3.9A) and through the addition of metal carboxylates, luminescence can be restored.[16] This behavior has been attributed to undercoordinated chalcogenides on the quantum dot surface that introduce hole traps.[94] Over the course of removing ligands from the nanocrystals, the luminescence from the band-edge emission drops quite rapidly during the initial washing steps; however, subsequent washing steps decrease the luminescence less. Emission from the trap states also decreases during the first couple of washings but remains somewhat constant in later washing steps. Trap state emission from cadmium sulfide quantum dots has been attributed to electron traps on surface cadmiums,[115] thus the removal of cadmium oleates from the surface decreases both band-edge and trap state emission.

Diluting the cadmium sulfide dots in tetrahydrofuran draws cadmium oleate ligands from the surface and should introduce hole traps[17,94] that decrease their quantum yield compared to the quantum dots in hexane (Figure 3.13). The addition of solid cadmium oleate to the solution increases the concentration of free ligands thus driving the ligand equilibrium towards more surface adsorbed ligands and increasing luminescence. However, even with significant excess of cadmium oleate in solution, the quantum yields do not recover to those of the quantum dots in hexane.

In providing a potential hypothesis for this phenomenon, several possible explanations must be examined. First, it is possible that the lower quantum yield results from significantly lower ligand coverage in THF compared to hexane. Anderson *et al.* showed that after cadmium oleate ligands were stripped from the surfaces of quantum dots and isolated from

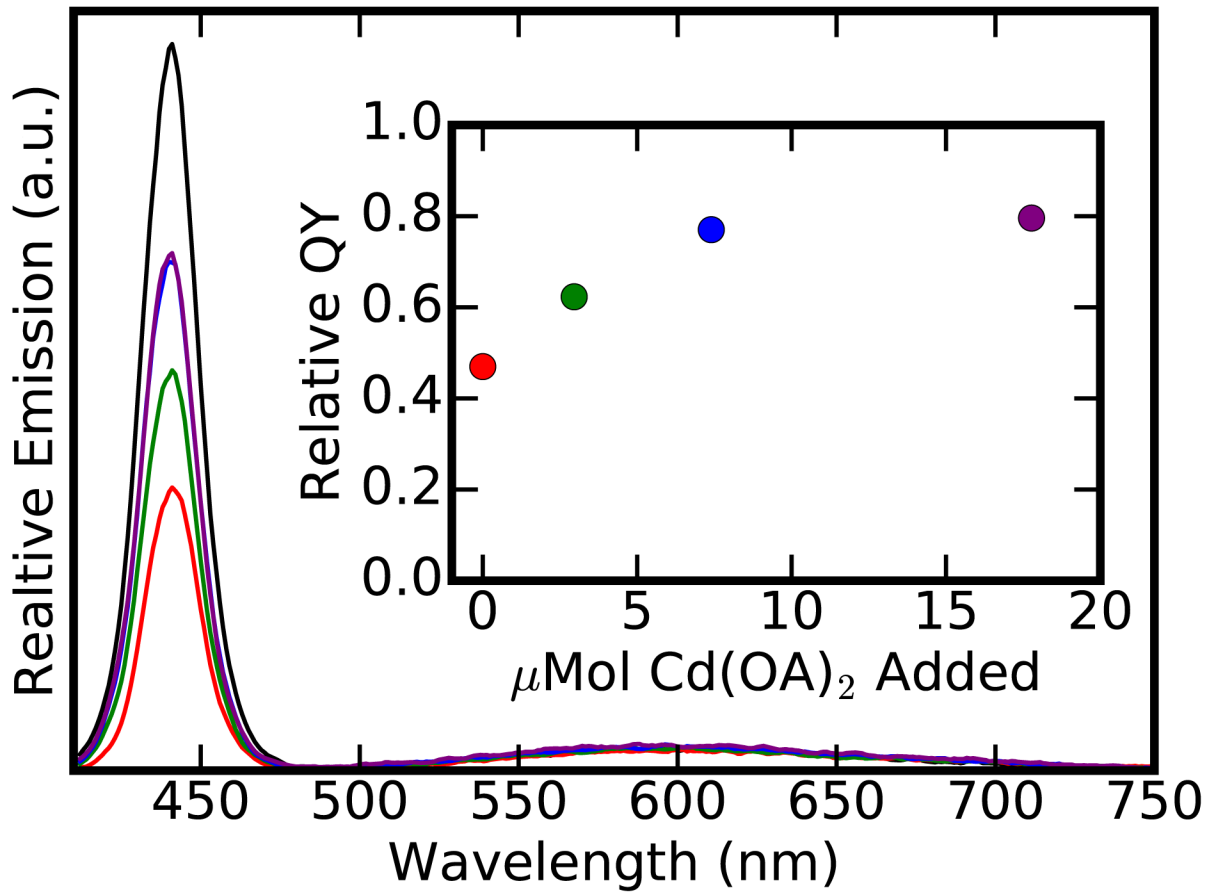


Figure 3.13: Luminescence increase upon adding solid cadmium oleate using a sample of dilute (0.56 µM) cadmium sulfide quantum dots washed in hexanes (black line) and ligand-deficient quantum dots in tetrahydrofuran (red line). After being thoroughly washed in THF, increasing amounts of cadmium oleate (blue, green, violet) are added back to the quantum dots. As more cadmium oleate is added, the luminescence increases but does not reach that of the quantum dots suspended in hexanes. Inset depicts the relative quantum yields of the quantum dots suspended in tetrahydrofuran compared to those in hexane, as a function of added cadmium oleate. The absolute quantum yield for cadmium sulfide quantum dots washed in hexanes was determined to be 7% via the integrating sphere method.

the stripping species, the addition of cadmium oleate at room temperature in toluene did not fully recover the quantum yield. A full recovery of quantum yield was only accomplished when solutions were heated.[16] This was subsequently attributed to a kinetic barrier in the surface reconstruction of the carboxylates.[16] If the addition of excess cadmium oleate to the cadmium sulfide quantum dots in tetrahydrofuran did not increase the surface coverage to that before any ligand stripping was performed, this could easily explain the observations. However, in this case, the surface coverage after the addition of cadmium oleate in tetrahydrofuran was found to be 3.51 $\pm$ 0.79 ligands/nm^2, which is comparable (within error) to the surface coverage of cadmium sulfide quantum dots isolated and washed in hexanes, was found to be 3.43 $\pm$ 0.79 ligands/nm2. Note that the error in these absolute nanocrystal coverages results mostly from uncertainty in nanocrystal size and concentration, but error in comparing relative coverages is on the order of 5%. This recovery of a saturated ligand coverage in even at room temperature is likely due to there being little kinetic barrier to the rearrangement of the ligand shell in this dynamic ligand environment.

Second, it is possible that the use of tetrahydrofuran as the solvent may also play a role beyond allowing the ligands to freely desorb and adsorb from the surface. Tetrahydrofuran has a different dielectric constant and polarity, and it can act as an L-type ligand in metal complexes.[16] However, it is unlikely that these dielectric solvent affects could have such a large impact on quantum yield.[116] In general, L-type ligands such as amines have been found to improve quantum yields in type II-VI semiconducting quantum dots.[94]

Thus, we hypothesize that it is the fluctuations in the dynamic shell that drives this lower quantum yield, even when it appears that saturation coverage of cadmium oleate has been reached. If the absence of metal carboxylates from the surface results in hole traps in type II-VI quantum dots, then the dynamic shell implies that transiently there are hole-traps on the surface. At a saturation of cadmium oleate, not only will there be a steady state concentration of such traps in an ensemble of quantum dots, the number of traps on any specific dot in solution will fluctuate over time. Further support for this hypothesis can be provided by the Ising model simulations using the thermodynamic parameters for the static and dynamic ligand shell (Table 3.3). Figure 3.14 shows histograms of the ligand coverages derived from 10,000 simulations of the Ising model grid after the final step in the simulation, where the initial conditions had 323 cadmium oleate ligands added per nanocrystal, and each nanocrystal has 210 possible sites. In the case of the dynamic ligand shell, while the most common ligand coverage is 210 (i.e., full coverage), there are noticeable fluctuations in the number of bound ligands resulting in an average ligand coverage of 209. Specifically, these fluctuations result in equilibrium ligand coverages that are less than 210 in more than 50% of the simulated nanocrystal surfaces. This implies that out of an ensemble of 10,000 nanocrystals at equilibrium, more than half of the nanocrystals would have empty sites at any given moment. These fluctuations transiently introduce empty sites on the quantum dot, lowering the quantum yield. In the case of the static ligand shell, ligands were tightly bound to the surface and in the 10,000 simulations all grids had unity coverage, as expected due to the much larger equilibrium constant calculated for the static ligand shell. Thus, we propose that while the average ligand coverage similar to those found in a static ligand shell

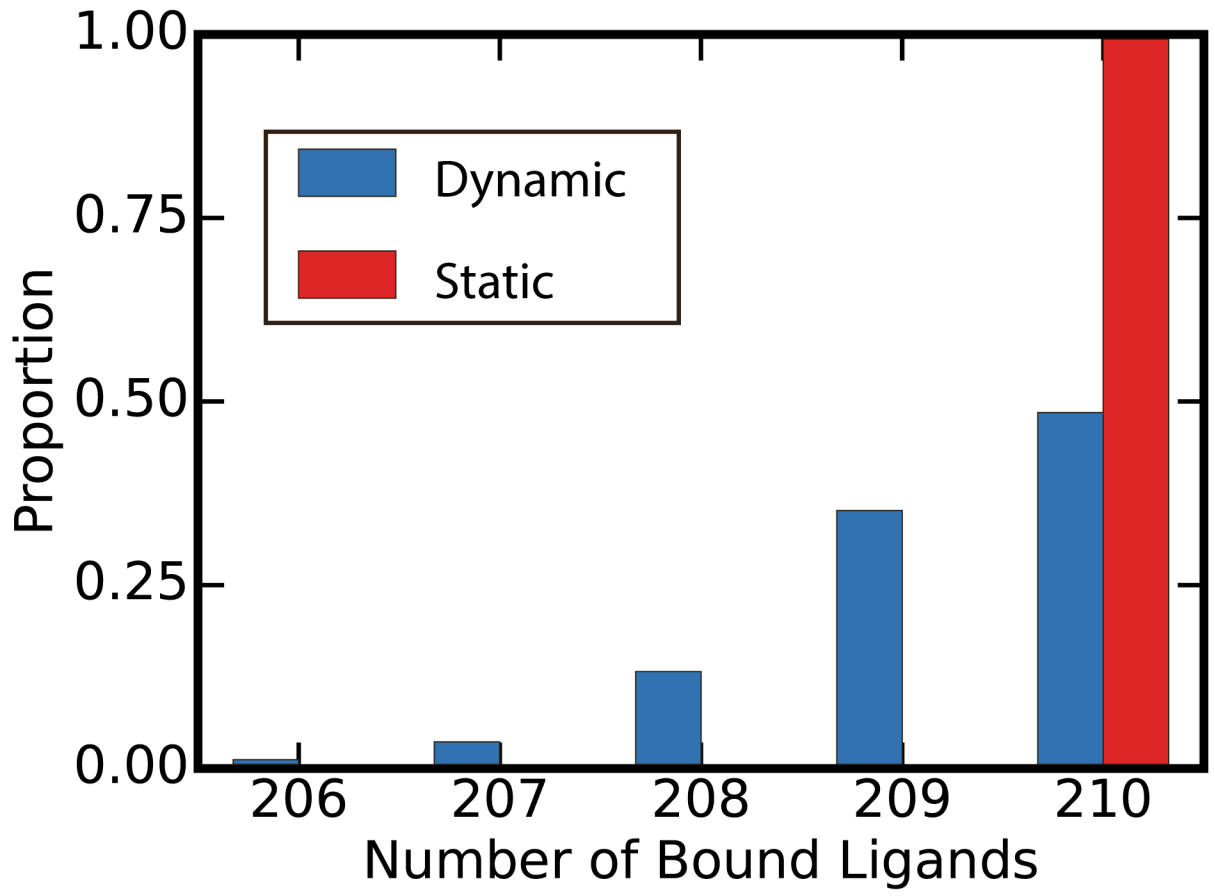


Figure 3.14: Histograms of the number of bound ligands of the Ising model simulations for grids representing the cadmium sulfide quantum dot surface. Blue bars represent the proportion of simulations that ended with a given number of bound ligands on the surface with the dynamic ligand shell parameters while red bars represent the proportion of simulations that ended with a given number of bound ligands on the surface with the static ligand shell parameters.

can be achieved in a dynamic ligand shell environment by driving ligands to the surface, these fluctuations of bound ligands in the ligand shell can reduce the measured quantum yield of the ensemble.

While this hypothesis may be satisfying for this specific case, the lead-halide perovskites would appear to invalidate the conclusion that dynamic ligand shells naturally lead to lower quantum yields, as there are multiple procedures which now report near unity quantum yields in these materials.[18,29,117,118] However, the nature of traps in lead-halide perovskites and type II-VI quantum dots is quite different. While traps due to missing ligands in lead-halide perovskites are quite shallow and can be thermally "de-trapped," traps in type II-VI quantum dots tend to be quite deep.[18,94] Additionally, the fluorescence lifetimes of lead-halide perovskites are approximately an order of magnitude faster than type II-VI quantum dots,[76,118,119] which may significantly affect the dynamics of radiative recombination with regards to a dynamic ligand shell.

The final consideration of these effects is on core-shell nanocrystals, which are often shelled with cadmium sulfide capped with carboxylate ligands. While the addition of the shell effectively works to eliminate defects associated with surfaces and isolates the luminescent core, defects at the surface of the shell material still influence their quantum yields, and surface treatments have been shown to improve optical properties.[120] In the pursuit of quantum dots that reach quantum yields sufficient for such applications as luminescence solar concentrators or more exotic uses, such as optical refrigeration and thermal energy storage in optical cavities,[76] optimization of every aspect of these quantum dots must be considered. Although we have illustrated that desorption of metal carboxylates in a non-coordinating solvent would be highly improbable, careful consideration of the environment surrounding these "static" materials may be important for future endeavors.

Chapter 4

Parameters Influencing Inter-Ligand Interactions

Reproduced in part with permission from Calvin, J. C.; O'Brien, E. A.; Sedlak, A. B.; Balan, A. D.; Alivisatos, A. P. "Thermodynamics of Composition Dependent Ligand Exchange on the Surfaces of Colloidal Indium Phosphide Quantum Dots" *ACS Nano* **2021**, *15*(1), 1407–1420. Copyright 2021 American Chemical Society.[121]

4.1 Investigating the Impact of Ligand Length

The inter-ligand interactions on the surface of colloidal quantum dots are evidently important to describe reactions on their surfaces. The nature of the organic tail on the surface, such as its length and geometry, should influence the magnitude of these inter-ligand interactions. In addition to the identity of the organic ligand on the surface, the density of the ligands on the surface should also impact those parameters due to the nature of the enthalpic and entropic interactions.

We elected to study these effects using ligand exchange reactions at the surface of colloidal indium phosphide nanocrystals. We used isothermal titration calorimetry and ^{1}H NMR to study the displacement of straight-chain ligands from the surface of the quantum dots using bent chain oleic acid ligands. Ligand coverages were monitored using the signal from vinylic and methyl protons on the oleate ligands in quantitative ^{1}H NMR. Once again, results were modeled with a modified Ising model. Additionally, we performed similar ligand exchange reactions with phosphonic acids to illustrate the role these inter-ligand interactions play in a reaction largely determined by binding of head groups.

Indium phosphide quantum dot samples were synthesized with one of four native capping ligands, stearate ($C_{18}H_{35}O_2$), palmitate ($C_{16}H_{31}O_2$), myristate ($C_{14}H_{27}O_2$), and oleate ($C_{18}H_{33}O_2$). Figure 4.1 depicts the absorption and fluorescence spectra of all of the synthesized indium phosphide quantum dot samples. The position of the first exciton peak and

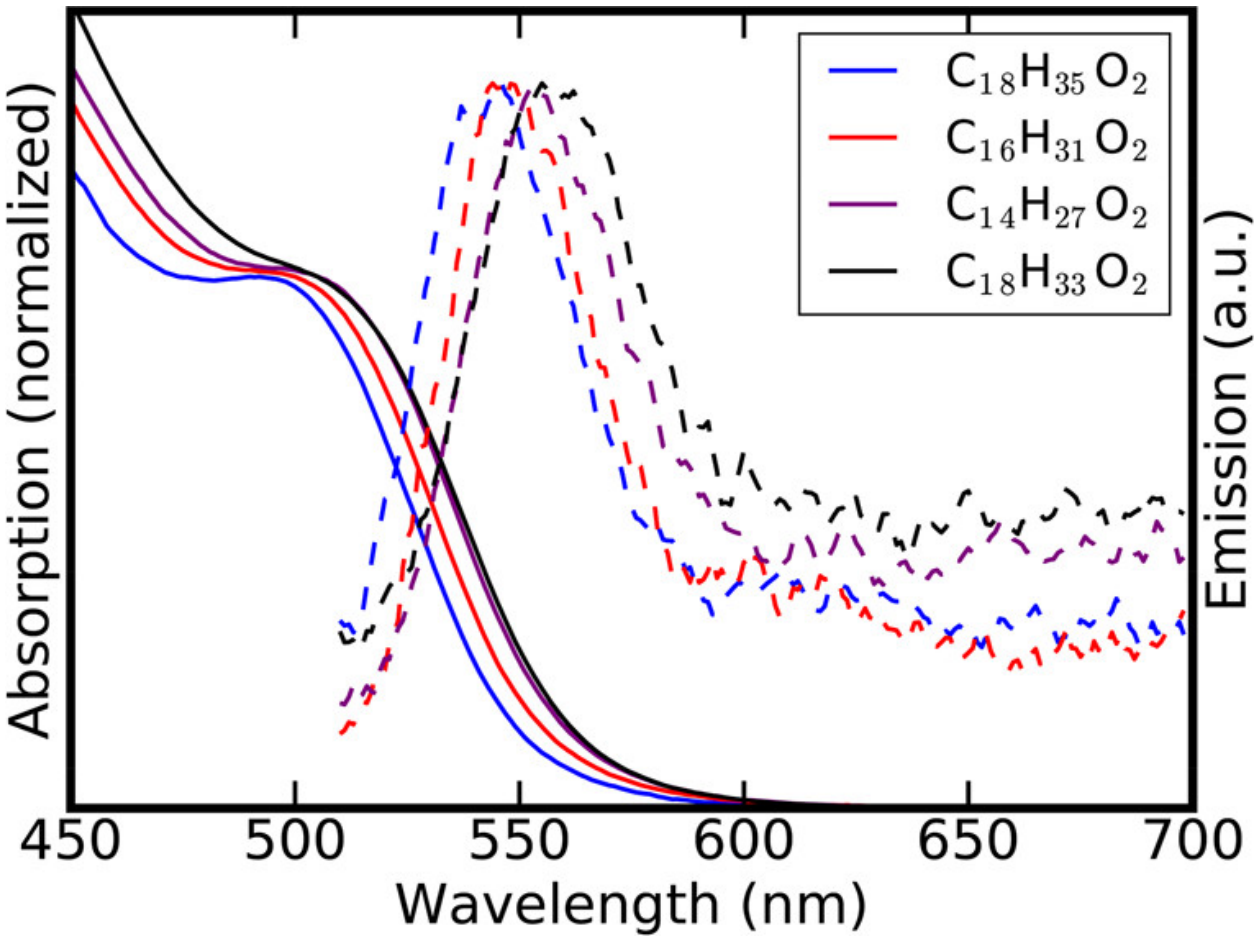


Figure 4.1: Optical measurements of InP quantum dots capped with carboxylic acids: stearate ($C_{18}H_{35}O_2$), palmitate ($C_{16}H_{31}O_2$), myristate acid ($C_{14}H_{27}O_2$), and oleic acid ($C_{18}H_{33}O_2$). Absorption spectra are depicted by solid lines and emission spectra are depicted by dashed lines. The wavelength of the first exciton peak and emission peaks for all samples are similar, indicating similarly sized particles (3.5 $\pm$ 0.4 nm in diameter). All spectra were boxcar averaged with a boxcar width of 5 nm.

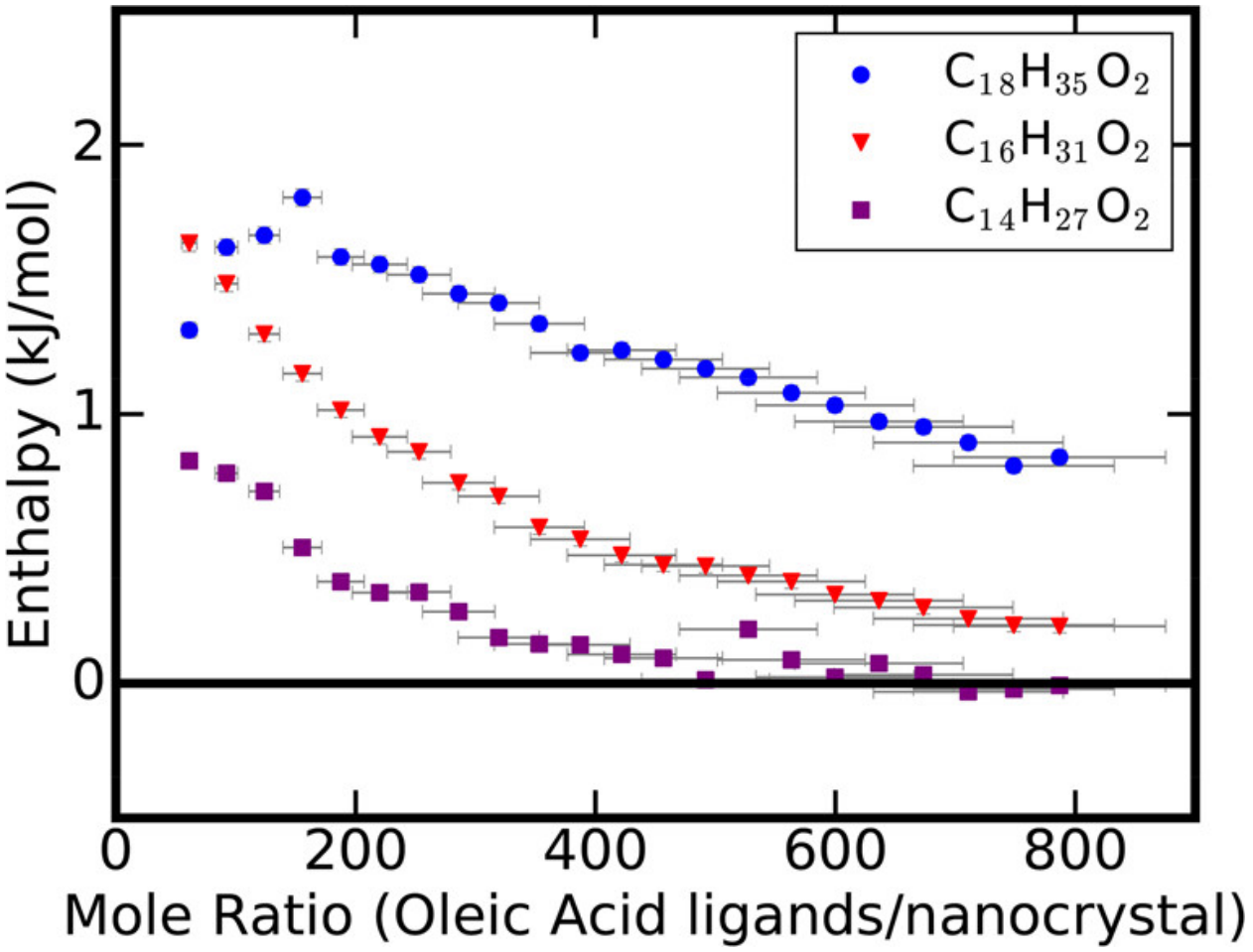


Figure 4.2: Isothermal titration calorimetry data of oleic acid titrations of indium phosphide quantum dots capped with stearate ($C_{18}H_{35}O_2$), palmitate ($C_{16}H_{31}O_2$), or myristate ($C_{14}H_{27}O_2$). Indium phosphide nanocrystals were measured at a concentration of 0.032 mM in THF and were titrated with oleic acid at a concentration of 93 mM in THF. Vertical and horizontal error bars represent the standard error in the enthalpy and mole ratio, respectively.

the wavelength of the band-edge fluorescence vary only by 20 nm among the samples, corresponding to an 0.8 nm change in calculated particle diameter based on the size calculator by Reiss *et al.*[99] (see Appendix C.2 for discussion on errors associated with this calculator). This is important for comparing the exchange reaction of each carboxylate ligand, and the synthetic conditions were adapted to achieve a uniform size and minimize size-dependent differences in surface structure.

Isothermal titration calorimetry measurements for titrations of oleic acid into indium phosphide nanocrystals capped with stearate ($C_{18}H_{35}O_2$), palmitate ($C_{16}H_{31}O_2$), and myristate ($C_{14}H_{27}O_2$) are shown in Figure 4.2. All of these titration reactions are endothermic,

although the total enthalpy of each exchange is relatively small. Longer alkyl chains in the native ligand shell appear to be correlated with more endothermic reactions, but the exchange behavior of the stearate capped nanoparticles is non-monotonic, in contrast to the other reactions. Additionally, the reaction with myristate capped particles appears to reach completion before the reactions with the stearate and palmitate capped particles. Taken together, these factors suggest that notable differences exist between the nanocrystal ligand exchanges.

Additional titrations, monitored with quantitative ^{1}H NMR, were performed alongside the isothermal titration calorimetry titrations to directly track surface ligands during the reaction. The methyl protons of the native and exchange ligands were used to calculate the total number of organic ligands on the quantum dots, while the vinylic protons of the oleate ligand were used to determine the number of oleate ligands on the quantum dots.[49,50] The separation between the bound and free NMR peaks for both the vinylic and methyl protons are depicted in Figure 4.3A and Figure 4.3C, respectively.

From these measurements the fractional coverage of bound oleates and the total number of bound ligands were calculated and are depicted, respectively, in Figure 4.3B and 4.3D. In monitoring the reaction progress, as oleates bind to the surface, a trend can be observed that the rate of displacement decreases as the native ligand length increases (Figure 4.3B). While the total ligand surface coverage remained within measurement error of the native sample for palmitate and myristate ligand systems, the total number of bound ligands clearly increases at the beginning of the reaction for the stearate capped quantum dots (Figure 4.3D). At saturation, the number of ligands per nanocrystal for the natively straight-chain capped nanocrystals are 410 $\pm$ 20 for native myristate capped particles, 450 $\pm$ 30 for native palmitate capped particles, and 410 $\pm$ 40 for native stearate capped particles. These correspond to ligand coverages of 12 $\pm$ 2 ligands/nm^2 for palmitate capped particles, 11 $\pm$ 2 ligands/nm^2 for myristate capped particles, and 11 $\pm$ 2 ligands/nm^2 for stearate capped particles at saturation, while as-synthesized stearate capped particles have a ligand coverage of only 8 $\pm$ 1 ligands/nm^2.

Understanding the ligand exchange for carboxylates mechanistically has been done previously, using ^{1}H NMR studies of the exchange between partially deuterated and fully protonated oleic acid on cadmium selenide quantum dots.[12,122] These measurements show that after the ligand exchange the native ligand has gained a proton from the exchange ligand, indicating that the ligands bind and exchange as carboxylates, and exchanging long-chain carboxylates should have a negligible effect on the head binding enthalpy component of the exchange thermodynamics.

While the experimentally measured enthalpy of replacing a ligand with a straight alkane tail with a bent chain alkene ligand is small, nevertheless the three ligand exchanges have a non-negligible difference in heat that we attribute to the effects of ligand tail length, consistent with results found by Elimelech *et al.*[30] On the native quantum dot surface the straight-chain carboxylates likely pack together maximizing van der Waals interactions. The difference in heat originates from changing the packing on the nanocrystal surface when the oleate, which packs less efficiently, is substituted for the native ligands. Longer ligand

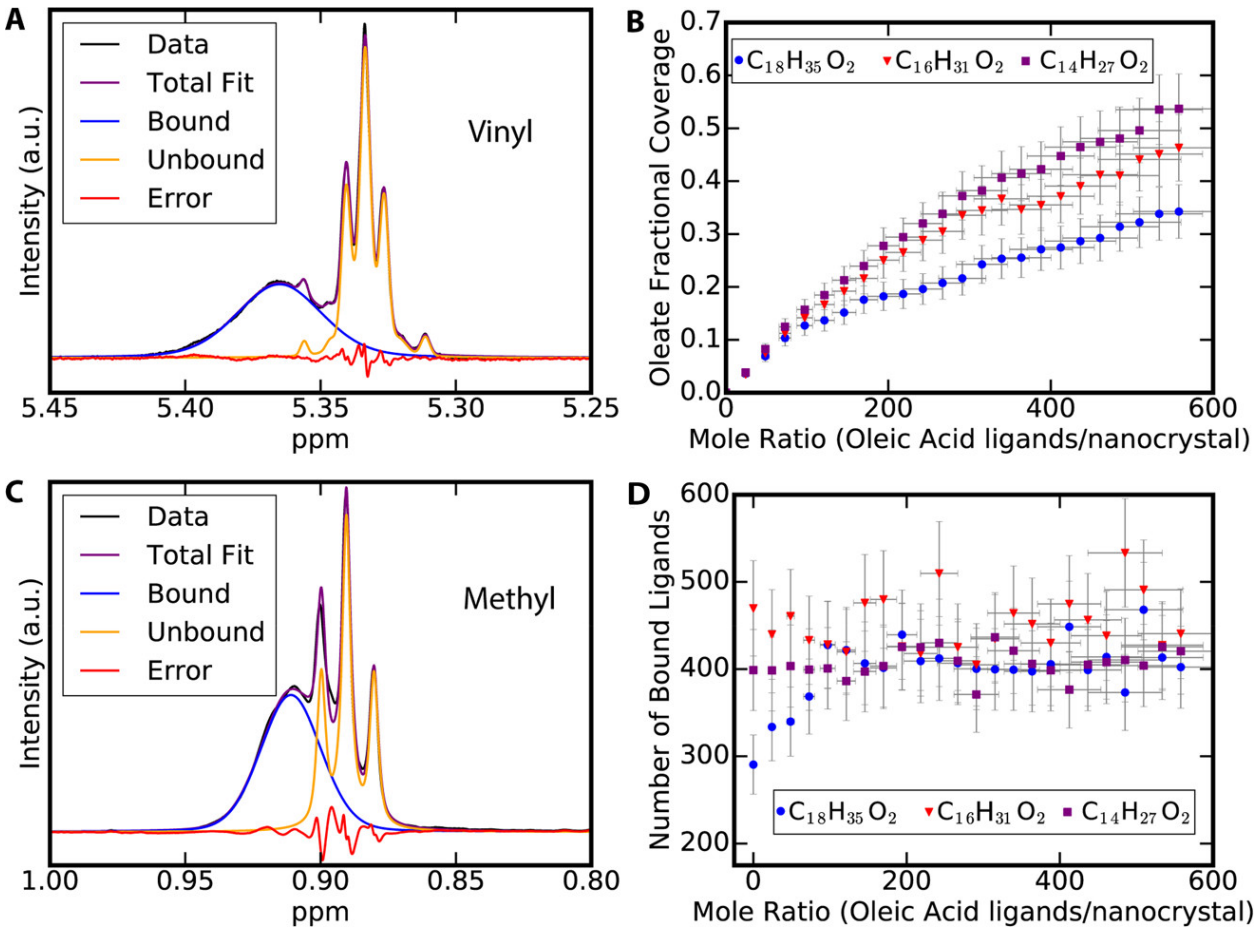


Figure 4.3: ^{1}H NMR of coverage of oleate ligands and native ligands when of oleic acid was titrated into solutions of indium phosphide quantum dots capped with stearate ($C_{18}H_{35}O_2$), palmitate ($C_{16}H_{31}O_2$), and myristate ($C_{14}H_{27}O_2$). (A) Example ^{1}H NMR spectrum of the vinylic protons of oleate used to distinguish bound oleates from free oleic acids. (B) Fractional coverage of bound oleate on indium phosphide quantum dots determined by the total maximum bound ligands observed. The ligand exchange occurs to a lesser extent with stearate capped quantum dots than with palmitate and myristate capped quantum dots. (C) Example ^{1}H NMR spectrum of the methyl protons on oleate and straight-chain carboxylates. Spectrum is fitted to separate the bound and free ligand peaks, following the same separation as the vinylic protons. (D) Total number of organic ligands on the quantum dots over the course of the ligand exchange. The total number of bound ligands remains steady throughout the reactions, with one exception: the native stearate particles see an increase in surface coverage during the first few oleic acid injections.

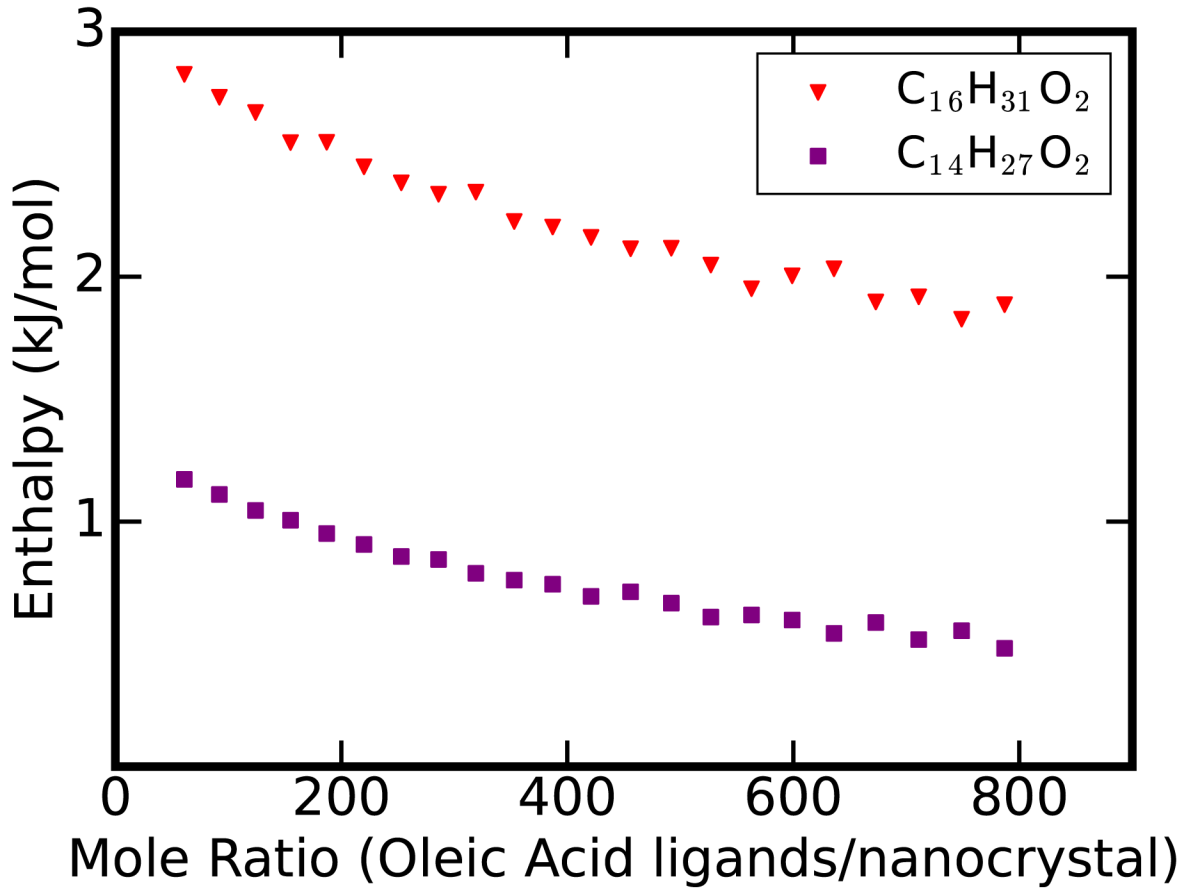


Figure 4.4: Binding enthalpy per exchange from isothermal titration calorimetry and ^{1}H NMR for the reactions of myristate ($C_{14}H_{27}O_2$) and palmitate ($C_{16}H_{31}O_2$) capped indium phosphide nanocrystals with oleic acid. As the reaction progresses, the enthalpy decreases. This is attributed to the changing composition of the ligand shell and fewer strong van der Waals interactions between straight-chains that must be broken as the reaction progresses.

tails have greater van der Waals interactions and thus require more energy to disrupt their packing and add an oleate to the surface. This is in accordance with the differences observed between carboxylates, where exchanges with longer chain carboxylates are generally more endothermic due to the greater number of inter-ligand interactions being broken.

For the palmitate and myristate capped indium phosphide nanocrystals, each subsequent titration is less endothermic than the previous one. This occurs not only because there are fewer exchangeable sites as the reaction progresses, but primarily because as more oleates are added to the surface, there are on average fewer strong van der Waals interactions that need to be broken to remove a straight-chain alkane. This explains why the exchange from

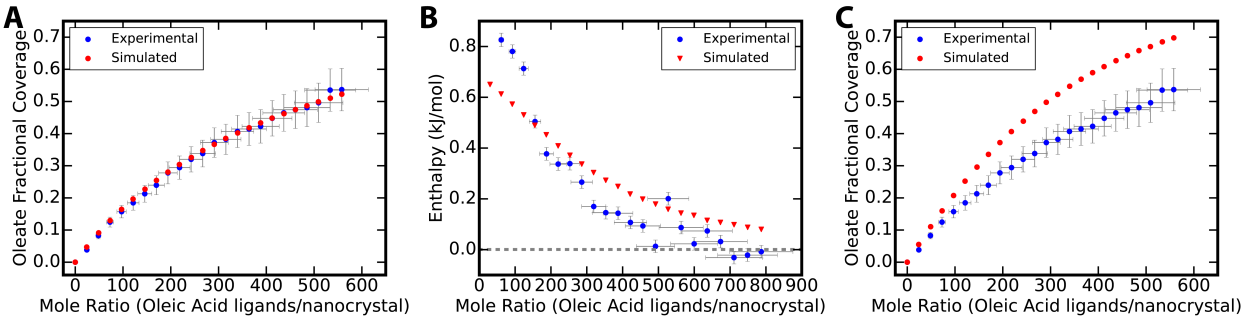


Figure 4.5: Langmuir modeling of ^{1}H NMR and isothermal titration calorimetry data of the reaction of oleic aicd with myristate ($C_{14}H_{27}O_2$) capped indium phosphide nanocrystals. (A) A Langmuir isotherm fit of the ^{1}H NMR data. (B) A Langmuir isotherm fit of the isothermal titration calorimetry data. (C) Resulting simulated ^{1}H NMR data from the Langmuir isotherm fit of the isothermal titration calorimetry data.

myristate to oleate appears to have completed from the isothermal titration calorimetry data, while ^{1}H NMR data shows that the reaction is still progressing. Thus, by combining the isothermal titration calorimetry data and ^{1}H NMR data, we can see that the binding energy of a given ligand changes substantially over the course of the reaction (Figure 4.4). The isothermal titration calorimetry data fails to capture the full extent of reaction because once enough of the native inter-ligand interactions are broken, there is no longer a measurable thermodynamic signal from the exchange. This contrasts with the work done by Elimelech *et al.*, which suggests that describing the thermodynamics of the exchange can be achieved using a single exchange energy model.[30] Rather, the binding energy is composition-dependent and changes with the average interaction of nearest neighbors. This illustrates the critical importance of combining both isothermal titration calorimetry and ^{1}H NMR data, as single binding energies or equilibrium constants can be fit to either dataset, but when combined they fail to be self-consistent, requiring a more nuanced approach discussed below.

As a further illustration of the inadequacy of typical models used to calculate thermodynamic values for ligand exchanges on colloidal quantum dots, the ^{1}H NMR data from the reaction of oleic acid with myristate capped indium phosphide quantum dots was naively fit to a Langmuir isotherm type Ising model (with no inter-ligand interactions). The value of ΔG was found to be 0.315 kJ/mol, while when the isothermal titration calorimetry data was fit with the same model (where both ΔH and TΔS can be extracted when used on isothermal titration calorimetry data, see Chapter 2), ΔH was found to be 0.711 kJ/mol, while TΔS was found to be 3.36 kJ/mol, resulting in a ΔG of -2.65 kJ/mol. Fits for both of these models can be found in Figure 4.5. While a good fit can be found for the ^{1}H NMR data and a somewhat adequate fit can be found for the isothermal titration calorimetry data, the differences in the determined ΔG values are quite stark. As a counter-argument, one could suggest that a two-site model could fit the isothermal titration calorimetry data, and

it almost certainly would, but regardless, it is unlikely that it would agree with the ^{1}H NMR data, and based on the previous results and the nature of the ligand length dependence on the isothermal titration calorimetry data, it seems that a model that includes inter-ligand interactions is required.

The first few points of the stearate exchange present a deviation from the otherwise monotonic trend in the isothermal titration calorimetry data as the reaction initially becomes more endothermic before gradually becoming less endothermic, in addition to showing a higher enthalpy of exchange than both the myristate and palmitate. This discrepancy is easily explained by the ^{1}H NMR data, which shows that the total number of bound ligands increases during the first few points of the exchange, indicating that as-synthesized stearate capped nanoparticles are ligand deficient. We attribute this to synthesis and processing conditions, including a dilute first washing step necessary to remove excess stearate precursor (Appendix A.9). A large excess of coordinating tetrahydrofuran molecules may lower the energy needed to remove a ligand and promote ligand stripping.[16] This observation has significant implications, because empty sites can result in distinct thermodynamic signatures. When ligands bind to empty sites, the new bonds and inter-ligand interactions release heat without the need to displace another ligand, reducing the enthalpy of exchange (making the exchange appear less endothermic) and resulting in the deviation observed. Thus, variations in synthesis and processing, which may result in ligand coverage differences in otherwise identical materials, could have notable effects on ligand exchange equilibria. Furthermore, the signatures from the empty ligand sites highlight the need to use both isothermal titration calorimetry to track the enthalpy and ^{1}H NMR to track the ligand shell composition in order to accurately describe ligand reactions at the surface of colloidal quantum dots.

All three of the tested carboxylate ligand exchanges are endothermic and therefore entropy must be the major driving force of the reactions. Based on our previous analyses of exchange reaction dynamics (Chapter 3), this entropy change likely originates from disrupting the packing order of straight-chain ligands on the nanocrystal with the oleate ligands. Such behavior has been observed previously in mixed straight and bent-chain ligand shells, where a greater proportion of bent ligands on the nanocrystal surface lead to a lower phase transition temperature for ligand shell liquification. Bent ligands are thought to disrupt ligand packing and favor the liquification, or "melting", of the organic ligand shell.[42] Assuming a somewhat constant disruption entropy between the ligands, the exchange that is least endothermic will be more strongly driven to exchange, evidence of which is illustrated in Figure 4.3B. The exchange of oleate onto myristate capped particles has the smallest signal in the isothermal titration calorimetry measurements as it has the weakest intermolecular interactions, but the extent of the reaction is greater than with the palmitate or stearate capped particles because it is easier to exchange for that same reason. In general, native ligands with shorter alkyl chains will produce lower signal in isothermal titration calorimetry measurements, but should also demonstrate greater extent of exchange under otherwise identical reaction conditions.

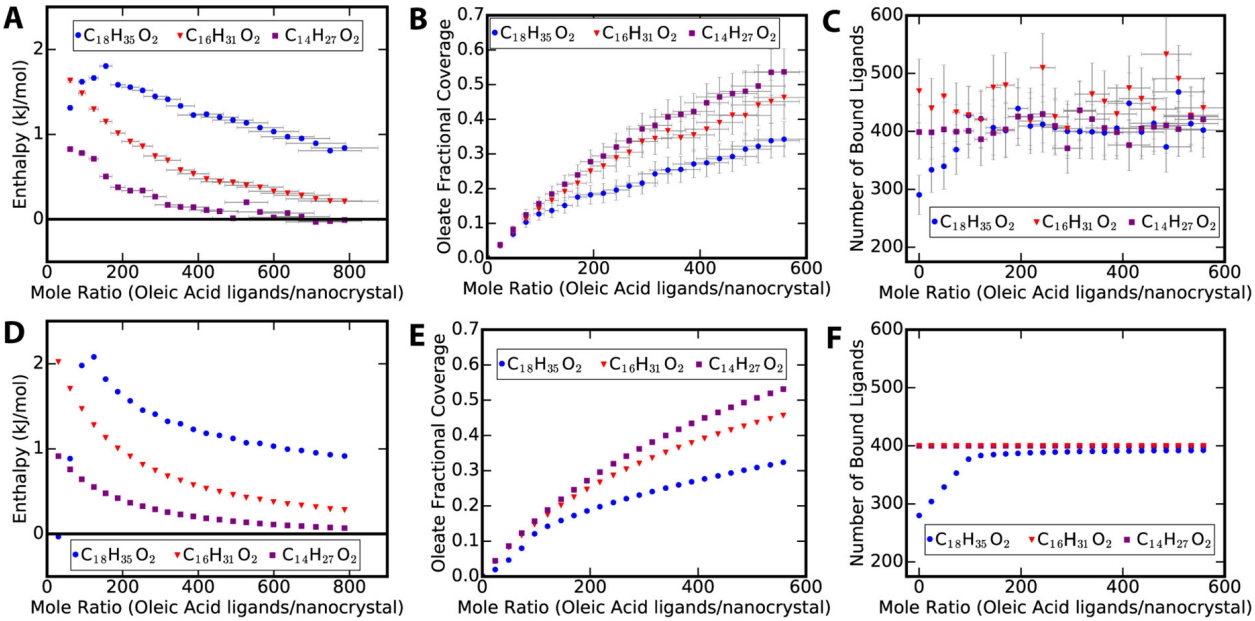


Figure 4.6: Ising model data from carboxylic acid exchanges on InP quantum dots. Data includes the enthalpy, oleate fractional coverage, and total ligand coverage compared with experimental results of the titration between oleic acid and the stearate ($C_{18}H_{35}O_2$), palmitate ($C_{16}H_{31}O_2$), and myristate ($C_{14}H_{27}O_2$) capped indium phosphide quantum dots. The Ising model for the stearate capped particles is slightly different than the model used for the palmitate and myristate capped particles, enabling accurate simulation of a ligand deficient surface. (A) Isothermal titration calorimetry experimental results of the titration reactions. (B) Oleate fractional coverage derived from ^{1}H NMR results. (C) Total ligand coverage derived from ^{1}H NMR results. (D) Simulated enthalpies of reaction from the Ising model. (E) Simulated oleate fractional coverage from the Ising model. (F) Simulated total ligand coverage during the reaction from the Ising model. While coverage gradually increases for stearate simulations, the total number of bound ligands for palmitate and myristate were constant, resulting in overlapping datapoints.

4.2 An Ising Model to Investigate the Effect of Ligand Length

A modified Ising model was used to simulate experimental data for the carboxylic acid exchanges in order to gain further insight into the experimental results, test our hypothesis, and suggest possible relative interaction energies between ligands that would be dependent on the length of the aliphatic tails. Plots of the simulated data alongside the experimental data for the carboxylic acid exchange can be found in Figure 4.6 and the parameters used to simulate the data are presented in Table 4.1; ligand shell composition maps can be found

	ΔH_{head}	$\Delta H_{tail}AA$	$\Delta H_{tail}AB$	$\Delta H_{tail}BB$	$T\Delta S_{head}$	$T\Delta S_{tail}AA$	$T\Delta S_{tail}AB$	$T\Delta S_{tail}BB$
$C_{18}H_{35}O_2$	-2.33	-6.30	-4.59	-3.02	-0.12	-3.82	-3.54	-2.58
$C_{16}H_{31}O_2$	-2.33	-3.42	-3.12	-3.02	-0.12	-2.90	-2.64	-2.58
$C_{14}H_{27}O_2$	-2.33	-3.35	-3.02	-3.02	-0.12	-2.66	-2.73	-2.58

Table 4.1: Parameters for the Ising model of the carboxylic acid exchanges depicted in Figure 4.6 in units of kJ/mol. The head binding enthalpy and entropy for the stearate ($C_{18}H_{35}O_2$) capped particles are relative to an empty space, which had zero head interaction energy and zero nearest-neighbor interaction energy. The models for the palmitate ($C_{16}H_{31}O_2$) and myristate ($C_{14}H_{27}O_2$) capped particles had no empty spaces and were thus referenced to the parameters obtained for stearate. In these simulations, A represents the initial ligand shell species, while B represents the exchanging species (oleate in all cases).

in the Figure 4.7. Several assumptions were made for these models. Each grid point in the simulation was either occupied by a native ligand, an exchange ligand, or an empty space (in the case of the stearate capped particles where empty sites were added). Additionally, only the four nearest ligand neighbor interactions were included when calculating the energies, although there may be longer range effects, particularly when considering entropy. Lastly, all ligands are set to have the same head binding enthalpy and head binding entropy. The nature of this modified Ising model inherently accounts for the entropy of mixing on the surface due to the random selection of free ligands. However, the inter-ligand entropy interactions are explicitly folded into the model with tail in the Gibbs free energy calculation. For this exchange, the entropy of the ligand shell will begin to increase as the ligand exchange reaction initially progresses and more oleates are incorporated into the structure of the ligand shell, due to the ordered straight chains becoming disrupted. This is most significant at the beginning of the exchange and is evident in our thermodynamic data. As indicated from the ^{1}H NMR data, these reactions are not strongly driven, and completing the exchange would likely take a large excess of oleic acid. For these measurements, oleic acid was only added in a ratio of 1.5–2 times of the original concentration of bound ligands on the quantum dots.

As nearest-neighbor interactions appear to determine the thermodynamics of the ligand exchange, it is expected that the exchange ligands may not be randomly distributed on the surface of the quantum dot. Ligand shell composition maps were constructed from these Ising models showing the locations of native and exchange ligands during the exchange (Figure 4.7). Simulated ligand shells were found to exhibit relatively homogeneous mixing of native and exchange ligands, which has been shown previously in mixed ligand shell Ising model simulations and experiments.[42] This indicates that although inter-ligand interactions and large steric differences can result in ligand clustering and island formation,[102,123] the packing enthalpy differences between carboxylates are insufficient to cause significant segregation.

The simulated Ising model was able to reproduce thermodynamic measurements when straight-chain ligands were modeled with stronger interaction energies than the bent-chain ligands. Additionally, the longer straight chain ligands were found to have the stronger interaction energies arising from their ability to pack together better than *cis*-unsaturated

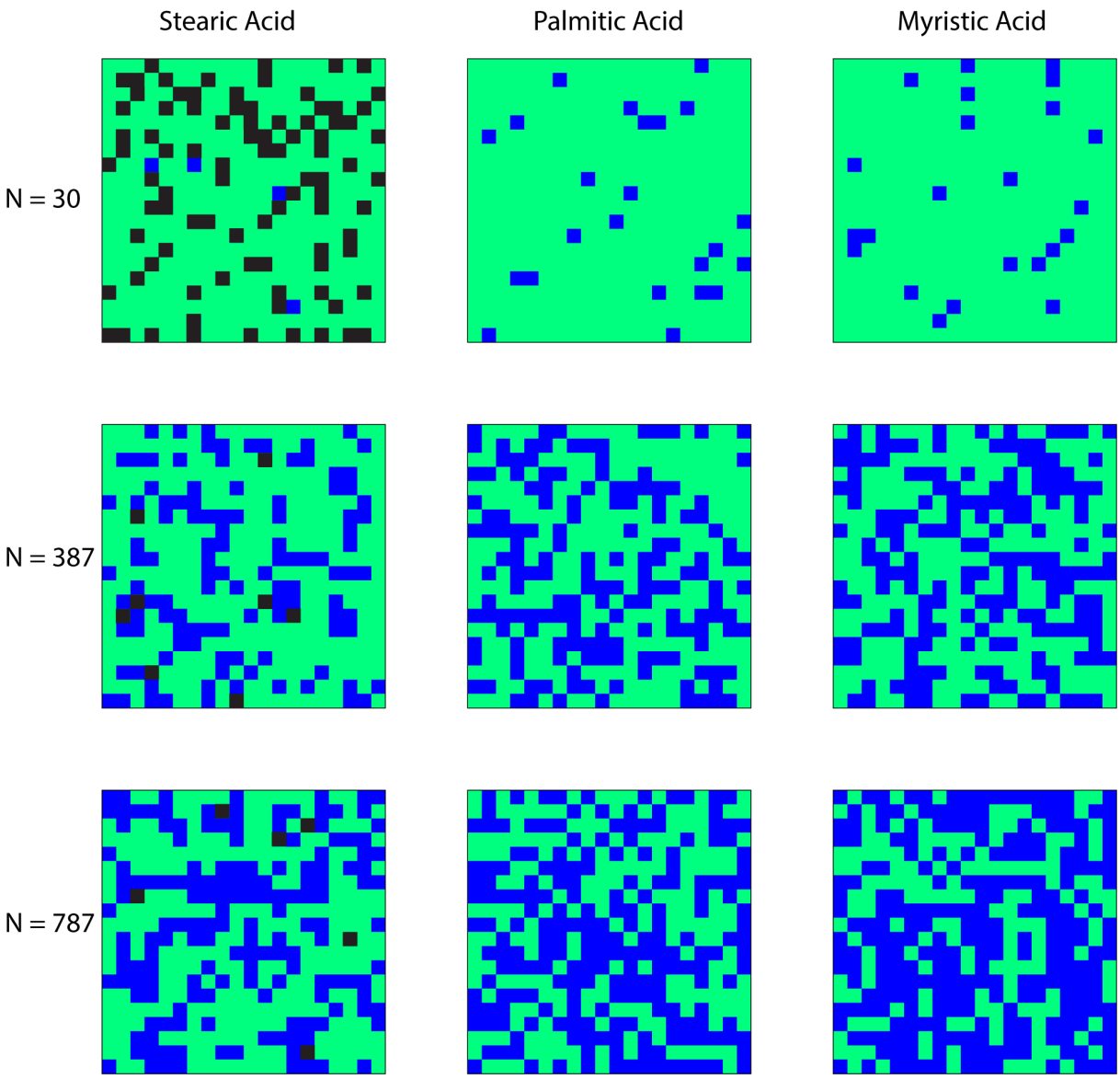


Figure 4.7: Composition maps of carboxylic acid exchange Ising models at varying mole ratios of exchange (represented by N) with different initial capping ligands. Mole ratio refers to the moles of oleic acid to moles of indium phosphide quantum dots, to mirror the experimental measurements, but as only one quantum dot is being simulated at a time, this mole ratio is just the number of oleic acid species introduced to the system. Green squares represent straight-chain carboxylates, blue squares represent bent-chain oleates, and black squares represent an empty site. The coverage maps are representative of the surface of the nanocrystal where each individual square represents a binding site on the nanocrystal.

fatty acids, and the longer the straight chain ligands are, the stronger their inter-ligand interactions are. Similarly, the model suggests that oleate chains also have stronger interactions with straight-chains than with each other. This is attributed to the rotational freedom that the straight chains have about fully saturated carbon-carbon bonds that allows them to somewhat conform to the more sterically hindered oleates.[42,124,125] The chain length dependence of the nearest neighbor interaction enthalpy and entropy appears to be more significant as the carboxylate chain length increases, *i.e.* the difference in nearest neighbor interactions between myristate and palmitate is less than that between palmitate and stearate. This may be related to the observation that in self-assembled monolayers a threshold chain length exists below that which the structure of the monolayer changes, becoming less ordered. In a less ordered ligand shell, inter-ligand interactions would be less significant and as a result, so would the observed chain length dependence.[126,127] Another interesting observation is to compare the inter-ligand interactions on indium phosphide with those on cadmium sulfide quantum dots (Chapter 3). Cadmium oleate was the ligand that was being added to the surface (i.e. there are two oleate ligands), and from the Ising model we can calculate that the inter-ligand van der Waals interactions per oleate is approximately -1.43 kJ/mol and the restriction of internal rotations is approximately -0.94 kJ/mol at room temperature. For indium phosphide, oleate has a much greater value calculated with these Ising models (-3.02 kJ/mol and -2.58 kJ/mol, respectively), and this is likely because the ligand density on indium phosphide nanocrystals is typically around 9 oleates/nm^2 (see Table 4.2 below) while the density on cadmium sulfide nanocrystals is closer to 7 oleates/nm^2, often ascribed to the greater number of carboxylates needed to passivate an indium rich surface as opposed to a cadmium rich surface.[72] This difference in ligand density tracks with the greater van der Waals interactions and restrictions of internal rotations found in these models.

While the Ising model faithfully replicated experimental data and expected enthalpy values, it is not without limitations. As expected, the binding enthalpy of the ligand to the surface is negative (favorable interaction that lowers the enthalpy), and interaction enthalpies between two straight chain ligands, between a straight chain ligand and an oleate ligand, and between two oleates ligands are negative. Additionally, interactions between straight chains are stronger than interactions between oleates. The quantitative interaction values, however, are all calculated relative to hypothetical empty sites, and the constraints of the Ising model may limit their accuracy. To begin with, the Ising model only accounts for nearest neighbor interactions and it is probable that there could be differences in the next nearest neighbor interactions depending on the species. Such differences would not be expected to be significant based on enthalpic interactions between the ligands that extend beyond the nearest neighbor, but rather due to entropic ones. For instance, an empty site on a nanocrystal does not leave a vacuum and bound neighboring ligands can occupy this empty space, meaning that formal next nearest neighbors may share smaller, but still significant interactions. As a result, the values in the Ising model are likely not the true interaction energies between two ligands. Additionally, the loss in ligand binding entropy when a ligand goes from solution to the surface of the nanocrystal is much less than would have been anticipated, since we expect the loss of both translational and rotational entropy for the

ligand. However, this reaction is being performed in solvating tetrahydrofuran molecules which likely form a solvation shell around individual ligands and decrease the entropy of the solution, creating more order in the free ligand environment. Entropy is increased when this solvation shell is relieved by addition of the ligand to the surface, balancing out loss of entropy from translational and rotational restrictions due to ligand binding. This may account for the much smaller entropy change than would be initially anticipated.

To further investigate the proposed implications of conformational ligand entropy on the surface of the indium phosphide quantum dots, computational calculations were performed. Free indium myristate was compared to indium myristate that was constrained by neighboring indium myristate complexes, simulating the surface of a quantum dot (see Appendix D.2 for images of the structures taken from Gaussian 16). Indium myristate was chosen for these calculations because the quantum dot surfaces are populated by indium carboxylate ligands and indium carboxylate exists in solution before addition of carboxylic acid exchange reagents, and the shortest ligand chain was selected for computational efficiency. From these calculations, the change in entropy of an indium myristate moving from the surface of a quantum dot to being free in the gas phase was calculated to be +620 J mol^{-1} K^{-1}, with 246 J mol^{-1} K^{-1} directly being gained from vibrational entropy. While the total entropy is overestimated because the ligand is not going into the gas phase, the calculated change in vibrational entropy is mostly unaffected because it represents a measurement of the freedom of internal rotations in the aliphatic ligand chains. At room temperature, this gain in vibrational entropy corresponds to a 73 kJ/mol change in TS at 298.15 K. Splitting this between the free ligands, from the calculations each aliphatic chain gains 24 kJ/mol in TS from internal rotations by being liberated from the surface, which is much larger than the at most 4 kJ/mol entropy gain calculated from the Ising model simulations. As mentioned above, the ligand is not moving into the gas phase and might experience constraints from the solvation shell, causing an overestimation in this parameter. These calculations suggest that our modified Ising model may underestimate nearest-neighbor parameters. The simulation of ligand exchange using current assumptions provides a clear picture of estimated surface reaction thermodynamics, but additional work may be needed to create a robust, quantitative, and generalizable model of surface exchange.

An important additional consideration in the Ising model that there is a free ligand population in solution before any of the exchange ligand has been added. Although the particles underwent extensive cleaning to remove excess ligand before the experiment, there is an equilibrium established between the ligands on the surface and in solution. This is unsurprising, as tetrahydrofuran is known to coordinate to and displace metal carboxylates, leaving behind undercoordinated anions on the surface.[16] The oleic acid ligands should be able to exchange with the indium straight-chain carboxylates in solution, generating additional "native" ligands that can exchange back with the surface. Because of this, additional native ligands were placed in the free pool of ligands for the simulation to match the measured ratio of bound and free ligands.

The presence of an initial ligand equilibrium introduces complications in the Ising model beyond altering the size and composition of the free ligand pool. It implies that the surface of

the quantum dots, even the myristate and palmitate capped quantum dots, have empty sites and the ligand coverage of carboxylates could theoretically be higher. However, previous work implies that these sites are undercoordinated phosphorus anions and are consequently unfavorable binding sites for anionic carboxylates or carboxylic acids. The metal-carboxylate binding equilibrium is assumed to be stable in the face of added carboxylic acid, but for the purposes of fitting ^{1}H NMR data, an indium carboxylate complex is functionally identical to three carboxylic acid molecules in the free ligand pool. To prevent these metal carboxylates from binding as if they were acidic ligands in the Ising model simulations, the system was constrained so that there must always a minimum number of free ligands present. Free exchange of acidic ligands with those in the metal-ligand complex is allowed, since there is no constraint on the identity of the non-bonding ligands, and the free ligand concentration is more accurately represented. For example, when modeling the stearate capped particles, there are hypothetically two populations of empty sites on the quantum dot initially, one resulting from ligand-stripping during sample processing and one formed by the bound/free equilibrium of indium carboxylate in the sample under experimental conditions. The first population can be filled by carboxylates, carboxylic acids, or metal carboxylates depending on the specifics of ligand stripping and the coordination environment of the exposed surface, while the second is defined as being in direct equilibrium with free metal carboxylates. Sites from the stripped population are given a representation in the model, while the empty sites corresponding to the number of free metal carboxylates in the native sample are not included.

Because palmitate and myristate reactions involve only direct 1:1 ligand exchange, the Ising model fit does not require explicit determination of ΔH_{head} and $T\Delta S_{head}$ for the carboxylate ligands. All of the fatty acids used in the carboxylate exchanges will exhibit the same head group binding thermodynamics, so these values do not influence the simulation and only relative tail group interactions must be considered. However, we have included these terms for all reactions in Table 4.1 for ease of comparison with the more complicated modeling of stearate capped quantum dots. In native stearate exchanges, the measured binding of free ligands to empty surface sites provides the data necessary to model binding and inter-ligand interactions for carboxylate head groups, although we acknowledge the possibility that ligand binding on a ligand-stripped surface could differ from native carboxylate binding. The carboxylate binding values derived there are used as a reference for the values in the other models.

4.3 Phosphonic Acid Ligand Exchanges

In order to expand our characterization of quantum dot surface reactions and develop a generalizable understanding of the subtle details of colloidal nanoparticle ligand exchange, we elected to study an additional binding system. Phosphonic acids were chosen as the exchange ligand because it is well known that these ligands bind tightly to the surface,[49,128] and recent work has indicated that they are good candidates for application-driven ligand engineering.[129] Indium phosphide quantum dots with a native oleate ligand shell were cho-

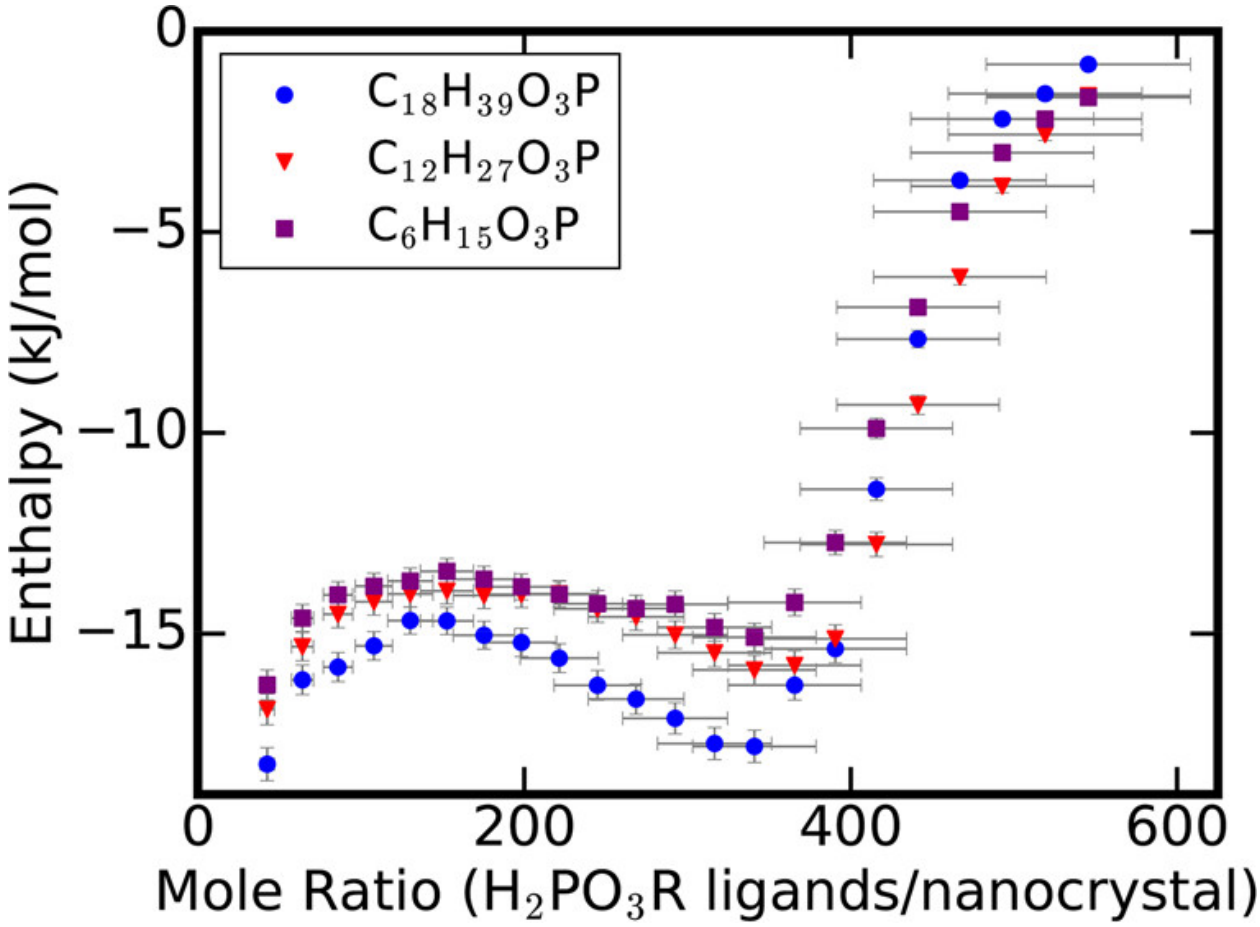


Figure 4.8: Isothermal titration calorimetry data of octadecylphosphonic acid ($C_{18}H_{39}O_3P$), dodecylphosphonic acid ($C_{12}H_{27}O_3P$), and hexylphosphonic acid ($C_6H_{15}O_3P$) titrations of indium phosphide quantum dots capped with oleic acid. As titrating acid chain length increases, the reaction generally becomes more exothermic. Indium phosphide nanocrystals were measured at a concentration of 0.008 mM in THF and were titrated with phosphonic acid at a concentration of 32 mM in THF. Standard error in mole ratio and enthalpy is depicted by error bars.

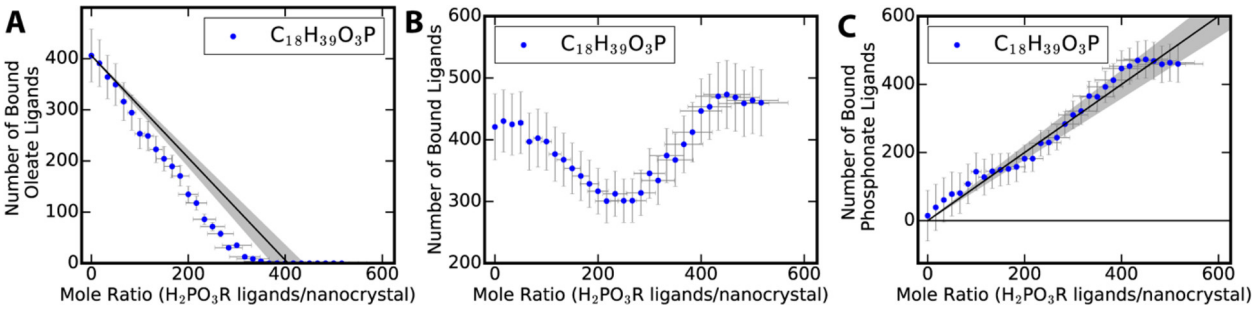


Figure 4.9: NMR plots of ligand coverages during reactions of with octadecylphosphonic acid ($C_{18}H_{39}O_3P$) with oleic acid capped indium phosphide quantum dots. (A) Number of bound oleate molecules as a function of mole ratio during the titration reaction with octadecylphosphonic acid. The black line representing a 1:1 displacement of oleates with octadecylphosphonic acid and that the oleate coverage falls below this line, indicating super-displacement of oleates. Error bars and error bands depicted in gray. (B) Total number of organic ligands on the quantum dots during the reaction with octadecylphosphonic acid. The total ligand coverage begins decreasing after partial ligand exchange, consistent with a super-displacement mechanism. Full surface coverage is then regained in the latter half of the exchange. (C) Calculated number of bound phosphonate ligands from the total number of ligands and the number of bound oleate ligands. The black line represents the coverage of phosphonates if every phosphonic acid added to the solution binds to the quantum dots. Error bands depicted in gray.

sen as the initial sample for these experiments for efficient ^{1}H NMR tracking, and straight chain phosphonic acid ligands of different lengths were added to the surface. The isothermal titration calorimetry measurements of this reaction are given in Figure 4.8 and show a strongly exothermic reaction for all three ligands tested. Previous studies have concluded that phosphonic acid exchanges, unlike those that titrate with carboxylic acids, are driven by the favorable binding energies of phosphonate groups with the surface of the quantum dots.[49,130] The general form of this reaction is much more like the reactions that are traditionally characterized using calorimetry than the carboxylate ligand exchanges. Changes to the enthalpy of reaction remain small throughout much of the titration, with ligands undergoing significant site exchange with each injection until the addition of phosphonic acid ceases to induce a measurable reaction and signal drops off rapidly. Similar to the exchanges with carboxylates, longer phosphonic acid ligand chains correlate to more exothermic reactions. Unlike the previous exchanges, however, after first displaying a gradual increase in reaction enthalpy (becoming slightly more endothermic), the reaction becomes more exothermic before rapidly reaching completion.

^{1}H NMR measurements were taken as octadecylphosphonic acid was titrated into a solution of nanocrystals capped with oleate, depicted in Figure 4.9. In Figure 4.9A, the oleate vinyl NMR peak was observed and the fractional coverage was calculated. Unlike the ex-

changes with carboxylates, where oleates were being added to the surface, in these reactions oleates are being removed and replaced by phosphonates. The most striking features of these measurements is that oleates are displaced to a greater degree than that associated with 1:1 exchange from the surface of the quantum dots, a phenomenon which has previously been observed in indium phosphide clusters.[130] If every phosphonic acid added to the system replaced a single oleate on the surface of the quantum dot, the oleate coverage would decrease following the black line on Figure 4.9A. However, the oleate coverage trends significantly below that line for most of the reaction, suggesting that more oleates are being displaced than phosphonic acids are being added. The total surface coverage calculated from the bound methyl peak and pictured in Figure 4.9B further confirms this observation, with the number of bound ligands decreasing substantially, after initially holding steady, and remaining lower than the native surface coverage for much of the reaction. We see that the ligand coverage increases again after most oleate has been displaced, eventually reaching native density for an overall 1:1 exchange. The ligand coverage before the exchange is 11 $\pm$ 2 ligands/nm^2, and reaches a minimum ligand coverage of 7 $\pm$ 1 ligands/nm^2 before increasing to a ligand coverage of 12 $\pm$ 2 ligands/nm^2. A slight increase in the ligand coverage after exchange with phosphonic acid is not surprising as phosphonic acids bind more tightly than carboxylates, evidenced from the exothermic titrations shown in Figure 4.8. Figure 4.9C shows the increase in phosphonate binding over the course of the reaction, derived from the measured total and oleate ligand coverages. Up to the point of saturation, within experimental error, each phosphonate that is added to the solution binds to the quantum dot, indicating a strongly driven exchange through all phases of the reaction, including super-quantitative oleate displacement. The saturation of the reaction occurs at a 1:1 mole ratio of phosphonic acids to native capping carboxylates. The mole ratios at which we observe decreasing total ligand coverage also correspond to decreased exothermicity in isothermal titration calorimetry measurements, however, so there may be notable binding enthalpy differences between singly and doubly bound phosphonate ligands.

4.4 Potential Reaction Mechanism for Phosphonic Acid Exchanges

Analysis of the isothermal titration calorimetry and ^{1}H NMR data for phosphonic acid ligand exchange shows that although all the reactions are strongly exothermic, the heat released in ligand exchange increases further as ligand length increases (Figure 4.8). As previously hypothesized, this is likely due to more favorable inter-ligand van der Waals interactions on longer ligand tails, leading to this more exothermic response. From the modeling of the carboxylic acid exchange measurements, the observed magnitude for this difference in enthalpy is reasonable for aliphatic inter-ligand interactions. The chain length dependence of the reaction enthalpy appears to increase as the phosphonic acid chain length increases, similar to the trend observed with the carboxylic acid exchange. There is also an

initial decrease in exothermicity of the reaction present for all phosphonic acid exchanges. Unlike observations of the reaction of oleic acid with stearate capped quantum dots, surface coverage measurements do not indicate significant binding to empty surface sites (Figure 4.9B), so this change in reaction enthalpy is likely to have another cause.

The observation that oleate ligands are displaced in greater numbers than octadecylphosphonate are bound, and that this exchange ratio evolves as the reaction progresses (Figure 4.9A), introduces added complexity to the potential thermodynamic analysis of phosphonate ligand exchange, and illustrates why ^{1}H NMR titrations must be used in tandem with isothermal titration calorimetry to accurately interpret isotherms. The ligand exchange of oleate capped cadmium selenide quantum dots with octadecylphosphonic acid has been studied previously, and it has been shown that after reaction with an excess of octadecylphosphonic acid every oleate ligand was replaced with one octadecylphosphonate ligand.[31,49,128] However, this is only an examination of the exchange at its end point and the results may not capture the full complexity of the exchange mechanism. This is also in contrast to recent work by Ritchhart and Cossairt which showed that during the phosphonic ligand exchange with indium phosphide magic-sized clusters, each phosphonic acid replaces approximately two carboxylates before the magic-size cluster decomposes.[130] In the process of reaching a full exchange the availability of two acidic protons on phosphonic acids leads to the displacement of an additional carboxylate from the surface. Secondary deprotonation of phosphonate is therefore a likely driver of excess oleate displacement in our indium phosphide quantum dot system. While the pKa of the second acidic proton is greater than that of carboxylic acids, the local environment or the head binding enthalpy may encourage a second displacement, leading to lower ligand coverage. The gain in entropy from the displacement of an extra ligand may also encourage this exchange. This contrasts with the work by Gee *et al.* on cadmium selenide quantum dots in which they describe the data with a two-site model, where singly deprotonated phosphonates bind to the surface of the quantum dot in an X-type ligand binding coordination while protonated phosphonic acids bind to a different site on the quantum dot in an L-type binding coordination.[31] We suggest that there is not appreciable L-type binding of phosphonic acid ligands in our system, as the total ligand surface coverage does not significantly increase after the reaction has reached saturation (Figure 4.9B).

The total ligand coverage monitored with the methyl NMR peak provides further insight into the exchange and displacement mechanism. Initially the quantum dot ligand coverage remains relatively constant, indicating an approximate 1:1 displacement of oleate for each phosphonate bound (Figure 4.9B). Then the ligand coverage decreases, as would be expected with a super-displacement mechanism, before increasing again as the reaction nears completion. This increase in ligand coverage at the end of the reaction suggests that additional phosphonic acids add to the surface by donating one of their protons to a phosphonate on the surface that has lost two protons. Phosphonate ligand binding is consistent with this hypothesis, with steady binding throughout the reaction, even after oleate displacement is complete. At the end of the reaction, each oleate has been replaced by approximately one phosphonic acid, suggesting that when excess phosphonic acid is available, it is more favorable for the ligand coverage to be higher. This observation may reconcile the results

from Ritchhart and Cossairt with those of Gomes *et al.* and Knauf *et al.* regarding the nature of exchanges between carboxylates and phosphonic acids on the surfaces of quantum dots. While many similarities exist between type II-VI and type III-V semiconducting quantum dots, we acknowledge that these exchange mechanisms may differ between systems and further studies are required to reach a definitive conclusion.[31,49,128,130,131]

Super-displacement of carboxylate ligands, along with the greater binding energy of phosphonate to the surface of indium phosphide, may explain why phosphonates can completely displace carboxylates so easily. Additionally, as more phosphonate groups are added to the surface, the number of adjacent carboxylates that can be displaced decreases, promoting a return to full surface coverage. If it is more enthalpically favorable to only displace one carboxylate per bound phosphonate, this rearrangement could be the cause of the decrease in reaction exothermicity at the beginning of the reaction and the increased reaction exothermicity as it approaches completion. Alternatively, from experience modeling the carboxylate ligand exchange, this increase in the exothermicity of the reaction could also be attributed to more favorable inter-ligand interactions as the composition of the ligand shell changes to higher coverage of straight-chain carboxylates. It is possible that both effects influence the reaction, and ideally a self-consistent Ising model simulation could be used to describe their relative magnitudes and contributions. The findings reported by Gee *et al.*[31] are consistent with this hypothesis as they also note variation in X-type exchange enthalpy for phosphonic acid binding, although they do not fully explore the phenomenon. However, reproduction of phosphonic acid exchanges with our current model is significantly more difficult than carboxylic acid exchange modeling. In addition to being computationally cumbersome, with up to four possible states for each lattice site and their associated interactions, the presence of transient super-displacement calls into question the assumptions of the Ising model for this system. We have already found evidence that entropy contributions to exchange may be larger than the model can account for, and such effects may be a significant driving force for the super-displacement of oleate. Future work for describing the exact thermodynamics of complicated reactions at the surface of colloidal nanocrystals will likely require a more robust or self-contained model to provide quantitative information about the reaction.

We have included this phosphonic acid exchange to illustrate how the principles of inter-ligand interactions likely play a role in reactions at the surface of nanocrystals, but it also shows how complicated these systems can become. While calorimetric measurements are powerful, they require well-supported assumptions for accurate interpretation. If there are too many steps in the reaction or factors that cannot be accounted for, the utility of the thermodynamics in describing reaction mechanisms is reduced. This further illustrates that careful ^{1}H NMR measurements to accompany isothermal titration calorimetry measurements yield valuable insights that may not have been gained from isothermal titration calorimetry measurements alone, and vice versa. Ligand exchange analysis that uses one of these techniques independently cannot account for composition dependence in either exchange stoichiometry or inter-ligand interactions, leading to oversimplifications of reaction thermodynamics. Our multi-faceted technique reveals when underlying assumptions for fitting simplistic models are invalid, like assuming that ligand exchange enthalpies are not composi-

tion dependent for the carboxylic acid exchange or a 1:1 exchange between carboxylates and phosphonates. In some controlled systems, like the phosphonic acid exchange presented, it is possible to draw preliminary conclusions about surface exchange without further modeling, but more complicated reactions are likely common. For example, ligand exchange in mixed ligand shell systems, such as the oleic acid exchanges with amine and phosphonate capped cadmium telluride quantum dots studied by Hassinen *et al.*, may be far too complex for an analysis similar to the one described here.[131]

From both the carboxylic acid and phosphonic acid ligand exchange reactions, it becomes apparent that clearly defining the thermodynamics of nanocrystal surfaces, often done by fitting ^{1}H NMR data to calculate equilibrium constants, can be difficult, particularly for reactions in which inter-ligand interactions become more influential or in strongly driven reactions. Since calculation of the equilibrium constant is often the end goal of many of these studies, we show that as the makeup of the ligand shell changes, the favorability of a particular ligand binding may shift, leading to an equilibrium constant that is dependent on shell composition. Furthermore, more quantitative analysis for estimations of the thermodynamic parameters is significantly assisted by using a simulated Ising model, and can provide support for suggested reaction mechanisms. When reactions become too complicated for exact analysis by a simulated Ising model, the coupling of isothermal titration calorimetry and ^{1}H NMR titrations still provides useful information for the suggestion of possible reaction mechanisms, as is the case for the ligand exchange with phosphonic acids.

4.5 The Role of Nanocrystal Size on Inter-Ligand Interactions

Recent isothermal titration calorimetry work by Elimelech *et al.* has also demonstrated the effect that nanocrystal curvature can have on the thermodynamics of ligand exchange reactions.[30] Through an analysis with a modified "single set of independent binding sites" model, greater nanocrystal curvature was found to correlate with increased exothermicity and greater spontaneity of the exchange reaction.[30] This finding is attributed to greater surface reactivity and the increased angle of separation between the aliphatic chains on higher curvature quantum dots, leading to a less hindered geometry for a ligand exchange.

Assuming the angle of separation between the aliphatic chains of ligands does modulate with nanocrystal curvature, as has been observed by ^{1}H NMR measurements on gold nanoparticles,[28] several other factors may influence reaction thermodynamics. In addition to creating hindered geometries, a decreased angle of separation between aliphatic chains would increase inter-ligand van der Waals interactions and decrease the entropy of surface coordinated aliphatic chains, due to the restrictions of internal rotations. In some cases, the restricted internal rotations of surface ligands could even result in an ordered organic coordinating ligand shell. We hypothesize that the angle of surface ligand separation, and thus curvature, may influence the thermodynamics of ligand exchange reactions beyond the

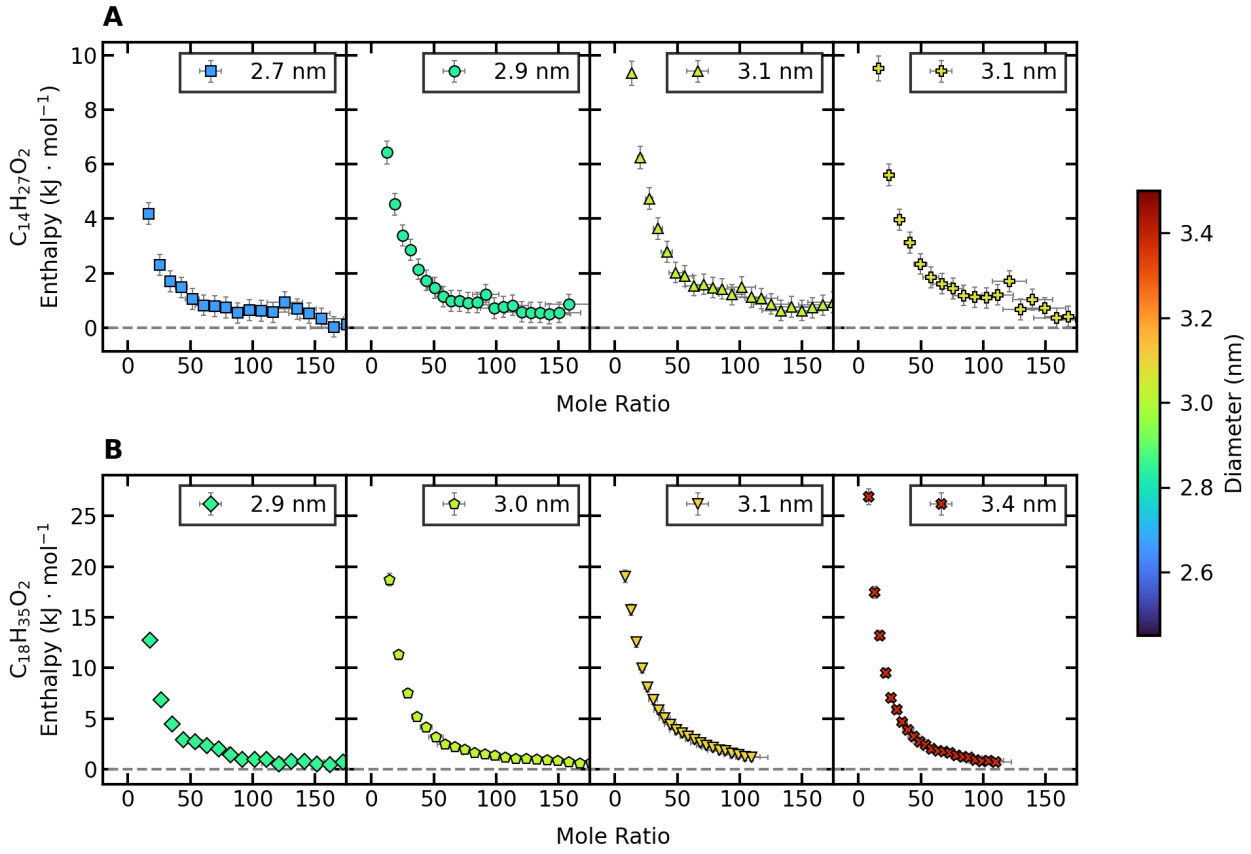


Figure 4.10: Isothermal titration calorimetry measurements of zinc chloride reacting with a size series of InP quantum dots capped with (A) myristate ligands ($C_{14}H_{27}O_2$) and (B) stearate ligands ($C_{18}H_{35}O_2$). Note that two samples capped with indium myristate are very close in size (to 0.1 nm in diameter).

previously attributed considerations.

As illustrated, a modified Ising model can be used to describe these ligand exchange reactions by simulating a nanocrystal surface that is exchanged with ligands until thermodynamic equilibrium is reached. Using an Ising model framework would prove ideal for testing the effects of curvature because it accounts for inter-ligand interactions and composition dependent surfaces. To investigate this, the previously studied ligand exchange reaction between indium carboxylate ligands and zinc chloride on the surface of indium phosphide quantum dots was of used (Chapter 3).

4.6 Measurements Varying Nanocrystal Size

Zinc chloride was titrated into two size series of indium phosphide quantum dots capped with myristate and stearate ligands, respectively, and monitored by isothermal titration calorimetry (Figure 4.10). The estimated sizes and concentrations of the quantum dots were determined from their absorption measurements.[132] Note that the calculator used from Ministro[132] is different than the one previously by Reiss *et al.*;[99] this choice is discussed extensively in Appendix C.2. In general, as nanocrystal size increases, the titrations become more endothermic. As discussed previously, the net endothermicity is ascribed to a greater endothermic contribution from the breaking of surface ligand van der Waals interactions between the aliphatic chains as indium tri-myristate is displaced by zinc chloride. Reactions with stearate ($C_{18}H_{35}O_2$) capped indium phosphide quantum dots are generally more endothermic than those capped with myristate ($C_{14}H_{27}O_2$). This finding is consistent with the previously discussed work, which found that coordinating ligands with longer aliphatic chains require more energy to displace as a result of stronger van der Waals interactions.

Quantitative ^{1}H NMR measurements were taken to determine the number of bound indium carboxylate ligands per quantum dot as a function of titrated mole ratio, moles zinc chloride to moles indium phosphide quantum dots, (Figure 4.11). As the titration progresses, the number of free indium tri-carboxylate ligands increases to a somewhat constant value, mirroring the reaction end point reached in isothermal titration calorimetry measurements. The calculated ligand coverages of indium carboxylates for the samples is included in Table 4.2. One interesting observation to note is the somewhat high variability of ligand coverage per quantum dot. The quantum dots did not always exhibit an increase in the number of ligands per quantum dot as the nanocrystal size, and surface area, increased. Similarly sized quantum dots with stearate and myristate ligand shells varied in the extent of ligand coverage as well. This variability illustrates an important feature of quantum dot syntheses; synthetic products may be inconsistent. Even when perceivably identical synthetic procedures are followed, nanocrystal properties, such as the degree of ligand coverage and luminescence, cannot be assumed. This variability was preserved to illustrate the robust nature of the modified Ising model in extracting thermodynamic parameters, and that thorough characterization of each nanocrystal sample is necessary for in-depth analyses. Additionally, based on the ^{1}H NMR measurements of bound and free fractions of ligands, the amount of free ligand before the titrations varied as well, particularly for the larger stearate capped nanoparticles, but these features were also encorporated in the analysis below.

4.7 A More Complex Ising Model with a Phase Transition

While isothermal titration calorimetry measurements show that the reaction becomes more endothermic as both the size of the nanocrystal and length of the ligand increase, a deeper analysis of these effects can be achieved by simulating the experimental isothermal

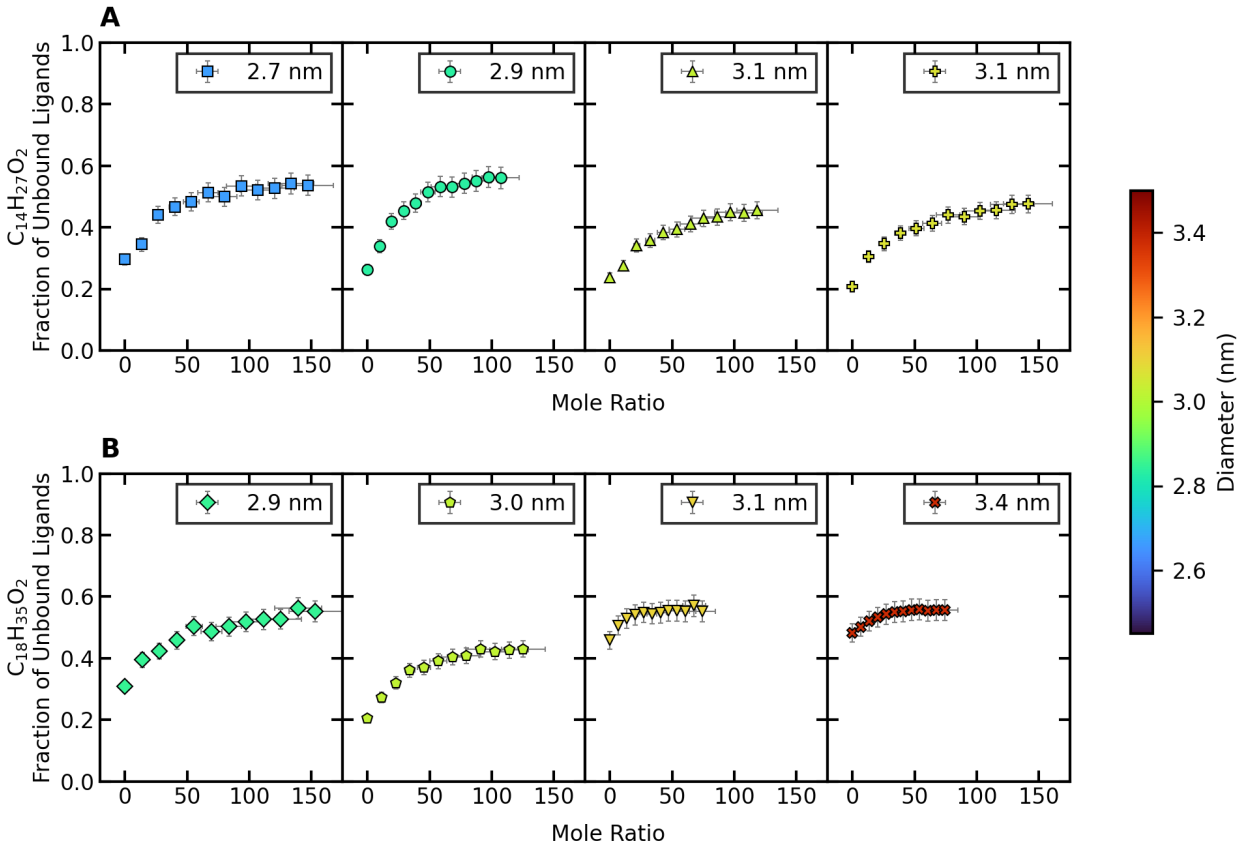


Figure 4.11: ^{1}H NMR measurements of zinc chloride reacting with a size series of InP quantum dots capped with (A) myristate ligands ($C_{14}H_{27}O_2$) and (B) stearate ligands ($C_{18}H_{35}O_2$). Note that two samples capped with indium myristate are very close in size (to 0.1 nm in diameter).

	MA 2.7	MA 2.9	MA 3.1	MA 3.1*	SA 2.9	SA 3.0	SA 3.1	SA 3.4
Ligand Coverage	2.7 ± 0.7	5.1 ± 1.0	3.1 ± 0.8	3.0 ± 0.7	2.7 ± 0.7	3.7 ± 0.9	2.5 ± 0.6	1.9 ± 0.5

Table 4.2: Ligand coverages for InP quantum dot size series, where a ligand refers to a indium tri-carboxylate unit, and is given in units of ligands/nm^2. MA refers to samples capped with myristate ($C_{14}H_{27}O_2$) and SA refers to samples capped with stearate ($C_{18}H_{35}O_2$). *Note that two samples capped with indium myristate are very close in size (to 0.1 nm in diameter). The second one listed is slightly larger based on the size calculator.

	ΔH_{head}	$\Delta H_{tail}AB$	$\Delta H_{tail}BB$	ΔH_{PT}	$T\Delta S_{head}$	$T\Delta S_{tail}AB$	$T\Delta S_{tail}BB$	$T\Delta S_{PT}$
MA 2.7	-40.46	12.22	22.76	0	-25.83	8.87	6.72	0
MA 2.9	-40.46	11.50	22.76	0	-25.83	9.27	6.72	0
MA 3.1	-40.46	13.86	22.76	0	-25.83	10.29	6.72	0
MA 3.1*	-40.46	14.16	22.76	0	-25.83	10.63	6.72	0
SA 2.9	-40.46	12.32	27.96	5.03	-30.67	10.93	5.13	3.12
SA 3.0	-40.46	11.28	27.96	5.03	-30.67	9.62	5.13	3.12
SA 3.1	-40.46	13.41	27.96	5.03	-30.67	11.82	5.13	3.12
SA 3.4	-40.46	17.01	27.96	5.03	-30.67	14.80	5.13	3.12

Table 4.3: Ising model parameters for InP quantum dot size series, given in units of kJ/mol. MA refers to samples capped with myristate ($C_{14}H_{27}O_2$) and SA refers to samples capped with stearate ($C_{18}H_{35}O_2$). *Note that two samples capped with indium myristate are very close in size (to 0.1 nm in diameter). The second one listed is slightly larger based on the size calculator.

titration calorimetry and ^{1}H NMR measurements with a modified Ising model. In an effort to accelerate the optimization process, parameters determined from Chapter 3 were set as the initial parameters for the model. Additionally, parameters that should remain consistent between samples, such as the head binding enthalpy (ΔH_{head}), were constrained in the optimization process. Through fitting this modified Ising model to experimental results, thermodynamic constants were extracted (Table 4.3) and experimental data was simulated (Figure 4.12). While fitting the previously employed Ising model to isothermal titration calorimetry and ^{1}H NMR data for the myristate capped indium phosphide quantum dots proved quite effective, accurate fits for the stearate capped samples were elusive. To alleviate these issues, additional phase transition terms (ΔH_{PT} and $T\Delta S_{PT}$) were added to the original Ising model.

A separate study that employed an Ising model to study organic-shell phase transitions observed supporting evidence for this structural difference in 18-carbon ligands. Through modeling cadmium selenide/cadmium sulfide core/shell quantum dots surfaces, a phase transition was found to occur in ligand shells, around room temperature, composed of purely straight chain 18-carbon, octadecylphosphonate, ligands.[42] Similar phase transitions have also been suggested for octadecanethiolate ($C_{18}H_{37}S$) ligand shells on silver nanocrystal assemblies through differential scanning calorimetry measurements.[133]

To account for greater ordering in stearate ligand shells an additional phase transition term was introduced to the modeling process. Starting with the previously employed modified Ising model, an additional enthalpic penalty—as well as an entropic gain—was added when an indium stearate surrounded by other indium stearates was replaced by zinc chloride, to reflect an exchange in which the crystalline phase is disrupted. In subsequent exchanges where indium stearate is not surrounded by all similar neighbors, these additional terms are not accounted for because that ligand is not considered to be in the more crystalline phase. Of course, like all of the other modified Ising models used to model the ligand exchange

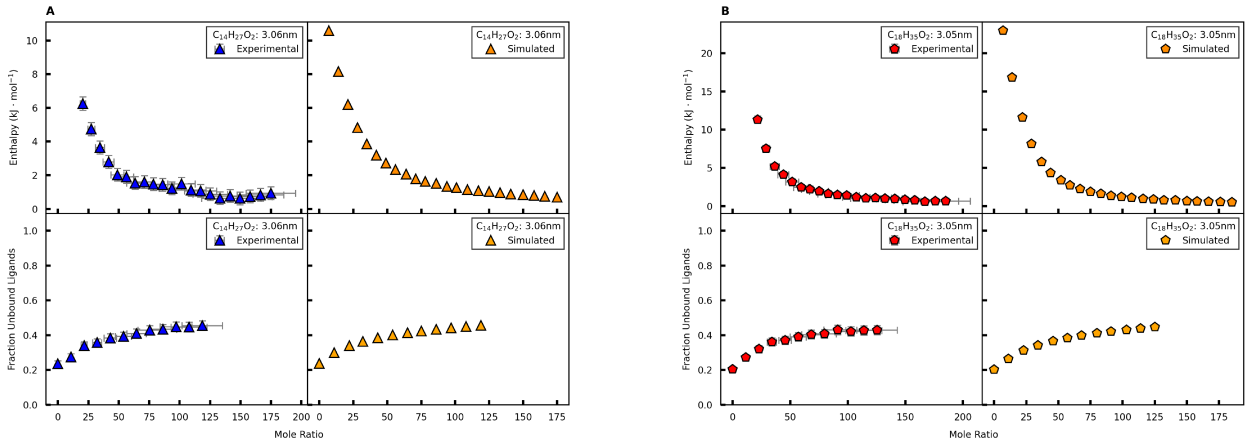


Figure 4.12: Example Ising model simulations of InP size models for 3.1 nm diameter indium phosphide quantum dots. Clockwise from top left, experimental calorimetry data; simulated calorimetry data (orange); simulated ^{1}H NMR data (orange); experimental ^{1}H NMR data. (A) myristate ($C_{14}H_{27}O_2$) capped nanocrystals (blue) and (B) stearate ($C_{18}H_{35}O_2$) capped nanocrystals (red).

on quantum dot surfaces,[42] the model is certainly not a perfect physical representation of a phase change nor of the inter-ligand interactions as only nearest neighbor interactions are considered. Indeed, predicted and experimental values for the experimental data can be plotted to show general goodness of fits for these models (Figure 4.13). Falling on the diagonal point indicates a perfect fit while deviations for this indicate a less good fit, and while most experimental data was fit well, the 3.4 nm stearate capped indium phosphide quantum dot sample fits more poorly than others. Certainly good fits can be obtained for all samples, but the restrictions on some parameters made the fits less than ideal. However, these restrictions were implemented to isolate the effect of nanocrystal size on the inter-ligand interactions, discussed below.

As the size of the nanocrystal increases, the inter-ligand interactions increase, such that the van der Waals interactions are stronger, and the rotational restriction is greater. To illustrate this, the Ising model parameters are plotted against the calculated spherical curvatures of the indium phosphide quantum dots (Figure 4.14A and 4.14B). The curvature of a spherical particle can be represented as the inverse of its radius, such that a flat surface would have a curvature of zero, and a point would have an infinite curvature. While assumption that the particles are spherical is certainly an approximation, transmission electron microscope imaging of these samples indicates this is a reasonable approximation (Appendix A.2). Assuming that surface ligands are isotropically distributed on the nanocrystal surfaces and that surface ligand densities are similar across samples, curvature should correlate linearly with surface ligand interactions. As nanocrystal surface curvature decreases, the angle between the coordinated ligand tails should also decrease (Figure 4.14C), resulting in an increase

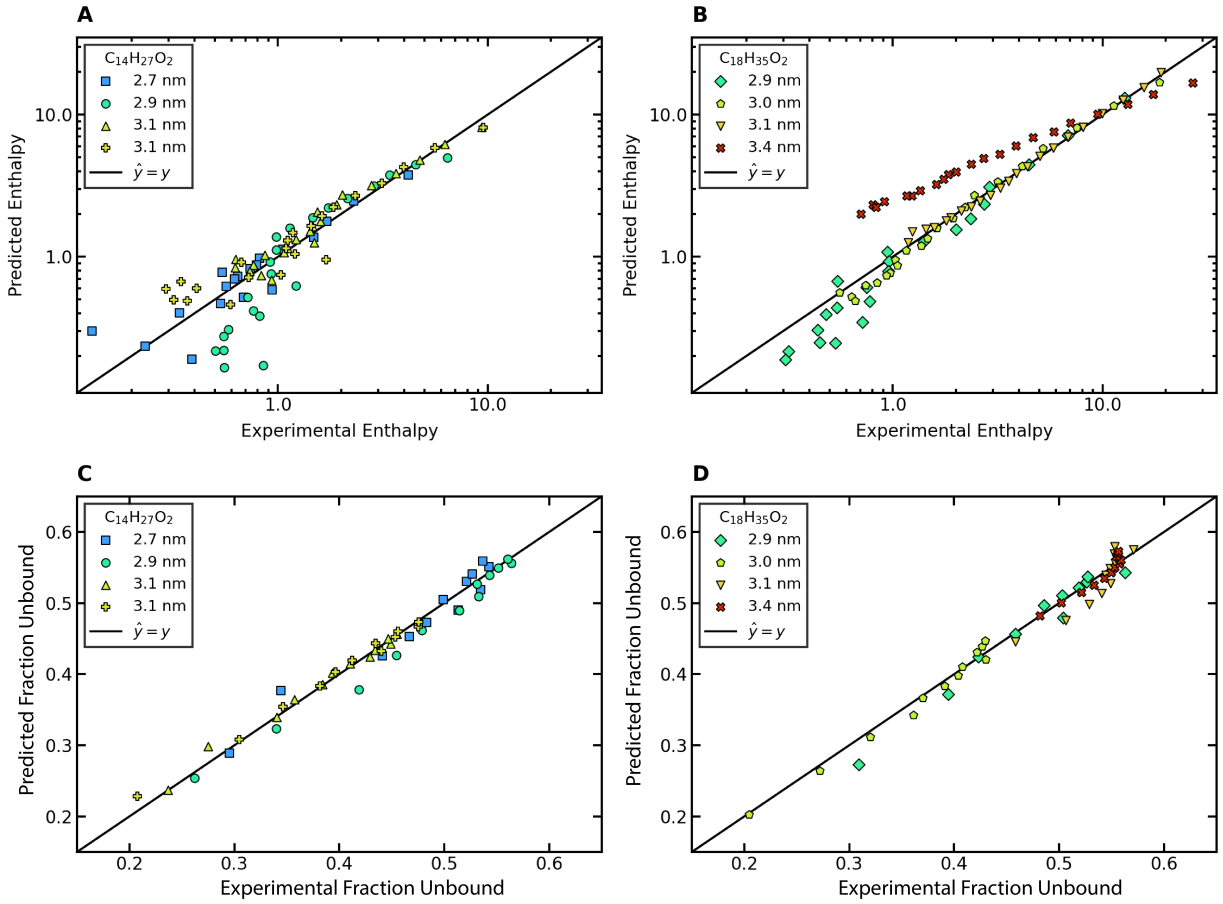


Figure 4.13: Predicted and experimental values generated from the modified Ising models for (A) isothermal titration calorimetry of myristate ($C_{14}H_{27}O_2$) capped indium phosphide, (B) isothermal titration calorimetry of stearate ($C_{18}H_{35}O_2$) capped indium phosphide, (C) ^{1}H NMR of myristate ($C_{14}H_{27}O_2$) capped indium phosphide, and (D) ^{1}H NMR of stearate ($C_{18}H_{35}O_2$) capped indium phosphide. The diameters determined from absorption measurements are included in the legends of the plots. Note that two samples capped with indium myristate are very close in size (to 0.1 nm in diameter). The second one listed is slightly larger based on the size calculator.

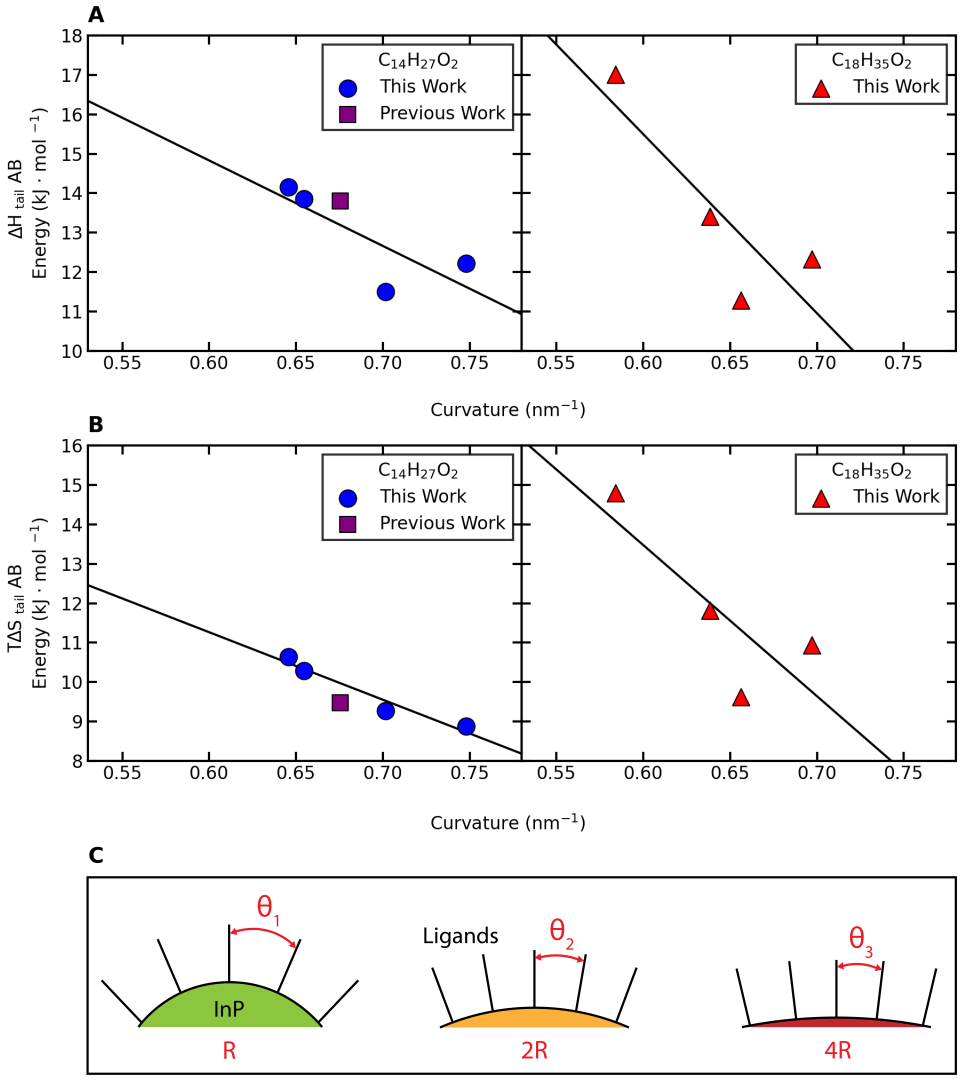


Figure 4.14: Thermodynamic Ising model fit parameters plotted against nanocrystal curvature, which is defined as the inverse radius of the particles. (A) Change in inter-ligand van der Waals interactions ($\Delta H_{tail}AB$) for myristate ($C_{14}H_{27}O_2$) and stearate ($C_{18}H_{35}O_2$) capped indium phosphide quantum dots. Note the inclusion of the data from Chapter 3, although it was reanalyzed using the sizing and concentration calculator from Ministro[132] (see Appendix C.2). (B) Change in inter-ligand confinement interactions ($T\Delta S_{tail}AB$) for myristate ($C_{14}H_{27}O_2$) and stearate ($C_{18}H_{35}O_2$) capped indium phosphide quantum dots. (C) Schematic illustrating that as the size of the nanocrystal increases (from $R < 2R < 4R$) the angle (θ) between isotropically distributed ligands, with a fixed ligand density, decreases ($\theta_1 > \theta_2 > \theta_3$) causing an increase in inter-ligand interactions.

of surface inter-ligand interactions. This increased ordering of ligands on low curvature nanocrystal surfaces has also been reported previously, most notably through careful NMR measurements on gold nanoparticles.[28] Thus, curvature can be utilized as a variable to more faithfully explain the change in inter-ligand interactions as a function of quantum dot size. Note the inclusion of the data from Chapter 3, although it was reanalyzed using the sizing and concentration calculator from Ministro[132] (see Appendix C.2).

From our results on a limited range of sizes of quantum dots, the relationship between inter-ligand interaction parameters and curvature appears linear. A least-squares fit of the parameters indicates that the $\Delta H_{tail}AB$ term becomes less endothermic with a slope of -22 $\pm$ 11 kJ·mol^{-1}·nm and -45 $\pm$ 20 kJ·mol^{-1}·nm for myristate and stearate capped quantum dots respectively, and this is interpreted to mean that particles with higher curvature have weaker inter-ligand van der Waals interactions. The $T\Delta S_{tail}AB$ term becomes less constraining with a slope of -17 $\pm$ 3 kJ·mol^{-1}·nm and -38 $\pm$ 19 kJ·mol^{-1}·nm for myristate and stearate capped quantum dots respectively, and this is interpreted to mean that particles with higher curvature also have fewer restrictions of internal rotations of the ligands on the surface. Assuming a linear trend with curvature, the $\Delta H_{tail}AB$ term for this reaction on a flat surface would be 28 $\pm$ 8 kJ·mol^{-1} and 43 $\pm$ 13 kJ·mol^{-1} for myristate and stearate capped quantum dots respectively, while $T\Delta S_{tail}AB$ term for this reaction on a flat surface would be 22 $\pm$ 2 kJ·mol^{-1} and 36 $\pm$ 12 kJ·mol^{-1} for myristate and stearate capped quantum dots respectively, although these extrapolations may certainly be incorrect.

While direct comparisons with similar work by Elimelech *et al.*[30] are difficult to make, broader comparisons can be made to better understand the nature of theses surface ligand interactions. Previously, Elimelech *et al.* reported isothermal titration calorimetry measurements of inter-ligand interactions on cadmium selenide quantum dots reacting with alkylthiols.[30] Due to the different chemical system and mixture of bent- and straight-chains ligands utilized in the exchange reaction, these results may not translate directly to our chemical system of study. However, qualitatively their observations on the effect of ligand length appear to agree with our own results. Their findings indicate that the ligand exchange reaction from bent-chain oleates (18 carbons) to straight-chain alkylthiolates becomes more exothermic as the alkythiolate ligand chains become longer, similar to our own results comparing myristate and stearate exchanges. Elimelech *et al.* also observed that the ligand exchange reaction becomes less exothermic as the quantum dot size increases.[30] This finding is attributed to low surface curvature causing coordinating oleate ligands to pack more closely creating less favorable geometries for alkylthiolates to penetrate the ligand shell. This conclusion is supported by work by Ravi *et al.*, which proposes that there is an increase in reactive facets on gold nanoparticles as size decreases resulting in a more exothermic reaction.[134] However, comparisons of that work to colloidal quantum dots in organic solvents may be limited due to the highly variable particle sizes, short capping alkyl chains, and aqueous reaction environment.

While this geometric argument appears to contradict our own work, this discrepancy could be a result of the different analysis techniques employed. For the shortest alkylthiols, a dip in the isothermal titration calorimetry plot from Elimelech *et al.* is observed

and attributed in the modeling process to the possible existence of two coordination sites on the nanocrystal surface.[30] However, this feature looks highly reminiscent of the titration of indium chloride into indium phosphide quantum dots, which we previously determined to be caused by breaking stronger inter-ligand interactions. Additionally, the reaction stoichiometry model parameter n—which is the ratio between the actual exchanged ligands and the available surface sites from the fit—decreased as nanocrystal size increased. Our own composition dependent modeling of bent and straight chain ligand inter-ligand interactions predict that the enthalpy of exchange parameter should be independent of the extent of the reaction.

Elimelech *et al.* used a "single set of independent binding sites" model for the analysis of isothermal titration calorimetry data;[30] however, this analysis does not account for composition dependent surfaces. While both isothermal titration calorimetry and ^{1}H NMR measurements were performed only the isothermal titration calorimetry data was used to fit their model. However, using only isothermal titration calorimetry data[30,31] or ^{1}H NMR data[64,65,106] to model nanocrystal surface reactions does not account for the composition changes of the ligand shell, and thus changes in the adsorption energy due to the inter-ligand interactions. Fitting data to a single site isothermal titration calorimetry model or an adsorption isotherm may yield incorrect results, particularly when small changes in enthalpy are observed. This once again illustrates the power of using a composition dependent model such as the Ising model that combines enthalpic data from isothermal titration calorimetry with the coverage data from ^{1}H NMR to give a more complete picture of the reaction on the surface of colloidal quantum dots.

Chapter 5

Direct Diffraction Measurements of Organic Ligand Shell Structure

Reproduced in part with permission from Calvin, J. C.; Kaufman, T. M.; Sedlak, A. B.; Crook, M. F.; Alivisatos, A. P. "Observation of Ordered Organic Capping Ligands on Semiconducting Quantum Dots via Powder X-ray Diffraction" *Nat. Commun.* **2021**, *12*, 2663 under a Creative Commons license CC BY 4.0.[135]

5.1 Structure of Ligands on Colloidal Nanocrystals

One of the interesting results from the isothermal titration calorimetry measurements is the idea of the entropy penalty of dense ligand coverage on colloidal nanocrystals due to a restriction of internal rotations of the aliphatic chains, and the degree of ligand ordering on colloidal inorganic nanocrystal surfaces has long been a topic of interest.[42,136–140] There are reports of the degree of ordering led by theoretical works[137,138] and extending to indirect probes, such as infrared spectroscopy,[42,141] small angle X-ray scattering of interparticle spacing,[133,141] and calorimetric measurements that infer entropy.[42,133,141] Such ordering is interesting fundamentally (these are well-defined finite size order-disorder transitions) and practically (influencing properties including optical, chemical, electrical, and structural). Oddly, there have been no reports of ordering between ligands detected using the most direct probes, wide angle powder X-ray diffraction and grazing incidence wide angle X-ray scattering (GIWAXS).

Conventionally, the contribution of ordering of aliphatic ligands to powder X-ray diffraction has been considered negligible, perhaps because the scattering factors of the organic nuclei are smaller than the inorganic nuclei.[142] However, there are good reasons to believe that ordering of ligands on nanomaterial surfaces may meaningfully contribute to powder X-ray diffraction. Previous published work provides thermodynamic and optical evidence of aliphatic chains ordering on quantum dot surfaces.[42] Work published from small angle X-ray scattering (SAXS) and small angle neutron scattering (SANS) techniques on lead sulfide

Reason	Material	Reference
Organic material	CdSe, InP, PbSe, ZnS	[7,154,155,161–165]
Forbidden reflection	CdSe	[37,46,153]
Substrate	CdSe, HgSe	[8,150]
Inorganic impurity	InP, ZnCuInS, ZnS	[148,149,151,152,166]
No reason given	Ag_2S, CdS, CdSe, CdTe, PbSe, InAs, InP, ZnS	[167–179]

Table 5.1: List of references where ligand peak is observed in powder X-ray diffraction along with the explanation given (if any) and the material system.

quantum dots in solution suggests possible ordering of ligands on the surface,[140] although this was not explicitly inferred. Additionally, ordered ligands have been reported to be observed by electron microscopy techniques.[136] Ordering of ligands has also been suggested to describe observations in melting superlattices.[133,143] The possibility that ligand ordering could be observed via quantum dot X-ray diffraction is promising considering that ordering of aliphatic chains in self-assembled monolayers has been observed in X-ray diffraction on gold surfaces.[144]

5.2 Assignment of the Peculiar Powder X-ray Diffraction Peak

A variety of speculations have been proposed to explain a peak around $q = 1.4$ Å^{-1}, or 20° 2θ for Cu K-α ($\lambda = 1.5418$ Å) radiation, often observed in routine powder X-ray diffraction characterizations of colloidal quantum dots, where q is the scattering length vector (Figure 5.1). Surface-sensitive GIWAXS measurements of superlattices of lead sulfide and cadmium selenide quantum dots show a similar peak.[145–147] Explanations include unique alloys at the quantum dot surfaces,[148,149] amorphous glass slides,[8,150] oxide formation,[151,152] forbidden reflections,[46,153] and unreacted organic precursors such as indium myristate and lead oleate.[154,155] Most reports opt to ignore this peak entirely, either with a lack of explanation or failing to include it in the reported spectrum.[77,145–147,156] When aliphatic capping ligands are not used in the synthesis, this peak invariably is not present.[157–160] A more comprehensive list of articles that depict this peak alongside the given explanation is given in Table 5.1.

Of proposed explanations, signal from unreacted organic precursors is most compelling because the powder X-ray diffraction pattern of indium myristate, for example, has a very similar peak at $q = 1.4$ Å^{-1}.[154] If the excess organic precursors are not effectively removed from the sample, this peak will be very prominent in the spectra[154,155] and after the quantum dots are purified, this peak will decrease.[155] Comparing the spectra of drop cast and recrystallized indium myristate around $q = 1.4$ Å^{-1}, where q is the scattering length vector (Figure 5.2), to that observed in the powder X-ray diffraction pattern of the indium phos-

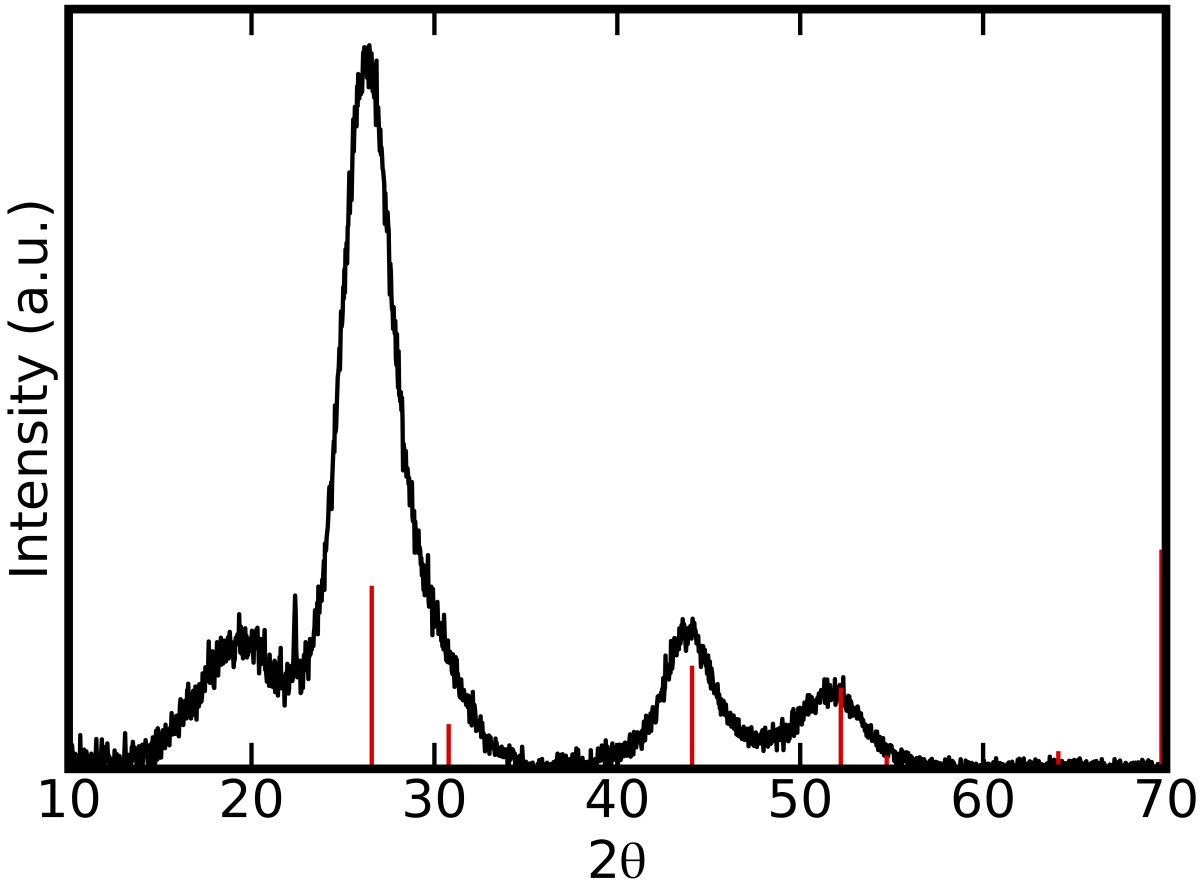


Figure 5.1: Powder X-ray diffraction spectra of InP quantum dots deposited on a silicon wafer. Reference data for zinc-blende indium phosphide depicted as red lines (ICSD 1600543). Cu K-α (λ = 1.5418 Å) is the X-ray source for the powder X-ray diffraction spectra.

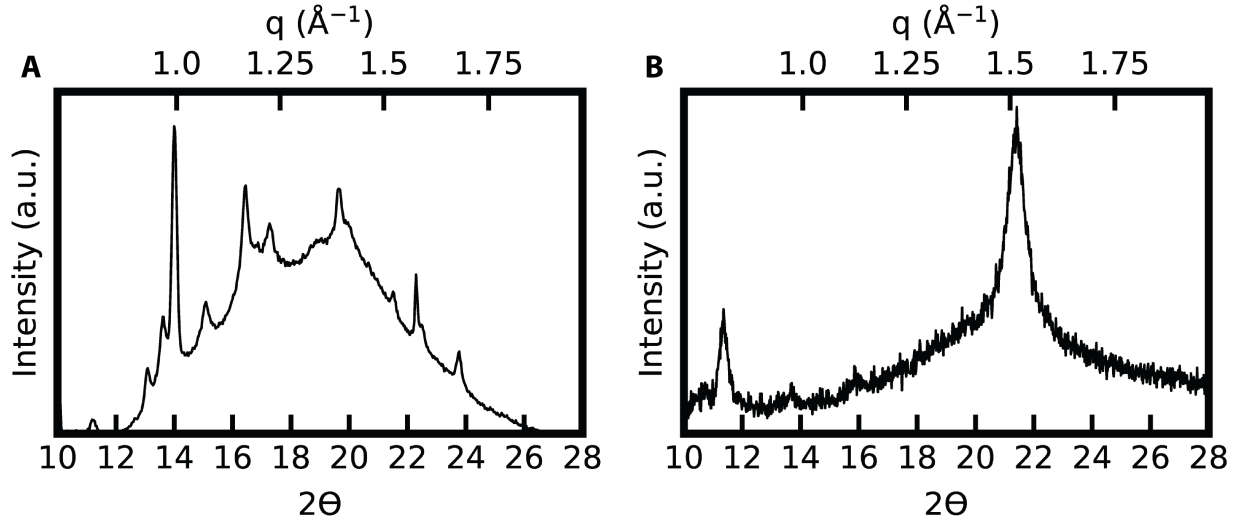


Figure 5.2: Powder X-ray diffraction spectra of synthesized indium myristate. (A) Drop cast from solution. (B) Recrystallized from acetone. Cu K-α ($\lambda = 1.5418$ Å) is the X-ray source for the powder X-ray diffraction spectra.

phide quantum dots (Figure 5.1), it is apparent why many would assume that this precursor is the source of the previously unassigned peak. Interestingly, the sharp peak at larger q values present in the recrystallized indium myristate is not present in the drop cast indium myristate, indicating greater ordering and decreased spacing between ligands in the former, which would be somewhat expected in a sample that was recrystallized rather than drop cast. Additionally, attributing this peak to aliphatic chains is consistent with the peak observed in self-assembled monolayers of aliphatic chains.[144]

However, the ^{1}H NMR spectrum (Figure 5.3) of the solutions used to drop cast the quantum dots for measurements depicted in Figure 5.1 indicates that excess organic precursor cannot cause this diffraction feature as it is not present. The spectrum shows the vinyl peak of the bound capping ligands, and only a broad peak appears. These measurements indicate that there is no unbound precursor after significant washing steps (Appendix A.9) and all of the organic ligands are bound to the surface of the nanocrystal, yet this peak remains. Thus, our hypothesis was that this peak originates from ligands bound to the surface of the nanocrystal, and by manipulating the organic ligand shell of the nanocrystal, this peak could be modulated.

5.3 Evidence Supporting the Ligand Peak Hypothesis

To help quantify the presence of the ligand peak, Gaussian peaks were used as a crude approximation to deconvolute the powder X-ray diffraction, although powder X-ray diffraction

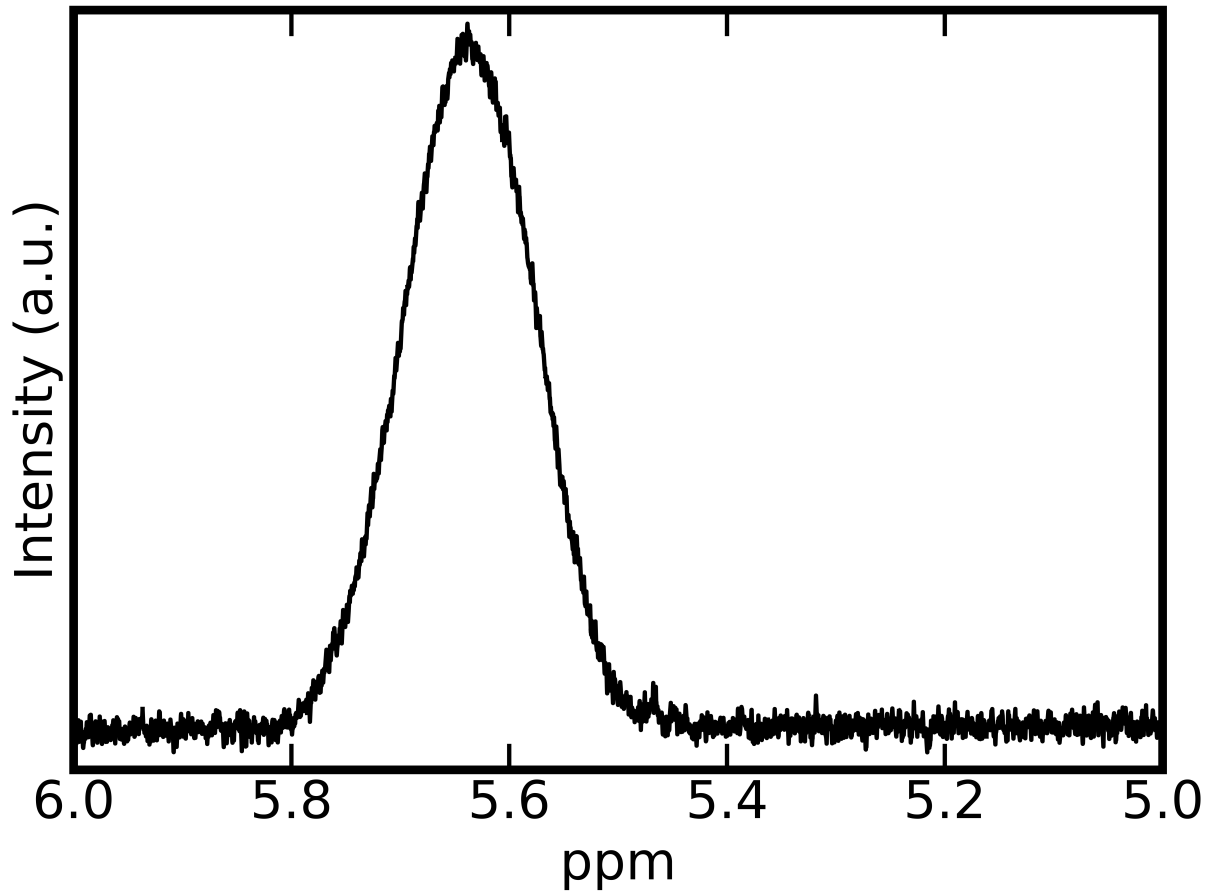


Figure 5.3: ^{1}H NMR of InP quantum dots, taken in toluene-d_8. The region of the spectrum shown are where the vinyl protons of oleate should appear, around 5.5 ppm.

peaks do not strictly have Gaussian or Lorentzian line shapes.[180] In addition to expected diffraction peaks, the peak attributed to the bound ligands is observed at approximately $q = 1.4$ Å^{-1}.

As a proof of concept, powder X-ray diffraction simulations were performed on an indium terminated charge balanced atomic structure of a tetrahedral indium phosphide quantum dot (Figure 5.5A), see Appendix D.3 for details of the simulations. The quantum dot was capped with ordered myristate ligands at ligand densities that have been observed for indium phosphide quantum dots (see Chapter 3 and 4). While the synthesized indium phosphide quantum dots are likely not perfectly faceted and the coordination of the capping carboxylates to the surface indium atoms is not precisely defined due to variability in their coordination motifs,[98] this provides a model system to evaluate the hypothesis that this peak comes from ordered capping aliphatic chains. The simulated powder X-ray diffraction pattern of the quantum

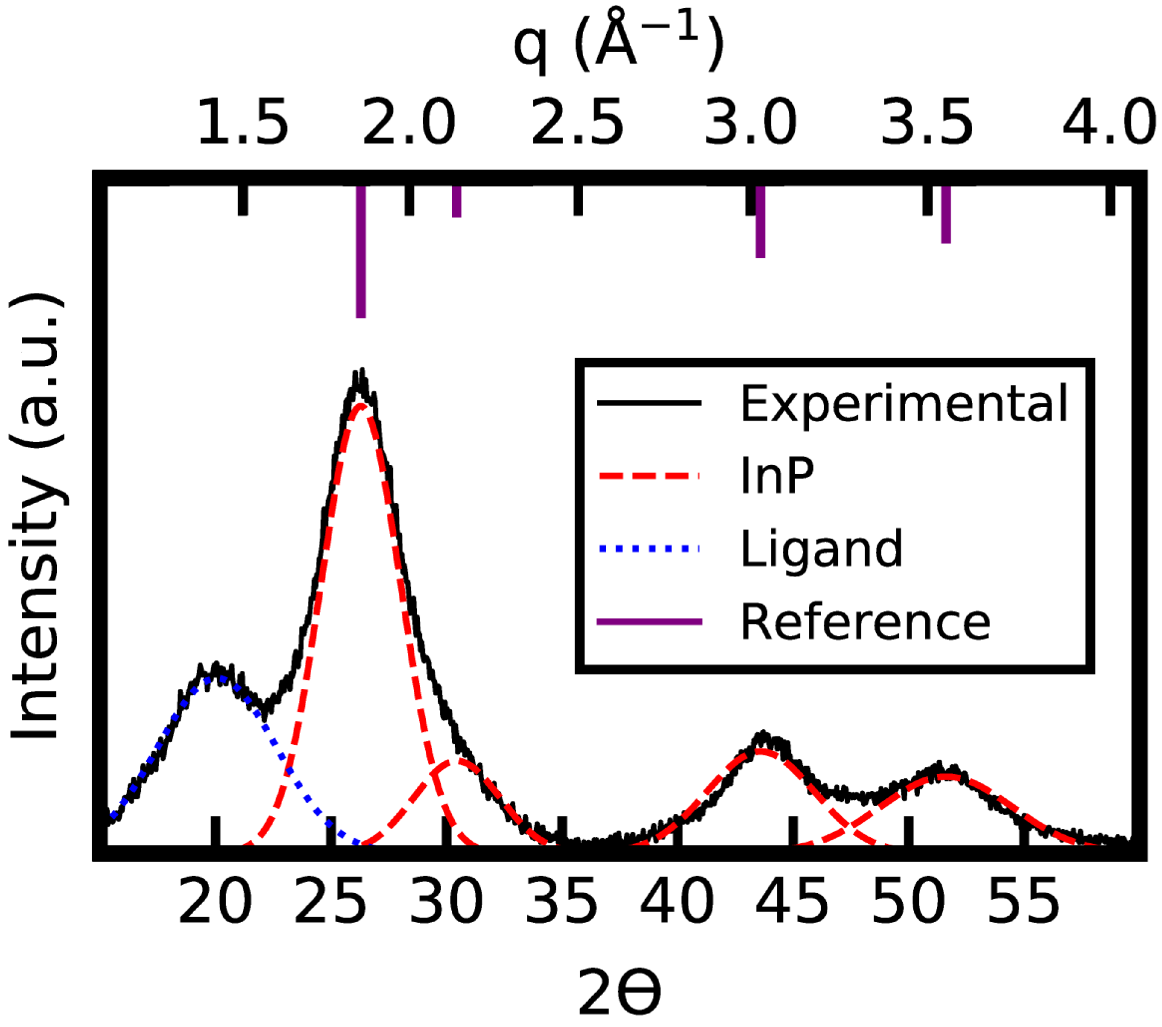


Figure 5.4: Fitted powder X-ray diffraction spectra of InP quantum dots capped with myristate. Gaussian peaks were used to fit the ligand peak and the inorganic peaks. Reference data for zinc-blende indium phosphide depicted as purple lines (ICSD 1600543). Cu K-α ($\lambda = 1.5418$ Å) is the X-ray source for the powder X-ray diffraction spectra.

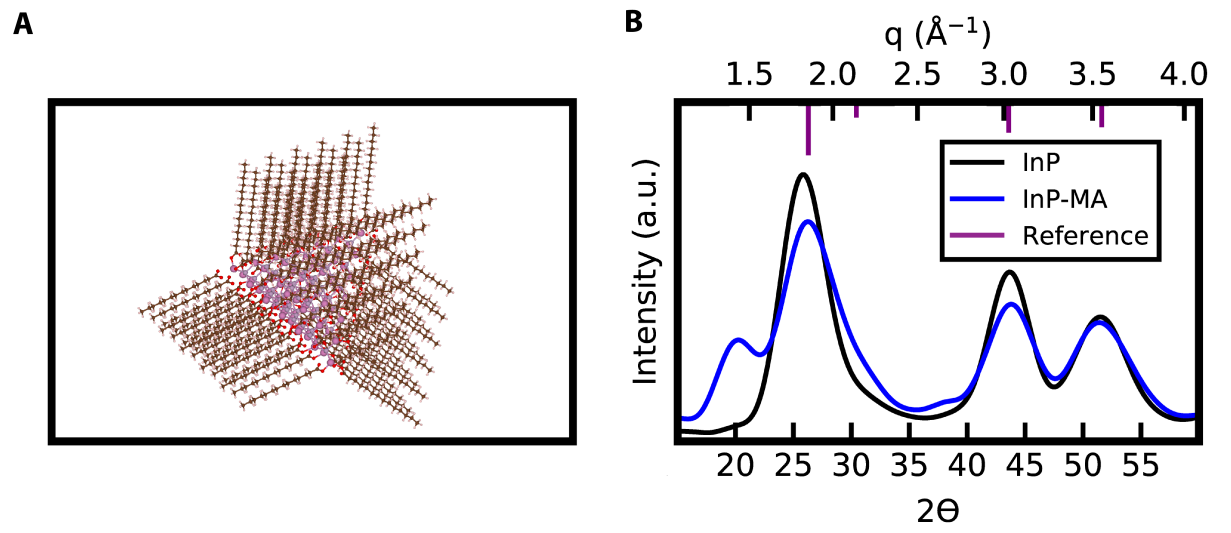


Figure 5.5: Simulated powder X-ray diffraction spectra of InP quantum dots with organic capping ligands. (A) Atomic model of a tetrahedral indium phosphide quantum dot capped with myristates. (B) Simulated powder X-ray diffraction patterns of indium phosphide quantum dots with and without capping myristates (MA). Reference data for zinc-blende cadmium selenide depicted as purple lines (ICSD 1600543). Cu K-α ($\lambda = 1.5418$ Å) is the X-ray source for the powder X-ray diffraction spectra.

dot with ligands contained a peak at $q = 1.4$ Å^{-1} while the powder X-ray diffraction pattern of the quantum dot without capping ligands lacked this previously unassigned peak (Figure 5.5B). The ability to reproduce this peak in the simulations provides further support that this feature originates from ordered myristates on the quantum dot surfaces.

The observation of the previously unassigned peak has been observed in other systems besides indium phosphide. Appendix A shows a powder X-ray diffraction patterns of zinc sulfide, cadmium sulfide, indium phosphide/zinc sulfide, lead sulfide, and cadmium oxide nanocrystals capped with oleates where the ligand peak also appears. However, when particles become much larger, such as in the case of the cadmium selenide particles (approximately 10 nm diameter), the ligand peak becomes much less apparent when viewing the entire powder X-ray diffraction pattern. However, while diminished, the peak can still be deconvoluted with careful baseline subtraction, shown in Figure 5.6.

5.4 Modulating the Ligand Peak

Different treatments to the indium phosphide quantum dots can modulate this peak (Figure 5.7). Treatment with indium chloride ($InCl_3$) reduces the relative intensity of the ligand peak to the (111) diffraction peak while treatment with hydrofluoric acid (HF) removes the

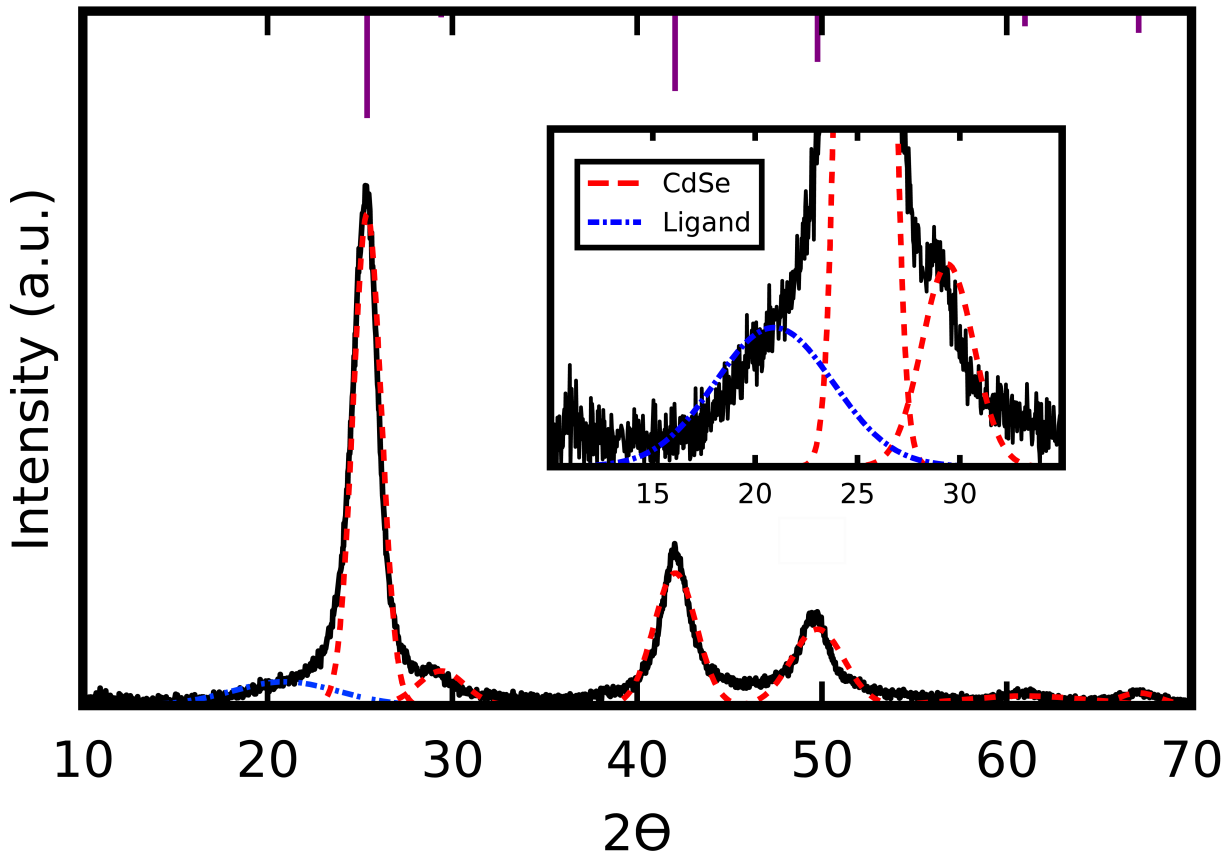


Figure 5.6: Fitted powder X-ray diffraction spectra of cadmium selenide quantum dots capped with oleate. Gaussian peaks were used to fit the ligand peak and the inorganic peaks. Reference data for zinc-blende cadmium selenide depicted as purple lines (ICSD 1611296). Cu K-α (λ = 1.5418 Å) is the X-ray source for the powder X-ray diffraction spectra.

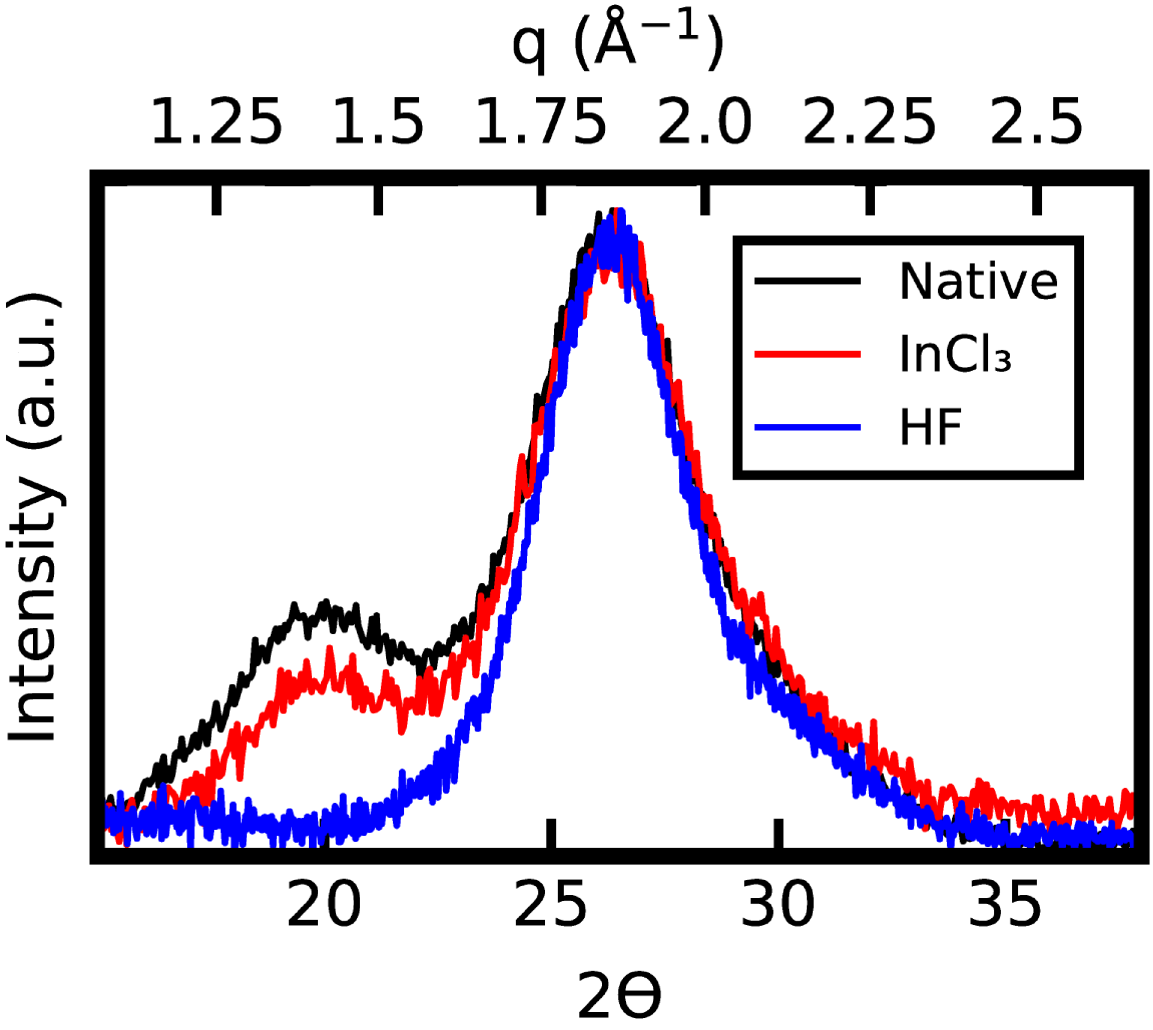


Figure 5.7: Experimental powder X-ray diffraction spectra of inorganic ligand exchanged InP quantum dots treated with indium chloride ($InCl_3$) and hydrofluoric acid (HF). Cu K-α ($\lambda = 1.5418$ Å) is the X-ray source for the powder X-ray diffraction spectra.

ligand peak entirely. Indium chloride has been shown to partially displace indium myristate from indium phosphide quantum dot surfaces in a Z-type ligand exchange (Chapter 3), while hydrofluoric acids protonates the carboxylates on the quantum dot surface and replaces them with fluorine.[22]

As mentioned above, as the nanocrystal size increases this peak becomes less significant. Larger quantum dots should have a smaller proportion of organic material represented in their powder X-ray diffraction, meaning this ligand peak should effectively disappear from the powder X-ray diffraction pattern once the nanocrystal size becomes sufficiently large (Figure 5.6). A series of experiments quantitatively demonstrated that as quantum dot size increases, the relative intensity of the organic ligand peak to the inorganic (111) diffraction peak decreases. Indium phosphide quantum dots were synthesized with diameters varying between 3.4 and 4.6 nm, as determined by their absorption spectra, and corresponding powder X-ray diffraction patterns were collected (Figure 5.8). Note that the size calculator by Reiss *et al.*[99] were used for this graph rather than the more accurate calculator provided by Ministro,[132] see Appendix C.2. As predicted, with increasing quantum dot size, the relative intensity of the ligand peak decreased in both experimental (Figure 5.8A and B) and simulated powder X-ray diffraction patterns (Figure 5.8C).

If this peak originates from packing of organic chains on the nanocrystal surface, changing the nature of the ligand on the surface should affect the shape of the previously unassigned powder X-ray diffraction peak. Powder X-ray diffraction patterns of indium phosphide quantum dots capped with myristate ($C_{14}H_{27}O_2$), palmitate ($C_{16}H_{31}O_2$), and stearate ($C_{18}H_{35}O_2$) ligands were collected (Figure 5.9A). As the length of the carbon chain increases, the relative intensity of the ligand peak increases due to a greater number of carbons atoms contributing to the diffraction signal. Powder X-ray diffraction simulations predict this same trend (Figure 5.9B). These results suggest that with very short ligands, the ligand peak may visibly disappear and not be observed unless purposely analyzed by peak deconvolution techniques.

Interestingly, the indium phosphide quantum dots capped with stearate have a more intense and sharper peak than those capped with myristate and palmitate. As previously determined by analyzing the thermodynamic data on the exchange of carboxylates on indium phosphide, internal rotation restriction of stearate is more severe than that of palmitate and myristate ligands, and stearate ligands also have stronger inter-ligand Van der Waals interactions than palmitate and myristate (Chapter 4). This further supports the evidence that organic ligand shells consisting of 18-carbon straight chains are in a different phase than those of bent ligands or shorter ligands. Shifting of the ligand powder X-ray diffraction peak to larger q values indicates a decrease in distance between chains, consistent with stronger van der Waals interactions and restrictions on internal rotations. Sharpening of the peak as well as greater intensity may also indicate possible ordering between ligands attached to different nanocrystals. Additionally, this sharp peak in the quantum dot powder X-ray diffraction pattern is similar in location and shape to that of recrystallized indium myristate; however, as stated it is unlikely to be the cause of this previously unassigned peak (Figure 5.2).

Providing further evidence for this hypothesis, Balan *et al.* predict a "melting" phase

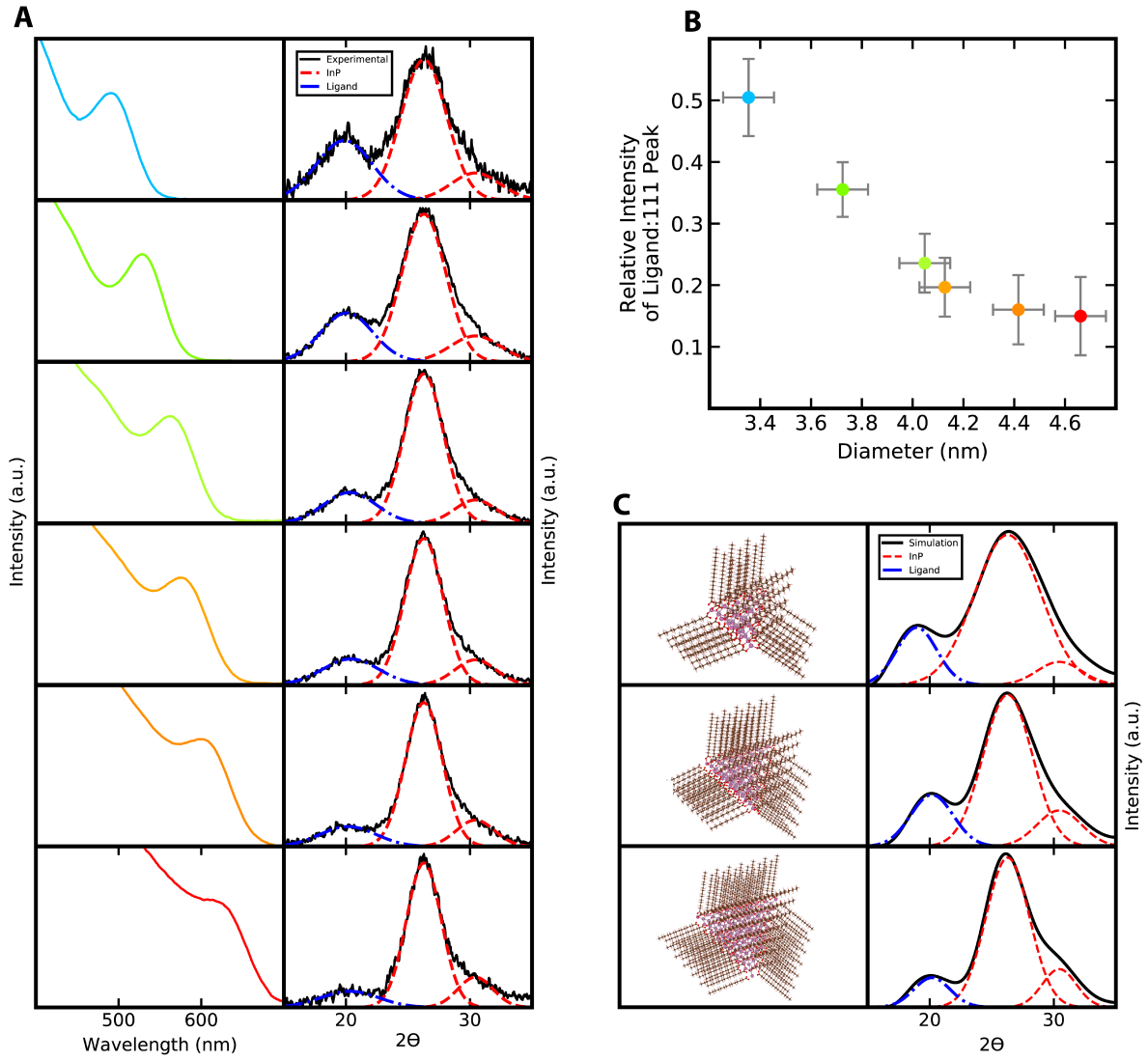


Figure 5.8: Experimental and simulated powder X-ray diffraction spectra of a size series of InP quantum dots determined by absorption spectra. (A) Absorption spectra of indium phosphide quantum dots indicating the size of the quantum dots coupled with the powder X-ray diffraction spectra. (B) Relative intensity of the ligand peak to the (111) diffraction peak of indium phosphide as a function of quantum dot size determined by powder X-ray diffraction peak deconvolution. Error in relative intensity was determined by propagation of the standard error in counts per second from the detector and error in nanocrystal size was taken at 10% from reported errors in sizing calculation functions determined by absorption spectroscopy. (C) Atomic models of a size series of indium phosphide quantum dots and the corresponding simulated powder X-ray diffraction patterns. Cu K-α ($\lambda = 1.5418$ Å) is the X-ray source for the powder X-ray diffraction spectra.

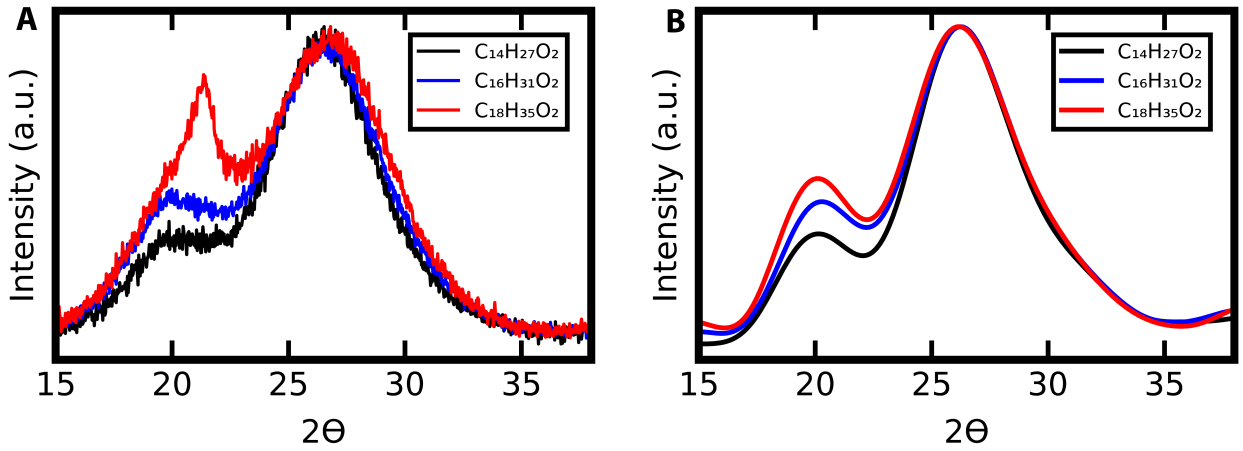


Figure 5.9: Experimental and simulated powder X-ray diffraction spectra of carboxylate capped InP quantum dots. (A) Experimental powder X-ray diffraction spectra of indium phosphide quantum dots capped with myristate ($C_{14}H_{27}O_2$), palmitate ($C_{16}H_{31}O_2$), and stearate ($C_{18}H_{35}O_2$) ligands. (B) Simulated powder X-ray diffraction spectra of indium phosphide quantum dots capped with myristate, palmitate, and stearate ligands. Cu K-α ($\lambda = 1.5418$ Å) is the X-ray source for the powder X-ray diffraction spectra.

transition in the ligand shell above room temperature for colloidal quantum dots capped solely with octadecylphosphonate ($C_{18}H_{38}O_3P$).[42] Indeed, for indium phosphide quantum dots, when oleate ($C_{18}H_{33}O_2$) capping ligands (a ligand containing a *cis*-alkene that hinders ordering and inter-ligand interactions) are exchanged for octadecylphosphonate ligands (a long, straight chained ligand) the resulting powder X-ray diffraction has the same sharpness observed in the stearate capped particle spectrum (Figure 5.10A). Similarly, when indium phosphide nanocrystals capped with stearate have their ligands partially exchanged for oleylamine ($C_{18}H_{37}N$), another ligand containing a *cis*-alkene, the peak broadens and shifts to smaller q values (Figure 5.10B).

Sandhyarani *et al.* provide further experimental evidence of this phenomenon through their study of superlattices of silver nanoparticles capped with alkylthiol ligands, particularly those capped with octadecanethiol ($C_{18}H_{37}S$).[133] Differential scanning calorimetry of the superlattices revealed two peaks in the heating curve: a smaller peak around 325 K and a larger peak around 405 K. The smaller peak was attributed to the transition to a liquid phase that still retained alkyl chain order, while the larger peak was attributed to the transition to a liquid phase where alkyl chain order was no longer present.[42] Ordering of the alkyl chains in these superlattices was also observed by Fourier transform infrared spectroscopy.[141] We suggest that myristate and palmitate capped particles are in the first liquid phase that still retains some order, while stearate capped particles are in the more crystalline phase. Interestingly, in the powder X-ray diffraction pattern reported by Sandhyarani *et al.*, a peak attributed to the superlattices around 20° 2θ is present that is wider than the other

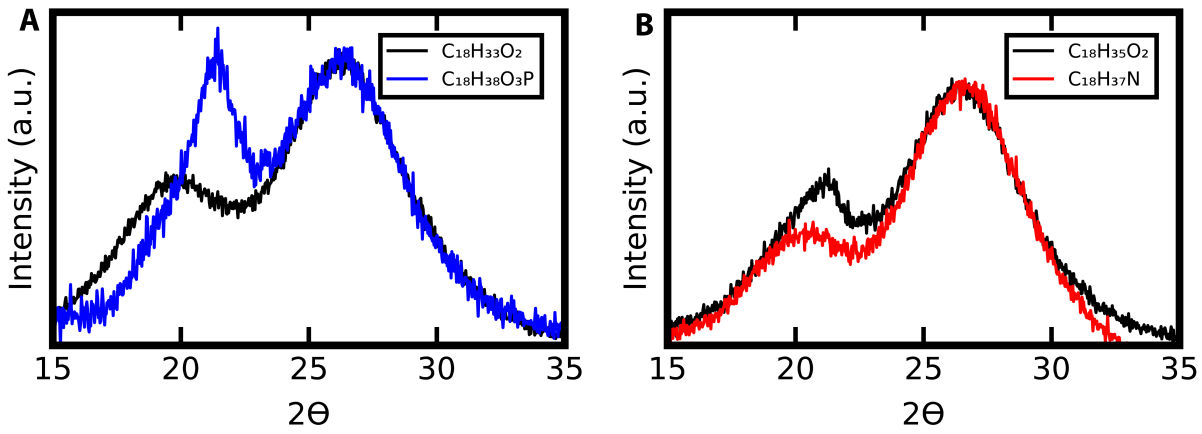


Figure 5.10: Experimental powder X-ray diffraction spectra of organic ligand exchanged InP quantum dots. (A) Experimental powder X-ray diffraction spectra of indium phosphide quantum dots initially capped with oleate ($C_{18}H_{33}O_2$) and after ligand exchange with octadecylphosphonate ($C_{18}H_{38}O_3P$). (B) Experimental powder X-ray diffraction spectra of indium phosphide quantum dots initially capped with stearate ($C_{18}H_{35}O_2$) and after a 10% ligand exchange with oleylamine ($C_{18}H_{37}N$). Note that the powder X-ray diffraction pattern of stearate capped indium phosphide quantum dots in Figure 5.9A differs from the one in panel (B) as the quantum dots are larger and from a separate synthesis. Cu K-α ($\lambda = 1.5418$ Å) is the X-ray source for the powder X-ray diffraction spectra.

superlattice peaks. We suspect this feature is actually from the ordering of ligands on the nanoparticle surfaces.[133] Furthermore, differential scanning calorimetry thermograms on indium phosphide magic clusters capped with myristate alongside ^{13}C NMR provide evidence of a small phase transition of the ligand shell at 339 K.[154] Similar differential scanning calorimetry measurements have reported a phase transition attributed to oleate ligands melting and freezing on the surface of lead sulfide nanocrystals in superlattices in the range of 240–270 K. These results are all consistent with our hypotheses about the nature of the ligand shell and its dependence on the types of aliphatic ligands and the temperature, where *cis*-alkenes cause a lowering of the phase transition and have weaker intermolecular interactions and less ordering while longer, straight-chain alkanes are more ordered.[42]

To further investigate our hypothesis concerning the ordering of the ligand shell, we performed temperature dependent molecular dynamics simulations on our atomic model and experimental temperature dependent powder X-ray diffraction on stearate capped indium phosphide quantum dots. Previous powder X-ray diffraction simulations were performed on atomic systems with perfectly aligned ligands on the nanocrystal, but this is not a strictly accurate representation, particularly of indium phosphide quantum dots capped with shorter chain ligands. After performing molecular dynamics simulations at 300 K, 400 K, and 500 K (Figures 5.11A–C), we observed that ligands are still fairly ordered at 300 K, forming clumps

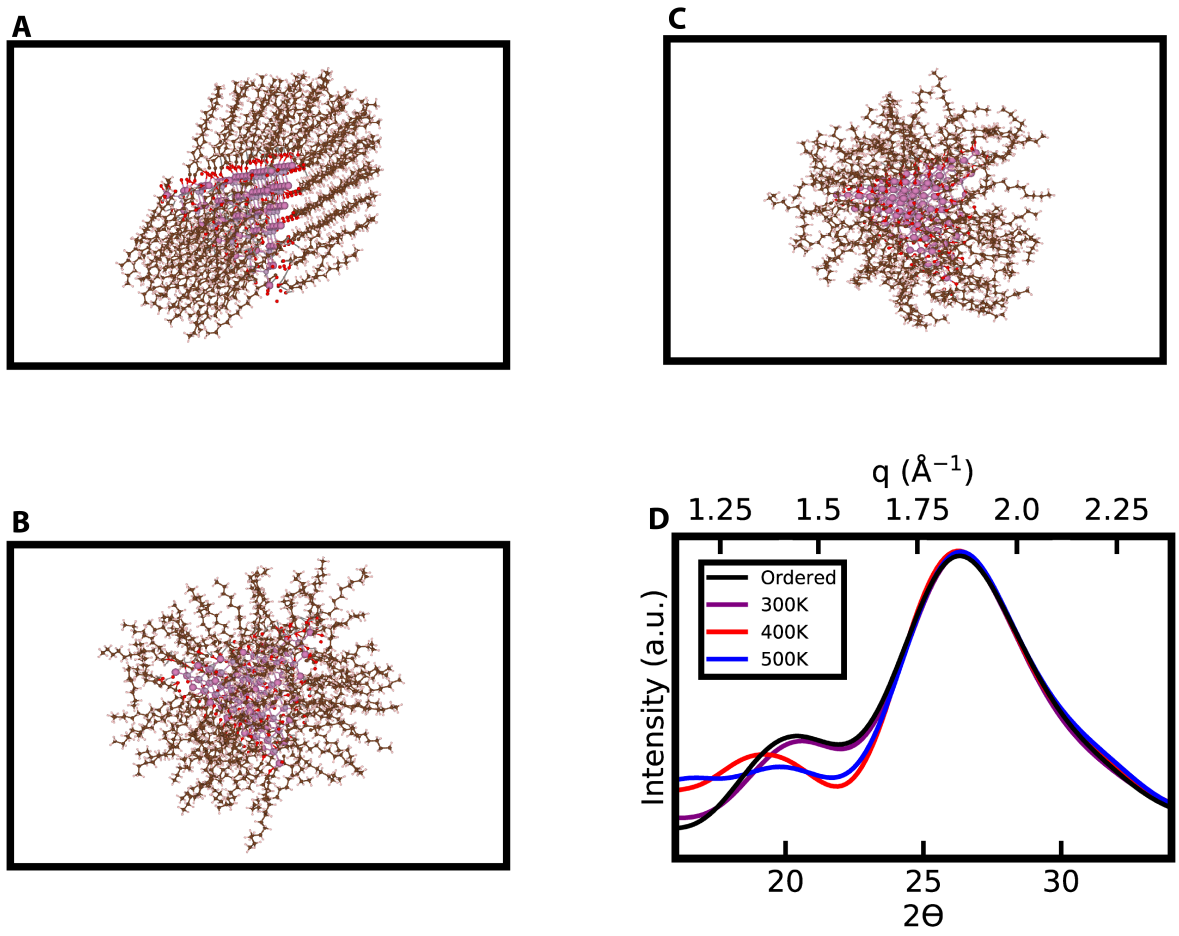


Figure 5.11: Simulated variable temperature powder X-ray diffraction spectra of InP quantum dots. (A) Atomic model of an indium phosphide quantum dot capped with myristates after molecular dynamics simulations at 300 K. (B) Atomic model of an indium phosphide quantum dot capped with myristates after molecular dynamics simulations at 400 K. (C) Atomic model of an indium phosphide quantum dot capped with myristates after molecular dynamics simulations at 500 K. (D) Simulated powder X-ray diffraction spectra of indium phosphide quantum dots before and after molecular dynamics simulations. Cu K-α ($\lambda = 1.5418$ Å) is the X-ray source for the powder X-ray diffraction spectra.

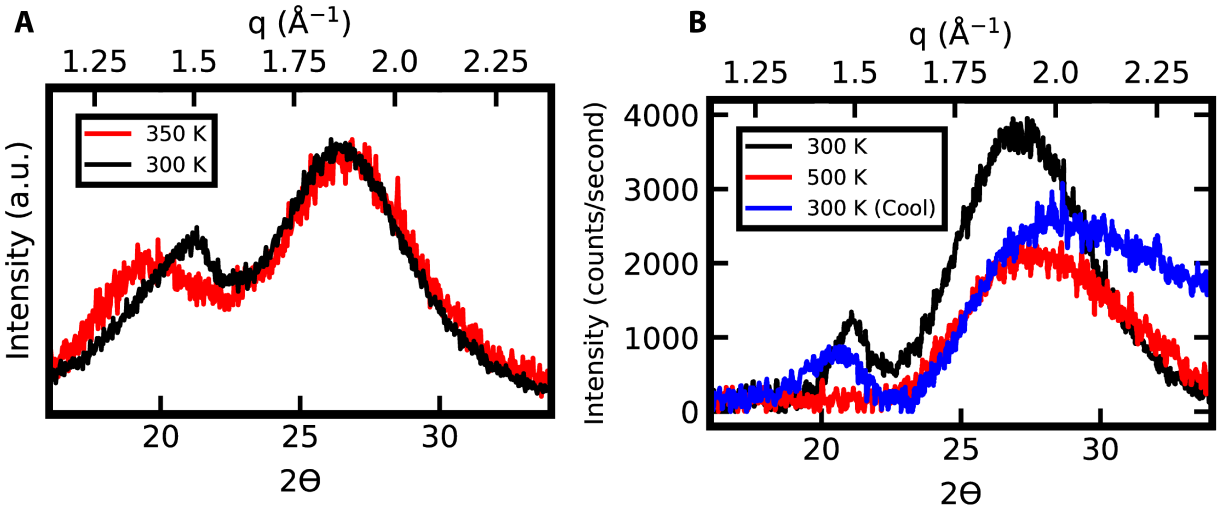


Figure 5.12: Experimental variable temperature powder X-ray diffraction spectra of InP quantum dots. (A) Experimental powder X-ray diffraction spectra of indium phosphide quantum dots capped with stearate depicting the peak shifting and decreasing in intensity at an increased temperature. (B) Experimental powder X-ray diffraction spectra of indium phosphide quantum dots capped with stearate showing the disappearance of the ligand peak at 500 K followed by its reappearance when cooled back to 300 K. Note that patterns depicted in (A) and (B) were measured on different instruments. The broadening of the (111) diffraction peak in the heated and cooled spectra is evidence that the sample may have slightly degraded due to sustained high temperatures. Cu K-α ($\lambda = 1.5418$ Å) is the X-ray source for the powder X-ray diffraction spectra.

of ligands that appear to be slightly less ordered at the edges. The ligands became more disordered as temperature increased, as seen from previous molecular dynamics simulations of ligands on the nanoparticle surfaces.[137,138] The simulated powder X-ray diffraction patterns show that as temperature increases, the peak broadens and shifts to smaller q values, indicating wider ligand spacing that is attributed to increased disorder and weaker interactions (Figure 5.11D).

Experimental powder X-ray diffraction patterns reveal that at room temperature the stearate ligand peak is sharp and located at larger q values; however, upon raising the temperature in the powder X-ray diffraction sample holder, from 300 K to the 350 K, the peak shifts to smaller q values and broadens (Figure 5.12A). This is consistent with the behavior observed in the molecular dynamics simulations and analysis in Figure 5.11. When the sample is heated from 300 K to 500 K the peak completely disappears, but when it is cooled back to 300 K the peak reappears (Figure 5.12B). These results confirm the reversibility of the ligand shell phase transition previously observed by Sandhyarani *et al.* with silver

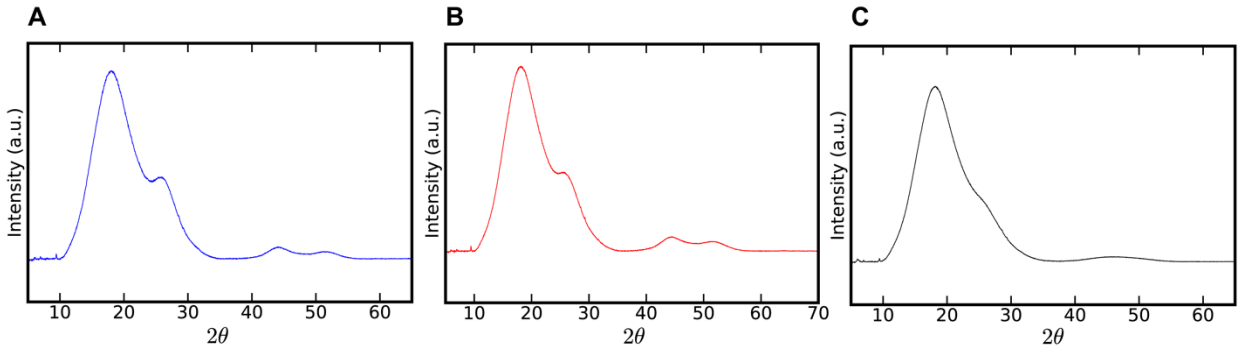


Figure 5.13: Raw X-ray diffraction spectra of solutions sealed in polyimide capillary tubes containing (A) myristate ($C_{14}H_{27}O_2$) capped indium phosphide quantum dots in toluene, (B) stearate ($C_{18}H_{35}O_2$) capped indium phosphide quantum dots in toluene, and (C) toluene. Cu K-α ($\lambda = 1.5418$ Å) is the X-ray source for the powder X-ray diffraction spectra.

nanocrystal superlattices.[133]

The measurements in Figures 5.12A and 5.12B were taken on different instruments to optimize different variables. The instrument used for Figure 5.12A's measurements provides better signal to noise ratio allowing us to clearly see nuances in the ligand peak shape at different temperatures. Whereas, the diffractometer used for Figure 5.12B's measurements could accommodate a wider range of temperatures allowing us to observe ligand shell behavior at temperature extremes.

5.5 Observing Ordered Ligands in Solution

While the previous measurements were done on dried nanocrystal powders, the question of ligand ordering in the solution state remained. To address this, X-ray diffraction measurements of dry indium phosphide quantum dots and solvated indium phosphide quantum dots in toluene sealed in polyimide capillary tubes were collected. Given that a phase transition term was required in the modeling process of stearate ligand shells (Chapter 4), it seemed plausible to attempt to directly observe ordered ligands on the surface of colloidal quantum dots by X-ray diffraction while the nanocrystals were suspended in solution. However, measurements of solvated quantum dots were complicated by the large background signal precisely in the region of the spectra that was being measured (Figure 5.13), which is attributed to solvent scattering.[147,181] By fitting a subtraction of both the diffraction pattern from the neat solvent and the inorganic peaks at fixed reflections, a background subtracted X-ray diffraction pattern was recovered (Figure 5.14). The peak attributed to the organic ligands shifts to around $q = 1.2$ Å^{-1} for both the myristate and stearate capped samples and broadens significantly (Figure 5.15). No difference in the peak is detected between the solvated myristate and stearate capped samples.

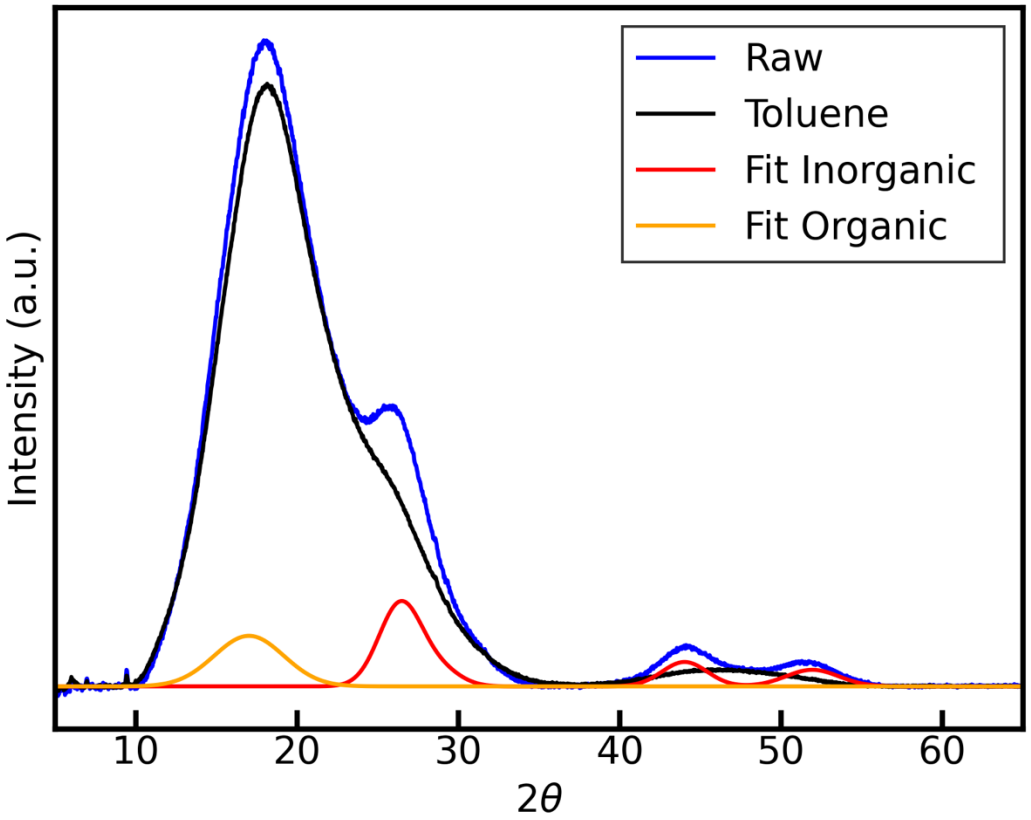


Figure 5.14: Fit X-ray diffraction spectrum of myristate ($C_{14}H_{27}O_2$) capped InP quantum dots in toluene (blue) fit with the toluene solvent spectrum (black), inorganic ligand peaks (red), and an organic ligand peak (orange). Cu K-α ($\lambda = 1.5418$ Å) is the X-ray source for the powder X-ray diffraction spectra.

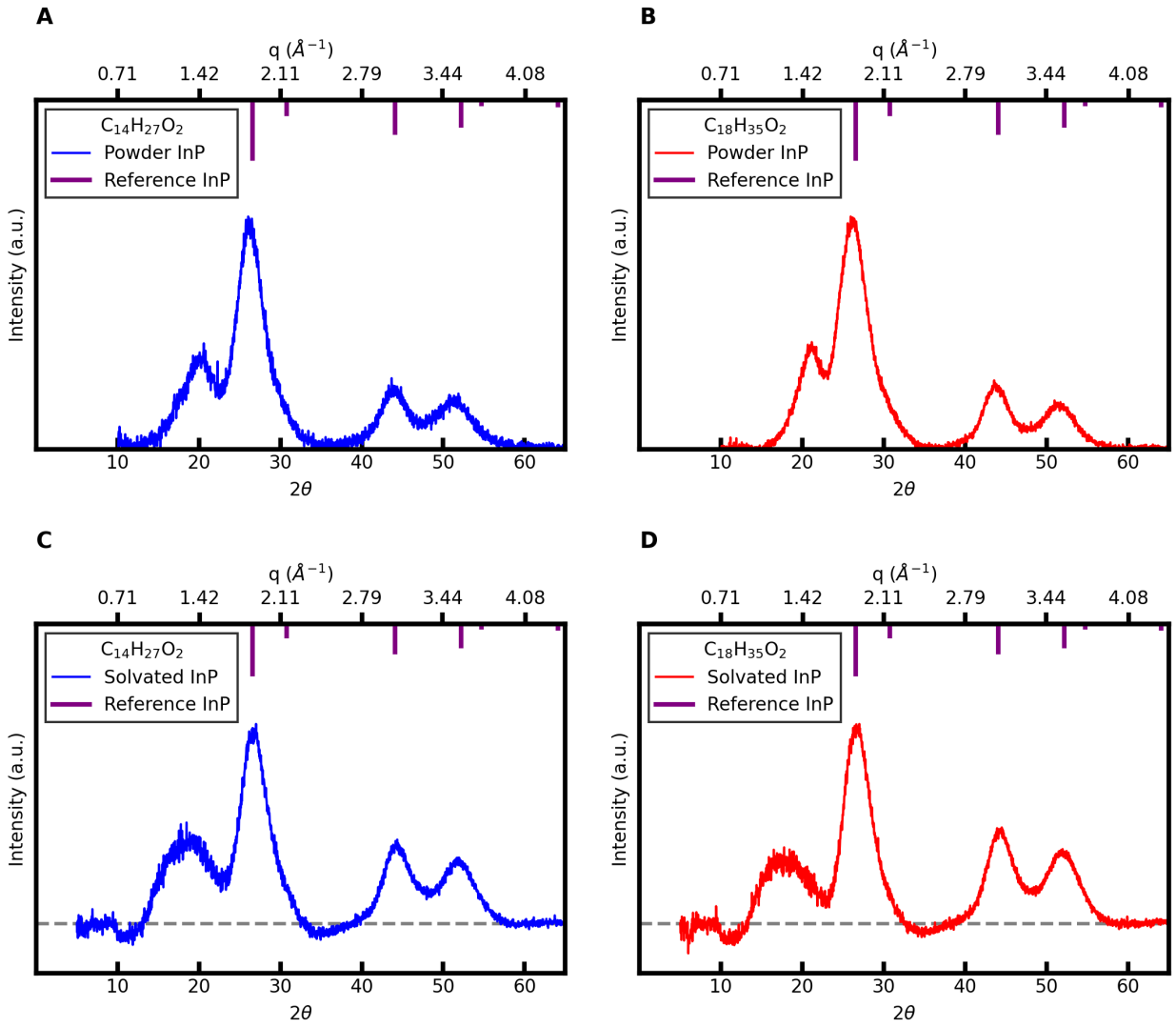


Figure 5.15: X-ray diffraction spectra of solvated InP quantum dots alongside the dry spectra and reference peaks (ICSD 1600543) for indium phosphide, depicted at the top of the spectra in purple. (A) Powder X-ray diffraction spectrum of indium phosphide quantum dots capped with myristate ($C_{14}H_{27}O_2$). (B) Powder X-ray diffraction spectrum of indium phosphide quantum dots capped with stearate ($C_{18}H_{35}O_2$). (C) X-ray diffraction spectrum of solvated indium phosphide quantum dots capped with myristate ($C_{14}H_{27}O_2$). (D) X-ray diffraction spectrum of solvated indium phosphide quantum dots capped with stearate ($C_{18}H_{35}O_2$). Cu K-α ($\lambda = 1.5418$ Å) is the X-ray source for the powder X-ray diffraction spectra.

Results from powder X-ray diffraction data do not provide strong insights into the nature of native solvated ligand shells. The peak attributed to the organic ligands in the solvated samples is significantly broader than the organic ligand peak in the dry samples and shifted to smaller angles in the X-ray diffraction spectra. This shift to smaller angles would indicate increased spacing between the surface ligands and is expected as solvent molecules intercalate the ligand shell.[59,182] This also suggests that the inter-ligand interactions in the dried nanocrystal state are almost certainly to be stronger than in the solution state. While the spectra of both myristate and stearate capped quantum dots show a similar feature, there appears to be no definitive difference between the spectra, either in position or intensity of the peak. This would indicate that the two ligand shells have similar structures and appears to contradict the different phases predicted from the modified Ising model. However, this observation may be a result of the background subtraction process or other limitations to this method. Oddly, the ligand shell peak, relative to inorganic peaks, is of greater total intensity in the solvated spectra when compared to powered spectra.

While it appears that ordered ligands on the surface of colloidal quantum dots can be detected by X-ray diffraction in the liquid state, it may be difficult to quantitatively infer much about the structure from the measurements, due to the challenges of subtracting the solvent peak. It certainly could be possible through creative manipulations of the fitting of the peaks to generate a difference between spectra with plausible explanations, yet any such determination should be rigorously scrutinized before any final claims are made. One avenue for future potential insight into the structure of the organic ligand shell in solution for these varying chain lengths may be small-angle X-ray scattering or small-angle neutron scattering measurements that have shown themselves to be successful at determining the diameter of the organic ligand shell.[140,183]

5.6 Implications for Nanocrystal Characterization

From this suite of measurements, we conclude that the previously unassigned peak often observed at $q = 1.4$ Å^{-1} originates from ordered aliphatic ligands on the quantum dot surfaces. Not only does this conclusion assist in clarifying commonly observed results in powder X-ray diffraction and GIWAXS patterns of small nanoparticles capped by long carbon chains, but it also has much broader implications. For example, structural information about the ligands on small quantum dot surfaces can be deduced from a relatively routine characterization method, powder X-ray diffraction. We encourage future characterization of nanocrystals to consider this peak. Although ligand peaks in larger nanocrystals may be significantly dwarfed by their inorganic counterparts, they should still be detectable through careful measurement and peak deconvolution (Figure 5.6).

More broadly, measurement and manipulation of surface ligand ordering can have significant impact on many properties of colloidal quantum dots. Highly ordered ligands on colloidal quantum dot surfaces can have detrimental effects on optical properties.[42–45] Disordered surface ligands also increase the solubility of nanoparticles, and understanding the

dynamics between ligand type and ligand length on their ordering could enable more precise tuning of solubility.[139] Additionally, ligands have been shown to cause tensile stress to the nanoparticle surfaces, which is likely enhanced by more crystalline phase ligands.[102,184,185] powder X-ray diffraction measurements could also potentially tease out the effects of ligand exchanges and mixed ligand shells. For example, evidence has been shown that mixed ligand shells may not randomly distribute their ligands, but rather form patchy surfaces.[102] In certain cases, powder X-ray diffraction may be used to observe these effects.

The field most likely to benefit from this work involves the formation of nanocrystal superlattices. As observed by Sandhyarani *et al.*, the melting behavior of superlattices depends on these types of ordering interactions.[133,143] The use of GIWAXS to identify and evaluate this feature alongside SAXS and grazing incidence small angle X-ray scattering (GISAXS) to characterize and analyze superlattices should yield further insight into the superlattice structures.[145–147,186] Altering the phase of the ligands could potentially manipulate the ligand ordering behavior to change distances between nanocrystals or modify superlattice assembly.[182,186–188] We anticipate that these techniques can assist in optimizing future superlattices through employment of ligands with appropriate crystallization properties and maintaining temperatures during superlattice formation that encourage certain ligand shell behavior. In general, these measurements can help develop design rules for ligands to engineer the preferred type of organic shell. Optimization of nanostructures requires a thorough understanding of their properties, particularly at their surfaces, and powder X-ray diffraction provides one additional tool for characterizing ligands on nanocrystal surfaces. This simple, yet effective method has revealed far more about the ligand shell structure than previously thought possible.

Chapter 6

Surface and Interface Energies of Colloidal Nanocrystals

6.1 Surface Energy and Nanocrystals

One of the fundamental thermodynamic quantities of nanomaterials that the previous work has not dealt with is the surface energy of these colloidal nanocrystals. As materials approach the nanoscale, surface energy plays an increasingly important role in their overall thermodynamic stability.[189–192] Almost invariably, surface energy, or surface tension, denoted as γ, is a positive quantity, where atoms or molecules at the surface of a material are considered to be in a less thermodynamically stable state than those in the interior due to broken bonds or fewer favorable interactions.[193,194] In general, this effect of surface energy encourages materials to adopt low surface area configurations, minimizing the overall energy of the system.[192,195] This size-dependent effect of surface energy on material stability can be so impactful that it has been observed to invert the phase stability in titania. While rutile is the most thermodynamically stable phase in bluk, nanocrystalline anatase is more thermodynamically stable than nanocrystalline rutile.[190]

The surface energy is of paramount importance when considering the shape of nanocrystals, and justifications for why nanocrystals adopt certain shapes or why they grow in a particular manner is often attributed to surface energy.[36,195–199] Wulff constructions of nanocrystal shapes are based on the surface energy of crystal facets, where different facets may have different surface energies attributed to different numbers of broken bonds or more or less favorable orientations of atoms at the surface of a given facet.[195,200] As a result, substantial effort has been devoted to calculating the surface energies of crystal facets for a variety of materials.[36,196,198,201]

While it may be convenient to consider and calculate properties for nanocrystals assuming perfect termination with bare, crystalline facets, in reality nanocrystals often have species adsorbed to their surface.[17,184,190–192,198,202,203] These species are often referred to as ligands, and the structure of molecules adsorbed at nanocrystal surfaces, their binding motifs, and

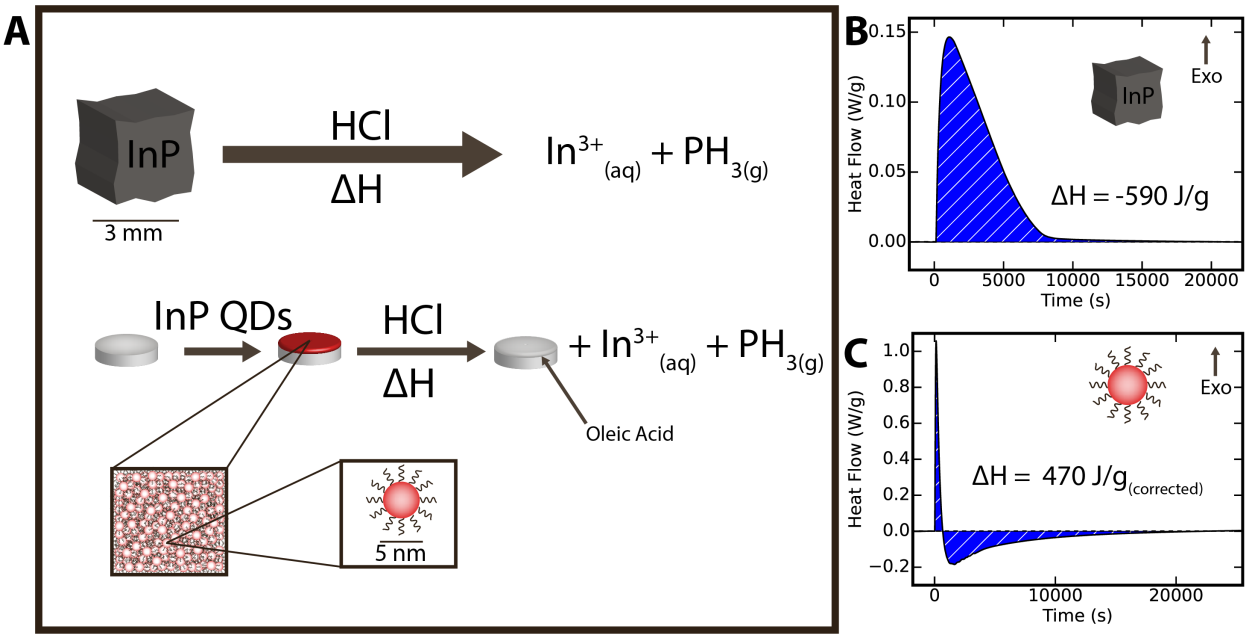


Figure 6.1: Experimental procedure and raw results of dissolution calorimetry experiments. (A) Reaction equations for the dissolution of bulk (top) and nanocrystals (bottom) of indium phosphide in hydrochloric acid. The indium phosphide quantum dots are deposited on a Teflon platform as an agglomeration. After dissolution of the indium phosphide quantum dots, oleic acid is left behind. (B) Heat flow measurements of the reaction of bulk indium phosphide with hydrochloric acid over time, with the integrated area in blue and the total enthalpy recorded as -590 J/g. Note that a positive heat flow is an exothermic reaction, while a negative heat flow is an endothermic reaction. (C) Heat flow measurements of the reaction of nanocrystals of indium phosphide with hydrochloric acid over time, with the integrated area in blue and the total corrected enthalpy recorded as 470 J/g. Note that the thermal effects of the Teflon platform and protonation of oleic acid must be corrected for, hence the corrected enthalpy.

their impact on nanocrystal properties cover a wide range of research in the nanocrystal field.[182,204] These ligands impact the growth,[36,196,199,204] colloidal stability,[13,182] optical and electronic properties,[16,17] self-assembly into superlattices,[59,182] and applications that nanomaterials can be used in.[93,205] Since ligands serve as stabilizing agents for atoms at the surface, theyshould substantially lower the surface energy of a material.[191,192,198,201,202,206]

6.2 Dissolution Calorimetry of Colloidal Quantum Dots

To study the thermodynamics of the surfaces of colloidal quantum dots, we measured the surface energy of quantum dots capped with oleate ($C_{18}H_{33}O_2$) using dissolution calorimetry. This technique that has been well established to measure the surface energies of nanocrystals,[190,191] but, to the best of our knowledge, has never applied to colloidal quantum dots. Changing the size of the nanocrystal modulates the proportion of atoms on the surface of the nanocrystal versus those in the interior. By dissolving these materials into atomic species and monitoring the heat flow during the reaction, the enthalpy of the reaction can be calculated. Figure 6.1A illustrates the experimental method for this technique. Indium phosphide, either as a bulk material or as agglomerated quantum dots deposited on a Teflon platform, is dissolved in hydrochloric acid in a sample chamber, and the differential heat flow between the sample chamber and a reference chamber filled with hydrochloric acid is recorded. The sample and reference chambers are maintained at an isothermal temperature of 25 °C. The heat flow during the reaction is depicted in Figure 6.1B and 6.1C for the bulk indium phosphide and quantum dots, respectively. An interesting observation from these measurements is that the heat flow for both measurements is initially exothermic, but the magnitude of the signal is much greater for the quantum dot sample. This is consistent with the dissolution of indium phosphide occurring at the surface, and considering the much higher surface area of the quantum dots, a larger heat flow is to be expected. However, rapidly the dissolution becomes endothermic for the quantum dot samples. Unfortunately, it is difficult to directly assign the cause of this switch to an endothermic signal as it could be due to a different reaction that may be occurring at a different rate, or it could be compensation by the instrument for overcorrection of the heat flow to maintain an isothermal temperature. The oleate ligands are protonated to create oleic acid (Figure 6.2), but as oleic acid is not soluble in aqueous solutions, it does not dissolve in the hydrochloric acid. If the signals are integrated over time, the total heat of the reaction, or the enthalpy of the reaction, can be calculated. If the enthalpy of dissolution of the material in terms of kJ/mol is plotted versus the molar surface area (m^2/mol), or surface area in m^2 per mole of material, the slope of that line represents the excess enthalpy of the reaction as a function of surface area (J/m^2). The negative of that slope represents the excess enthalpy of the reverse reaction,[191] or the formation of nanocrystals from atomic species as a function of surface area. This excess enthalpy is defined as the surface enthalpy of a material. Often no distinction between surface enthalpy and surface energy is made,[189–191] but rigorously this calorimetric method measures enthalpy and there may be an entropic contribution to the Gibbs free energy of formation of these surfaces, or a surface Gibbs free energy. Except where specified, surface energy and surface enthalpy will be treated interchangeably.

Figure 6.3 depicts the enthalpy measured by dissolution calorimetry experiments plotted against the molar surface area for a size series of indium phosphide quantum dots. The molar surface area was determined using scanning transmission electron microscopy (STEM) imag-

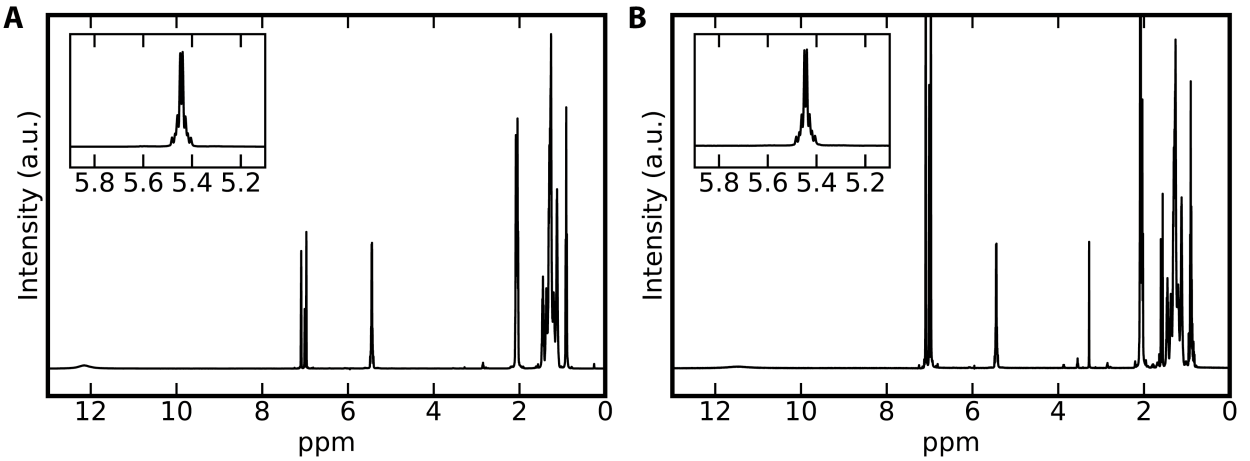


Figure 6.2: ^{1}H NMR spectra of oleic acid. (A) ^{1}H NMR spectra of 99% oleic acid in toluene-d_8 with inset of the vinyl proton region. (B) ^{1}H NMR spectra of recovered oleic acid from the calorimetry experiments in toluene-d_8 with inset of the vinyl proton region. Note solvent peaks at 7.09, 7.00, 6.98, and 2.09 ppm as well as a peak attributed to water in the spectra of the recovered oleic acid at 3.28 ppm.

ing (extensive sample characterization can be found in Appendix A.2 as well as Appendix B.8). A critical aspect of these measurements is ensuring pristine surfaces that are well defined. As indium phosphide is particularly susceptible to oxidation, even during the synthetic process, a unique hydrogen atmosphere synthesis[207] was used and no surface oxidation was detected by solid state NMR (see Appendix A.2). Unlike past measurements of nanocrystal surface energies,[191] the slope of this plot is positive, indicating that the surface energy of these indium phosphide quantum dots is negative, or that the atoms on the surface of the nanocrystals are more stable than the atoms in the interior. This result is highly unusual, as surface energies are typically regarded as positive values.

To investigate the generality of this phenomenon, size series of zinc sulfide, cadmium sulfide, and lead sulfide quantum dots capped with oleate were synthesized and interrogated via dissolution calorimetry, and the results are depicted in Figure 3 (extensive sample characterization can be found in Appendix A and B.8). For each of these materials, the surface energy was negative, although less negative than that of indium phosphide. This indicates that a negative surface energy may be a general property of colloidal semiconductor nanocrystals capped with carboxylate ligands and is not unique to indium phosphide nanocrystals. Although it is well accepted that these surface species, such as oleate ligands, lower the surface energy of a material,[191,198,201,202] there has been substantial controversy regarding whether the surface energy of a material can be lowered enough to become negative. It has been suggested that a negative surface energy implies that smaller nanocrystals would be more thermodynamically stable than larger ones, and that nanocrystals would disintegrate in the

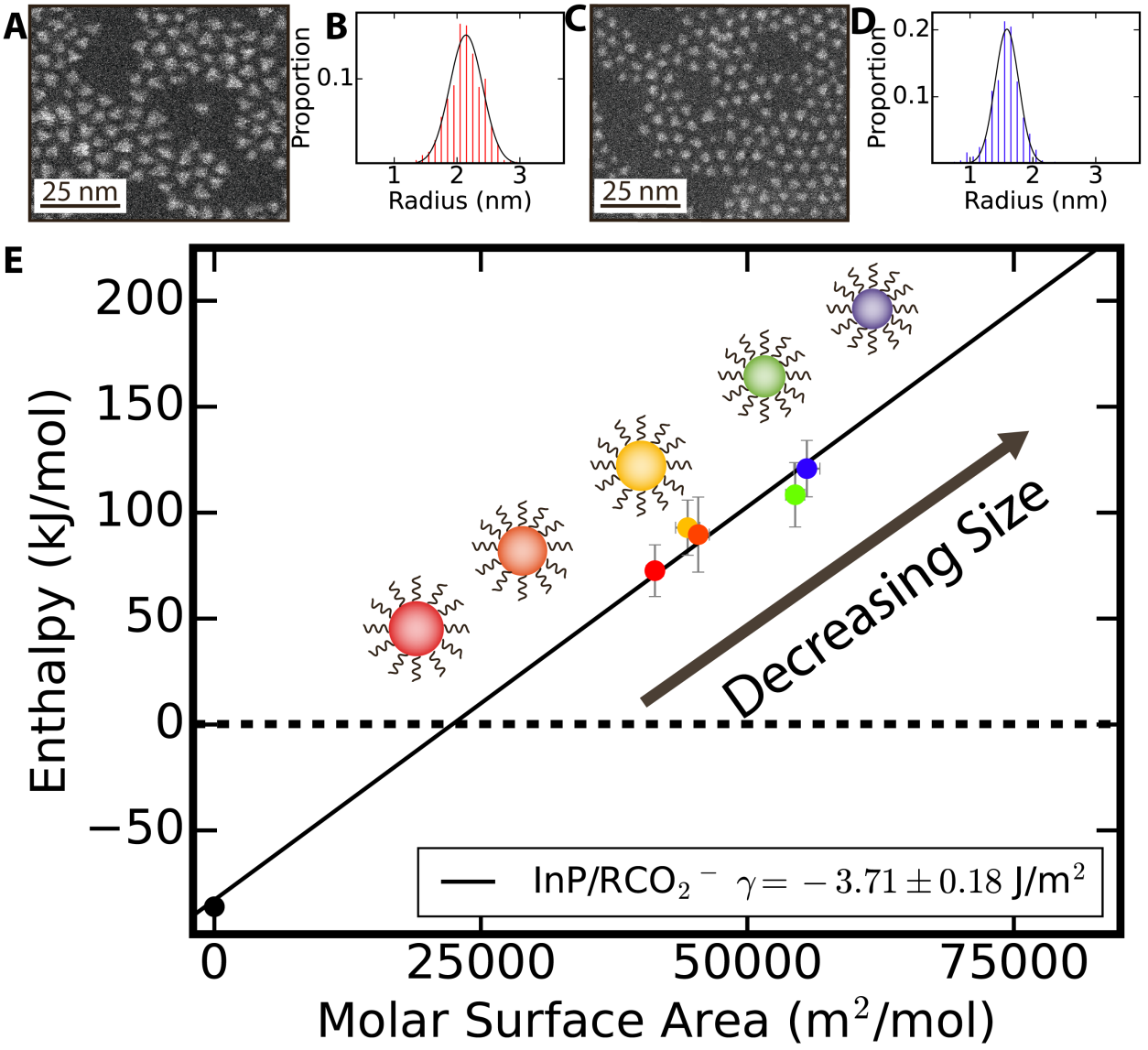


Figure 6.3: Measurements of the dissolution enthalpy of differently sized InP quantum dots. (A) STEM image of the largest quantum dot sample used in these measurements with inset scale bar. (B) Histogram fit with a Gaussian distribution of the largest quantum dot sample used in these measurements. (C) STEM image of the smallest quantum dot sample used in these measurements with inset scale bar. (D) Histogram fit with by a Gaussian distribution of the smallest quantum dot sample used in these measurements. (E) Plot of the enthalpy measured in kJ/mol against the molar surface area in m^2/mol for the samples with a fit line where the negative slope of the fit line is the measured surface energy of the quantum dots (-3.71 ± 0.18 J/m^2).

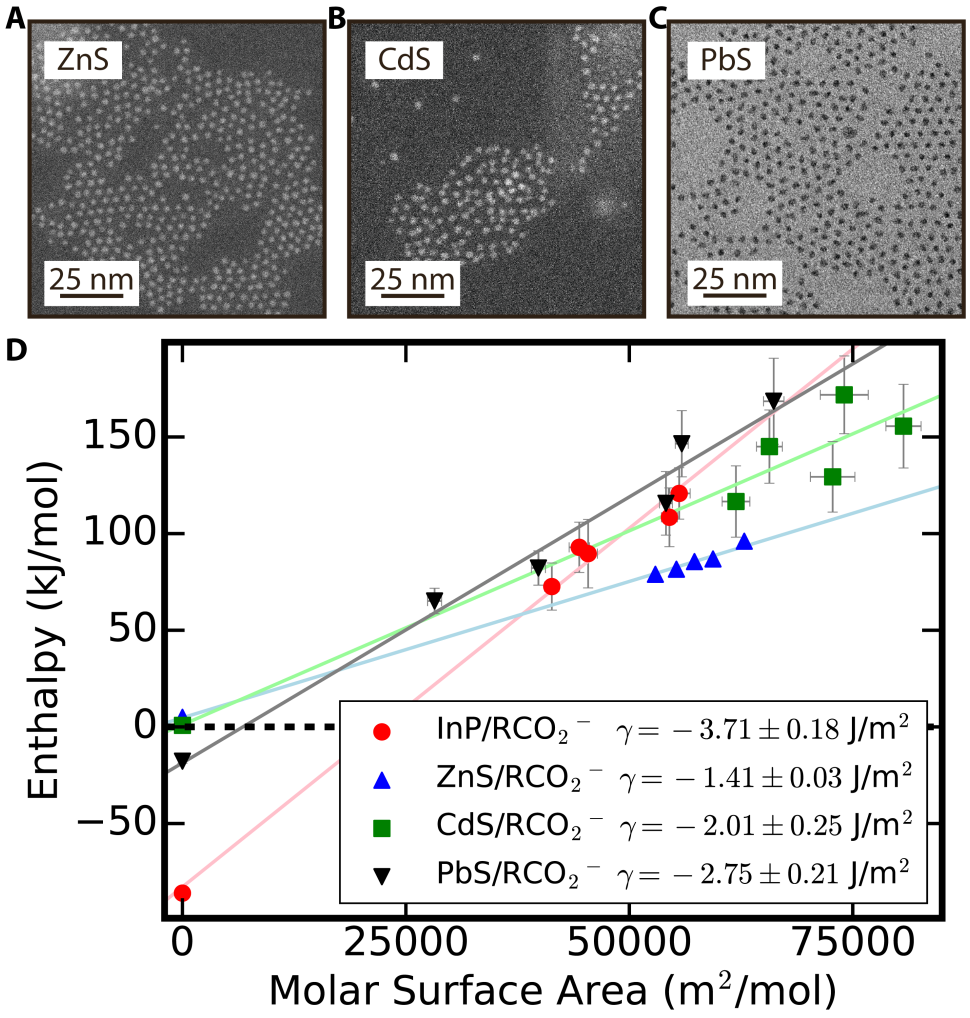


Figure 6.4: Measurements of the dissolution enthalpy of size series of different quantum dots. (A) STEM image of a sample of zinc sulfide quantum dots used in these measurements with inset scale bar. (B) STEM image of a sample of cadmium sulfide quantum dots used in these measurements with inset scale bar. (C) Transmission electron microscope image of a sample of lead sulfide quantum dots used in these measurements with inset scale bar. (D) Plot of the enthalpy measured in kJ/mol against the molar surface area in m^2/mol for the different material samples with fits line for the different samples where the negative slope of the fit line is the measured surface energy of the quantum dots, and the measured surface energy for each material is reported in the legend.

thermodynamic limit, and this implication has caused concern.[194] For example, a DFT study claimed that negative surface energies could be possible on alumina with strongly adsorbed water,[206] and the publication of this paper "caused confusion in the scientific community." This report prompted a follow up correspondence that called the use of the phrase negative surface energy "provocative" but that it is "possible to predict positive and negative surface energies for any number of multicomponent systems..."[208] Although a negative surface energy implies that nanocrystals are not in their most thermodynamically stable state, metastable systems certainly exist. Likewise, the existence of a positive surface energy suggests that larger nanocrystals would be more stable, and that any size of nanocrystal is in a metastable state. One cause of this controversy stems from different interpretations of the definition of surface energy. If the assumption is that atoms at a surface have fewer bonds than atoms in the interior, then indeed it follows that the surface energy will be positive (Figure 6.5A). However, the presence of these ligands means that surface atoms do not necessarily have dangling bonds, and if the surface ligands bind more tightly to the surface atoms than their interior bonds, the material will have a negative surface energy (Figure 6.5B). It may be more appropriate to refer to this quantity not as a surface energy, but perhaps an interface energy, where the thermodynamic stability of the interface between the nanocrystal and the adsorbed species is being studied. The interfacial energy would then be the sum of the surface energy of a bare nanocrystal surface plus the energy of adsorption of the surface species.[195,196]

6.3 Origins of a Negative Surface Energy

While the vast majority of literature assumes that surface energies must be positive, there are a few reports of negative surface stresses, negative surface tension, and negative surface energy, although these have exclusively been reported to the field of experimental X-ray diffraction.[184,192,203] With these studies, surface stress should be carefully defined as

$$f = \gamma + A \cdot \frac{d\gamma}{dA}$$

such that f is the surface stress, γ is the surface energy, and A is the area of a particle.[193,209,210] It has been proposed that the derivative term can be positive or negative, and hence the surface stress can be positive or negative while avoiding the assertion that the surface energy is negative.[193,209,210] In X-ray diffraction studies, only the surface stress can be measured, although the terms surface stress, surface tension, and surface energy are often used interchangeably.[192] On the other hand, calorimetric measurements can directly measure the surface energy, and are therefore more appropriate for surface thermodynamics studies. However, multiple studies have attributed the binding of ligands to cause this surface stress, and it is interesting that the measured surface tension by Bertolotti et al. for lead sulfide nanocrystals capped with oleate was -0.618 J/m^2 and -0.537 J/m^2 in different publications,[184,203] and the estimated "surface energy" by Zhao et al. for cesium lead iodie

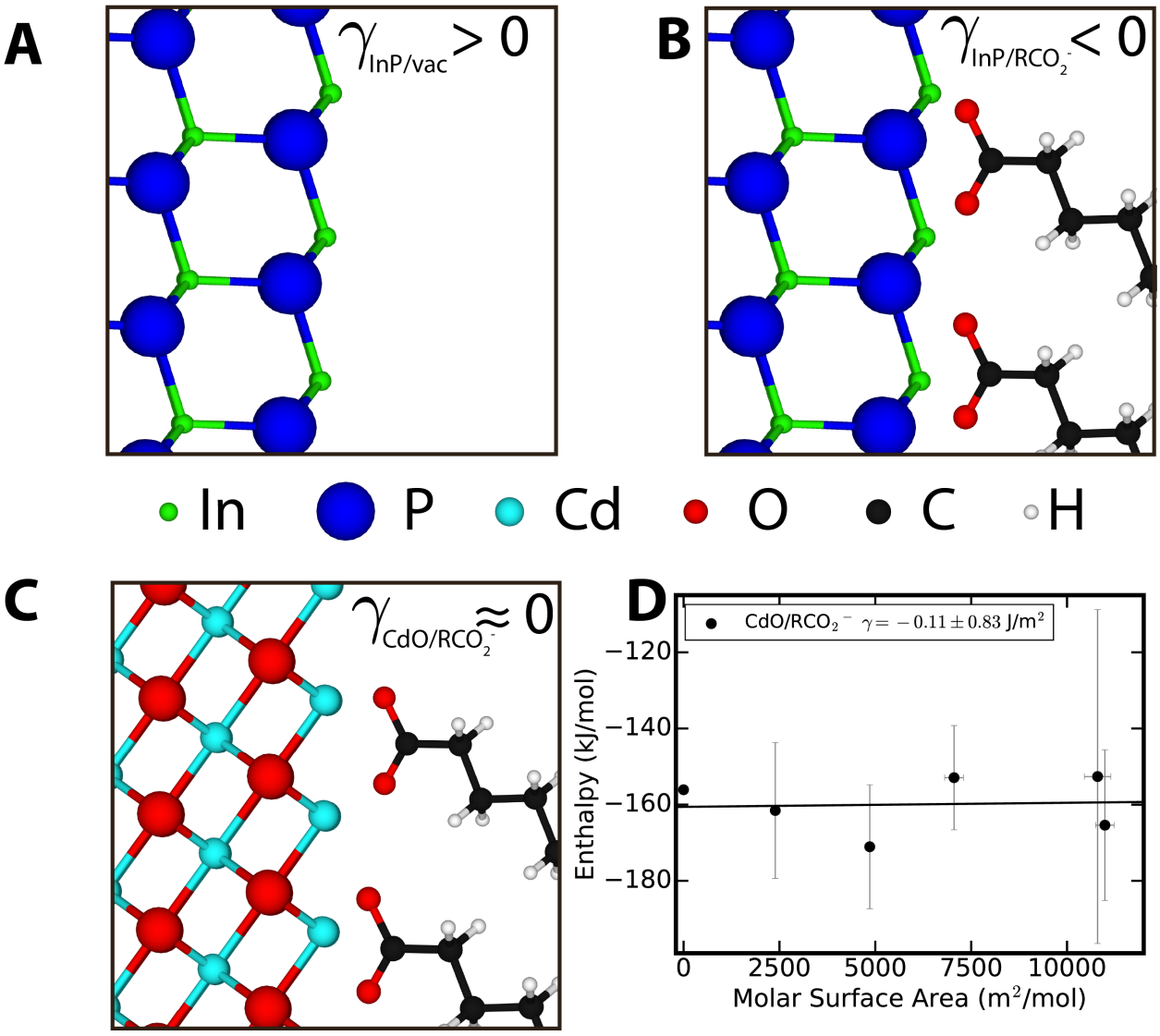


Figure 6.5: Models of surfaces and measurements of cadmium oxide nanocrystal surface energy. (A) Model of the surface of indium phosphide in vacuum, where the terminating indiums have fewer bonds than the interior indiums and thus have a positive surface energy. (B) Model of the surface of indium phosphide terminated with coordinating carboxylates, and if these bonds are stronger than the interior bonds, the surface energy will be negative. (C) Model of the surface of cadmium oxide terminated with coordinating carboxylates, where the interior and exterior oxygen bonds have similar enthalpies, resulting in a near zero surface energy. (D) Plot of the enthalpy measured in kJ/mol against the molar surface area in m^2/mol for the cadmium oxide samples with a fit line where the negative slope of the fit line is the measured surface energy of the cadmium oxide nanocrystals (-0.11 $\pm$ 0.83 J/m^2).

nanocrystals capped with oleic acid and oleylamine was between -0.48 and -0.82 J/m^2.[192] Discrepancies between measurements herein and those by Bertolotii *et al.* can likely be attributed to the difference between surface energy, surface tension, and surface Gibbs free energy, but could also arise from differences in synthetic methods or ligand coverages.

From our initial data, we hypothesized that negative surface energies originate from the tightly binding ligands on nanocrystal surfaces. It is well known that in carboxylate terminated quantum dots the carboxylate coordinates to metal cations on the surface, and if the oxygens from the carboxylates were binding more tightly to the metal cations on the surface than the underlying inorganic crystal lattice, this would result in a negative surface energy (Figure 6.5B). Further, as indium would be trivalent, the carboxylate could coordinate more strongly to indium than to divalent cadmium, zinc, or lead, potentially further explaining why the surface energy of indium phosphide is more negative than the other quantum dots. A logical extension of our hypothesis is that if the ligands coordinating the surface of the nanocrystal had similar bond strength to the underlying inorganic crystal lattice, the measured surface energy would be approximately zero (Figure 6.5C). To test this, we synthesized cadmium oxide nanocrystals capped with oleates and measured their dissolution enthalpy (extensive sample characterization can be found in Appendix A.8 as well as Appendix B.8). As expected, the surface energy of these nanocrystals was close to zero (Figure 6.5D), indicating that the atoms on the surface and interior had similar bond enthalpies, which was reasonable considering oxygen was coordinating to cadmium on the exterior and interior.

6.4 Interfacial Energy of Indium Phosphide/Zinc Sulfide Core/Shell Nanocrystals

Having established a framework to measure the surface energies of colloidal quantum dots, we were able to measure the energy of the interface of a core/shell nanocrystal heterostructure. While organic ligands can be used to passivate defects on the surface of colloidal quantum dots to improve their luminescence, the growth of a wider band gap material to coat the surface of the core quantum dot, or a shell, has resulted in quantum dots with near unity quantum yields that are better suited for optoelectronic applications.[74,76,77] For this measurement, indium phosphide/zinc sulfide core shell structures were synthesized with a variety of core sizes, resulting in different molar interfacial areas (extensive sample characterization can be found in Appendix A.2 and A.6 as well as Appendix B.8). The samples were dissolved in the same manner, and the resulting enthalpies were corrected for the zinc sulfide content and the surface energy of the zinc sulfide shell, which were calculated from the surface energy measurements of the zinc sulfide nanocrystals. Figure 6.6 depicts the results of these measurements, which show a negative interface energy between indium phosphide and zinc sulfide. These measurements indicate that the formation of the zinc sulfide shell on the indium phosphide nanocrystal is highly favorable, stabilizing the surface indium atoms

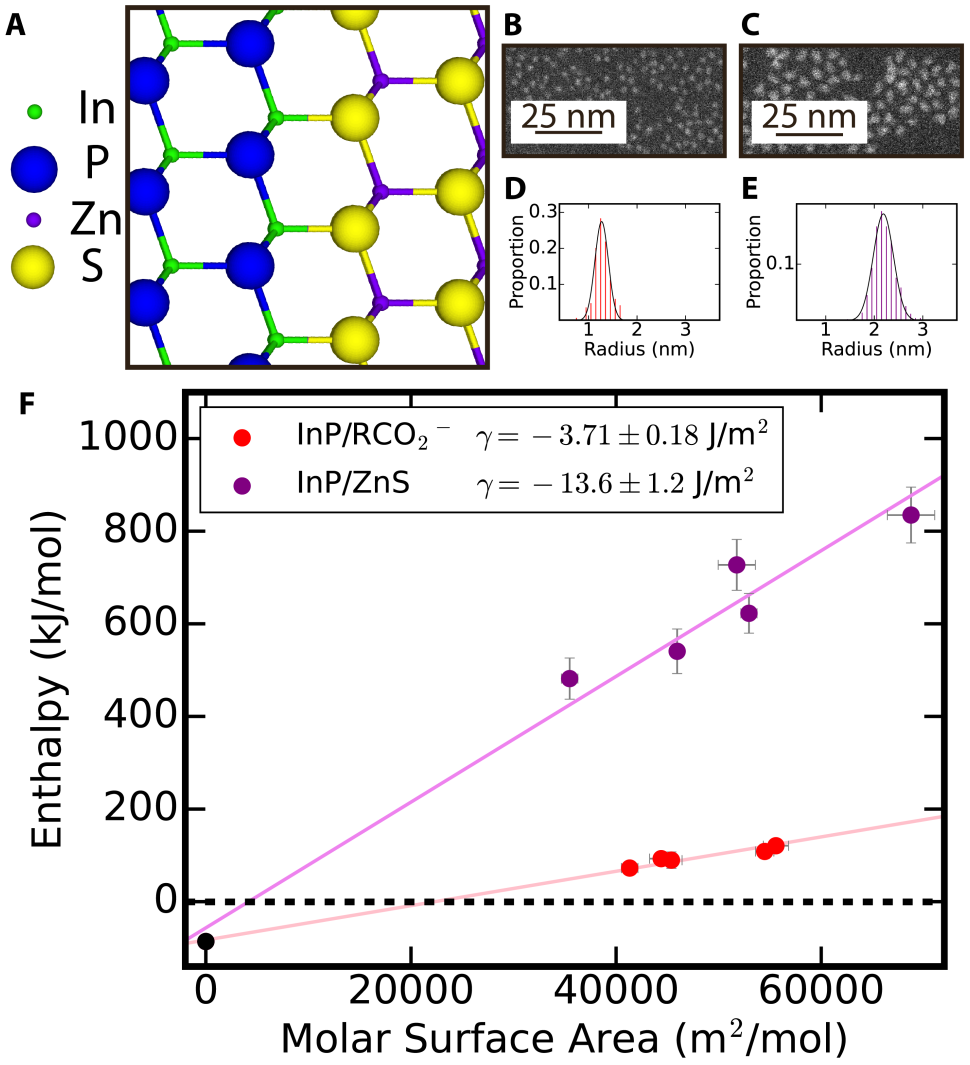


Figure 6.6: Measurements of the interfacial energy of InP/ZnS quantum dots. (A) Model of the interface of indium phosphide and zinc sulfide core/shell nanocrystals. (B) STEM image of the smallest sample that was shelled with zinc sulfide with inset scale bar. (C) Histogram fit with a Gaussian distribution of the smallest sample that was shelled with zinc sulfide. (D) STEM image of the smallest sample after shelling used in these measurements with inset scale bar. (E) Histogram fit with a Gaussian distribution of the smallest sample after shelling used in these measurements. (F) Plot of the enthalpy measured in kJ/mol against the molar surface area in m^2/mol for the samples with a fit line where the negative slope of the fit line is the measured interfacial energy (-13.6 ± 1.2 J/m^2) alongside the indium phosphide/carboxylate surface energy for comparison.

much more significantly than the carboxylate ligands. As with the surface energy measurements, this negative interface energy result is unexpected. Beyond the convenience of using materials that had already been studied as the core and shell material and their relevance as more environmentally friendly quantum dot materials,[74,77] indium phosphide and zinc sulfide were selected due to their large lattice mismatch. It was anticipated that this would result in a positive interfacial energy due to lattice strain,[211–213] however, the bond enthalpy between these materials must be much more favorable than the lattice strain to result in such a negative interfacial energy. In retrospect, the existence of core/shell heterostructures at all indicates that the formation of the interface must be favorable, else the separate formation of nanocrystals consisting only of the shelling material or Janus type nanostructures, rather than a coating of the core nanocrystal, would be more likely. From cross polarized ^{1}H-^{31}P magic-angle spinning solid state NMR measurements, it is evident that the indium phosphide nanocrystals are completely coated in a zinc sulfide shell (see Appendix A.6). Beyond the initial coating, however, the strain energy in the shell would likely result in a non-uniform shell, which has been observed in these systems as well.[74,212–214] In many ways, this is similar to atomic layer deposition of materials on a substrate, where often two dimensional growth is first observed before the growth of islands to relieve lattice strain.[215–217] For this particular heterostructure, it would be expected that sulfur anions would coordinate to the indium rich surface as the shell is grown, but the exact chemical nature of this interface is still ambiguous.[218–220] Particularly from a charge balancing perspective, simple growth of a zinc blende zinc sulfide shell would not passivate a zinc blende indium phosphide surface. It is plausible that extra sulfur atoms at the interface maintain the charge balance while contributing to the large negative interfacial energy observed. Regardless of the exact nature of the interface, the results unambiguously indicate that the formation of these core/shell structures is more thermodynamically stable than separated nanocrystals or bulk materials.

6.5 Implications of Negative Surface and Interfacial Energies

From these measurements, we have experimentally demonstrated that surface energies of colloidal nanoparticles can be negative, and the assumption that surface energies should be positive values may be incorrect when considering molecules binding to the surface. These results require the re-evaluation previous work assuming positive surface energies, particulary of for growth models of nanocrystals. The most common model for nanocrystal nucleation, the LaMer model,[197] assumes that the surface energy is positive, and thus there is a critical cluster size for stability in the nucleation of the nanocrystal. If the surface energy is negative, then there would be no critical cluster size. A negative surface energy implies that smaller nanocrystals are more favorable than larger nanocrystals, and in the thermodynamic limit, bulk inorganic crystals and ligands would favor the formation of nanocrystals. This raises questions as to why nanocrystals would form at all, rather than staying as molecular species

or perhaps magic-sized clusters, and if there is a most thermodynamically stable size of a nanocrystal. It is important to note that the surface energies of these nanocrystals were measured at standard state conditions, but nanocrystal nucleation often occurs at high temperatures, and it is likely that the surface energy could be temperature dependent where the organic ligands may not bind as tightly or at the density of the ligands at standard state. Additionally, entropy contributions at higher temperatures will be more significant, particularly with ligands that can be free in solution or bound to the nanocrystal, and careful discussion about surface enthalpies and surface Gibbs free energies is likely necessary. However, nanocrystals such as lead bromide perovskite nanocrystals can be synthesized at room temperature,[221,222] and based on X-ray diffraction measurements by Zhao *et al.* for cesium lead iodide perovskite nanocrystals,[192] it seems plausible that the surface energies of lead bromide perovskite nanocrystals may also be negative. However, the chemical potential of reactive precursor species such as benzoyl bromide might help drive the formation of these nanocrystals.

Regarding shape formation in nanocrystals, where Wulff constructions, which predict that the lowest surface energy facet should form, should still apply although the surface energies are negative. However, another question to be raised is why nanocrystals do not typically form concave shapes, as this would increase the surface area. This could be related to a kinetic argument of nanocrystal growth, or potentially the temperature dependence of surface energies. For example, it has been observed that tetrapods of cadmium selenide nanocrystals tend to grow at lower temperatures,[36] which have a fairly high surface area to volume ratio. Our hypothesis is that while the surface energies are important, nanocrystal shape is likely driven by the kinetics of nucleation. On the other hand, the thermodynamics of nanocrystal formation are more likely driven by the thermodynamic chemical potentials of starting materials, such as reactive phosphorus and sulfur precursors, but this should be a rich area of future study.

The observation of negative surface energies and a negative interface energy in indium phosphide/zinc sulfide core/shell nanocrystals has wide implications, from practical considerations to interesting new directions in experimental and theoretical materials science. First and foremost, these negative values indicate that these nanocrystals are more thermodynamically stable than their bulk counterparts. This is supportive of findings on notoriously unstable materials, such as lead halide perovskites,[223–225] that appear to be more stable as nanoparticles than in bulk.[192] Second, the vast body of literature that calculates surface energies of nanoparticles or uses surface energy as a justification for observed phenomena when it is implicitly assumed that surface energy must be positive must be re-evaluated. Third, the elimination of what was considered to be a fundamental assumption opens the door to new theories regarding the stability of nanomaterials and possible materials that can be formed. We expect that this technique of measuring the surface energy of nanoparticles will be widely adopted to further investigate the field of experimental thermodynamics of nanocrystals, particularly regarding colloidal nanocrystals.

Chapter 7

Future Perspectives on Colloidal Nanocrystal Surface Thermodynamics

Reproduced in part with permission from Calvin, J. C.; Brewer, A. S.; Alivisatos, A. P. "The Role of Organic Ligand Shell Structures in Colloidal Nanocrystal Synthesis" *Nat. Synth.* **2022**, *1*, 127–137. Copyright 2022 Springer Nature Limited.[1]

Significant work has been done on understanding the organic ligand shell of colloidal quantum dots. Several examples in the literature indicate that the ligand shell structure can influence optical properties of colloidal nanocrystals,.[42–46] The steric bulkiness of organic ligands has also been proposed as an explanation for poor photoluminescence of carboxylate-capped indium phosphide quantum dots, as there are too few carboxylate groups to passivate all of the surface indium atoms, leading to electron traps.[26,27] From these examples, it is evident that the structure of the ligand shell plays a significant role in the properties of colloidal nanocrystals. Previous work has also shown that these organic structures cause strain at the inorganic-organic interface, which can cause changes in the optical properties.[46,125,185] Considering that higher quantum yields are necessary for exotic applications of quantum dots,[76] it stands to reason that engineering a more perfect quantum dot will require a thorough understanding of the ligand shell structure.

In addition to optical properties, the structure of the ligand shell has significant impacts on the self-assembly of colloidal nanocrystals. Generating complex structures may be possible through manipulation of the organic ligand shell. The formation of mini-band structures using colloidal quantum dots as artificial atoms, which requires a very high degree of crystallinity, has proven elusive.[14] While long range transport phenomena may occur transiently through nanocrystals with long aliphatic capping ligands at high optical excitation densities via multi-electron Auger effects,[226] the tunneling barrier of the organic ligands generally prevents self-assemblies from achieving the couplings required. However, recent work has demonstrated that ligands can assist in creating template structures for a potential synthetic pathway for these superlattices.[14] Thus, engineering the organic ligand shell is likely to play a critical role towards new electrically active nanocrystal solids.

From the work presented herein, knowledge of the structure and the thermodynamics of the organic ligand shell has been elucidated in several different ways. While at this point there remains significant work to be done on further defining the ligand shell structure, this knowledge should prove critical in informing the synthesis and rational design of colloidal nanocrystals. The thermodynamic measurements of the inter-ligand Van der Waals and entropic interactions show that the ligand shell has strong collective effects, and these effects are certain to influence the properties of the nanocrystal as a whole. For more unstable nanocrystals, it stands to reason that the organic ligand shell may contribute to their instability, and tuning the ligand shell structure could potentially lessen that effect or even reverse it. Particularly with small nanocrystals, where the organic component makes up a significant proportion of the overall structure, it is likely that stabilizing the shell structure could lead to more durable materials, particularly when considering inorganic lead halide perovskite nanocrystals and nanoplatelets.[9,18,34,125,205,221]

Considering the potential effect that the organic ligand shell has on the synthesis of colloidal nanocrystals by controlling the diffusion of precursors to the surface,[34,125] there may be significant work remaining to further control syntheses, particularly when making anisotropic nanocrystals. While materials can be easily tuned via temperature and time constraints,[34,36,125] the organic ligand shell structure should also be considered a tunable synthetic parameter.

Beyond these practical considerations in the syntheses and properties of colloidal nanocrystals, there is likely still much to discover about the organic ligand shell structure and this basic research should yield insights into other material systems. For example, the work done on the structure and thermodynamics of micelles has helped inform the structure of the organic ligand shell in colloidal nanostructures. The research done in the field of colloidal nanostructures may also be applicable in the reverse direction or in other systems where collective effects are important. The thermodynamics of these collective effects, particularly in small systems, are interesting from a statistical mechanics perspective as well, where normal considerations about large populations that are often taken as general assumptions no longer apply. The organic ligand shell structure is critical for understanding these materials as a whole, and as these materials become more specialized and more finely engineered, it is almost certain that these considerations will become critical for the next generation of materials.

Regarding thermodynamics and calorimetry, the high surface area of nanocrystals allows calorimetry to easily probe thermodynamic properties of surfaces. It is likely that further thermodynamic insights into surface chemistry will utilize the versatile structure of colloidal nanocrystals. Additionally, the solution based reactions that can occur with colloidal nanocrystals makes them an excellent platform to study the thermodynamics of well defined surfaces. The observation of colloidal nanocrystals posessing a negative surface energy not only opens the door to many more theoretical studies, but also serves as a foundation for further insights into the thermodynamics of nanocrystals, surface energy, and general materials science.

The only roadblock for the field of nanocrystal thermodynamics is the lack of calorimetry

expertise in the colloidal nanocrystal community and the effort required to do these measurements. However, in the last few years more isothermal titration calorimetry experiments have been performed, and it looks to be a fruitful field for many more years. It is anticipated that future studies and interesting insights into complicated nanostructures will be forthcoming, and the studies herein have laid the groundwork for understanding the thermodynamic stability of nanomaterials.

Bibliography

(1) Calvin, J. J.; Brewer, A. S.; Alivisatos, A. P. *Nat. Synth.* **2022**, *1*, 127–137.

(2) Alivisatos, A. P. *Science* **1996**, *271*, 933–937.

(3) Heath, J. R. *Chem. Soc. Rev.* **1998**, *27*, 65–71.

(4) Albani, D.; Vilé, G.; Mitchell, S.; Witte, P. T.; Almora-Barrios, N.; Verel, R.; López, N.; Pérez-Ramírez, J. *Catal. Sci. Technol.* **2016**, *6*, 1621–1631.

(5) Calvin, J. J.; Asplund, M.; Zhang, Y.; Huang, B.; Woodfield, B. F. *J. Chem. Thermodyn.* **2017**, *112*, 77–85.

(6) Kittel, C., *Introduction to Solid State Physics*, 2004.

(7) Lokteva, I.; Radychev, N.; Witt, F.; Borchert, H.; Parisi, J.; Kolny-Olesiak, J. *J. Phys. Chem. C* **2010**, *114*, 12784–12791.

(8) McElroy, N.; Page, R.; Espinbarro-Valazquez, D.; Lewis, E.; Haigh, S.; O'Brien, P.; Binks, D. *Thin Solid Films* **2014**, *560*, 65–70.

(9) Yang, W. S.; Park, B.-W.; Jung, E. H.; Jeon, N. J.; Kim, Y. C.; Lee, D. U.; Shin, S. S.; Seo, J.; Kim, E. K.; Noh, J. H., et al. *Science* **2017**, *356*, 1376–1379.

(10) Chandler, D., *Introduction to Modern Statistical Mechanics*; Oxford University Press: 1987.

(11) Hill, T. L., *Thermodynamics of Small Systems*; Courier Corporation: 1994.

(12) De Nolf, K.; Cosseddu, S. M.; Jasieniak, J. J.; Drijvers, E.; Martins, J. C.; Infante, I.; Hens, Z. *J. Am. Chem. Soc.* **2017**, *139*, 3456–3464.

(13) Pang, Z.; Zhang, J.; Cao, W.; Kong, X.; Peng, X. *Nat. Commun.* **2019**, *10*, 1–8.

(14) Ondry, J. C.; Philbin, J. P.; Lostica, M.; Rabani, E.; Alivisatos, A. P. *ACS Nano* **2020**, *15*, 2251–2262.

(15) Luther, J. M.; Law, M.; Song, Q.; Perkins, C. L.; Beard, M. C.; Nozik, A. J. *ACS Nano* **2008**, *2*, 271–280.

(16) Anderson, N. C.; Hendricks, M. P.; Choi, J. J.; Owen, J. S. *J. Am. Chem. Soc.* **2013**, *135*, 18536–18548.

(17) Kirkwood, N.; Monchen, J. O.; Crisp, R. W.; Grimaldi, G.; Bergstein, H. A.; Du Fossé, I.; Van Der Stam, W.; Infante, I.; Houtepen, A. J. *J. Am. Chem. Soc.* **2018**, *140*, 15712–15723.

(18) Nenon, D. P.; Pressler, K.; Kang, J.; Koscher, B. A.; Olshansky, J. H.; Osowiecki, W. T.; Koc, M. A.; Wang, L.-W.; Alivisatos, A. P. *J. Am. Chem. Soc.* **2018**, *140*, 17760–17772.

(19) Fan, Z.; Grünwald, M. *J. Am. Chem. Soc.* **2019**, *141*, 1980–1988.

(20) Nagaoka, Y.; Tan, R.; Li, R.; Zhu, H.; Eggert, D.; Wu, Y. A.; Liu, Y.; Wang, Z.; Chen, O. *Nature* **2018**, *561*, 378–382.

(21) Lee, H.; Yoon, D.-E.; Koh, S.; Kang, M. S.; Lim, J.; Lee, D. C. *Chem. Sci.* **2020**, *11*, 2318–2329.

(22) Kim, T.-G.; Zherebetskyy, D.; Bekenstein, Y.; Oh, M. H.; Wang, L.-W.; Jang, E.; Alivisatos, A. P. *ACS Nano* **2018**, *12*, 11529–11540.

(23) Boles, M. A.; Ling, D.; Hyeon, T.; Talapin, D. V. *Nat. Mater.* **2016**, *15*, 141–153.

(24) Weiss, E. A. *Acc. Chem. Res.* **2013**, *46*, 2607–2615.

(25) Zhang, J.; Zhang, H.; Cao, W.; Pang, Z.; Li, J.; Shu, Y.; Zhu, C.; Kong, X.; Wang, L.; Peng, X. *J. Am. Chem. Soc.* **2019**, *141*, 15675–15683.

(26) Hughes, K. E.; Stein, J. L.; Friedfeld, M. R.; Cossairt, B. M.; Gamelin, D. R. *ACS Nano* **2019**, *13*, 14198–14207.

(27) Stein, J. L.; Mader, E. A.; Cossairt, B. M. *J. Phys. Chem. Lett.* **2016**, *7*, 1315–1320.

(28) Wu, M.; Vartanian, A. M.; Chong, G.; Pandiakumar, A. K.; Hamers, R. J.; Hernandez, R.; Murphy, C. J. *J. Am. Chem. Soc.* **2019**, *141*, 4316–4327.

(29) Zhang, B.; Goldoni, L.; Zito, J.; Dang, Z.; Almeida, G.; Zaccaria, F.; De Wit, J.; Infante, I.; De Trizio, L.; Manna, L. *Chem. Mater.* **2019**, *31*, 9140–9147.

(30) Elimelech, O.; Aviv, O.; Oded, M.; Banin, U. *Nano Lett.* **2020**, *20*, 6396–6403.

(31) Gee, M. Y.; Shen, Y.; Greytak, A. B. *J. Phys. Chem. C* **2020**, *124*, 23964–23975.

(32) Lv, L.; Li, J.; Wang, Y.; Shu, Y.; Peng, X. *J. Am. Chem. Soc.* **2020**, *142*, 19926–19935.

(33) Liz-Marzán, L. M.; Kagan, C. R.; Millstone, J. E. *ACS Nano* **2020**, *14*, 6359–6361.

(34) Pan, A.; He, B.; Fan, X.; Liu, Z.; Urban, J. J.; Alivisatos, A. P.; He, L.; Liu, Y. *ACS Nano* **2016**, *10*, 7943–7954.

(35) Zhuang, Z.; Lu, X.; Peng, Q.; Li, Y. *Chem. – Eur. J.* **2011**, *17*, 10445–10452.

(36) Liu, L.; Zhuang, Z.; Xie, T.; Wang, Y.-G.; Li, J.; Peng, Q.; Li, Y. *J. Am. Chem. Soc.* **2009**, *131*, 16423–16429.

(37) Li, Z.; Peng, X. *J. Am. Chem. Soc.* **2011**, *133*, 6578–6586.

(38) Ahmadi, T. S.; Wang, Z. L.; Green, T. C.; Henglein, A.; El-Sayed, M. A. *Science* **1996**, *272*, 1924–1925.

(39) Paula, S.; Sues, W.; Tuchtenhagen, J.; Blume, A. *J. Phys. Chem.* **1995**, *99*, 11742–11751.

(40) Golub, T. P.; de Keizer, A. *Langmuir* **2004**, *20*, 9506–9512.

(41) Fathi, H.; Kelly, J. P.; Vasquez, V. R.; Graeve, O. A. *Langmuir* **2012**, *28*, 9267–9274.

(42) Balan, A. D.; Olshansky, J. H.; Horowitz, Y.; Han, H.-L.; O'Brien, E. A.; Tang, L.; Somorjai, G. A.; Alivisatos, A. P. *ACS Nano* **2019**, *13*, 13784–13796.

(43) Wuister, S. F.; de Mello Donegá, C.; Meijerink, A. *J. Am. Chem. Soc.* **2004**, *126*, 10397–10402.

(44) Wuister, S. F.; Van Houselt, A.; de Mello Donegá, C.; Vanmaekelbergh, D.; Meijerink, A. *Angew. Chem., Int. Ed.* **2004**, *116*, 3091–3095.

(45) Zenkevich, E.; Stupak, A.; Göhler, C.; Krasselt, C.; von Borczyskowski, C. *ACS Nano* **2015**, *9*, 2886–2903.

(46) Antanovich, A.; Achtstein, A.; Matsukovich, A.; Prudnikau, A.; Bhaskar, P.; Gurin, V.; Molinari, M.; Artemyev, M. *Nanoscale* **2017**, *9*, 18042–18053.

(47) Yang, W.; Vansuch, G. E.; Liu, Y.; Jin, T.; Liu, Q.; Ge, A.; Sanchez, M. L.; K. Haja, D.; Adams, M. W.; Dyer, R. B., et al. *ACS Appl. Mater. Interfaces* **2020**, *12*, 35614–35625.

(48) Moreels, I.; Martins, J. C.; Hens, Z. *Sens. Actuators, B* **2007**, *126*, 283–288.

(49) Gomes, R.; Hassinen, A.; Szczygiel, A.; Zhao, Q.; Vantomme, A.; Martins, J. C.; Hens, Z. *J. Phys. Chem. Lett.* **2011**, *2*, 145–152.

(50) Hens, Z.; Martins, J. C. *Chem. Mater.* **2013**, *25*, 1211–1221.

(51) Yu, W. W.; Qu, L.; Guo, W.; Peng, X. *Chem. Mater.* **2003**, *15*, 2854–2860.

(52) Maes, J.; Balcaen, L.; Drijvers, E.; Zhao, Q.; De Roo, J.; Vantomme, A.; Vanhaecke, F.; Geiregat, P.; Hens, Z. *J. Phys. Chem. Lett.* **2018**, *9*, 3093–3097.

(53) Elimelech, O.; Aviv, O.; Oded, M.; Peng, X.; Harries, D.; Banin, U. *ACS Nano* **2022**, *16*, 4308–4321.

(54) Jharimune, S.; Sathe, A. A.; Rioux, R. M. *Nano Lett.* **2018**, *18*, 6795–6803.

(55) Navrotsky, A. *J. Chem. Thermodyn.* **2007**, *39*, 1–9.

(56) Lang, B. E.; Boerio-Goates, J.; Woodfield, B. F. *J. Chem. Thermodyn.* **2006**, *38*, 1655–1663.

(57) Lashley, J.; Hundley, M.; Migliori, A.; Sarrao, J.; Pagliuso, P.; Darling, T.; Jaime, M.; Cooley, J.; Hults, W.; Morales, L., et al. *Cryogenics* **2003**, *43*, 369–378.

(58) Navrotsky, A. *J. Am. Ceram. Soc.* **2014**, *97*, 3349–3359.

(59) Quan, Z.; Wu, D.; Zhu, J.; Evers, W. H.; Boncella, J. M.; Siebbeles, L. D.; Wang, Z.; Navrotsky, A.; Xu, H. *Proc. Natl. Acad. Sci. U. S. A.* **2014**, *111*, 9054–9057.

(60) Demarse, N. A.; Quinn, C. F.; Eggett, D. L.; Russell, D. J.; Hansen, L. D. *Anal. Biochem.* **2011**, *417*, 247–255.

(61) Christensen, J.; Izatt, R.; Hansen, L. *Rev. Sci. Instrum.* **1965**, *36*, 779–783.

(62) Sigurskjold, B. W. *Anal. Biochem.* **2000**, *277*, 260–266.

(63) Cliff, M. J.; Gutierrez, A.; Ladbury, J. E. *J. Mol. Recognit.* **2004**, *17*, 513–523.

(64) Drijvers, E.; De Roo, J.; Martins, J. C.; Infante, I.; Hens, Z. *Chem. Mater.* **2018**, *30*, 1178–1186.

(65) Singh, S.; Leemans, J.; Zaccaria, F.; Infante, I.; Hens, Z. *Chem. Mater.* **2021**, *33*, 2796–2803.

(66) Kessler, M. L.; Dempsey, J. L. *Chem. Mater.* **2020**, *32*, 2561–2571.

(67) Anderson, N. C.; Owen, J. S. *Chem. Mater.* **2013**, *25*, 69–76.

(68) Doniach, S. *J. Chem. Phys.* **1978**, *68*, 4912–4916.

(69) Mouritsen, O.; Boothroyd, A.; Harris, R.; Jan, N.; Lookman, T.; MacDonald, L.; Pink, D.; Zuckermann, M. *J. Chem. Phys.* **1983**, *79*, 2027–2041.

(70) Almeida, P. F. *Langmuir* **2018**, *35*, 21–40.

(71) Calvin, J. J.; Swabeck, J. K.; Sedlak, A. B.; Kim, Y.; Jang, E.; Alivisatos, A. P. *J. Am. Chem. Soc.* **2020**, *142*, 18897–18906.

(72) Cossairt, B. M. *Chem. Mater.* **2016**, *28*, 7181–7189.

(73) Chopra, S. S.; Theis, T. L. *Environ. Sci.: Nano* **2017**, *4*, 244–254.

(74) Won, Y.-H.; Cho, O.; Kim, T.; Chung, D.-Y.; Kim, T.; Chung, H.; Jang, H.; Lee, J.; Kim, D.; Jang, E. *Nature* **2019**, *575*, 634–638.

(75) Grim, J. Q.; Manna, L.; Moreels, I. *Chem. Soc. Rev.* **2015**, *44*, 5897–5914.

(76) Hanifi, D. A.; Bronstein, N. D.; Koscher, B. A.; Nett, Z.; Swabeck, J. K.; Takano, K.; Schwartzberg, A. M.; Maserati, L.; Vandewal, K.; van de Burgt, Y., et al. *Science* **2019**, *363*, 1199–1202.

(77) Kim, Y.; Ham, S.; Jang, H.; Min, J. H.; Chung, H.; Lee, J.; Kim, D.; Jang, E. *ACS Appl. Nano Mater.* **2019**, *2*, 1496–1504.

(78) Xu, G.; Zeng, S.; Zhang, B.; Swihart, M. T.; Yong, K.-T.; Prasad, P. N. *Chem. Rev.* **2016**, *116*, 12234–12327.

(79) Li, C.; Ando, M.; Murase, N. *Chem. Lett.* **2008**, *37*, 856–857.

(80) Mahmoud, W. E.; Chang, Y.; Al-Ghamdi, A.; Al-Marzouki, F.; Bronstein, L. M. *Superlattices Microstruct.* **2013**, *56*, 86–91.

(81) Kim, K.; Yoo, D.; Choi, H.; Tamang, S.; Ko, J.-H.; Kim, S.; Kim, Y.-H.; Jeong, S. *Angew. Chem., Int. Ed.* **2016**, *55*, 3714–3718.

(82) Mićić, O. I.; Sprague, J.; Lu, Z.; Nozik, A. J. *Appl. Phys. Lett.* **1996**, *68*, 3150–3152.

(83) Adam, S.; Talapin, D.; Borchert, H.; Lobo, A.; McGinley, C.; De Castro, A.; Haase, M.; Weller, H.; Möller, T. *J. Chem. Phys.* **2005**, *123*, 084706.

(84) Kim, K.; Lee, H.; Ahn, J.; Jeong, S. *Appl. Phys. Lett.* **2012**, *101*, 073107.

(85) Dupont, D.; Tessier, M. D.; Smet, P. F.; Hens, Z. *Adv. Mater.* **2017**, *29*, 1700686.

(86) Ramasamy, P.; Kim, N.; Kang, Y.-S.; Ramirez, O.; Lee, J.-S. *Chem. Mater.* **2017**, *29*, 6893–6899.

(87) Ip, A. H.; Thon, S. M.; Hoogland, S.; Voznyy, O.; Zhitomirsky, D.; Debnath, R.; Levina, L.; Rollny, L. R.; Carey, G. H.; Fischer, A., et al. *Nat. Nanotechnol.* **2012**, *7*, 577–582.

(88) Page, R. C.; Espinobarro-Velazquez, D.; Leontiadou, M. A.; Smith, C.; Lewis, E. A.; Haigh, S. J.; Li, C.; Radtke, H.; Pengpad, A.; Bondino, F., et al. *Small* **2015**, *11*, 1548–1554.

(89) Van Der Stam, W.; Du Fossé, I.; Grimaldi, G.; Monchen, J. O.; Kirkwood, N.; Houtepen, A. J. *Chem. Mater.* **2018**, *30*, 8052–8061.

(90) Owen, J. S.; Park, J.; Trudeau, P.-E.; Alivisatos, A. P. *J. Am. Chem. Soc.* **2008**, *130*, 12279–12281.

(91) Zanella, M.; Maserati, L.; Pernia Leal, M.; Prato, M.; Lavieville, R.; Povia, M.; Krahne, R.; Manna, L. *Chem. Mater.* **2013**, *25*, 1423–1429.

(92) Greaney, M. J.; Couderc, E.; Zhao, J.; Nail, B. A.; Mecklenburg, M.; Thornbury, W.; Osterloh, F. E.; Bradforth, S. E.; Brutchey, R. L. *Chem. Mater.* **2015**, *27*, 744–756.

(93) Lee, W. S.; Kang, Y. G.; Woo, H. K.; Ahn, J.; Kim, H.; Kim, D.; Jeon, S.; Han, M. J.; Choi, J.-H.; Oh, S. J. *Chem. Mater.* **2019**, *31*, 9389–9399.

(94) Houtepen, A. J.; Hens, Z.; Owen, J. S.; Infante, I. *Chem. Mater.* **2017**, *29*, 752–761.

(95) Sayevich, V.; Guhrenz, C.; Sin, M.; Dzhagan, V. M.; Weiz, A.; Kasemann, D.; Brunner, E.; Ruck, M.; Zahn, D. R.; Leo, K., et al. *Adv. Funct. Mater.* **2016**, *26*, 2163–2175.

(96) Biswas, K.; Varghese, N.; Rao, C. N. *Small* **2008**, *4*, 649–655.

(97) Jiang, J.; Huang, Z.; Xiao, Q.; Liu, Y.; Mi, Y.; Li, Y. *Thermochim. Acta* **2010**, *503*, 136–140.

(98) Cros-Gagneux, A.; Delpech, F.; Nayral, C.; Cornejo, A.; Coppel, Y.; Chaudret, B. *J. Am. Chem. Soc.* **2010**, *132*, 18147–18157.

(99) Reiss, P.; Protiere, M.; Li, L. *Small* **2009**, *5*, 154–168.

(100) García-Rodríguez, R.; Liu, H. *Chem. Commun.* **2013**, *49*, 7857–7859.

(101) Liu, M.; Wang, Y.-Y.; Liu, Y.; Jiang, F.-L. *J. Phys. Chem. C* **2020**, *124*, 4613–4625.

(102) Sologan, M.; Marson, D.; Polizzi, S.; Pengo, P.; Boccardo, S.; Pricl, S.; Posocco, P.; Pasquato, L. *ACS nano* **2016**, *10*, 9316–9325.

(103) Meena, S. K.; Goldmann, C.; Nassoko, D.; Seydou, M.; Marchandier, T.; Moldovan, S.; Ersen, O.; Ribot, F.; Chanéac, C.; Sanchez, C., et al. *ACS Nano* **2017**, *11*, 7371–7381.

(104) Lien, D.-H.; Uddin, S. Z.; Yeh, M.; Amani, M.; Kim, H.; Ager III, J. W.; Yablonovitch, E.; Javey, A. *Science* **2019**, *364*, 468–471.

(105) Tamukong, P. K.; Peiris, W. D.; Kilina, S. *Phys. Chem. Chem. Phys.* **2016**, *18*, 20499–20510.

(106) Li, X.; Nichols, V. M.; Zhou, D.; Lim, C.; Pau, G. S. H.; Bardeen, C. J.; Tang, M. L. *Nano Lett.* **2014**, *14*, 3382–3387.

(107) Morris-Cohen, A. J.; Vasilenko, V.; Amin, V. A.; Reuter, M. G.; Weiss, E. A. *ACS Nano* **2012**, *6*, 557–565.

(108) Masel, R. I., *Principles of Adsorption and Reaction on Solid Surfaces*; John Wiley & Sons: 1996; Vol. 3.

(109) Bain, C. D.; Troughton, E. B.; Tao, Y. T.; Evall, J.; Whitesides, G. M.; Nuzzo, R. G. *J. Am. Chem. Soc.* **1989**, *111*, 321–335.

(110) Laibinis, P. E.; Nuzzo, R. G.; Whitesides, G. M. *J. Phys. Chem.* **1992**, *96*, 5097–5105.

(111) Barnes, J. C.; Duncan, C. *J. Chem. Soc. A* **1969**, 1746–1748.

(112) Darensbourg, D. J.; Holtcamp, M. W.; Khandelwal, B.; Klausmeyer, K. K.; Reibenspies, J. H. *J. Am. Chem. Soc.* **1995**, *117*, 538–539.

(113) Darensbourg, D. J.; Niezgoda, S. A.; Holtcamp, M. W.; Draper, J. D.; Reibenspies, J. H. *Inorg. Chem.* **1997**, *36*, 2426–2432.

(114) Searle, M. S.; Williams, D. H. *J. Am. Chem. Soc.* **1992**, *114*, 10690–10697.

(115) Veamatahau, A.; Jiang, B.; Seifert, T.; Makuta, S.; Latham, K.; Kanehara, M.; Teranishi, T.; Tachibana, Y. *Phys. Chem. Chem. Phys.* **2015**, *17*, 2850–2858.

(116) Karpulevich, A.; Bui, H.; Wang, Z.; Hapke, S.; Palencia Ramírez, C.; Weller, H.; Bester, G. *J. Chem. Phys.* **2019**, *151*, 224103.

(117) Dutta, A.; Behera, R. K.; Pal, P.; Baitalik, S.; Pradhan, N. *Angew. Chem., Int. Ed.* **2019**, *58*, 5552–5556.

(118) Koscher, B. A.; Nett, Z.; Alivisatos, A. P. *ACS Nano* **2019**, *13*, 11825–11833.

(119) Gong, K.; Zeng, Y.; Kelley, D. F. *J. Phys. Chem. C* **2013**, *117*, 20268–20279.

(120) Pu, C.; Peng, X. *J. Am. Chem. Soc.* **2016**, *138*, 8134–8142.

(121) Calvin, J. J.; O'Brien, E. A.; Sedlak, A. B.; Balan, A. D.; Alivisatos, A. P. *ACS Nano* **2021**, *15*, 1407–1420.

(122) Fritzinger, B.; Capek, R. K.; Lambert, K.; Martins, J. C.; Hens, Z. *J. Am. Chem. Soc.* **2010**, *132*, 10195–10201.

(123) Kim, A.; Zhou, S.; Yao, L.; Ni, S.; Luo, B.; Sing, C. E.; Chen, Q. *J. Am. Chem. Soc.* **2019**, *141*, 11796–11800.

(124) Luo, B.; Pu, Y.-C.; Lindley, S. A.; Yang, Y.; Lu, L.; Li, Y.; Li, X.; Zhang, J. Z. *Angew. Chem., Int. Ed.* **2016**, *55*, 8864–8868.

(125) Cho, J.; Jin, H.; Sellers, D. G.; Watson, D. F.; Son, D. H.; Banerjee, S. *J. Mater. Chem. C* **2017**, *5*, 8810–8818.

(126) Schreiber, F. *Prog. Surf. Sci.* **2000**, *65*, 151–257.

(127) Porter, M. D.; Bright, T. B.; Allara, D. L.; Chidsey, C. E. *J. Am. Chem. Soc.* **1987**, *109*, 3559–3568.

(128) Knauf, R. R.; Lennox, J. C.; Dempsey, J. L. *Chem. Mater.* **2016**, *28*, 4762–4770.

(129) De Roo, J.; Huang, Z.; Schuster, N. J.; Hamachi, L. S.; Congreve, D. N.; Xu, Z.; Xia, P.; Fishman, D. A.; Lian, T.; Owen, J. S., et al. *Chem. Mater.* **2020**, *32*, 1461–1466.

(130) Ritchhart, A.; Cossairt, B. M. *Inorg. Chem.* **2019**, *58*, 2840–2847.

(131) Hassinen, A.; Gomes, R.; De Nolf, K.; Zhao, Q.; Vantomme, A.; Martins, J. C.; Hens, Z. *J. Phys. Chem. C* **2013**, *117*, 13936–13943.

(132) Ministro, J. A Study on the Synthesis and the Optical Properties of InP-based Quantum Dots, 2014.

(133) Sandhyarani, N.; Pradeep, T.; Chakrabarti, J.; Yousuf, M.; Sahu, H. *Phys. Rev. B* **2000**, *62*, R739.

(134) Ravi, V.; Binz, J. M.; Rioux, R. M. *Nano Lett.* **2013**, *13*, 4442–4448.

(135) Calvin, J. J.; Kaufman, T. M.; Sedlak, A. B.; Crook, M. F.; Alivisatos, A. P. *Nat. Commun.* **2021**, *12*, 2663.

(136) Jackson, A. M.; Myerson, J. W.; Stellacci, F. *Nat. Mater.* **2004**, *3*, 330–336.

(137) Ghorai, P. K.; Glotzer, S. C. *J. Phys. Chem. C* **2007**, *111*, 15857–15862.

(138) Widmer-Cooper, A.; Geissler, P. *Nano Lett.* **2014**, *14*, 57–65.

(139) Yang, Y.; Qin, H.; Jiang, M.; Lin, L.; Fu, T.; Dai, X.; Zhang, Z.; Niu, Y.; Cao, H.; Jin, Y., et al. *Nano Lett.* **2016**, *16*, 2133–2138.

(140) Weir, M. P.; Toolan, D. T.; Kilbride, R. C.; Penfold, N. J.; Washington, A. L.; King, S. M.; Xiao, J.; Zhang, Z.; Gray, V.; Dowland, S., et al. *J. Phys. Chem. Lett.* **2019**, *10*, 4713–4719.

(141) Sandhyarani, N.; Resmi, M.; Unnikrishnan, R.; Vidyasagar, K.; Ma, S.; Antony, M.; Selvam, G. P.; Visalakshi, V.; Chandrakumar, N.; Pandian, K., et al. *Chem. Mater.* **2000**, *12*, 104–113.

(142) Cromer, D. T.; Mann, J. B. *Acta Crystallogr., Sect. A: Cryst. Phys., Diffr., Theor. Gen. Crystallogr.* **1968**, *24*, 321–324.

(143) Sandhyarani, N.; Antony, M.; Selvam, G. P.; Pradeep, T. *J. Chem. Phys.* **2000**, *113*, 9794–9803.

(144) Fenter, P.; Eisenberger, P.; Liang, K. *Phys. Rev. Lett.* **1993**, *70*, 2447.

(145) Altamura, D.; Lassandro, R.; Vittoria, F.; De Caro, L.; Siliqi, D.; Ladisa, M.; Giannini, C. *J. Appl. Crystallogr.* **2012**, *45*, 869–873.

(146) Ushakova, E. V.; Cherevkov, S. A.; Litvin, A. P.; Parfenov, P. S.; Volgina, D.-O. A.; Kasatkin, I. A.; Fedorov, A. V.; Baranov, A. V. *J. Phys. Chem. C* **2016**, *120*, 25061–25067.

(147) Weidman, M. C.; Smilgies, D.-M.; Tisdale, W. A. *Nat. Mater.* **2016**, *15*, 775–781.

(148) Hansen, E. C.; Bertram, S. N.; Yoo, J. J.; Bawendi, M. G. *Small* **2019**, *15*, 1901462.

(149) Wang, X.; Liang, Z.; Xu, X.; Wang, N.; Fang, J.; Wang, J.; Xu, G. *J. Alloys Compd.* **2015**, *640*, 134–140.

(150) Mirzai, H.; Nordin, M.; Curry, R.; Bouillard, J.-S.; Zayats, A.; Green, M. *J. Mater. Chem. C* **2014**, *2*, 2107–2111.

(151) Shweky, I.; Aharoni, A.; Mokari, T.; Rothenberg, E.; Nadler, M.; Popov, I.; Banin, U. *Mater. Sci. Eng., C* **2006**, *26*, 788–794.

(152) Granada-Ramirez, D.; Arias-Cerón, J.; Gómez-Herrera, M.; Luna-Arias, J.; Pérez-González, M.; Tomás, S.; Rodríguez-Fragoso, P.; Mendoza-Alvarez, J. *J. Mater. Sci.: Mater. Electron.* **2019**, *30*, 4885–4894.

(153) Chen, D.; Gao, Y.; Chen, Y.; Ren, Y.; Peng, X. *Nano Lett.* **2015**, *15*, 4477–4482.

(154) Friedfeld, M. R.; Johnson, D. A.; Cossairt, B. M. *Inorg. Chem.* **2018**, *58*, 803–810.

(155) Lucey, D. W.; MacRae, D. J.; Furis, M.; Sahoo, Y.; Cartwright, A. N.; Prasad, P. N. *Chem. Mater.* **2005**, *17*, 3754–3762.

(156) Li, Y.; Pu, C.; Peng, X. *Nano Res.* **2017**, *10*, 941–958.

(157) Dey, P. C.; Das, R. *J. Lumin.* **2017**, *183*, 368–376.

(158) Zhou, J.; Guo, W., et al. *Nanotechnology* **2010**, *21*, 175601.

(159) Chen, M.; Pan, L.; Cao, J.; Ji, H.; Ji, G.; Ma, X.; Zheng, Y. *Mater. Lett.* **2006**, *60*, 3842–3845.

(160) Khanna, P.; Eum, M.-S.; Jun, K.-W.; Baeg, J.-O.; Seok, S. I. *Mater. Lett.* **2003**, *57*, 4617–4621.

(161) Mohapatra, P.; Dung, M. X.; Choi, J.-K.; Jeong, S.-H.; Jeong, H.-D. *Bull. Korean Chem. Soc.* **2011**, *32*, 263–272.

(162) Sahoo, Y.; Poddar, P.; Srikanth, H.; Lucey, D.; Prasad, P. *J. Phys. Chem. B* **2005**, *109*, 15221–15225.

(163) Wegner, K. D.; Pouget, S.; Ling, W. L.; Carrière, M.; Reiss, P. *Chem. Commun.* **2019**, *55*, 1663–1666.

(164) Du, H.; Chen, C.; Krishnan, R.; Krauss, T. D.; Harbold, J. M.; Wise, F. W.; Thomas, M. G.; Silcox, J. *Nano Lett.* **2002**, *2*, 1321–1324.

(165) Bennett, E.; Greenberg, M. W.; Jordan, A. J.; Hamachi, L. S.; Banerjee, S.; Billinge, S. J.; Owen, J. S. *Chem. Mater.* **2022**, *34*, 706–717.

(166) Lee, D.; Koh, S.; Yoon, D.-E.; Lee, S.; Kim, W. D.; Kim, D.; Bae, W. K.; Lim, J.; Lee, D. C. *Korean J. Chem. Eng.* **2019**, *36*, 1518–1526.

(167) Zhuang, Z.; Peng, Q.; Wang, X.; Li, Y. *Angew. Chem., Int. Ed.* **2007**, *46*, 8174–8177.

(168) Pan, D.; Jiang, S.; An, L.; Jiang, B. *Adv. Mater.* **2004**, *16*, 982–985.

(169) Katsaba, A.; Ambrozevich, S.; Vitukhnovsky, A.; Fedyanin, V.; Lobanov, A.; Krivobok, V.; Vasiliev, R.; Samatov, I. *J. Appl. Phys.* **2013**, *113*, 184306.

(170) Murray, C.; Norris, D. J.; Bawendi, M. G. *J. Am. Chem. Soc.* **1993**, *115*, 8706–8715.

(171) Sokolikova, M.; Vasiliev, R.; Gaskov, A. *Russ. J. Inorg. Chem.* **2014**, *59*, 413–418.

(172) Lim, S. J.; Chon, B.; Joo, T.; Shin, S. K. *J. Phys. Chem. C* **2008**, *112*, 1744–1747.

(173) Capitani, C.; Pinchetti, V.; Gariano, G.; Santiago-González, B.; Santambrogio, C.; Campione, M.; Prato, M.; Brescia, R.; Camellini, A.; Bellato, F., et al. *Nano Lett.* **2019**, *19*, 1307–1317.

(174) Vasiliev, R. B.; Dorofeev, S. G.; Dirin, D. N.; Belov, D. A.; Kuznetsova, T. A. *Mendeleev Commun.* **2004**, *14*, 169–171.

(175) Tamang, S.; Lee, S.; Choi, H.; Jeong, S. *Chem. Mater.* **2016**, *28*, 8119–8122.

(176) Wegner, K. D.; Dussert, F.; Truffier-Boutry, D.; Benayad, A.; Beal, D.; Mattera, L.; Ling, W. L.; Carrière, M.; Reiss, P. *Front. Chem.* **2019**, 466.

(177) Ramasamy, P.; Ko, K.-J.; Kang, J.-W.; Lee, J.-S. *Chem. Mater.* **2018**, *30*, 3643–3647.

(178) Liu, Z.; Kumbhar, A.; Xu, D.; Zhang, J.; Sun, Z.; Fang, J. *Angew. Chem., Int. Ed.* **2008**, *47*, 3540–3542.

(179) Battaglia, D.; Peng, X. *Nano Lett.* **2002**, *2*, 1027–1030.

(180) Scardi, P.; Leoni, M. *J. Appl. Crystallogr.* **1999**, *32*, 671–682.

(181) Raman, C. V.; Sogani, C. M. *Nature* **1927**, *120*, 514–514.

(182) Boles, M. A.; Talapin, D. V. *J. Am. Chem. Soc.* **2014**, *136*, 5868–5871.

(183) Schindler, T.; Schmiele, M.; Schmutzler, T.; Kassar, T.; Segets, D.; Peukert, W.; Radulescu, A.; Kriele, A.; Gilles, R.; Unruh, T. *Langmuir* **2015**, *31*, 10130–10136.

(184) Bertolotti, F.; Dirin, D. N.; Ibáñez, M.; Krumeich, F.; Cervellino, A.; Frison, R.; Voznyy, O.; Sargent, E. H.; Kovalenko, M. V.; Guagliardi, A.; Masciocchi, N. *Nat. Mater.* **2016**, *15*, 987–994.

(185) Jana, S.; de Frutos, M.; Davidson, P.; Abécassis, B. *Sci. Adv.* **2017**, *3*, e1701483.

(186) Toso, S.; Baranov, D.; Altamura, D.; Scattarella, F.; Dahl, J.; Wang, X.; Marras, S.; Alivisatos, A. P.; Singer, A.; Giannini, C., et al. *ACS Nano* **2021**, *15*, 6243–6256.

(187) Wu, L.; Willis, J. J.; McKay, I. S.; Diroll, B. T.; Qin, J.; Cargnello, M.; Tassone, C. J. *Nature* **2017**, *548*, 197–201.

(188) Gong, J.; Newman, R. S.; Engel, M.; Zhao, M.; Bian, F.; Glotzer, S. C.; Tang, Z. *Nat. Commun.* **2017**, *8*, 1–9.

(189) McHale, J.; Auroux, A.; Perrotta, A.; Navrotsky, A. *Science* **1997**, *277*, 788–791.

(190) Levchenko, A. A.; Li, G.; Boerio-Goates, J.; Woodfield, B. F.; Navrotsky, A. *Chem. Mater.* **2006**, *18*, 6324–6332.

(191) Xu, F.; Zhou, W.; Navrotsky, A. *J. Mater. Res.* **2011**, *26*, 720–725.

(192) Zhao, Q.; Hazarika, A.; Schelhas, L. T.; Liu, J.; Gaulding, E. A.; Li, G.; Zhang, M.; Toney, M. F.; Sercel, P. C.; Luther, J. M. *ACS Energy Lett.* **2019**, *5*, 238–247.

(193) Diehm, P. M.; Ágoston, P.; Albe, K. *ChemPhysChem* **2012**, *13*, 2443–2454.

(194) Chan, S.-W.; Wang, W. *Mater. Chem. Phys.* **2021**, *273*, 125091.

(195) Marks, L.; Peng, L. *J. Phys.: Condens. Matter* **2016**, *28*, 053001.

(196) Bealing, C. R.; Baumgardner, W. J.; Choi, J. J.; Hanrath, T.; Hennig, R. G. *ACS Nano* **2012**, *6*, 2118–2127.

(197) Polte, J. *CrystEngComm* **2015**, *17*, 6809–6830.

(198) Yoo, H.; Lee, K.-S.; Nahm, S.; Hwang, G. W.; Kim, S. *Appl. Surf. Sci.* **2022**, *578*, 151972.

(199) Mule, A. S.; Mazzotti, S.; Rossinelli, A. A.; Aellen, M.; Prins, P. T.; van der Bok, J. C.; Solari, S. F.; Glauser, Y. M.; Kumar, P. V.; Riedinger, A., et al. *J. Am. Chem. Soc.* **2021**, *143*, 2037–2048.

(200) Barmparis, G. D.; Lodziana, Z.; Lopez, N.; Remediakis, I. N. *Beilstein J. Nanotechnol.* **2015**, *6*, 361–368.

(201) Manna, L.; Wang, L. W.; Cingolani, R.; Alivisatos, A. P. *J. Phys. Chem. B* **2005**, *109*, 6183–6192.

(202) Zherebetskyy, D.; Scheele, M.; Zhang, Y.; Bronstein, N.; Thompson, C.; Britt, D.; Salmeron, M.; Alivisatos, P.; Wang, L.-W. *Science* **2014**, *344*, 1380–1384.

(203) Bertolotti, F.; Proppe, A. H.; Dirin, D.; Liu, M.; Voznyy, O.; Cervellino, A.; Billinge, S. J.; Kovalenko, M. V.; Sargent, E. H.; Masciocchi, N., et al. *Chem. Sq.* **2018**, *2*, 1.

(204) Huang, J.; Kovalenko, M. V.; Talapin, D. V. *J. Am. Chem. Soc.* **2010**, *132*, 15866–15868.

(205) Swarnkar, A.; Marshall, A. R.; Sanehira, E. M.; Chernomordik, B. D.; Moore, D. T.; Christians, J. A.; Chakrabarti, T.; Luther, J. M. *Science* **2016**, *354*, 92–95.

(206) Łodziana, Z.; Topsøe, N.-Y.; Nørskov, J. K. *Nat. Mater.* **2004**, *3*, 289–293.

(207) Baquero, E. A.; Virieux, H.; Swain, R. A.; Gillet, A.; Cros-Gagneux, A.; Coppel, Y.; Chaudret, B.; Nayral, C.; Delpech, F. *Chem. Mater.* **2017**, *29*, 9623–9627.

(208) Mathur, A.; Sharma, P.; Cammarata, R. *Nat. Mater.* **2005**, *4*, 186–186.

(209) Cammarata, R. C.; Sieradzki, K. *Annu. Rev. Mater. Sci.* **1994**, *24*, 215–234.

(210) Shreiber, D.; Jesser, W. *Surf. Sci.* **2006**, *600*, 4584–4590.

(211) Rafipoor, M.; Dupont, D.; Tornatzky, H.; Tessier, M. D.; Maultzsch, J.; Hens, Z.; Lange, H. *Chem. Mater.* **2018**, *30*, 4393–4400.

(212) Rafipoor, M.; Tornatzky, H.; Dupont, D.; Maultzsch, J.; Tessier, M. D.; Hens, Z.; Lange, H. *J. Chem. Phys.* **2019**, *151*, 154704.

(213) Lange, H.; Kelley, D. F. *J. Phys. Chem. C* **2020**, *124*, 22839–22844.

(214) Cao, Y.; Banin, U. *J. Am. Chem. Soc.* **2000**, *122*, 9692–9702.

(215) Shklyaev, O.; Beck, M.; Asta, M.; Miksis, M. J.; Voorhees, P. W. *Phys. Rev. Lett.* **2005**, *94*, 176102.

(216) Chen, G.; Sanduijav, B.; Matei, D.; Springholz, G.; Scopece, D.; Beck, M.; Montalenti, F.; Miglio, L. *Phys. Rev. Lett.* **2012**, *108*, 055503.

(217) Oh, M. H.; Cho, M. G.; Chung, D. Y.; Park, I.; Kwon, Y. P.; Ophus, C.; Kim, D.; Kim, M. G.; Jeong, B.; Gu, X. W., et al. *Nature* **2020**, *577*, 359–363.

(218) Freymeyer, N. J.; Click, S. M.; Reid, K. R.; Chisholm, M. F.; Bradsher, C. E.; McBride, J. R.; Rosenthal, S. J. *J. Chem. Phys.* **2020**, *152*, 161104.

(219) Park, N.; Eagle, F. W.; DeLarme, A. J.; Monahan, M.; LoCurto, T.; Beck, R.; Li, X.; Cossairt, B. M. *J. Chem. Phys.* **2021**, *155*, 084701.

(220) Cui, Z.; Mei, S.; Wen, Z.; Yang, D.; Qin, S.; Xiong, Z.; Yang, B.; He, H.; Bao, R.; Qiu, Y., et al. *Small* **2022**, 2108120.

(221) Dahl, J. C.; Wang, X.; Huang, X.; Chan, E. M.; Alivisatos, A. P. *J. Am. Chem. Soc.* **2020**, *142*, 11915–11926.

(222) Naghadeh, S. B.; Luo, B.; Pu, Y.-C.; Schwartz, Z.; Hollingsworth, W. R.; Lindley, S. A.; Brewer, A. S.; Ayzner, A. L.; Zhang, J. Z. *J. Phys. Chem. C* **2019**, *123*, 4610–4619.

(223) Wang, B.; Navrotsky, A. *Thermochim. Acta* **2021**, *695*, 178813.

(224) Nagabhushana, G.; Shivaramaiah, R.; Navrotsky, A. *Proc. Natl. Acad. Sci. U. S. A.* **2016**, *113*, 7717–7721.

(225) Ciccioli, A.; Latini, A. *J. Phys. Chem. Lett.* **2018**, *9*, 3756–3765.

(226) Gao, J.; Kidon, L.; Rabani, E.; Alivisatos, A. P. *Nano Lett.* **2019**, *19*, 4804–4810.

(227) Swabeck, J. K.; Fischer, S.; Bronstein, N. D.; Alivisatos, A. P. *J. Am. Chem. Soc.* **2018**, *140*, 9120–9126.

(228) Gary, D. C.; Terban, M. W.; Billinge, S. J.; Cossairt, B. M. *Chem. Mater.* **2015**, *27*, 1432–1441.

(229) Tessier, M. D.; Baquero, E. A.; Dupont, D.; Grigel, V.; Bladt, E.; Bals, S.; Coppel, Y.; Hens, Z.; Nayral, C.; Delpech, F. *Chem. Mater.* **2018**, *30*, 6877–6883.

(230) Vikram, A.; Zahid, A.; Bhargava, S. S.; Jang, H.; Sutrisno, A.; Khare, A.; Trefonas, P.; Shim, M.; Kenis, P. J. *ACS Appl. Nano Mater.* **2020**, *3*, 12325–12333.

(231) Talapin, D. V.; Gaponik, N.; Borchert, H.; Rogach, A. L.; Haase, M.; Weller, H. *J. Phys. Chem. B* **2002**, *106*, 12659–12663.

(232) Talapin, D. V. Experimental and Theoretical Studies on the Formation of Highly Luminescent II-VI, III-V and Core-shell Semiconductor Nanocrystals, Staats-und Universitätsbibliothek Hamburg Carl von Ossietzky, 2002.

(233) Dhaene, E.; Billet, J.; Bennett, E.; Van Driessche, I.; De Roo, J. *Nano Lett.* **2019**, *19*, 7411–7417.

(234) Liu, Z.; Zhong, Y.; Shafei, I.; Jeong, S.; Wang, L.; Nguyen, H. T.; Sun, C.-J.; Li, T.; Chen, J.; Chen, L., et al. *Nano Lett.* **2020**, *20*, 2821–2828.

(235) Bronstein, N. D.; Yao, Y.; Xu, L.; O'Brien, E.; Powers, A. S.; Ferry, V. E.; Alivisatos, A. P.; Nuzzo, R. G. *ACS Photonics* **2015**, *2*, 1576–1583.

(236) Gunn, S. R.; Green, L. G. *J. Phys. Chem.* **1961**, *65*, 779–783.

(237) Cox, J.; Wagman, D. D.; Medvedev, V. A.; Wagman, D. P., et al., *CODATA Key Values for Thermodynamics*; Hemisphere Pub: 1989.

(238) Vasil'Ev, V.; Gachon, J.-C. *Inorg. Mater.* **2006**, *42*, 1171–1175.

(239) Deore, S.; Navrotsky, A. *Am. Mineral.* **2006**, *91*, 400–403.

(240) Schuffenecker, L.; Balesdent, D.; Houriez, J. *J. Chem. Thermodyn.* **1981**, *13*, 849–856.

(241) Franzosini, P.; Sanesi, M., *Thermodynamic and Transport Properties of Organic Salts: International Union of Pure and Applied Chemistry*; Elsevier: 2013.

(242) Wagman, D. D.; Evans, W. H.; Parker, V. B.; Schumm, R. H.; Halow, I., *The NBS Tables of Chemical Thermodynamic Properties. Selected Values for Inorganic and C1 and C2 Organic Substances in SI Units*, 1982.

(243) Tsukerman, E.; Veomett, E. *The American Mathematical Monthly* **2017**, *124*, 922–929.

(244) Jasieniak, J.; Smith, L.; Van Embden, J.; Mulvaney, P.; Califano, M. *J. Phys. Chem. C* **2009**, *113*, 19468–19474.

(245) Hamachi, L. S.; Jen-La Plante, I.; Coryell, A. C.; De Roo, J.; Owen, J. S. *Chem. Mater.* **2017**, *29*, 8711–8719.

(246) Li, J.; Chen, J.; Shen, Y.; Peng, X. *Nano Res.* **2018**, *11*, 3991–4004.

(247) Maes, J.; Castro, N.; De Nolf, K.; Walravens, W.; Abécassis, B.; Hens, Z. *Chem. Mater.* **2018**, *30*, 3952–3962.

(248) Aubert, T.; Golovatenko, A. A.; Samoli, M.; Lermusiaux, L.; Zinn, T.; Abécassis, B.; Rodina, A. V.; Hens, Z. *Nano Lett.* **2022**, *22*, 1778–1785.

(249) Wang, X.; Li, J.; Ha, H. D.; Dahl, J. C.; Ondry, J. C.; Moreno-Hernandez, I.; Head-Gordon, T.; Alivisatos, A. P. *JACS Au* **2021**, *1*, 316–327.

(250) Bawendi, M.; Kortan, A.; Steigerwald, M.; Brus, L. *J. Chem. Phys.* **1989**, *91*, 7282–7290.

(251) Ferri, F.; Bertolotti, F.; Guagliardi, A.; Masciocchi, N. *Sci. Rep.* **2020**, *10*, 1–11.

(252) Xie, R.; Li, Z.; Peng, X. *J. Am. Chem. Soc.* **2009**, *131*, 15457–15466.

(253) Karel Čapek, R.; Moreels, I.; Lambert, K.; De Muynck, D.; Zhao, Q.; Van Tomme, A.; Vanhaecke, F.; Hens, Z. *J. Phys. Chem. C* **2010**, *114*, 6371–6376.

(254) Cho, E.; Jang, H.; Lee, J.; Jang, E. *Nanotechnology* **2013**, *24*, 215201.

(255) Toufanian, R. Synthesis and Characterization of Indium Phosphide-based Quantum Dot Heterostructures, Boston University, 2021.

(256) Mićić, O.; Cheong, H.; Fu, H.; Zunger, A.; Sprague, J.; Mascarenhas, A.; Nozik, A. *J. Phys. Chem. B* **1997**, *101*, 4904–4912.

(257) Guzelian, A.; Katari, J. B.; Kadavanich, A. V.; Banin, U.; Hamad, K.; Juban, E.; Alivisatos, A.; Wolters, R.; Arnold, C.; Heath, J. *J. Phys. Chem.* **1996**, *100*, 7212–7219.

(258) Trigg, E. B. Controlled Folding In Precisely Functionalized Polyethylenes: Designing Nanoscale Lamellar Structures For Ion Transport, 2018.

(259) Leonardi, A.; Bish, D. L. *J. Appl. Crystallogr.* **2016**, *49*, 1593–1608.

(260) Neese, F. *Wiley Interdiscip. Rev.: Comput. Mol. Sci.* **2012**, *2*, 73–78.

(261) Neese, F.; Hansen, A.; Liakos, D. G. *J. Chem. Phys.* **2009**, *131*, 064103.

(262) Hait, D.; Tubman, N. M.; Levine, D. S.; Whaley, K. B.; Head-Gordon, M. *J. Chem. Theory Comput.* **2019**, *15*, 5370–5385.

(263) Majer, V.; Svoboda, V., *Enthalpies of Vaporization of Organic Compounds: A Critical Review and Data Compilation*; Blackwell Scientific: 1986.

(264) Lebedev, B.; Lityagov, V. Y. *Polym. Sci. U.S.S.R.* **1977**, *19*, 2618–2627.

Appendix A

Chemicals, Synthesis, and Characterization of Studied Materials

Reproduced in part with permission from Calvin, J. C.; Swabeck J. K.; Sedlak, A. B.; Kim, Y.; Jang, E.; Alivisatos, A. P. "Thermodynamic Investigation of Increased Luminescence in Indium Phosphide Quantum Dots by Treatment with Metal Halide Salts" *J. Am. Chem. Soc.* **2020**, *142*(44), 18897–18906. Copyright 2020 American Chemical Society.[71]

Reproduced in part with permission from Calvin, J. C.; O'Brien, E. A.; Sedlak, A. B.; Balan, A. D.; Alivisatos, A. P. "Thermodynamics of Composition Dependent Ligand Exchange on the Surfaces of Colloidal Indium Phosphide Quantum Dots" *ACS Nano* **2021**, *15*(1), 1407–1420. Copyright 2021 American Chemical Society.[121]

Reproduced in part with permission from Calvin, J. C.; Kaufman, T. M.; Sedlak, A. B.; Crook, M. F.; Alivisatos, A. P. "Observation of Ordered Organic Capping Ligands on Semiconducting Quantum Dots via Powder X-ray Diffraction" *Nat. Commun.* **2021**, *12*, 2663 under a Creative Commons license CC BY 4.0.[135]

A.1 Chemicals

Cadmium oxide (99.99%), cadmium acetate dihydrate (≥98.0%), palmitic acid (99%), oleic acid (technical grade, 90%), dodecylphosphonic acid (99.7%), hexylphosphonic acid (95%), oleylamine (technical grade, 70%), *1*-octadecene (90%), *n*-hexadecane (99%), and hydrofluoric acid (99.99%, 48 wt % in H_2O) were purchased from Sigma Aldrich and used as received. Indium acetate (99.99%), diethyl zinc (≥52 wt % Zn basis), cadmium acetate (99.995%), cadmium acetylacetonate (≥99.9%), lead oxide (>99.9%), sulfur (99.998%), selenium (99.99%), myristic acid (≥99%), oleic acid (≥99%), zinc chloride (99.999%), zinc bromide (99.999%), zinc iodide (99.999%), indium chloride (99.999%), indium bromide (99.999%), indium iodide (99.998%), anhydrous hexanes (>99%), anhydrous methyl acetate

(99.5%), anhydrous toluene (99.8%), tetrahydrofuran-d_8 (≥99.5%), toluene-d_8 (99.6%), and mesitylene (98%) were purchased from Sigma-Aldrich and stored in an argon glovebox and used as received. Anhydrous tetrahydrofuran (≥99.9%, Sigma-Aldrich) was distilled from a solvent still immediately prior to being stored in an argon glovebox. Indium (99.9999%), zinc (99.9999%), cadmium (99.999%), indium phosphide (99.9999%), zinc sulfide (99.995%), cadmium sulfide (99.999), and stearic acid (98%) were purchased from Alfa Aesar and used as received. Lead sulfide (99.995%), dimethyl sulfoxide (99.9%), and hydrochloric acid (37%, ACS Reagent) were purchased from Fisher Scientific and used as received. Octadecylphosphonic acid (>99%, PCI Synthesis), , argon (99.999%, Airgas), and hydrogen (5% in argon, Airgas) were used as received. Zinc acetate (99.98%, Alfa Aesar), tris(trimethylsilyl)phosphine (98%, Strem Chemicals), bis(trimethylsilyl)sulfide (98%, Beantown Chemical), bis(trimethylsilyl)amine (98%, Acros Organics), and anhydrous acetone (99.5%, Fisher Scientific) were stored in an argon glovebox and used as received.

A.2 Indium Phosphide Quantum Dots

The synthesis of indium phosphide quantum dots was generally inconsistent. Almost invariably, save for one reaction to demonstrate differences in oxidation based on synthesis route, a magic-sized cluster approach was used to synthesize indium phosphide quantum dots.[154,227,228] While for a given synthesis letting the reaction proceed longer would result in larger quantum dots (as observed by the color of the reaction flask *in situ*), replicating the size, size distribution, or luminescence was unreliable between syntheses.

In an attempt to create indium phosphide quantum dots with no oxidation on the surface for studying the surface energy (Chapter 6), a reported synthesis using a hydrogen atmosphere was investigated.[207] However, it was serendipity that the only available gas was a 5% hydrogen in argon cylinder (typically called regen gas, to regenerate oxygen and water free glovebox catalysts). The synthesis done with this atmosphere was markedly different from that with the ultrahigh-purity argon atmosphere, and the nanocrystals grown were typically larger, brighter, and they had a more monodisperse size distribution as evidenced by their absorbance spectra. Additionally, there is no evidence of oxidation on the surface, and this further muddles the understanding of the role of oxidation on brightness of indium phosphide based quantum dots with other recent reports that suggest oxidation on the surface of indium phosphide nanocrystals enables them to be brighter,[227,229,230] and more agrees with evidence that surface oxidation on indium phosphide is deleterious to their properties,[74] although the exact arguments regarding passivation by carboxylates, fluorine, oxygen, and hydrogen are still unclear despite how much research effort has been devoted to it.[22,74,83,207,219,227,229–232]

Unfortunately, over the course of years, the synthesis was tweaked for a variety of reasons, including the improved control and properties of using the 5% hydrogen atmosphere. Additionally, it was brought to our attention that the use of *1*-octadecene could result in polymerized *1*-octadecene that is apparently difficult to separate from the colloidal nanocrystals.[233] To avoid complications in reality or with reviewers, we opted to swap the organic

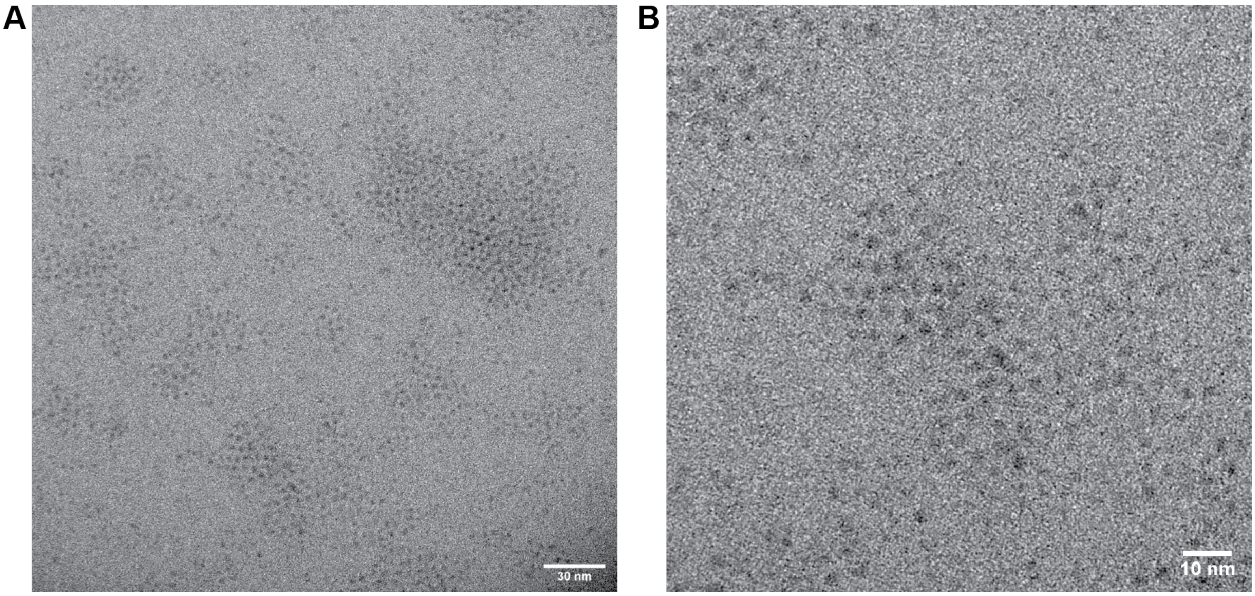


Figure A.1: TEM images of InP quantum dots synthesized under argon.

solvent for synthesis to *n*-hexadecane, particularly for the surface energy measurements as we were dealing with dried nanocrystal powders, and it was critical that the samples only consisted of inorganic nanocrystals and surface bound ligands. This resulted in having to degas samples at 80 °C rather than 90 °C, and in this scenario all of the indium acetate would not dissolve. Instead, the temperature was raised to 130 °C while not under an active vacuum and then allowed to cool before opening up the full vacuum. It is suspected that the exact temperature that the samples were degassed at influenced the size and size distribution of the nanocrystals, where beginning the degassing as the solution cooled around temperatures of 95 to 120 °C resulted in generally more monodisperse samples with smaller sizes as opposed to starting the degassing around temperatures of 85 to 90 °C. This made the synthesis more unreliable, and attempting to make an exact size in the synthesis was a nearly fruitless endeavor.

Specificity in how samples of indium phosphide were synthesized for different experiments is provided in the main text (such as temperatures and ligands used as well as washing procedures), while more general instructions with details is provided herein.

Magic-Sized Cluster Approach

The synthesis followed closely the procedure in Swabeck *et al.*[227] where first "magic-sized" clusters of indium phosphide are synthesized before they are grown into larger quantum dots.[100,154] An oven-dried, three-neck, 50 mL round-bottom flask was charged with 0.350 g (1.20 mmol) of indium acetate, 3.60 mmol of myristic acid, palmitic acid, stearic acid, or

90% oleic acid, 10 mL of *1*-octadecene, and a Teflon coated stir bar. Two necks of the flask were sealed with a thermocouple adapter and septa cap, and an air condenser column was attached to the central neck; the entire assembly was placed under vacuum by using a Schlenk line. All glass joints were sealed with Apiezon H grease. The temperature was slowly raised to 110 °C by using a heating mantle, as measured by a thermocouple, to degas the solvent without bumping the reaction mixture. After the solution stopped bubbling, no solids were present in the flask and the Schlenk line pressure dropped below 60 mTorr; the solution was kept at this temperature under vacuum for 1 hour, forming a clear solution. The flask was then pressurized with ultrahigh-purity argon (99.999%, Airgas) to slightly over atmospheric pressure, the temperature was raised to 130 °C, and glass wool was used to insulate the flask. In an argon glovebox, 0.152 g (0.607 mmol) of tris(trimethylsilyl)-phosphine was dissolved in 1.578 g of *1*-octadecene that had been previously degassed at 110 °C for an hour under vacuum in a similar setup as described above. This solution was swiftly injected into the flask and stirred vigorously for 2 minutes. Upon injection, the solution quickly turned a faint to dark yellow color. The temperature was then rapidly raised to 230 °C at a rate of approximately 20 °C/minute by using the heating mantle, where the solution generally transitioned to a deep red. The solution was kept at this temperature for 5 minutes, after which the heating mantle and glass wool were removed, and a stream of nitrogen was used to cool the flask to 40 °C. The solution generally transitioned from a dark red color to an orange or red color during cooling, depending on the size of nanocrystals grown. The solution was cannulated to an oven-dried vial under argon and transferred to an argon glovebox. After cleaning (see below) TEM images (Figure A.1), ^{1}H NMR measurements (Figure A.2), and powder X-ray diffraction (Figure A.3) measurements were taken to characterize the nanocrystals.

Hot Injection Method

Synthesis of oxidized indium phosphide quantum dots was done in a similar manner to the preparation of the less oxidized quantum dots, following the procedure of Battaglia and Peng.[179] For this synthesis, 0.117 g (0.401 mmol) of indium acetate, 0.274 g (1.20 mmol) of myristic acid, and 25 mL of *1*-octadecene was degassed in a three neck round-bottom flask held at 110 °C under vacuum for one hour, and then the atmosphere was replaced with argon and the temperature was raised to 300 °C. An injection solution was prepared with 0.050 g (0.200 mmol) of tris(trimethylsilyl)phosphine dissolved in 1.95 g of degassed *1*-octadecene, and this was injected to the flask. The temperature was allowed to drop to 270 °C, after which the solution was kept at this temperature for 5 minutes before being cooled to room temperature under a stream of nitrogen and hexanes.

^{31}P NMR spectroscopy was performed to measure the amount of phosphate present on the surface of the different syntheses of indium phosphide quantum dots. The cross-polarization measurement, which is most sensitive to phosphorous on the surface of the quantum dots, shows that there is very little oxidation on the synthesis using the magic-sized cluster approach, as seen by the minimal peak around 0 ppm (Figure A.2B).[98,207,229] In contrast, an

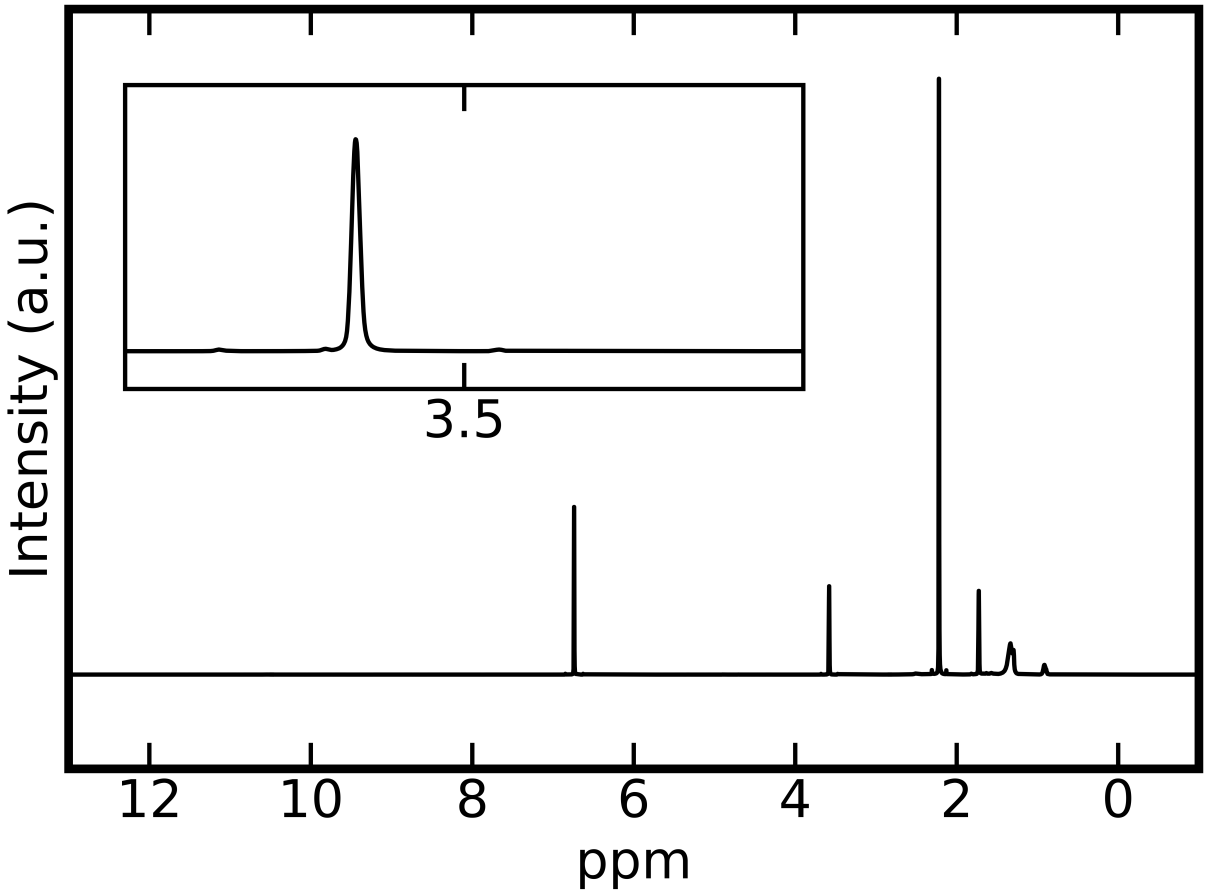


Figure A.2: ^{1}H NMR of indium phosphide quantum dots. Enlarged region shows THF peak where no broad peak corresponding to coordinated THF to the surface appears. Solvent peaks appear at 3.6 ppm and 1.7 ppm from deuterated THF, and the mesitylene peaks appear at 6.8 and 2.3 ppm used for quantitative calculations.

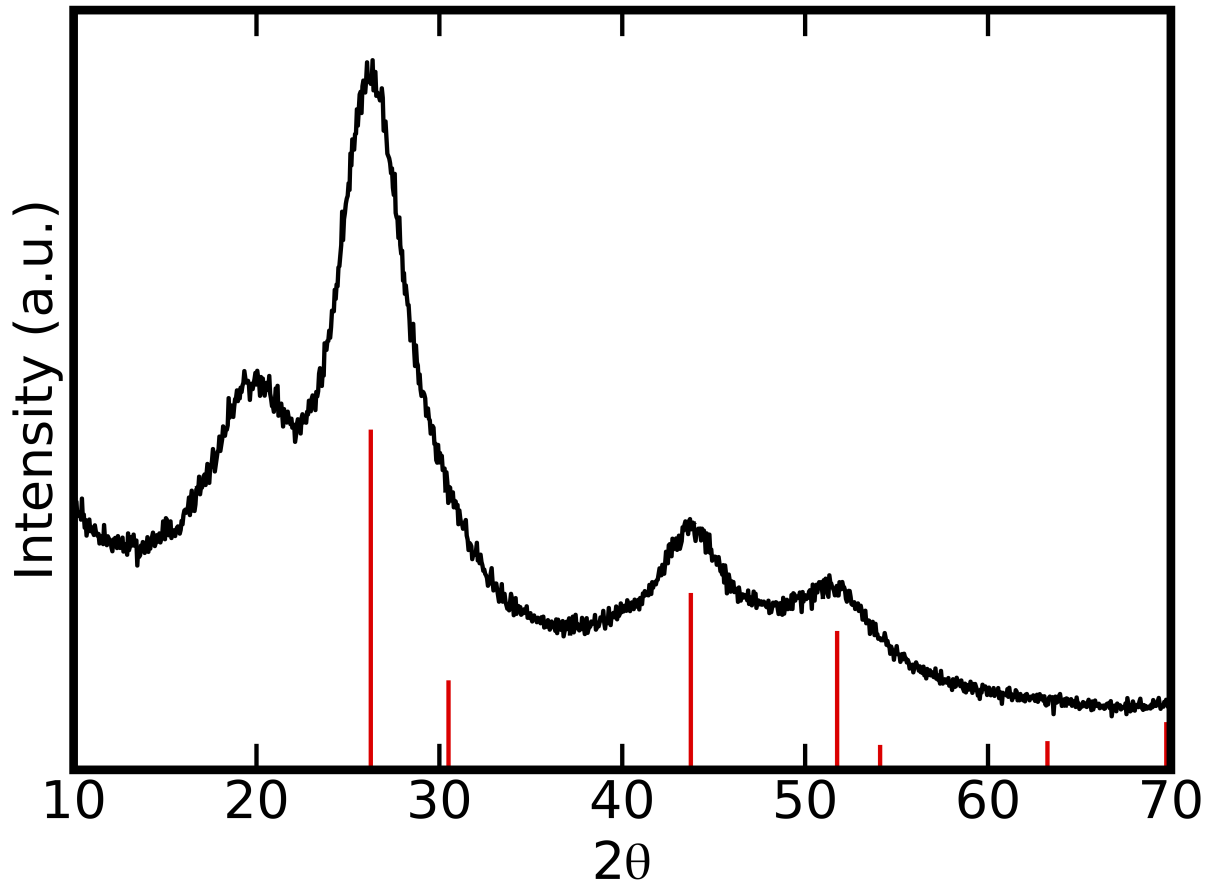


Figure A.3: Powder X-ray diffraction pattern from indium phosphide quantum dots deposited on a silicon wafer. Reference data for zinc-blende indium phosphide depicted as red lines. Note the peak around 20 °2θ discussed in Chapter 5.

identical experiment was performed on indium phosphide quantum dots synthesized with the hot injection method which shows significant oxidation (Figure A.2D). Additionally, the bulk indium phosphide peak on the high temperature sample is narrower than that of the low temperature sample, indicating that the range of chemical environments may be smaller due to the absence of non-oxidized phosphorous on the surface. Additionally, in the XPS spectra of phosphorous for these quantum dots we see no evidence of a phosphate peak (Figure A.2). These measurements indicate that treating the surface as indium phosphide terminated with coordinating carboxylates is a sound assumption if the magic-sized cluster synthesis is used.

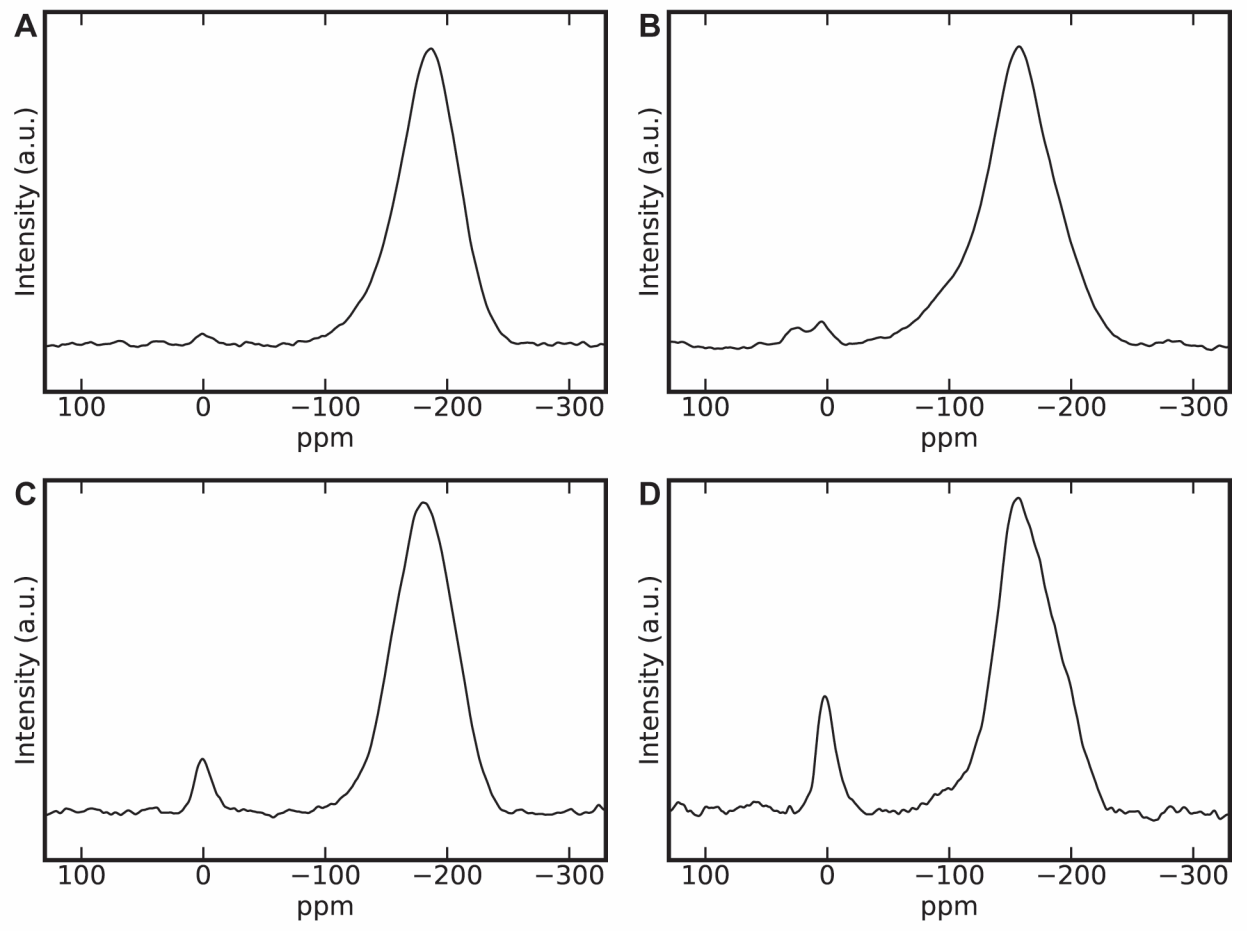


Figure A.4: Solid state NMR spectra of InP quantum dots comparing low and high temperature syntheses. (A) ^{31}P MAS NMR spectra of the low temperature synthesis of InP quantum dots. (B) ^{31}P MAS NMR spectra of the high temperature synthesis of InP quantum dots. (C) ^{31}P^{1}H MAS NMR spectra of the low temperature synthesis of InP quantum dots. (D) ^{31}P^{1}H MAS NMR spectra of the high temperature synthesis of InP quantum dots.

Using a 5% Hydrogen Atmosphere

For the synthesis, 0.350 grams (1.20 mmol) of indium acetate with 3.60 mmol of myristic acid or 90% oleic acid was combined with 10 mL of *1*-octadecene or *n*-hexadecane in an oven-dried, 50 mL three neck round-bottom flask with a Teflon coated stir bar. After an air condenser column, septa, and thermocouple adapter were attached to the flask and all glass joints greased with Apiezon H grease, the flask was evacuated via Schlenk line. The temperature of the flask was raised slowly to 70 °C, after which the vacuum line was closed. The solution was slowly heated to 80 °C, and the line to the vacuum was then opened slightly. The solution was then slowly heated to 120 °C, and all solids disappeared, resulting in a clear solution. Maximum temperature reached by the solution tended to be 130 °C. The temperature was lowered to 90 °C or 80 °C for *1*-octadecene and *n*-hexadecane, respectively, after which the vacuum line was fully opened, reaching a pressure below 60 mTorr. The system was flushed with 5% hydrogen in argon gas and placed back under vacuum, and this process was repeated three times in intervals of ten minutes. In total, the degassing process lasted one hour. The system was filled with 5% hydrogen in argon and the temperature was raised to 130 °C or 110 °C, depending on the exact synthesis. In an argon glovebox, 1.578 g of *1*-octadecene or 1.540 g of *n*-hexadecane that had previously been heated and degassed for an hour at 110 °C or 90 °C, respectively, at 60 mTorr was combined with 0.152 g of tris(trimethylsilyl)phosphine (0.607 mmol) and loaded into a syringe. This solution was then swiftly injected into the flask, and temperature was maintained for two minutes, resulting in a yellow solution. The temperature was then raised to 190 °C at a rate of 20 °C/minute and maintained at this temperature between 1 and 45 minutes, with longer reaction times generally yielding larger particles. The solution turned a deep red to completely black depending on the length of the growth period, and then the flask was then rapidly cooled under a stream of nitrogen and hexanes. After cooling the solution was cannulated to be purified in an argon glovebox. After cleaning, (see below) the nanocrystals were characterized. Characterization included absorption and luminescence measurements, STEM images, powder X-ray diffraction, ^{1}H NMR measurements, and solid state ^{31}P and ^{1}H-^{31}P NMR measurements that can be found in Figure A.5.

A.3 Cadmium Sulfide Quantum Dots

Sulfur and *1*-Octadecene Method

In an oven-dried, three-neck, 50 mL round-bottom flask, 0.064 g of sulfur (2.0 mmol) was added to 20 mL of *1*-octadecene with a Teflon-coated stir bar. A Schlenk line was attached to a condenser column on the middle neck of the three-neck flask while the other necks were sealed with a thermocouple adapter and a septa cap. All glass joints were sealed with Apiezon H grease. The solution was stirred and heated to 90 °C until the sulfur dissolved and the solution stopped degassing, typically taking one hour. The solution was then cannulated under an argon atmosphere to a large vial and stored in an argon glovebox.

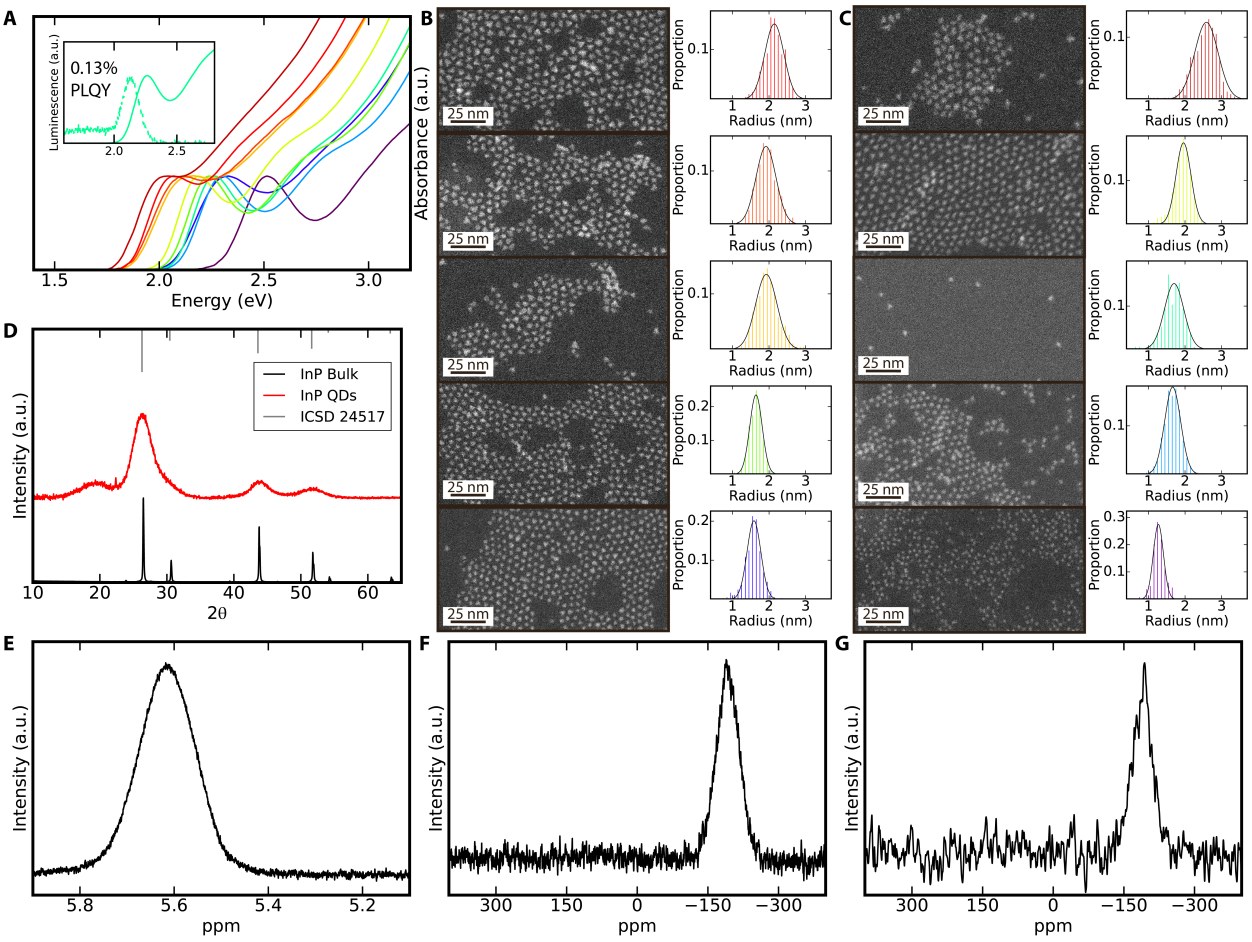


Figure A.5: Characterization of size series of InP quantum dots. (A) Absorbance measurements of the ten samples used with inset including absorbance and luminescence measurements for one representative sample with the measured photoluminescence quantum yield (PLQY). (B) STEM images of the samples used for the indium phosphide/carboxylate surface energy measurements with inset scale bar to the left, and matched histograms fit with by Gaussian distributions to the left. (C) STEM images of the samples to be shelled with zinc sulfide with inset scale bars to the left, and matched histograms fit by Gaussian distributions to the left. (D) Powder X-ray diffraction measurements of bulk and a representative sample with the reference lines for zinc blende indium phosphide from the inorganic crystal structure database (ICSD 24517). (E) ^{1}H NMR measurements of the vinyl proton region of a representative sample of indium phosphide quantum dots in toluene-d_8. (F) Solid state ^{31}P magic-angle spinning measurements of a representative sample of indium phosphide quantum dots. (G) Solid state cross-polarized ^{1}H-^{31}P magic-angle spinning measurements of a representative sample of indium phosphide quantum dots.

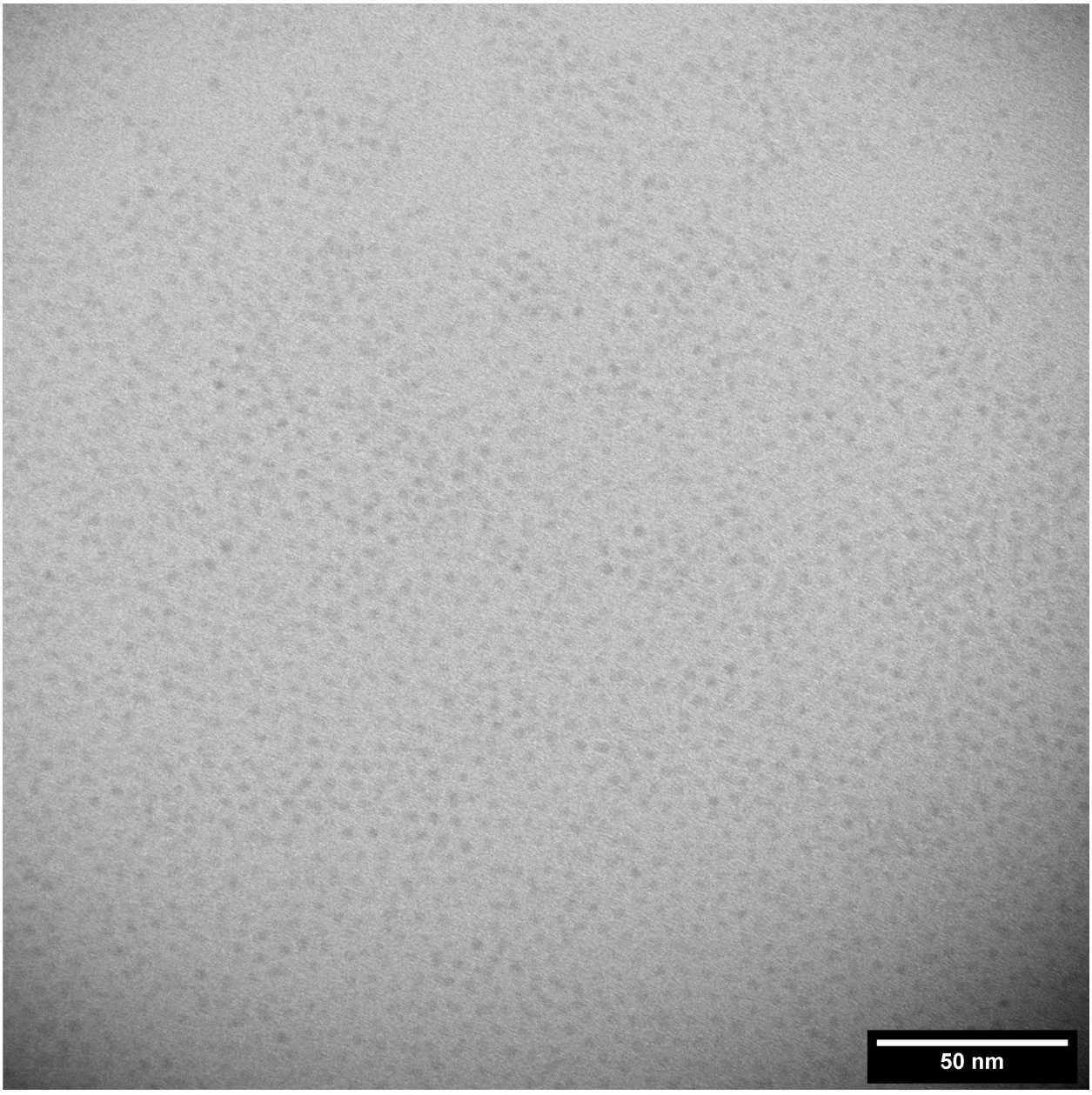


Figure A.6: TEM image of CdS quantum dots

In an oven-dried, three-neck, 50 mL round-bottom flask, 0.052 g of cadmium oxide (0.40 mmol) was added to 16 mL of *1*-octadecene and 2.4 mL of technical grade oleic acid (7.6 mmol) with a Teflon-coated stir bar. A Schlenk line was attached to a condenser column on the middle neck, and the other necks were sealed with a thermocouple adapter and a septa cap. Joints were sealed with Apiezon H grease, and the exposed top half of the flask was insulated using glass wool. The solution was stirred and heated to 90 °C using a heating mantle under vacuum until all visible bubbling stopped, which occurred at a pressure of 60 mTorr in the flask. To complex the cadmium, the solution was then placed under argon and heated at a rate of 20 °C per minute to 250 °C, until complete dissolution of the cadmium oxide was achieved and no red solids were observed, leaving a clear solution. At this point, the temperature was lowered to 90 °C, and the solution was placed back under vacuum for an hour until the solution reached 60 mTorr and stopped degassing. Then, the solution was placed back under argon, and the temperature was raised to 250 °C at a rate of 20 °C per minute, after which 2 mL of the sulfur precursor (0.20 mmol) was injected swiftly through the septum, turning the solution yellow. The temperature was held constant for 3 minutes, and then the flask was removed from heat and cooled to room temperature using a stream of nitrogen gas. The yellow crude nanoparticle solution was cannulated under argon to a large vial and transferred to an argon glovebox. Quantum dot solutions were washed via multiple methods (see below) and a TEM image (Figure A.6), ^{1}H NMR spectra (Figures A.7 and A.8), and powder X-ray diffraction measurements (Figure A.9) were taken to characterize them.

Bis(trimethylsilyl)sulfide Method

In an oven-dried, three-neck, 50 mL round-bottom flask, 0.278 g of cadmium acetate (1.2 mmol) was added to 10 mL of *n*-hexadecane and 0.678 g of technical grade oleic acid (2.4 mmol) with a Teflon-coated stir bar. A Schlenk line was attached to a condenser column on the middle neck, and the other necks were sealed with a thermocouple adapter and a septa cap. Joints were sealed with Apiezon H grease and the flask was evacuated via Schlenk line. The temperature of the flask was raised slowly to 70 °C, after which the vacuum line was closed. The solution was slowly heated to 80 °C, and the line to the vacuum was then opened slightly. The solution was then slowly heated to 120 °C, the vacuum was closed, and then the solution was heated to 150 °C until all solids disappeared, resulting in a clear solution. The temperature was lowered to 80 °C after which the vacuum line was fully opened, reaching a pressure below 60 mTorr. The system was flushed with argon gas and placed back under vacuum, and this process was repeated three times in intervals of ten minutes. In total, the degassing process lasted one hour. Then, the solution was placed back under argon, and the temperature was raised to between 150 and 270 °C at a rate of 20 °C per minute. In an argon glovebox, 1.540 g of *n*-hexadecane that had previously been heated and degassed for an hour at 90 °C at 60 mTorr was combined with 0.108 g of bis(trimethylsilyl)sulfide (0.6 mmol) and loaded into a syringe. This solution was then swiftly injected into the flask, and temperature was maintained for five minutes. The flask was then rapidly cooled under a stream of nitrogen

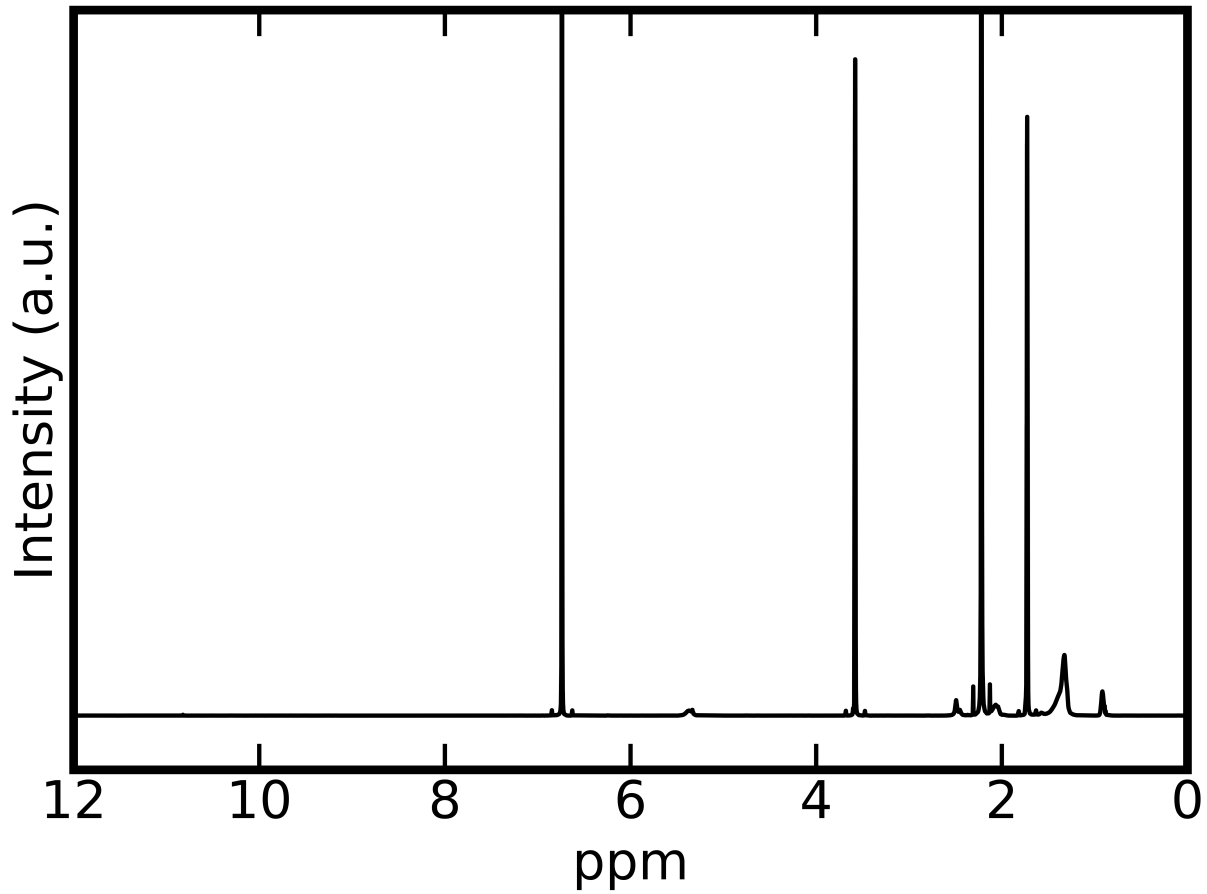


Figure A.7: ^{1}H NMR of cadmium sulfide quantum dots washed in tetrahydrofuran in tetrahydrofuran-d_8. Solvent peaks present at 3.58 ppm and 1.73 ppm, and internal mesitylene standard present at 6.74 ppm and 2.22 ppm.

and hexanes. After cooling the solution was cannulated to be purified in an argon glovebox. After cleaning, (see below) the nanocrystals were characterized. Characterization included absorption and luminescence measurements, STEM images, powder X-ray diffraction, and ^{1}H NMR measurements that can be found in Figure A.10.

A.4 Cadmium Selenide Quantum Dots

Procedure was adapted from that reported by Liu *et al.* to form zinc-blende cadmium selenide nanocubes.[36] In a three-neck, oven-dried, 50 mL round- bottom flask 0.078 g of selenium (1.0 mmol) was combined with 15 mL of *1*-octadecene with the inclusion of a Teflon-coated stir bar. After attaching a thermocouple adapter, septa cap, and air condenser

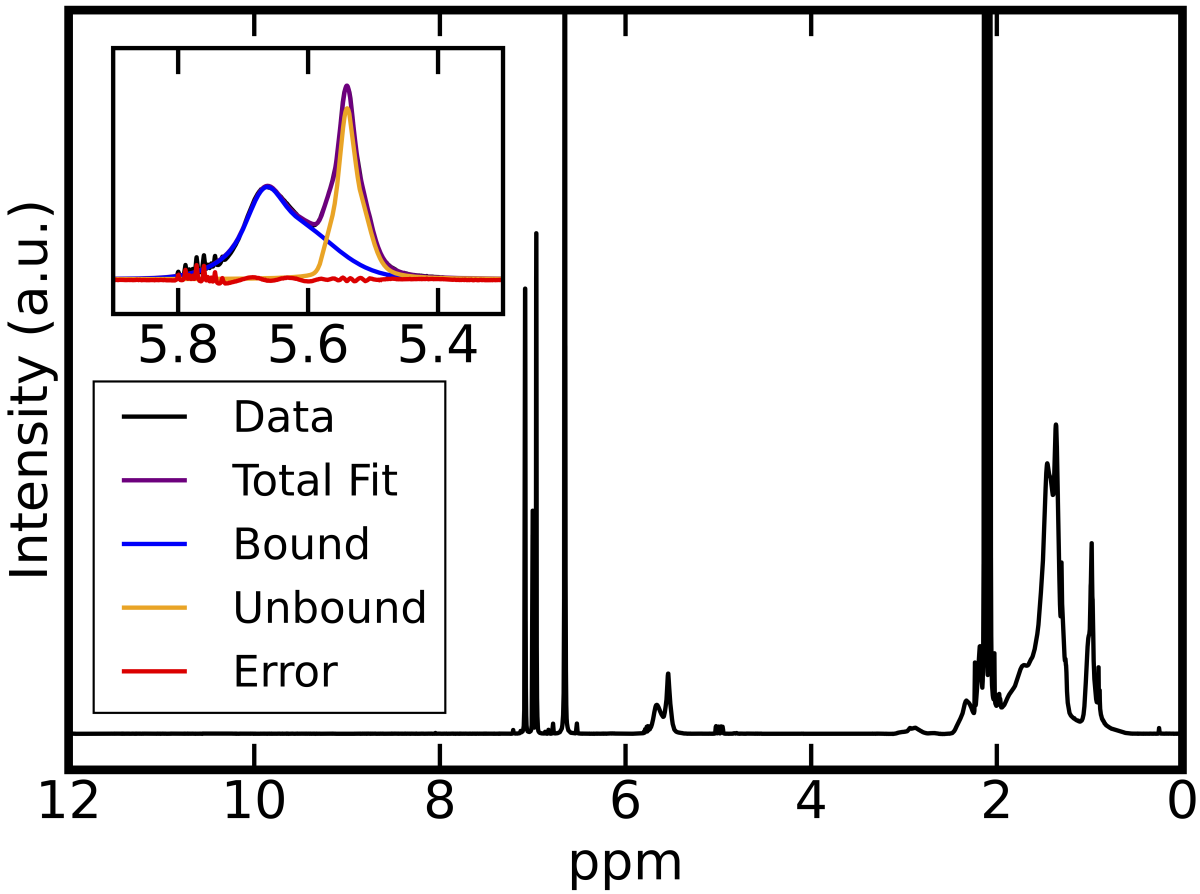


Figure A.8: ^{1}H NMR of cadmium sulfide quantum dots washed in hexane in toluene-d_8. Solvent peaks present at 7.08 ppm, 7.00 ppm, 6.96 ppm, and 2.07 ppm, and internal mesitylene standard present at 6.65 ppm and 2.13 ppm. Inset depicts fitting of vinyl protons of oleate to determine adsorbed ligand concentration; methyl protons near 1 ppm were not used for adsorbed ligand concentration determination as they overlap with the majority of the aliphatic protons.

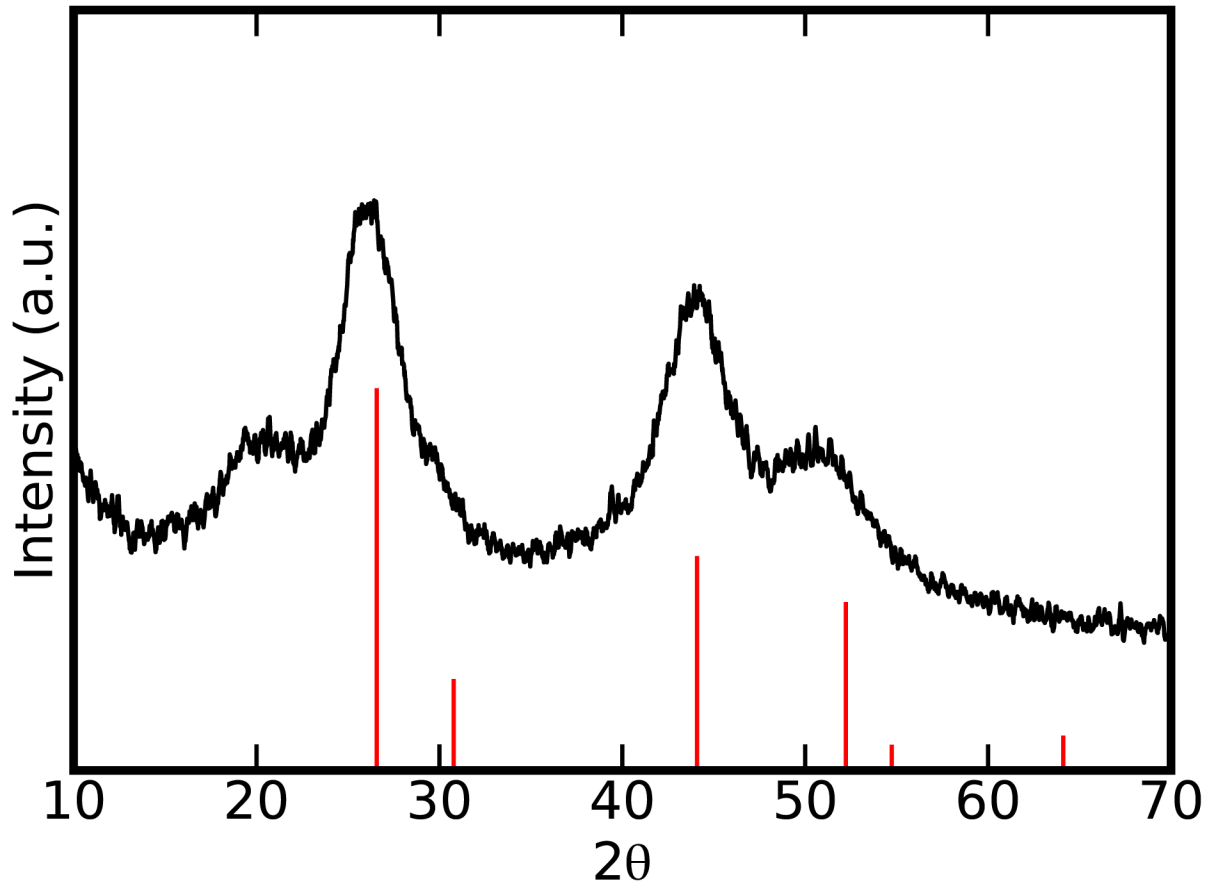


Figure A.9: Powder X-ray diffraction of cadmium sulfide quantum dots deposited on a silicon wafer. Reference data for zinc-blende cadmium sulfide depicted as red lines. Note the peak around 20 °2θ discussed in Chapter 5.

column to the flask and greasing all glass joints with Apiezon H grease, the flask was attached to a Schlenk line, and evacuated at room temperature for one hour, reaching a pressure below 60 mTorr. The solution was the placed under argon and heated to 280 °C and maintained at this temperature for 30 minutes, transitioning to a clear, yellow solution. In tandem, in a three- neck, oven-dried, 50 mL round-bottom flask, 0.266 g of cadmium acetate dihydrate (1.00 mmol) was combined with 5 mL of 90% oleic acid with the inclusion of a Teflon-coated stir bar. After attaching a thermocouple adapter, septa cap, and air condenser column to the flask and greasing all glass joints with Apiezon H grease, the flask was attached to a Schlenk line, and evacuated at room temperature for 15 minutes, reaching a pressure below 60 mTorr. The solutions were heated under argon to 150 °C and then quickly drawn into a syringe and injected into the selenium flask, forming a red solution. The solution was then stirred at

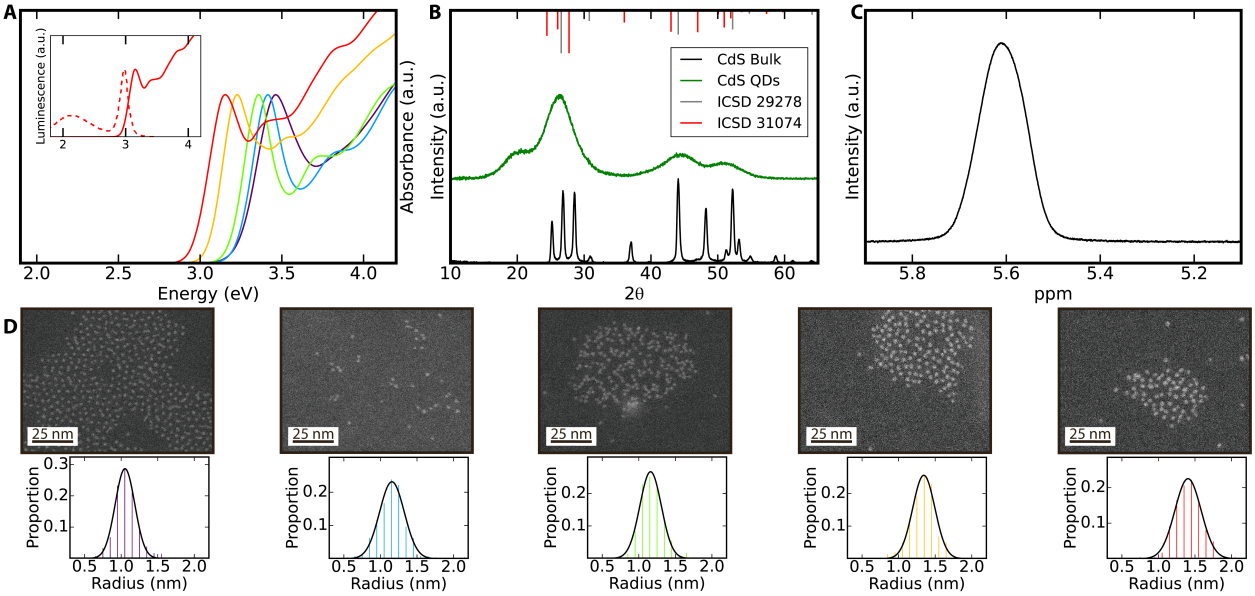


Figure A.10: Characterization of size series of CdS quantum dots. (A) Absorbance measurements of the five cadmium sulfide quantum dot samples used herein with inset including absorbance and luminescence measurements for one representative sample. (B) Powder X-ray diffraction measurements of bulk and a representative quantum dot sample of zinc sulfide with the reference lines of both zinc blende and wurtzite cadmium sulfide from the inorganic crystal structure database (ICSD 29278 and 31074, respectively). (C) ^{1}H NMR measurements of the vinyl proton region of a representative sample of cadmium sulfide quantum dots in toluene-d_8. (D) Scanning transmission electron microscope images of the cadmium sulfide quantum dot samples used for the cadmium sulfide/carboxylate surface energy measurements with inset scale bars to the top, and matched histograms fit by Gaussian distributions to the bottom.

265 °C for 2 minutes to form the small cadmium selenide quantum dots and 40 minutes to form the large cadmium selenide quantum dots before being rapidly cooled with a stream of hexanes and nitrogen, resulting in a black solution. The solution was cannulated under argon and transferred to an argon glovebox. Absorption and luminescence measurements as well as a TEM image can be found in Figure A.11, while powder X-ray diffraction can be found in Chapter 5.

A.5 Zinc Sulfide Quantum Dots

In an oven-dried, three-neck, 50 mL round-bottom flask, 0.220 g of zinc acetate (1.2 mmol) was added to 10 mL of *n*-hexadecane and 0.678 g of technical grade oleic acid (2.4 mmol) with a Teflon-coated stir bar. A Schlenk line was attached to a condenser column

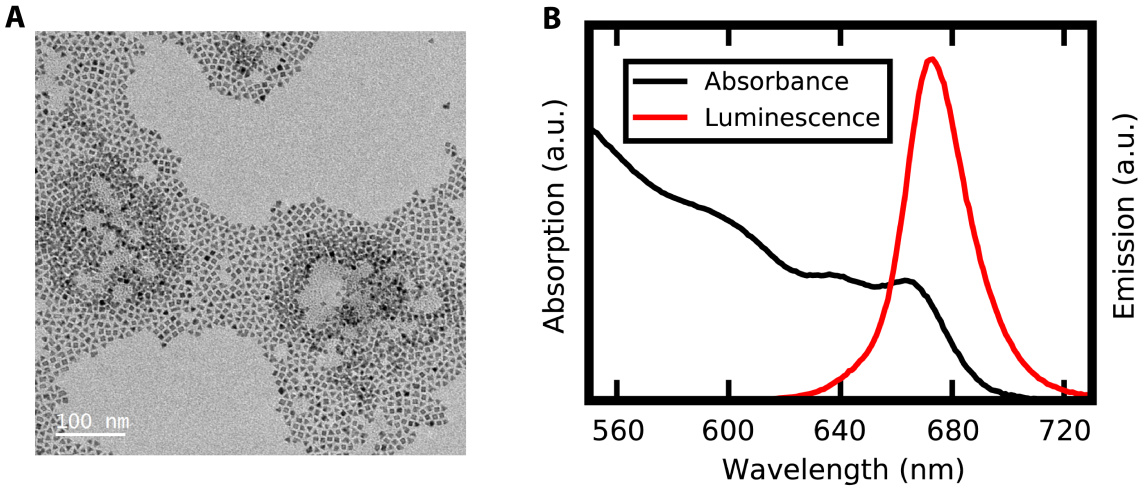


Figure A.11: Characterization of CdSe quantum dots. (A) TEM image of synthesized CdSe quantum dots. (B) Absorbance and luminescence measurements of synthesized CdSe quantum dots.

on the middle neck, and the other necks were sealed with a thermocouple adapter and a septa cap. Joints were sealed with Apiezon H grease and the flask was evacuated via Schlenk line. The temperature of the flask was raised slowly to 70 °C, after which the vacuum line was closed. The solution was slowly heated to 80 °C, and the line to the vacuum was then opened slightly. The solution was then slowly heated to 120 °C until all solids disappeared, resulting in a clear solution. The temperature was lowered to 80 °C after which the vacuum line was fully opened, reaching a pressure below 60 mTorr. The system was flushed with 5% hydrogen in argon gas and placed back under vacuum, and this process was repeated three times in intervals of ten minutes. In total, the degassing process lasted one hour. Then, the solution was placed back under 5% hydrogen in argon, and the temperature was raised to 250 °C at a rate of 20 °C per minute. In an argon glovebox, 1.540 g of *n*-hexadecane that had previously been heated and degassed for an hour at 90 °C at 60 mTorr was combined with 0.108 g of bis(trimethylsilyl)sulfide (0.6 mmol) and loaded into a syringe. This solution was then swiftly injected into the flask, and temperature was maintained for five minutes. The flask was then rapidly cooled under a stream of nitrogen and hexanes. After cooling the solution was cannulated to be purified in an argon glovebox. Characterization included absorption and luminescence measurements, STEM images, powder X-ray diffraction, and ^{1}H NMR measurements that can be found in Figure A.12.

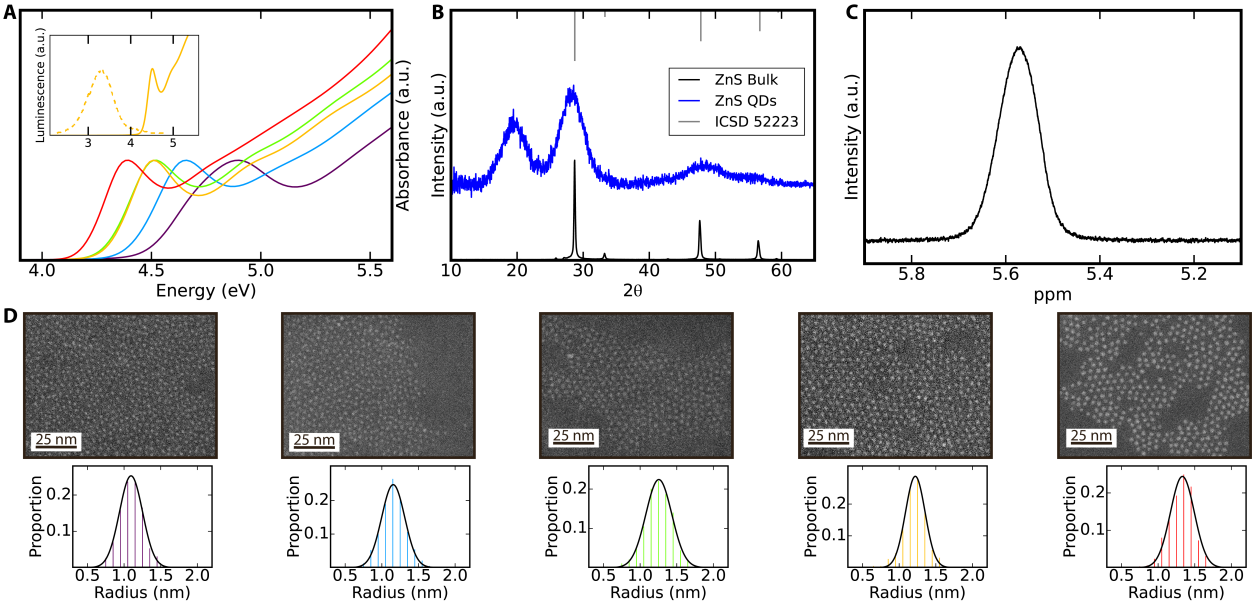


Figure A.12: Characterization of size series of ZnS quantum dots. (A) Absorbance measurements of the five zinc sulfide quantum dot samples used herein with inset including absorbance and luminescence measurements for one representative sample. (B) Powder X-ray diffraction measurements of bulk and a representative quantum dot sample of zinc sulfide with the reference lines of zinc blende zinc sulfide from the inorganic crystal structure database (ICSD 52223). (C) ^{1}H NMR measurements of the vinyl proton region of a representative sample of zinc sulfide quantum dots in toluene-d_8. (D) Scanning transmission electron microscope images of the zinc sulfide quantum dot samples used for the zinc sulfide/carboxylate surface energy measurements with inset scale bars to the top, and matched histograms fit by Gaussian distributions to the bottom.

A.6 Indium Phosphide/Zinc Sulfide Core/Shell Quantum Dots

Once the indium phosphide quantum dots under a hydrogen atmosphere were synthesized, some were coated, or shelled, with a layer of zinc sulfide. Two main approaches were utilized and will be discussed here. The first was to make zinc oleate *in situ*, add the quantum dots and then add a bis(trimethylsilyl)sulfide at an elevated temperature to grow a layer of zinc sulfide, and was similar to a previously published approach.[74] This approach was ultimately abandoned because while indium phosphide/zinc sulfide core/shell quantum dots were synthesized, zinc sulfide byproducts made up a significant portion of the nanocrystals (see Figure A.13 for scanning transmission electron microscopy and energy-dispersive X-ray spectroscopy mapping images). While these materials were not used, the details are reported here to illustrate the contamination of shell only nanocrystal that may be present in some

reported core/shell nanocrystal syntheses. The next approach undertaken was a layer by layer growth synthesis by injecting a sulfur precursor followed by zinc oleate in small, ideally monolayer amounts. However, without a stabilizing ligand that would coordinate to the sulfur rich surface the nanocrystals aggregated. The settled on synthesis involved simultaneously injecting a zinc precursor with bis(trimethylsilyl)sulfide. Unfortunately the zinc oleate precursor would precipitate during the injection period, resulting in a low zinc concentration in the reaction flask and precipitation of the nanocrystals. Diethyl zinc was used instead, and may have improved the synthesis overall due to high reactivity of the zinc and sulfur precursors. Additionally, a thin shell approach was used to make more spherical core/shell nanocrystals, making the assignment of surface areas easier and making the interfacial atoms a larger mass percent of the total sample for interface energy measurements.

Unlike the other reactions reported herein, the amounts of each reagent were not uniform across each synthesis as they depended on the amount of indium phosphide used for shelling. The calculation of the amount of each reagent to use will be discussed.

Zinc Oleate Method

In an oven-dried, three-neck, 50 mL round-bottom flask, a calculated amount of zinc acetate (discussed below) was added to 10 mL of *1*-octdecene or *n*-hexadecane and a calculated amount of technical grade oleic acid with a Teflon-coated stir bar. A Schlenk line was attached to a condenser column on the middle neck, and the other necks were sealed with a thermocouple adapter and a septa cap. Joints were sealed with Apiezon H grease and the flask was evacuated via Schlenk line. The temperature of the flask was raised slowly to 70 °C, after which the vacuum line was closed. The solution was slowly heated to 80 °C, and the line to the vacuum was then opened slightly. The solution was then slowly heated to 120 °C until all solids disappeared, resulting in a clear solution. The temperature was lowered to 80 °C after which the vacuum line was fully opened, reaching a pressure below 60 mTorr. The system was flushed with 5% hydrogen in argon gas and placed back under vacuum, and this process was repeated three times in intervals of ten minutes. In total, the degassing process lasted one hour. The solution was placed back under 5% hydrogen in argon. A calculated amount of indium phosphide quantum dots in hexanes was loaded into a syringe in an argon glovebox, and this solution was injected. Very slowly the vacuum line was opened to prevent bumping of the solution, and the solution was degassed until it reached a pressure of 100 mTorr. The temperature of the solution was then raised to 190 °C or 280 °C. The solution was placed back under 5% hydrogen in argon. In an argon glovebox, 1.540 g of *1*-octdecene or *n*-hexadecane that had previously been heated and degassed for an hour at 90 °C at 60 mTorr was combined with a calculated amount of bis(trimethylsilyl)sulfide and loaded into a syringe. This solution was then injected into the flask using a syringe pump over the course of 1 hour, and then the solution was allowed to stir for another 15 minutes. The flask was then rapidly cooled under a stream of nitrogen and hexanes. After cooling the solution was cannulated to be purified in an argon glovebox.

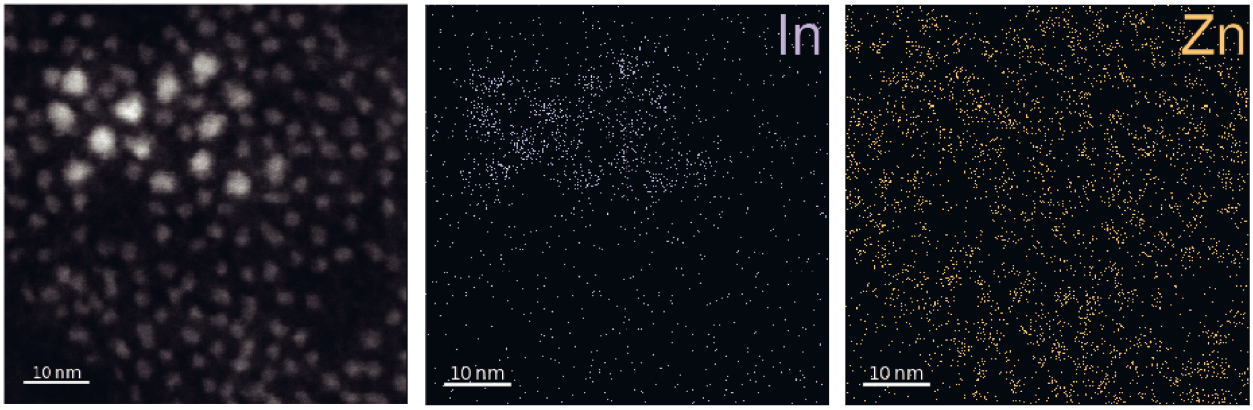


Figure A.13: High-angle annular dark-field scanning transmission electron microscope images of InP/ZnS with energy-dispersive X-ray spectroscopy mapping showing ZnS nanocrystal contamination

To determine the correct amount of reagents, the radius and concentration of the indium phosphide quantum dots was calculated using the calculator provided by Reiss *et al.* or Ministro (see Appendix 3.2).[99,132] An amount of indium phosphide quantum dot solution was selected for shell growth. Next, assuming that each monolayer of zinc sulfide was 0.269 nm thick and there are 7.97×10^{18} zinc atoms/m^2 based on the (111) lattice constants and crystal structure of zinc sulfide (ICSD 52223), the number of sulfur atoms to cover the surface area of the indium phosphide quantum dots was computed. This added 0.134 nm to the radius, and then the number of zinc atoms to cover the surface area of the new nanocrystal was computed, adding another 0.134 nm. This process was repeated until the amount needed to add ten layers of sulfur and ten layers of zinc to the nanocrystals were computed. The total number of moles of zinc and sulfur was calculated and converted into a mass of zinc acetate and bis(trimethylsilyl)sulfide needed. To calculate the amount of oleic acid need, the number of moles of zinc acetate was multiplied by two and coverted into a mass of oleic acid.

Diethyl Zinc Method

In an oven-dried, three-neck, 50 mL round-bottom flask, a Teflon-coated stir bar was added to 10 mL of *n*-hexadecane. A Schlenk line was attached to a condenser column on the middle neck, and the other necks were sealed with a thermocouple adapter and a septa cap. Joints were sealed with Apiezon H grease and the flask was evacuated via Schlenk line.

The temperature of the flask was raised to 80 °C, and the flask was evacuated for 30 minutes at a pressure below 60 mTorr. The solution was placed under 5% hydrogen in argon. A calculated amount of indium phosphide quantum dots in hexanes was loaded into a syringe in an argon glovebox, and this solution was injected. Very slowly the vacuum line was opened to prevent bumping of the solution, and the solution was degassed until it reached a pressure of 100 mTorr. The solution was placed back under 5% hydrogen in argon. The temperature of the solution was then raised to 280 °C. In an argon glovebox, three separate vials of 1.540 g of *n*-hexadecane that had previously been heated and degassed for an hour at 90 °C at 60 mTorr was combined with a calculated amount of bis(trimethylsilyl)sulfide, a calculated amount of technical grade oleic acid that had previously been heated and degassed for an hour at 90 °C at 60 mTorr, and a calculated amount of diethyl zinc, respectively, and loaded into a syringe. The bis(trimethylsilyl)sulfide and diethyl zinc solutions were then injected into the flask using a syringe pump over the course of 1 hour, where 0.5 mL of the solution was injected in the first 45 minutes and the final 1.5 mL of solution was injected in the last 15 minutes, and simultaneously the oleic acid solution was injected in 0.1 mL increments every 3 minutes. The solution was allowed to stir for another 15 minutes. The flask was then rapidly cooled under a stream of nitrogen and hexanes. After cooling the solution was cannulated to be purified in an argon glovebox. After cleaning, (see below) the nanocrystals were characterized. Characterization included absorption and luminescence measurements, STEM images, powder X-ray diffraction, ^{1}H NMR measurements, and solid state ^{31}P and ^{1}H-^{31}P NMR measurements that can be found in Figure A.14.

To determine the correct amount of reagents, the radius and concentration of the indium phosphide quantum dots was calculated using the calculator provided by Ministro (see Appendix 3.2).[132] Due to low yield of indium phosphide quantum dots, 3.5 mL of indium phosphide quantum dots was used (total yield was 4 mL) in the synthesis of the core/shell nanocrystals. Next, assuming that each monolayer of zinc sulfide was 0.269 nm thick and there are 7.97×10^{18} zinc atoms/m^2 based on the (111) lattice constants and crystal structure of zinc sulfide (ICSD 52223), the number of sulfur atoms to cover the surface area of the indium phosphide quantum dots was computed. This added 0.134 nm to the radius, and then the number of zinc atoms to cover the surface area of the new nanocrystal was computed, adding another 0.134 nm. This process was repeated until the amount needed to add three layers of sulfur and three layers of zinc to the nanocrystals were computed. The total number of moles of zinc and sulfur was calculated and converted into a mass of diethyl zinc and bis(trimethylsilyl)sulfide needed. To calculate the amount of oleic acid need, the number of moles of diethyl zinc was multiplied by two and converted into a mass of oleic acid.

A.7 Lead Sulfide Quantum Dots

In an oven-dried, three-neck, 50 mL round-bottom flask, 0.268 g of lead oxide (1.2 mmol) was added to 10 mL of *n*-hexadecane and 0.678 g of technical grade oleic acid (2.4 mmol)

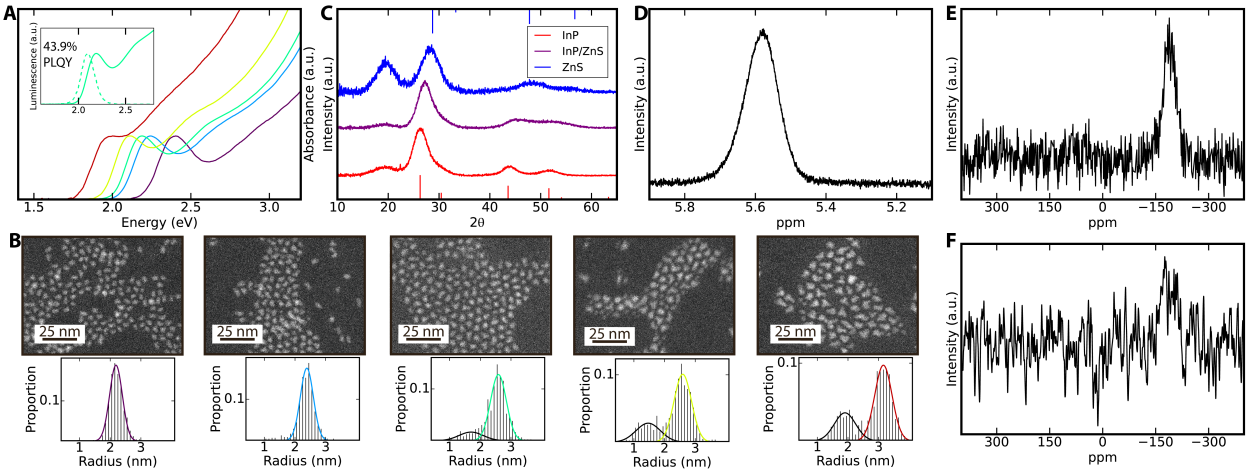


Figure A.14: Characterization of indium phosphide/zinc sulfide core/shell nanocrystals. (A) Absorbance measurements of the five indium phosphide/zinc sulfide core/shell nanocrystal samples used herein with inset including absorbance and luminescence measurements for one representative sample with the measured photoluminescence quantum yield (PLQY). (B) Scanning transmission electron microscope (STEM) images of the indium phosphide/zinc sulfide core/shell nanocrystal samples used for the indium phosphide/zinc sulfide interface energy measurements with inset scale bar to the top, and matched histograms fit with by Gaussian distributions to the bottom. (C) Powder X-ray diffraction measurements of representative nanocrystal samples of indium phosphide, zinc sulfide, and indium phosphide/zinc sulfide with the reference lines for zinc blende indium phosphide and zinc blende zinc sulfide from the inorganic crystal structure database (ICSD 24517 and 52223, respectively). (D) ^{1}H NMR measurements of the vinyl proton region of a representative sample of indium phosphide/zinc sulfide core/shell nanocrystals in toluene-d_8. (E) Solid state ^{31}P magic-angle spinning measurements of a representative sample of indium phosphide/zinc sulfide core/shell nanocrystals. (G) Solid state cross-polarized ^{1}H-^{31}P magic-angle spinning measurements of a representative sample of indium phosphide/zinc sulfide core/shell nanocrystals.

with a Teflon-coated stir bar. A Schlenk line was attached to a condenser column on the middle neck, and the other necks were sealed with a thermocouple adapter and a septa cap. Joints were sealed with Apiezon H grease and the flask was evacuated via Schlenk line. The temperature of the flask was raised slowly to 70 °C, after which the vacuum line was closed. The solution was slowly heated to 80 °C, and the line to the vacuum was then opened slightly. The solution was then slowly heated to 120 °C, until all solids disappeared, resulting in a clear solution. The temperature was lowered to 80 °C after which the vacuum line was fully opened, reaching a pressure below 60 mTorr. The system was flushed with argon gas and placed back under vacuum, and this process was repeated three times in intervals of ten minutes. In total, the degassing process lasted one hour. Then, the solution was placed back under argon, and the temperature was raised or lowered to between 60 and 180 °C. In an argon glovebox, 1.540 g of *n*-hexadecane that had previously been heated and degassed for an hour at 90 °C at 60 mTorr was combined with 0.108 g of bis(trimethylsilyl)sulfide (0.6 mmol) and loaded into a syringe. This solution was then swiftly injected into the flask, and temperature was maintained for five minutes. The flask was then rapidly cooled under a stream of nitrogen and hexanes. After cooling the solution was cannulated to be purified in an argon glovebox. Characterization included absorption and luminescence measurements, TEM images, powder X-ray diffraction, and ^{1}H NMR measurements that can be found in Figure A.15.

A.8 Cadmium Oxide Nanocrystals

Unlike the other syntheses reported herein, the synthesis of cadmium oxide nanocrystals used a thermal decomposition route, adapted from Liu *et al.*[234] This approach resulted in less uniformly shaped nanoparticles overall.

In an oven-dried, three-neck, 50 mL round-bottom flask, 0.466 g of cadmium acetylacetonate (1.5 mmol) was added to 10 mL of *n*-hexadecane and 2.4 mL of technical grade oleic acid (7.5 mmol) with a Teflon-coated stir bar. A Schlenk line was attached to a condenser column on the middle neck, and the other necks were sealed with a thermocouple adapter and a septa cap. Joints were sealed with Apiezon H grease and the flask was evacuated via Schlenk line. The temperature of the flask was raised slowly to 80 °C, eventually reaching a pressure below 60 mTorr. In an argon glovebox, 1.540 g of *n*-hexadecane that had previously been heated and degassed for an hour at 90 °C at 60 mTorr was combined with between 0.061 and 0.484 g of bis(trimethylsilyl)amine (0.375 and 3.0 mmol) depending on the synthesis, and this solution was loaded into a syringe. The reaction flask was then flushed with argon, and the bis(trimethylsilyl)amine solution was injected. The temperature was raised to 293 °C, and the solution was vigorously refluxing. The solution was refluxed for between 30 minutes and 3 hours, depending on the synthesis, where higher amounts of bis(trimethylsilyl)amine resulted in quicker syntheses. The reaction was considered finished when the brown solution changed to a dark grey, vaguely greenish color rapidly that coincided with a drop in temperature. The flask was then rapidly cooled under a stream of nitrogen and hexanes. After

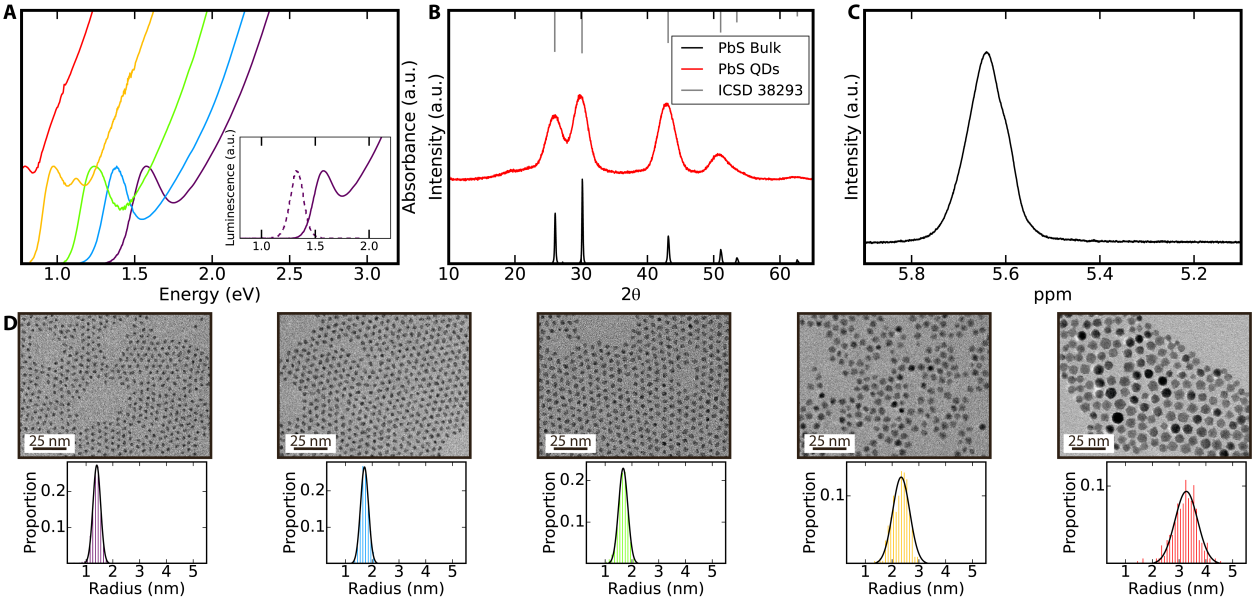


Figure A.15: Characterization of lead sulfide quantum dots. (A) Absorbance measurements of the five lead sulfide quantum dot samples used herein with inset including absorbance and luminescence measurements for one representative sample. (B) Powder X-ray diffraction measurements of bulk and a representative quantum dot sample of lead sulfide with the reference lines of rock salt lead sulfide from the inorganic crystal structure database (ICSD 38293). (C) ^{1}H NMR measurements of the vinyl proton region of a representative sample of lead sulfide quantum dots in toluene-d_8. (D) Transmission electron microscope images of the lead sulfide quantum dot samples used for the lead sulfide/carboxylate surface energy measurements with inset scale bars to the top, and matched histograms fit by Gaussian distributions to the bottom.

cooling the solution was cannulated to be purified in an argon glovebox. Characterization included absorption and luminescence measurements, TEM images, powder X-ray diffraction, and ^{1}H NMR measurements that can be found in Figure A.16.

A.9 Washing Procedures

As has been said by Dhaene *et al.*,[233] "In literature, subtle 'tricks' and delicate procedures are reported, giving NC purification the aura of art instead of science." This is certainly true, particularly when syntheses yield different amounts of nanocrystals or different sizes of a given nanocrystal. Because of this, this section will be somewhat generalized with specific insights given for particular syntheses. All washing steps were performed in an argon glovebox using 50 mL centrifuge tubes. The synthesis solvent was invariably *1*-octadecene or *n*-hexadecane, where the switch to *n*-hexadecane was adopted due to reports of polymerization

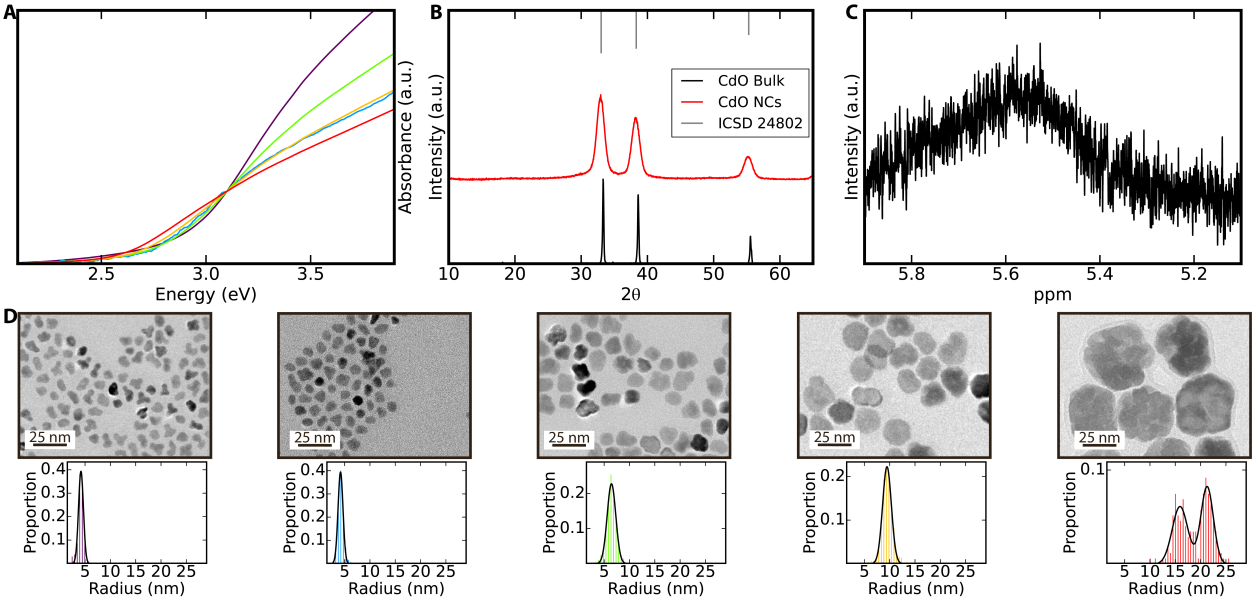


Figure A.16: Characterization of cadmium oxide nanocrystals. (A) Absorbance measurements of the five cadmium oxide nanocrystal samples used herein. (B) Powder X-ray diffraction measurements of bulk and a representative nanocrystal sample of cadmium oxide with the reference lines of rock salt cadmium oxide from the inorganic crystal structure database (ICSD 24802). (C) ^{1}H NMR measurements of the vinyl proton region of a representative sample of cadmium oxide quantum dots in toluene-d_8. (D) Transmission electron microscope images of the cadmium oxide nanocrystal samples used for the cadmium oxide/carboxylate surface energy measurements with inset scale bars to the top, and matched histograms fit by Gaussian distributions to the bottom.

of *1*-octadecene.[233] The favorable solvent for the nanocrystals was either tetrahydrofuran, toluene, or hexanes, while the unfavorable solvent was either acetone, methyl acetate, or ethyl acetate. As a note, if the tetrahydrofuran was not distilled (see Appendix A.1), the integrity of indium phosphide quantum dots would be compromised, and this was attributed to even very low concentrations of peroxides. As a rule, anywhere from a 2:1 up to a 4:1 ratio of unfavorable solvent to favorable solvent could be used to precipitate nanocrystals, and typically 4 mL of favorable solvent was used to resuspend precipitate nanocrystals, although exceptions to this below will be detailed. In general, methyl and ethyl acetate were more gentle than acetone, allowing for better separation of magic-sized clusters from the rest of the nanocrystals, but could result in no precipitation of nanocrystals when nanocrystal concentration was low. An easy adjustment to this was to evaporate all of the solvent and add a minimal amount of favorable solvent followed by the unfavorable solvent. Of course, low volumes also concentrated the undesirable impurities, so ideally a balance could be struck. Typically the solutions were centrifuged for 5 minutes at 10000 RPM (5702 RCF)

to form a pellet where the supernatant could be decanted, although 8000 RPM was also a commonly used speed and for larger nanocrystals or greater amounts of unfavorable solvent these numbers could be adjusted down easily. Typically three cycles of precipitation were used to thoroughly clean the nanocrystals. A significant issue with these steps was the prescence of metal carboxylate precursors. To remove these precursors, tetrahydrofuran was the best solvent to use, and this is attributed to its ability to breakup polymerized metal carboxylate chains.[100] However, tetrahydrofuran enables the ligand shell to become dynamic (see Chapter 3) so a ^{1}H NMR in tetrahydrofuran-d_8 will show evidence of unbound precursor even after thorough washing. Rather, washing particles twice with hexanes and doing a final suspension and precipitation in tetrahydrofuran and acetone, followed by a suspension in hexanes or toluene will given solutions that potentially have no free ligand signature when investigated by ^{1}H NMR in toluene-d_8. In general for most solutions, the time between cannulation and cleaning was not critically important (although should be done soon after) except in situations detailed below.

Indium Phosphide Quantum Dots

The indium phosphide quantum dots followed the generally detailed procedures from above, although to remove the free indium carboxylate the quantum dots needed to be washed all three times with tetrahydrofuran, and to get a highly pure sample each precipitation step was preceded by one day of sitting in tetrahydrofuran. For the indium phosphide/zinc sulfide core/shell nanocrystals, which were terminated with zinc carboxylate, no such procedure was needed. However, rapid precipitation from the crude solution was required or else separation of the core/shell quantum dots from the excess zinc oleate precursor proved futile.

When synthesizing indium phosphide nanocrystals capped with stearate ($C_{18}H_{35}O_2$) it was found that invariably the solution would solidify into a gel unless the solution was first diluted with anhydrous hexanes or tetrahydrofuran. Hexanes could be added once the solution reached a temperature of around 60 °C, although with this step, the first precipitation step must be rapidly initiated or separation of the quantum dots from the excess indium stearate precursor proved futile. Alternatively, if the solution is allowed to solidify, the entire flask can be sealed and transferred to an argon glovebox. To this solid, 30 mL of anhydrous tetrahydrofuran was added and mixed until all of the solid went into solution. The solution was divided into four large centrifuge tubes and 30 mL of anhydrous acetone was added to each, causing an orange precipitate to form that could be later resuspended.

Cadmium Sulfide Quantum Dots

In the case of the cadmium sulfide quantum dots, the washing procedure was critical to the results, and so is detailed more here. All washing steps were performed under argon. After diluting the crude nanoparticle solution to a total volume of 20 mL with tetrahydrofuran, 30 mL of acetone was added to precipitate the nanoparticles in a large centrifuge tube. The suspension was centrifuged at 5702 RCF for 5 minutes, and then the supernatant

was decanted. The nanoparticle pellet was suspended in 5 mL of tetrahydrofuran, optical measurements were taken, and then the solution was diluted to 20 mL in tetrahydrofuran. This process of adding acetone to precipitate the particles, centrifuging the solution, and resuspending in tetrahydrofuran was repeated four more times.

Measurements were also performed on quantum dots that were initially washed with hexanes and acetone. These dots were prepared by the same steps as above, however, tetrahydrofuran was replaced by hexanes, and the washing steps were only repeated twice.

Zinc Sulfide Quantum Dots

The only notable difference in the separation of zinc sulfide quantum dots is that the first precipitation step must be rapidly initiated or separation of the quantum dots from the excess zinc carboxylate precursor proved futile.

Cadmium Oxide Nanocrystals

These nanocrystals proved different in their separation than the other nanocrystals, likely due to their thermal decomposition synthesis. After removing the solution to the glovebox, the solution was centrifuged at around 8000 RPM for five minutes. This caused all of the nanocrystals to precipitate, after which 4 mL of hexanes was added to the pellet. Pellet was shaken and placed in a sonicating bath (sealed in a centrifuge tube) for five minutes. The solution was then centrifuged at 3000 RPM for two minutes, and the precipitate (generall green) was discarded, leaving a black solution. This solution was washed two more times using hexanes and methyl acetate as normal, using the sonicator when necessary to suspend the particles, before being suspended in hexanes and being centrifuged one last time at 3000 RPM for two minutes. The supernatant was collected, and appeared to be colloidally stable indefinitely.

A.10 Indium Myristate

An oven-dried, three-neck 50 mL round-bottom flask was charged with 1.000 gram (3.425 mmol) of indium acetate, 2.347 grams (10.28 mmol) of myristic acid, 20 mL *1*-octadecene, and a Teflon-coated stir bar. The flask was placed under vacuum and the temperature was raised to 110 °C for one hour. The flask was then pressurized with ultra-high purity argon (99.999%, Airgas) to slightly over atmospheric pressure, and the temperature was lowered to room temperature, and a white precipitate formed. The flask was then put under vacuum, after which the stopcock was closed. The flask was then transferred to an argon glovebox and the flask was filled with argon through the stopcock. The septum was removed, and the solution was poured into a centrifuge tube. After the solution was centrifuged, the supernatant was removed, and 20 mL of anhydrous acetone was added to the solid. After thoroughly washing the precipitate, it was centrifuged again, and the supernatant

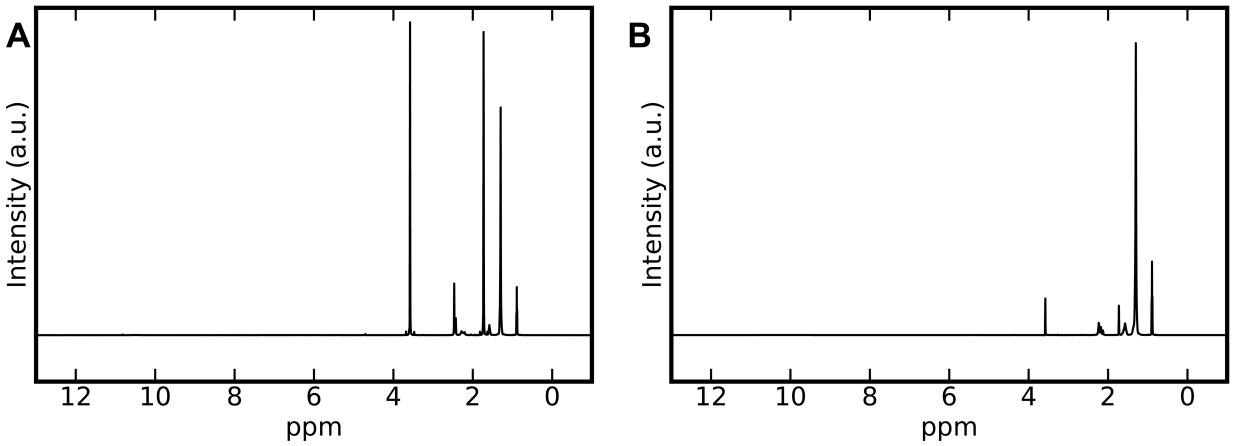


Figure A.17: ^{1}H NMR of indium myristate. (A) Precipitate from zinc chloride reaction and (B) as synthesized. Note that solvent peaks present at 1.7 ppm and 3.6 ppm are much more pronounced in the spectra of the precipitate as the concentration is much lower due to lack of sample.

	Theoretical	Synthesized	Precipitate
Carbon	63.30%	61.03%	62.99%
Hydrogen	10.24%	9.07%	10.07%

Table A.1: Elemental analysis of indium myristate precipitate from reaction of zinc chloride with indium phosphide quantum dots and synthesized indium myristate. Error is estimated at 0.30% for elemental percentages.

was discarded. This process was repeated three times to remove as much *1*-octadecene and residual myristic acid as possible. The precipitate was then transferred to a glass vial and another 20 mL of anhydrous acetone was added. The vial was capped tightly, and the solution was heated on a hot plate until the precipitate dissolved. The hotplate was turned off and the solution was allowed to cool slowly back to room temperature, and the white precipitate reappeared. The solution was centrifuged one more time, the supernatant was removed, and the indium myristate was transferred to a vial with a septa cap and was placed under a vacuum line at room temperature to remove residual acetone overnight. Characterization of the indium myristate was done through ^{1}H NMR (Figure A.17), FTIR (Figure A.18), and elemental analysis (Table A.1), and was compared with the isolated precipitate from the reactions with zinc chloride.

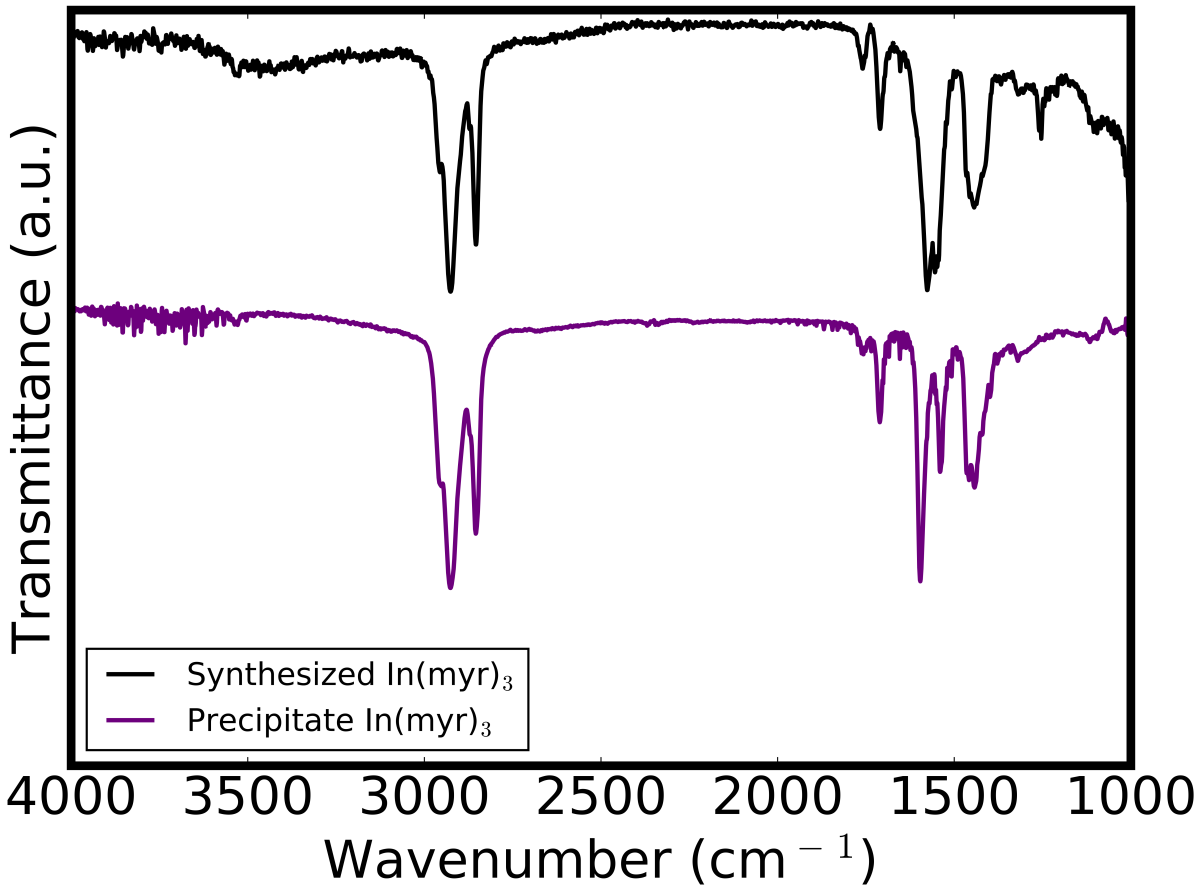


Figure A.18: FTIR spectra of indium myristate precipitate (purple) and as synthesized indium myristate (black).

A.11 Cadmium Oleate

In a three-neck, 50 mL round-bottom flask, 0.518 g (4.03 mmol) of cadmium oxide was added to 4.550 g of >99% oleic acid (16.11 mmol) with a Teflon-coated stir bar. A Schlenk line was attached to a condenser column on the middle neck, and the other necks were sealed with a thermocouple adapter and a septa cap. Joints were sealed with Apiezon H grease. After being placed under vacuum, the solution was stirred and heated to 90 °C until the solution stopped degassing at a pressure of 60 mTorr. Under an argon atmosphere, the solution was heated to 190 °C until the cadmium was complexed. After dissolution, the solution was cooled to 90 °C and placed under vacuum for an hour after the solution stopped degassing at a pressure of 60 mTorr. Once cooled to room temperature, the solution was transferred in air to a large centrifuge tube, and 10 mL of acetone was added to the solution to precipitate the cadmium oleate as a white solid. The solution was centrifuged

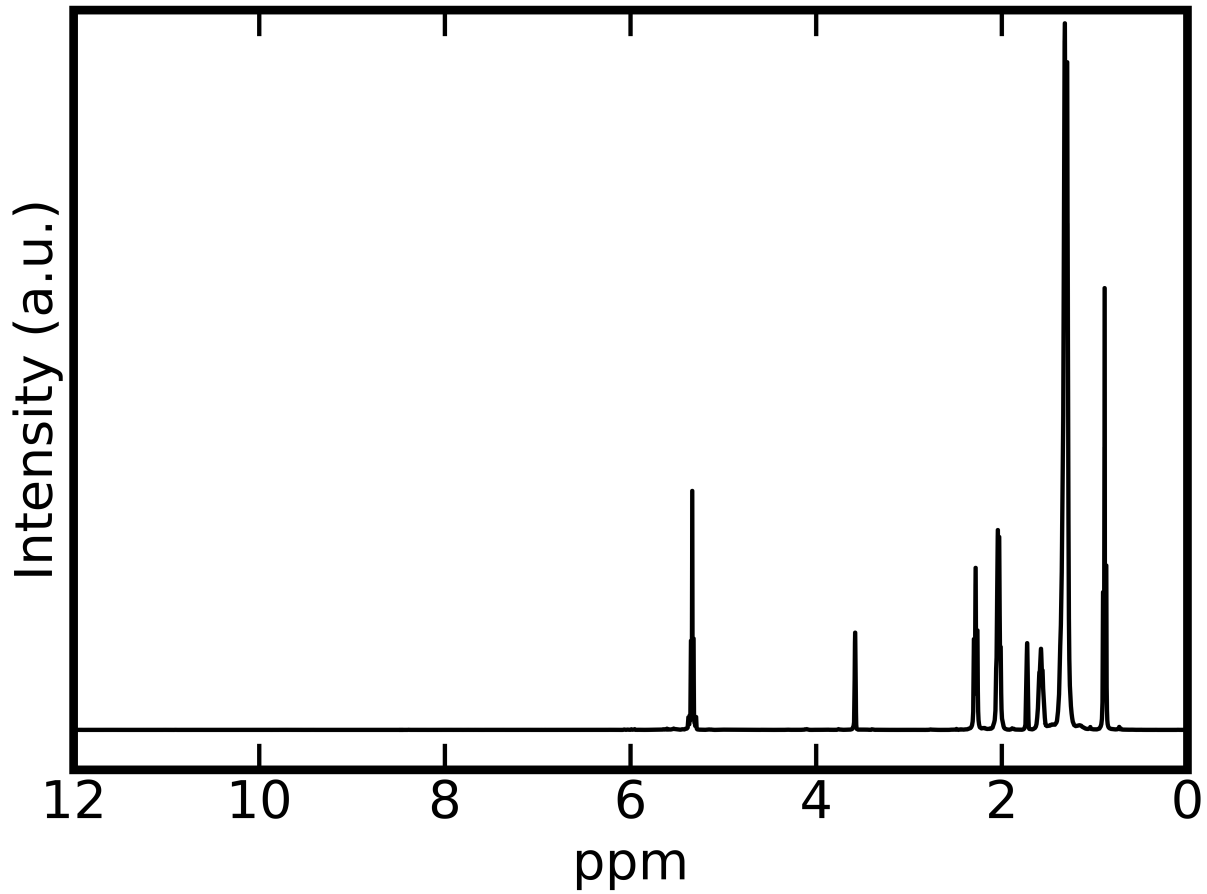


Figure A.19: ^{1}H NMR of synthesized cadmium oleate in tetrahydrofuran-d_8. Solvent peaks present at 3.58 ppm and 1.73 ppm.

for 5 minutes at 5702 RCF, and then the supernatant was discarded. This process of adding 10 mL of anhydrous acetone, mixing, and centrifuging was repeated five more times, after which the solution was left to dry under laboratory vacuum overnight.

The synthesized cadmium oleate was dissolved in tetrahydrofuran-d_8 and an ^{1}H NMR was taken (Figure A.19). Comparison to previously published spectra indicate that cadmium oleate was synthesized.[16,100] CHNS elemental analysis was performed on the synthesized cadium oleate. Carbon content was 63.98 (64.00) %, and hydrogen content was 9.62 (9.90) % where theoretical values are in parentheses. Experimental uncertainty is 0.3%. Additionally, FTIR measurements were taken on the synthesized cadmium oleate (Figure A.20).[16] Cadmium oleate was dissolved in anhydrous carbon tetrachloride for measurements. The carbon tetrachloride spectrum was subtracted to give the spectrum of cadmium oleate, and unfortunately there is a significant overlapping stretch around 1550 cm^{-1} between cadmium

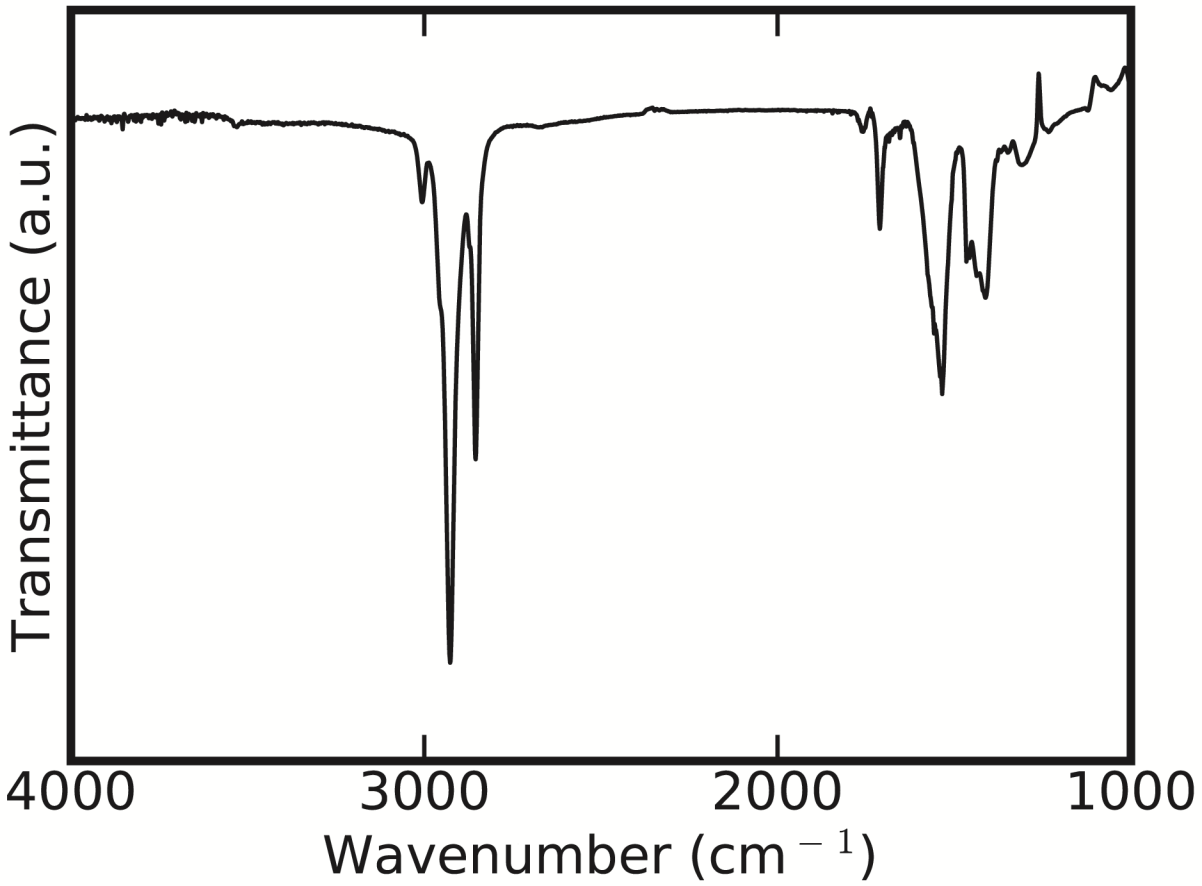


Figure A.20: FTIR spectra of synthesized cadmium oleate dissolved in CCl_4 after background correction.

oleate and carbon tetrachloride. However, the peak still appears after the subtraction. Note the carbonyl stretch at 1535 cm^{-1} is attributed to the cadmium oleate while the stretch at 1711 cm^{-1} is likely caused by a small oleic acid contamination. However, this contamination is minimal considering the intensity of carboxylic acid carbonyl stretches and the absence of the broad OH stretch in the FTIR around 3000 cm^{-1}.

Appendix B

Experimental Methods and Data

Reproduced in part with permission from Calvin, J. C.; Swabeck J. K.; Sedlak, A. B.; Kim, Y.; Jang, E.; Alivisatos, A. P. "Thermodynamic Investigation of Increased Luminescence in Indium Phosphide Quantum Dots by Treatment with Metal Halide Salts" *J. Am. Chem. Soc.* **2020**, *142*(44), 18897–18906. Copyright 2020 American Chemical Society.[71]

Reproduced in part with permission from Calvin, J. C.; O'Brien, E. A.; Sedlak, A. B.; Balan, A. D.; Alivisatos, A. P. "Thermodynamics of Composition Dependent Ligand Exchange on the Surfaces of Colloidal Indium Phosphide Quantum Dots" *ACS Nano* **2021**, *15*(1), 1407–1420. Copyright 2021 American Chemical Society.[121]

Reproduced in part with permission from Calvin, J. C.; Kaufman, T. M.; Sedlak, A. B.; Crook, M. F.; Alivisatos, A. P. "Observation of Ordered Organic Capping Ligands on Semiconducting Quantum Dots via Powder X-ray Diffraction" *Nat. Commun.* **2021**, *12*, 2663 under a Creative Commons license CC BY 4.0.[135]

B.1 Isothermal Titration Calorimetry

All measurements were performed by using a TA Instruments Nano isothermal titration calorimeter. Measurements were performed in a nitrogen drybox to prevent oxidation of the nanoparticles. For measurement, 1.198 ± 0.006 mL of sample solution was placed in the sample cell (effective volume of 965 ± 5 μL) and 1.198 ± 0.006 mL of distilled tetrahydrofuran was placed in the reference cell with the reference needle. The syringe was loaded with 250 μL of ligand solution in tetrahydrofuran. The temperature was maintained at 25 °C through the titration. After stirring was initiated at 250 RPM, the samples were allowed to equilibrate until the differential heating slope was <0.1 μW/hour and the standard deviation in the differential heating was <0.01 μW over a period of lasting approximately 40 minutes. After equilibration, an initial baseline was taken for 2400 seconds, and then the desired amount of titrant solution was injected per injection. Between each injection the solution was stirred

	MA 2.7	MA 2.9	MA 3.1	MA 3.1*	SA 2.9	SA 3.0	SA 3.1	SA 3.4
Concentration (μM)	7.7 ± 0.8	10.5 ± 1.0	9.5 ± 1.0	8.0 ± 0.8	7.4 ± 0.7	9.0 ± 0.9	15.2 ± 2.0	15.2 ± 2.0

Table B.1: Isothermal titration calorimetry concentrations for InP quantum dot size series. MA refers to samples capped with myristate ($C_{14}H_{27}O_2$) and SA refers to samples capped with stearate ($C_{18}H_{35}O_2$). *Note that two samples capped with indium myristate are very close in size (to 0.1 nm in diameter). The second one listed is slightly larger based on the size calculator.

for 2400 seconds to allow the system to return to equilibrium. Integration of titration peaks calculates the heat of reaction. The standard error in the heat of injection is 23 μJ for 10 μL injections and was determined by injecting water into water.[60]

Background subtractions were performed by injecting the ligand solution into neat tetrahydrofuran in an identical manner to the sample measurements and subtracting the integrated heat from the sample measurements.

For reactions involving the indium phosphide quantum dots with the metal halides discussed in Chapter 4, the quantum dot stock solution was diluted to between 7.4 and 15.2 μM with tetrahydrofuran, and the metal halide salts were at a concentration of 6.2 ± 0.1 mM in tetrahydrofuran. For each injection 10 μL was injected. The concentration of the quantum dot solutions were calculated by UV–vis absorption measurements by Ministro,[132] and the choice of this calculator is discussed extensively in Appendix C.2. In addition, this choice is the origin of the variable concentrations in the reactions (Table B.1).

For reactions involving the indium phosphide quantum dots with the metal halides discussed in Chapter 3, the quantum dot stock solution was diluted to 32 ± 3 μM with tetrahydrofuran, and the metal halide salts were at a concentration of 30.8 ± 0.7 mM in tetrahydrofuran. For each injection 10 μL was injected. The concentration of the quantum dot solutions were calculated by UV–vis absorption measurements by Reiss *et al.*,[99] and the issue with this calculator is discussed extensively in Appendix C.2.

For reactions involving the washed cadmium sulfide nanoparticles from Chapter 3, the quantum dots were diluted to a concentration of 22.9 ± 1.5 μM in tetrahydrofuran, and a 20.1 ± 0.15 mM concentration solution of cadmium oleate in tetrahydrofuran was made. For each injection 5.14 ± 0.05 μL of solution was injected. Each measurement (including the background measurements) were repeated twice and averaged due to low signal. The concentration of the quantum dot solutions were calculated by absorption measurements by Yu *et al.*,[51] and the choice for this calculator is discussed extensively in Appendix C.3.

For reactions involving the indium phosphide quantum dots with the carboxylic acids discussed in Chapter 4, the quantum dot stock solutions were diluted to 32 ± 3 μM with tetrahydrofuran, and the carboxylic acids were diluted in tetrahydrofuran to a concentration of 93.1 ± 0.4 mM. The quantum dots were diluted to a concentration of 8 ± 1 μM in tetrahydrofuran for the reactions with phosphonic acids, which were diluted to a concentration of 16.0 ± 0.3 mM. For each injection 10 μL was injected. The concentration of the quantum dot

solutions were calculated by absorption measurements by Reiss *et al.*,[99] and the issue with this calculator is discussed extensively in Appendix C.2. For the X-ray diffraction measurements after octadecylphosphonic acid exchange discussed in Chapter 5, after treatment the solution was washed with acetone in a 3:1 ratio to precipitate the quantum dots, after which the solution was centrifuged at 5702 RCF for 5 minutes and the supernatant was discarded. The quantum dots were then resuspended in 1 mL of tetrahydrofuran and the process of adding acetone and resuspending in tetrahydrofuran was repeated.

B.2 ^{1}H Nuclear Magnetic Resonance

Titration Experiments Mirroring Calorimetry Experiments

Measurements were performed on a Bruker Avance 700 instrument. A determined quantity of the quantum dot solutions was dried of solvent in a vial and then resuspended in a 72 $\pm$ 2 mM solution of mesitylene in tetrahydrofuran-d_8 to the same volume in an argon glovebox. Titrant solutions were prepared in the same way, resulting in a constant molarity of mesitylene during measurement. Samples were prepared in oven-dried NMR tubes in an argon glovebox by adding 0.600 mL of quantum dot solutions in tetrahydrofuran-d_8 to the tubes, and for each titration the sample tube was returned to the glovebox. The chemical shift was referenced to the α hydrogens in tetrahydrofuran with a chemical shift of 3.580 ppm. The 90°pulse was calibrated for every measurement, and samples were allowed to relax for 20 seconds between pulses to acquire quantitative ratios between ligands bound to the surface of the quantum dots as well as the mesitylene peaks to calculate ligand concentrations. Uncertainty in integration areas for peaks was estimated at 5%.

An additional note about these ^{1}H NMR measurements. When available, the vinyl protons on a ligand like oleate should be used as there is generally less interference with impurities in this region of the spectrum than the methyl protons, the other easily fit set of protons. With the isothermal titration calorimetry measurements with the size series of indium phosphide quantum dots (Chapter 4), as the quantum dots were capped with straight-chained carboxylates, only the methyl peak was available, but considering the lower concentrations that were used due to lack of sample, these impurities became problematic. During titrations, it was observed that the NMR spectra began to show a broad peak centered around 0.87 ppm, which did not correspond to the bound ligand peak nor the free ligand peaks (Figures B.1 and B.2). We suspected that there was some contamination present that was being added during measurement, and this was confirmed by taking spectra of the solvent (tetrahydrofuran-d_8) before and after it had been soaked in a plastic pipette that was like the one used for titrations (Figure B.2). While some small contamination was present in the neat solvent, soaking in the pipette introduced a broad peak that had been observed in the spectra. This contamination was accounted for by fitting a broad peak in that region during the peak fitting (igure B.1) and this area was not used in calculating the bound ligand concentration.

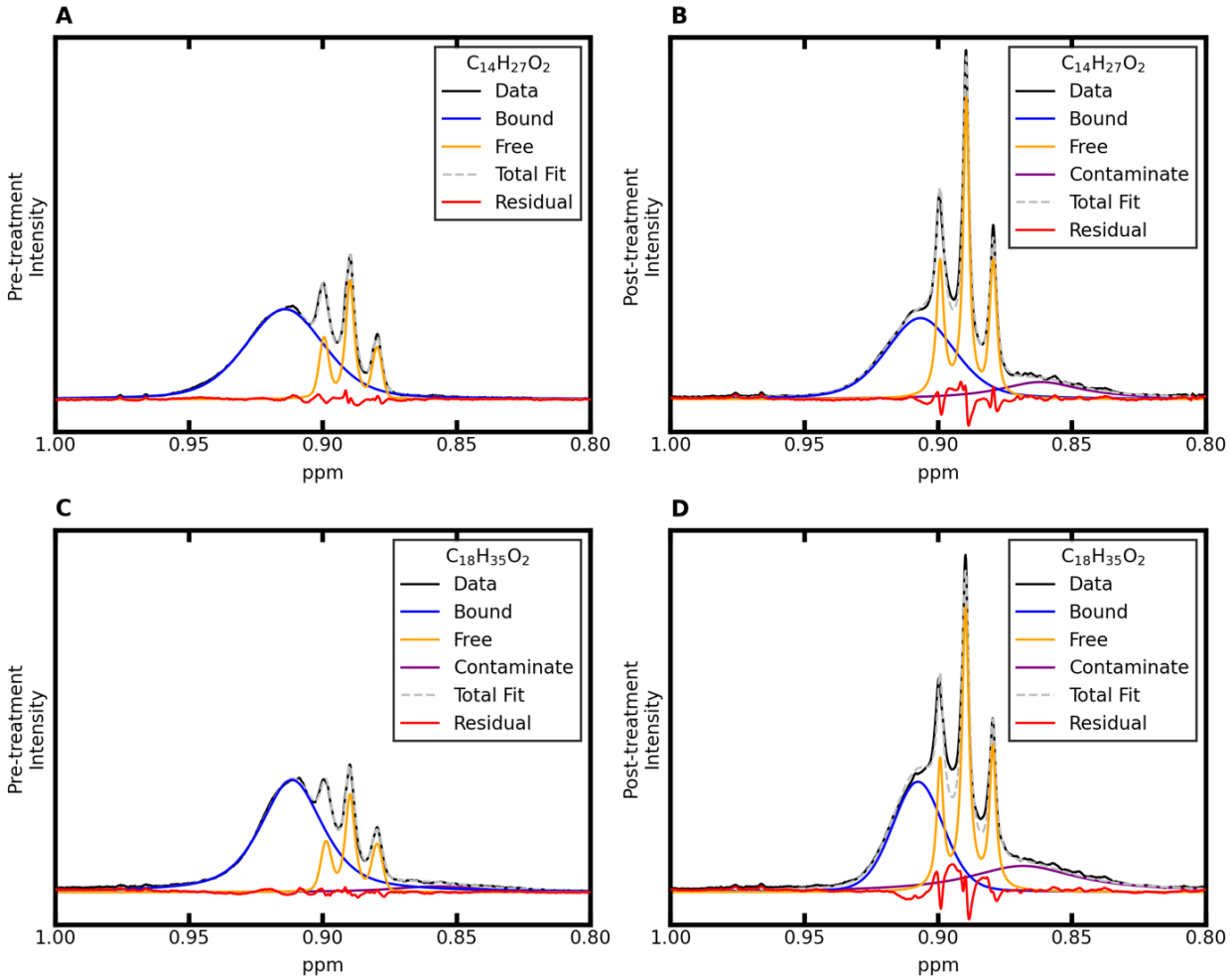


Figure B.1: ^{1}H NMR spectrum showing impurity of the methyl group of myristate and the fitting of the bound and unbound peaks that make up the spectrum. The raw spectrum is colored black, total fit is dashed grey, bound peak is blue, unbound peak is yellow, and residual error is red. (A) The spectrum for as-synthesized 3.1 diameter indium phosphide quantum dots capped with myristate ($C_{14}H_{27}O_2$). (B) The spectrum for 3.1 diameter indium phosphide quantum dots capped with myristate ($C_{14}H_{27}O_2$) at an after zinc chloride exchange. (C) The spectrum for as-synthesized 3.9 diameter indium phosphide quantum dots capped with stearate ($C_{18}H_{35}O_2$). (D) The spectrum for 3.9 diameter indium phosphide quantum dots capped with stearate ($C_{18}H_{35}O_2$) after zinc chloride exchange.

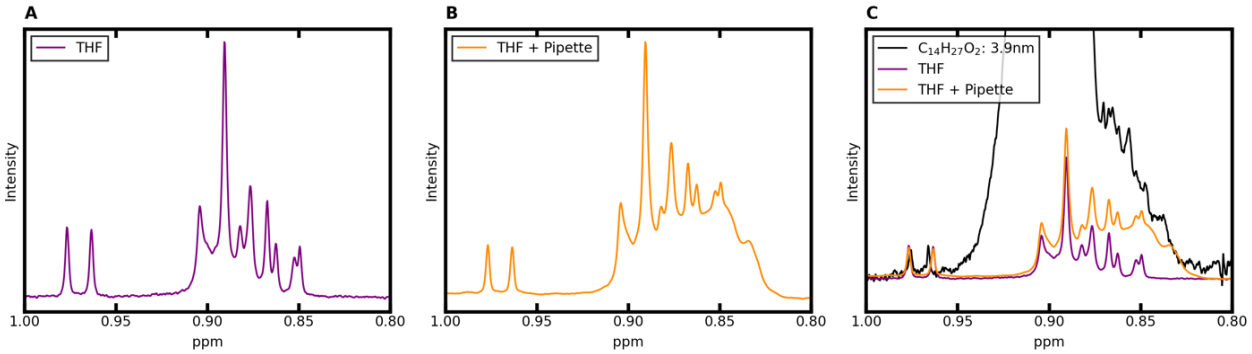


Figure B.2: ^{1}H NMR evidence of pipette contamination. (A) ^{1}H NMR of the tetrahydrofuran-d_8 used to solvate quantum dot samples for ^{1}H NMR measurements, (B) ^{1}H NMR of a tetrahydrofuran-d_8 after soaking in a plastic pipette tip similar to the one used to add zinc chloride during ^{1}H NMR titrations. Note the broad multiplet centered around 0.875ppm as well as two singlets around 0.975ppm. (C) Spectrum for 3.9 diameter indium phosphide quantum dots capped with myristate ($C_{14}H_{27}O_2$) after zinc chloride addition (black). Scaled spectra of THF (purple) and plastic pipette tip left in THF (orange) relative to sample singlet at 0.975ppm.

Metal Carboxylate Characterization

Characterization of the indium myristate precipitate and synthesized indium myristate was performed a Bruker Avance 700 instrument in tetrahydrofuran-d_8. Characterization of synthesized cadmium oleate was performed on a Bruker Avance 400.

B.3 Solid State Nuclear Magnetic Resonance

Quantum dot solutions were dried of solvent under vacuum to form a paste. The sample that was treated with zinc chloride was diluted to the same concentration as the isothermal titration calorimetry measurements and a proportional amount of zinc chloride ligand solution was added before drying. Samples were then packed in a ZrO_2 rotor under an argon atmosphere. For measurement, samples were spun at a speed of 10,000 to 40,000 RPM under a flow of nitrogen gas. Cross polarization measurements were performed by exciting ^{1}H nuclei on the organic ligands and transferring that excitation to the surface phosphorous.

	A_1	τ_1	A_1	τ_2	A_3	τ_3	χ^2
InP	4300 ± 234	5.656 ± 0.341	1999.0 ± 55.3	36.703 ± 0.860	308.8 ± 10.3	175.65 ± 3.86	1.180
InP + $ZnCl_2$	4607 ± 193	6.545 ± 0.314	3938.1 ± 60.9	31.022 ± 0.409	648.5 ± 13.7	120.93 ± 1.63	1.076
InP + $ZnBr_2$	4616 ± 198	7.240 ± 0.351	3720.3 ± 64.4	31.641 ± 0.455	451.1 ± 12.2	138.00 ± 2.46	1.094
InP + $InCl_3$	4520 ± 187	6.052 ± 0.283	3444.1 ± 59.5	27.594 ± 0.402	507.7 ± 11.9	119.44 ± 1.88	1.067

Table B.2: Fitting parameters for fluorescent lifetimes of InP quantum dots. Units for the A terms are given in counts and the time constant units are in nanoseconds.

B.4 Optical Measurements

Absorption Spectroscopy

Stock solutions of quantum dots were diluted in neat solvent by adding typically between 30 and 100 μL of the stock solution to 3 mL of the desired solvent in a 1 cm path length quartz cuvette prepared in an argon glovebox. The cuvettes were sealed, and absorption measurements were taken on a Shizmadu UV-3600 spectrometer with a slit width of 1.0 nm and a scanning speed of 350 nm/minute with a resolution of 1.0 nm and were baselined corrected to a matched cuvette of pure solvent.

Luminescence Spectroscopy

The luminescence of the quantum dots was measured by a Horiba Jobin Yvon TRIAX 320 Fluorolog or an Edinburgh FLS 980 Spectrometer. Solutions were prepared in an identical fashion as the absorption measurements and were generally done sequentially on the same solution. For quantitative measurements of increases or decreases in luminescence after treatments, the spectra were concentration corrected from absorption measurements, assuming luminescence is linear with concentration over small changes in concentration.

Fluoresence Lifetime Measurements

Luminescence lifetime measurements were performed on these samples by a Picoquant Fluotime 300 luminescence spectrometer. Excitation was performed with an LDH-P-C-405 diode laser set at a wavelength of 407.7 nm, and luminescence was collected with a PMA 175 detector. The slit width was 1.8 nm with a sample-dependent repetition rate of 876712, 1481481, 1207547, and 1523810 Hz for the untreated sample, sample treated with zinc chloride, sample treated with zinc bromide, and sample treated with indium chloride, respectively.

Fluorescent lifetimes were fit to a triple exponential decay of the form:

$$I(t) = \sum_{i=1}^{3} A_i e^{-\frac{t}{\tau_i}}$$

Parameters are included in Table B.2, and χ^2 values indicating goodness of fit are included as well.

Photoluminescence Quantum Yield Measurements

Absolute quantum yield measurements were performed by a custom-built spectrometer, the details of which have been published elsewhere,[235] or in the case of the cadmium sulfide nanocrystals, an Edinburgh FLS 980 Spectrometer equipped with an integrating sphere. Solutions were transferred in an argon glovebox to a cylindrical, capped quartz cuvette for measurement.

Fourier Transform Infrared Spectroscopy

Infrared absorption measurements of the metal carboxylates was performed by a Bruker IFS 66v/S vacuum FT-IR between 1000 and 4000 cm^{-1}. Several milligrams of sample were dissolved in 2 mL of carbon tetrachloride and this solution was placed as a thin film between CaF_2 salt plates for measurement. Background measurements were performed on neat carbon tetrachloride.

B.5 X-ray Photoelectron Spectroscopy

Quantum dot solutions recovered from isothermal titration calorimetry measurements were cleaned in an argon glovebox by adding anhydrous acetone in a 2:1 acetone to solution mixture to precipitate the nanocrystals, after which they were centrifuged and resuspended to their original volume in anhydrous hexanes. This procedure was repeated to remove any excess metal halides or organic ligands, both of which are soluble in the tetrahydrofuran/acetone and hexane/acetone mixture. The solutions were then drop-cast onto small pieces of silicon wafers that had been soaked the hexane, and then acetone, and then cleaned for 1 minute in a UV plasma cleaner in vacuum. Samples were measured on a Thermo Fisher Scientific K-Alpha Plus XPS instrument and exposed to atmosphere only during sample mounting. Samples were irradiated with aluminum K-α X-rays with an energy of 1.487 keV. Survey spectra were collected with electron energies up to 1350 eV, and element specific spectra were collected as well in narrow energy ranges. Unfortunately, due to measurement errors in XPS and the very low concentrations of the metal halide salts quantitative information about the elements was impossible.

	In:P	Zn:In
InP	1.43	-
InP + $ZnCl_2$	1.37	0.067
InP + $ZnBr_2$	1.37	0.056
InP + $InCl_3$	1.46	-

Table B.3: ICP-OES measurements on metal halide treated InP quantum dots.

B.6 Inductively Coupled Plasma Optical Emission Spectroscopy

Inductively coupled plasma optical emission spectroscopy (ICP-OES) measurements were performed using a Perkin Elmer ICP Optima 7000 DV Spectrometer. For measurements of samples treated with metal halides, samples were washed twice with acetone and resuspended in hexane after treatment to remove free indium myristate and excess metal halides. Samples were then dried of hexane under vacuum and dissolved in Optima for Ultra Trace Elemental Analysis 67–69% nitric acid, then diluted. Standard solutions of indium, phosphorus, zinc, and cadmium ions were prepared at concentrations of 25, 5, 1, 0.5, and 0.1 ppm, and all solutions were analyzed. For the cadmium oxide samples, the mass of dried nanoparticles was recorded to measure mass percent cadmium.

The results of the measurement of indium phosphide treated with metal halides are recorded in Table B.3 and show a slight decrease in the ratio of indium to phosphorus after treatment with the zinc halide salts. The slight increase in the indium to phosphorous ratio after treatment with indium chloride is attributed to the stronger binding strength of indium chloride to the quantum dots than indium myristate, and indium myristate is likely lost during the washing process. Results of measurements on samples used in the surface and interface energy measurements are found in Table B.4.

B.7 X-ray Diffraction

Powder X-ray Diffraction

Quantum dot solutions were drop-cast onto a single crystal silicon wafer from high vapor point solvents such as tetrahydrofuran and hexanes. Samples varied in thickness, but a visible coating of material obscuring the underlying silicon was the goal. They were allowed to dry quickly to prevent superlattice formation of the nanocrystal powder and instead produce randomly oriented nanocrystals. Measurements were done on a Bruker D2 Phaser instrument and samples were irradiated with copper K-α X-rays with a wavelength of 1.5418 Å. Spectra were collected at angles between 10°and 70°2θ under ϕ angular rotation of 72°/s. Spectra were baselined using a rubber-band baseline construction using a spectrum of the blank

Sample	In:P	In:Zn	Zn:S	Cd:S	Pb:S	Cd%
InP 532	1.34 ± 0.01	-	-	-	-	-
InP 554	1.40 ± 0.09	-	-	-	-	-
InP 576	1.28 ± 0.04	-	-	-	-	-
InP 585	1.3 ± 0.1	-	-	-	-	-
InP 600	1.22 ± 0.03	-	-	-	-	-
InP/ZnS 493	1.35 ± 0.05	0.30 ± 0.01	1.86 ± 0.06	-	-	-
InP/ZnS 538	1.28 ± 0.03	0.364 ± 0.003	2.14 ± 0.08	-	-	-
InP/ZnS 548	1.24 ± 0.05	0.35 ± 0.01	2.17 ± 0.09	-	-	-
InP/ZnS 566	1.26 ± 0.07	0.37 ± 0.009	1.89 ± 0.06	-	-	-
InP/ZnS 608	1.11 ± 0.03	0.34 ± 0.01	1.66 ± 0.05	-	-	-
ZnS 253	-	-	1.81 ± 0.09	-	-	-
ZnS 266	-	-	1.64 ± 0.07	-	-	-
ZnS 274	-	-	1.47 ± 0.06	-	-	-
ZnS 275	-	-	1.57 ± 0.06	-	-	-
ZnS 282	-	-	1.47 ± 0.05	-	-	-
CdS 358	-	-	-	1.8 ± 0.1	-	-
CdS 363	-	-	-	1.7 ± 0.1	-	-
CdS 369	-	-	-	1.71 ± 0.09	-	-
CdS 384	-	-	-	1.62 ± 0.08	-	-
CdS 393	-	-	-	1.55 ± 0.07	-	-
PbS 787	-	-	-	-	1.60 ± 0.01	-
PbS 896	-	-	-	-	1.47 ± 0.08	-
PbS 1000	-	-	-	-	1.40 ± 0.07	-
PbS 1271	-	-	-	-	1.27 ± 0.05	-
PbS 1565	-	-	-	-	1.16 ± 0.04	-
CdO 2.00:1	-	-	-	-	-	72.6 ± 0.9
CdO 1.00:1	-	-	-	-	-	77 ± 2
CdO 0.75:1	-	-	-	-	-	80.6 ± 0.8
CdO 0.50:1	-	-	-	-	-	80.3 ± 0.7
CdO 0.25:1	-	-	-	-	-	83 ± 1

Table B.4: Elemental ratios of samples used in dissolution calorimetry experiments. Samples are given labels based on the wavelength in nanometers of the first exciton peak in the absorption spectrum except in the case of cadmium oxide nanocrystals, and instead the ratio of bis(trimethylsilyl)amine to cadmium acetylacetonate is used. Count refers to the number of nanocrystals whose area was measured. Note that the indium phosphide samples for shelling with zinc sulfide were not measured by ICP-OES elemental analysis.

silicon wafer as a guide. For the elevated temperature dependent powder X-ray diffraction, a custom holder was built to fit the Bruker D2 Phaser instrument using a thermocouple and heating element beneath the silicon wafer.

For the high temperature dependent powder X-ray diffraction, quantum dot solutions were dried into a thick paste in the sample holder. The X-ray diffraction patterns of the samples were collected using a Rigaku MiniFlex 6G X-ray diffractometer with a copper K-α radiation ($\lambda = 1.5418$ Å). The voltage and current were 40 kV and 15 mA respectively. The scanning rate was 5 °C/min in the range of 2θ from 10°– 40°.

Solution X-ray Diffraction

Indium phosphide quantum dot solutions were dried of anhydrous tetrahydrofuran in an argon glovebox and resuspended to a concentration of approximately 0.5 mM in anhydrous toluene. These solutions were loaded into 1 mm inner diameter/1.1 mm outer diameter polyimide tubes that were sealed with tapered plastic plugs and mounted on top of the silicon wafer using Scotch tape to adhere the ends of the tube to the wafer holder. Measurements were performed on a Bruker D2 Phaser instrument and samples were irradiated with copper K-α X-rays with a wavelength of 1.5418 Å. The air-scatter screen above the wafer was set to 1 mm, which allowed it to sit directly on top of the parallel polyimide capillary. Spectra were collected at angles between 5°and 70°2θ, and points were taken every 0.03°2θ and measurements were averaged for 36.0 s at each point. Spectra were baselined using a rubber-band baseline construction.

Due to significant scattering in the desired regions, careful background subtraction of a sample of anhydrous toluene were performed using a custom least squares curve fitting program. The spectrum of the anhydrous toluene was subtracted from the sample spectra using a varying weight parameter, and Gaussian peaks centered at the inorganic reflections were also fit. Consistently an additional fitting peak was required to get an optimal fit around 17°2θ, which is attributed to the organic ligands on the surface of the quantum dots.

B.8 Drop Solution Calorimetry

Calorimetry measurements were performed on a Setaram C80 calorimeter with custom built quartz reaction cells (Figure B.3). The sample and reference cells were filled with 5 mL of 37% hydrochloric acid each and were maintained at a temperature of 25 °C. After approximately 10 hours of equilibration, samples were dropped into the sample chamber and the heat flow recorded. Measurements were typically completed and the heat flow returned to baseline after approximately 10 hours, depending on the sample. For the measurement of bulk materials, samples were dropped as pieces or chunks, while for the nanocrystal samples, solutions of the colloidal nanocrystals were dropcast onto a Teflon platform from hexanes until approximately 5–10 mg had been deposited, and then the sample was placed under a vacuum at 60 mTorr for 30 minutes before the final mass deposited was recorded.

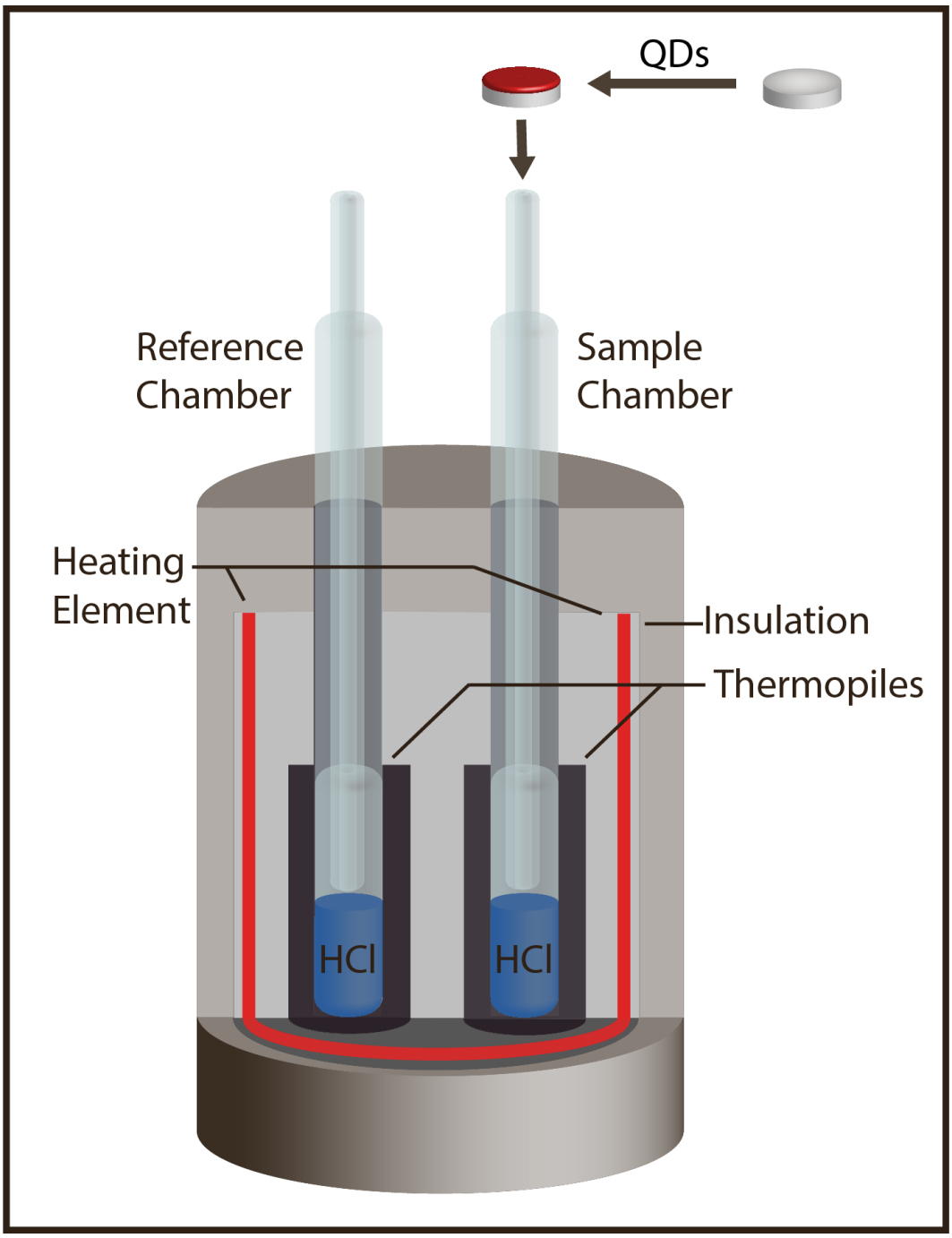


Figure B.3: Schematic of Setaram C80 calorimeter and using a Teflon platform to deposit nanocrystals and dissolve them in hydrochloric acid.

Sample	Mass (mg)	Mass OA (mg)	Enthalpy (mJ)	Protonation Enthalpy (mJ)	Enthalpy (J/g)	MW (g/mol)	Molar Surface Area (m^2/mol)	Enthalpy (kJ/mol)
InP 532	5.80	3.00±0.02	2800	78±7	760±80	158±2	56000±1000	120±10
InP 554	5.12	2.33±0.02	2600	60±5	680±80	160±10	54500±900	110±20
InP 576	5.78	2.88±0.02	2400	75±6	600±80	156±5	44000±1000	90±10
InP 585	4.05	1.79±0.02	1900	46±4	600±100	160±10	45000±1000	90±20
InP 600	5.56	2.55±0.02	2100	66±6	470±80	154±4	41300±800	70±10
InP/ZnS 493	4.99	1.89±0.02	5400	49±4	5300±300	158±6	69000±2000	830±60
InP/ZnS 538	4.97	1.90±0.02	4800	49±4	4000±200	156±4	53000±800	620±40
InP/ZnS 548	4.84	2.11±0.02	4700	55±5	4700±300	155±6	52000±2000	730±60
InP/ZnS 566	5.09	1.80±0.02	4400	47±4	3500±200	155±8	46000±600	540±50
InP/ZnS 608	4.61	1.49±0.02	3600	39±3	3200±300	150±4	35500±800	480±40
ZnS 253	8.43	5.79±0.03	3200	150±10	900±90	107±5	63000±1000	100±10
ZnS 266	4.67	2.98±0.02	2100	77±7	800±100	106±4	59000±1000	90±20
ZnS 274	6.06	3.86±0.02	2400	100±9	800±100	104±4	55000±1000	80±10
ZnS 275	6.01	3.68±0.02	2600	95±8	800±100	105±4	57000±1000	90±10
ZnS 282	9.19	5.15±0.04	3800	130±10	760±60	104±3	53900±800	79±7
CdS 358	5.36	3.32±0.02	2600	86±7	900±100	170±10	81000±2000	160±20
CdS 363	5.85	3.63±0.02	3000	94±8	1000±100	165±9	74000±3000	170±20
CdS 369	5.86	3.54±0.02	2500	92±8	800±100	166±9	73000±2000	130±20
CdS 384	5.18	2.98±0.02	2600	77±7	900±100	163±8	66000±1000	150±20
CdS 393	4.79	2.64±0.02	2200	68±6	700±100	162±7	62000±2000	120±20
PbS 787	5.72	2.41±0.02	2700	62±5	600±70	280±20	66000±1000	170±20
PbS 896	6.83	2.64±0.03	2400	69±6	420±60	270±10	54100±700	120±20
PbS 1000	6.40	2.35±0.03	2900	61±5	550±60	270±10	55900±700	150±20
PbS 1271	10.55	3.13±0.04	3000	81±7	320±30	260±10	39800±800	82±9
PbS 1565	11.86	2.36±0.05	3100	61±5	260±10	252±8	28200±800	65±7
CdO 2.00:1	8.02	1.49±0.03	-7300	39±3	-1220±40	140±20	11000±200	-170±20
CdO 1.00:1	5.00	0.76±0.02	-4000	20±2	-1080±60	140±40	10800±300	-150±40
CdO 0.75:1	7.59	0.65±0.03	-7500	17±2	-1160±30	130±10	7100±200	-150±10
CdO 0.50:1	6.02	0.66±0.02	-5900	17±2	-1210±40	140±10	4860±90	-170±20
CdO 0.25:1	12.95	0.74±0.05	-14400	19±2	-1230±20	130±10	2400±100	-160±20

Table B.5: Calorimetry data for the nanocrystal samples. Samples are given labels based on the wavelength in nanometers of the first exciton peak in the absorption spectrum except in the case of cadmium oxide nanocrystals, and instead the ratio of bis(trimethylsilyl)amine to cadmium acetylacetonate is used. The mass recorded has an error of 0.01 mg, and mass of oleate (OA) was determined by CHNS elemental analysis. The calculated error for the enthalpy measurements is 165 mJ.

Background measurements of the Teflon platform dropped into 37% hydrochloric acid were performed, measuring at an average of 600 mJ with a standard deviation of 165 mJ, and these measurements were used for the error on individual measurements from the calorimeter. Data on samples used for surface and interface energy measurements are found in Table B.5 and B.6, and measurements on bulk materials and references for thermodynamic cycles can be found in Table B.7.

B.9 Electron Microscopy

Transmission Electron Microscopy

Imaging of nanocrystals was done on a FEI Technai T20 S-TWIN TEM operating at 200 kV with a LaB_6 filament. Ultrathin or holey carbon TEM grids were typically used to increase contrast in the images.

Sample	Mass ZnS QDs (mg)	ZnS Shell (mJ)	ZnS QDs (mJ)
InP/ZnS 493	-	1020±50	-
InP/ZnS 538	-	990±40	-
InP/ZnS 548	0.111±0.009	820±40	70±6
InP/ZnS 566	0.23±0.01	950±50	159±8
InP/ZnS 608	0.27±0.01	760±30	147±7

Table B.6: Extra calorimetry data for the core/shell nanocrystal samples. Samples are given labels based on the wavelength in nanometers of the first exciton peak in the absorption spectrum. For the three largest indium phosphide/zinc sulfide core/shell nanocrystal samples that had detectable zinc sulfide contamination, the calculated mass of the excess zinc sulfide material is reported.

Material	Mass (mg)	Enthalpy (mJ)	Enthalpy (kJ/mol)	Experimental ΔH_f (kJ/mol)	Reference ΔH_f (kJ/mol)	Reference
$In_{(s)}$	167.7±0.1	-248600	-170.2±0.2	-	-	-
$Zn_{(s)}$	42.1±0.1	-106300	-165.1±0.5	-	-	-
$Cd_{(s)}$	178.1±0.1	-200700	-126.6±0.1	-	-	-
$PH_{3(g)}$	-	-	-	-	5.47±0.4	[236]
$H_2S_{(g)}$	-	-	-	-	-20.6±0.5	[237]
$H_2O_{(l)}$	-	-	-	-	-285.83±0.04	[237]
$InP_{(s)}$	243.6±0.1	-143700	-86.0±0.1	-78.7±0.4	-69±3	[238]
$ZnS_{(s)}$	40.6±0.1	2100	5.0±0.4	-190.7±0.8	-207±4	[239]
$CdS_{(s)}$	75.4±0.1	400	0.8±0.3	-148.0±0.6	-148±4	[239]
$PbS_{(s)}$	37.2±0.1	-2800	-18±1	-	-98±4	[239]
$CdO_{(s)}$	62.3±0.1	-75600	-155.8±0.4	-256.6±0.5	-255.7±2	[240]
$Zn(OAc)_{2(s)}$	71.29±0.01	-17100	-43.9±0.4	-	-1078.6±0.1	[241]
$Cd(OAc)_{2(s)}$	20.22±0.01	-6400	-73±2	-1011±2	-	-
$Cd(OA)_{2(s)}$	6.47±0.01	-700	-70±20	-	-	-
$OAc^-_{(aq)}$	-	-	-	-	-486.01±0.1	[242]
$HOAc_{(aq)}$	-	-	-	-478.7±0.3	-	-

Table B.7: Calorimetry data for bulk materials measured and reference data used. The calculated error for the enthalpy measurements is 165 mJ.

Scanning Transmission Electron Microscopy

STEM imaging of the nanocrystals was performed on the FEI TitanX 60-300 microscope at the National Center for Electron Microscopy, Lawrence Berkeley National Laboratory. STEM was performed at 300 kV with a beam convergence semiangle of 10 mrad using a Fischione HAADF detector with an inner collection half angle of 36 mrad.

High-Angle Annular Dark-Field Scanning Transmission Electron Microscopy

Energy-dispersive X-ray spectroscopy imaging was done on a Zeiss LIBRA. Ultrathin carbon TEM grids were used to increase contrast in the images.

B.10 Sizing Image Analysis for Surface Energy Calculations

While some nanocrystal samples appeared fairly spherical, such as the zinc sulfide, cadmium sulfide, and lead sulfide nanoparticles (Appendix A), which made for easy sizing and calculation of the radius, surface area, and volume of the nanoparticles, some indium phosphide samples, some indium phosphide/zinc sulfide core/shell samples, and the cadmium oxide samples were less spherical (Appendix A). To accurately measure the surface area of all of these particles, regardless of how spherical they were, the projected areas were measured free hand. Using Cauchy's surface formula, it was assumed that the large number of nanoparticles measured were equivalent to random orientations of a convex, non-spherical object, and multiplying these areas by four gave an estimation of the surface area.[243] From this, a radius and volume was then estimated (see Table B.8). Although assumptions must be made, and not all of the nanocrystals were convex (some of the indium phosphide/zinc sulfide and cadmium oxide particles) based on the size distributions developed, the large number of particles analyzed, and the surface energy fitting, we conclude that this method is adequate. As the measurement of the enthalpy was done on an ensemble of particles, only the average molar surface area was important, and as nearly all size distributions appeared to follow a Gaussian distribution, the standard error in the average molar surface area is equal to the standard deviation of the molar surface area divided by the square root of the number of particles measured. However, for three of the indium phosphide/zinc sulfide core/shell nanocrystal samples and one of the cadmium oxide nanocrystal samples, the distribution was not Gaussian. In some of the core/shell samples it was evident that secondary nucleation of zinc sulfide had occurred, creating a second population of nanocrystals, and one sample of cadmium oxide had two populations. For the cadmium oxide samples, the actual molar surface area is relatively unimportant as the measured enthalpy does not significantly change with molar surface area, and so this was ignored. As can be seen from some of the sizing measurements of the indium phosphide/zinc sulfide core/shell samples, there

Sample	Count	Radius (nm)	Surface Area (nm^2)	Volume (nm^3)
InP 532	500	1.57 ± 0.01	31.8 ± 0.4	17.3 ± 0.3
InP 554	501	1.63 ± 0.008	33.9 ± 0.3	18.9 ± 0.3
InP 576	502	1.95 ± 0.01	49.1 ± 0.7	33.5 ± 0.7
InP 585	501	1.93 ± 0.01	47.6 ± 0.6	31.8 ± 0.6
InP 600	512	2.14 ± 0.01	58.2 ± 0.6	42.7 ± 0.7
InP 493	170	1.28 ± 0.01	21.0 ± 0.4	9.3 ± 0.3
InP 538	1087	1.656 ± 0.007	35.1 ± 0.3	20.1 ± 0.2
InP 548	215	1.68 ± 0.02	36.4 ± 0.7	21.3 ± 0.6
InP 566	1000	1.919 ± 0.008	47.1 ± 0.4	31.0 ± 0.3
InP 608	506	2.55 ± 0.02	83 ± 1	73 ± 1
InP/ZnS 493	518	2.21 ± 0.01	61.7 ± 0.5	46.3 ± 0.6
InP/ZnS 538	503	2.34 ± 0.01	70.2 ± 0.7	56.5 ± 0.9
InP/ZnS 548	504	2.59 ± 0.01	85.2 ± 0.8	75 ± 1
InP/ZnS 566	905	2.59 ± 0.01	85.6 ± 0.7	76 ± 1
InP/ZnS 608	504	3.15 ± 0.02	125 ± 1	134 ± 2
ZnS 253	500	1.094 ± 0.007	15.3 ± 0.2	5.8 ± 0.1
ZnS 266	505	1.156 ± 0.008	17.1 ± 0.2	6.9 ± 0.1
ZnS 274	510	1.244 ± 0.008	19.8 ± 0.2	8.6 ± 0.2
ZnS 275	500	1.211 ± 0.007	18.7 ± 0.2	7.8 ± 0.1
ZnS 282	834	1.312 ± 0.006	22.0 ± 0.2	9.9 ± 0.1
CdS 358	509	1.069 ± 0.007	14.7 ± 0.2	5.5 ± 0.1
CdS 363	295	1.15 ± 0.01	17.2 ± 0.3	7.0 ± 0.2
CdS 369	317	1.185 ± 0.009	18.0 ± 0.3	7.4 ± 0.2
CdS 384	373	1.330 ± 0.009	22.6 ± 0.3	10.3 ± 0.2
CdS 393	312	1.41 ± 0.01	25.4 ± 0.4	12.3 ± 0.3
PbS 787	500	1.394 ± 0.007	24.7 ± 0.2	11.8 ± 0.2
PbS 896	584	1.717 ± 0.007	37.4 ± 0.3	21.8 ± 0.2
PbS 1000	814	1.654 ± 0.006	34.8 ± 0.3	19.6 ± 0.2
PbS 1271	501	2.30 ± 0.01	67.4 ± 0.8	53.3 ± 0.9
PbS 1565	298	3.23 ± 0.03	133 ± 2	149 ± 3
CdO 2.00:1	457	4.14 ± 0.03	220 ± 3	316 ± 6
CdO 1.00:1	208	4.24 ± 0.04	230 ± 4	335 ± 9
CdO 0.75:1	221	6.43 ± 0.06	530 ± 10	1180 ± 30
CdO 0.50:1	394	9.53 ± 0.05	1150 ± 10	3740 ± 60
CdO 0.25:1	175	18.8 ± 0.2	4500 ± 100	30000 ± 1000

Table B.8: Size characterization of samples used in dissolution calorimetry experiments. Samples are given labels based on the wavelength in nanometers of the first exciton peak in the absorption spectrum except in the case of cadmium oxide nanocrystals, and instead the ratio of bis(trimethylsilyl)amine to cadmium acetylacetonate is used. Count refers to the number of nanocrystals whose area was measured.

was some contamination of zinc sulfide nanocrystals in three of the indium phosphide/zinc sulfide core/shell nanocrystal samples. However, as the enthalpy of zinc sulfide nanocrystals synthesized in a similar fashion as a function of size was previously computed, it was relatively simple to correct for this heat effect. Using the molar masses estimated for the size series of zinc sulfide and indium phosphide, the mass fraction of the zinc sulfide nanocrystals was calculated and based on the size and surface area the heat of the dissolution of these nanocrystals was subtracted from the total measurement, which resulted in a small number (see Table B.6).

B.11 CHNS Elemental Analysis

Elemental analysis was performed by a Perkin Elmer 2400 Series II combustion analyzer. A few milligrams of dried sample is weighed and then combusted in oxygen, yielding carbon dioxide, water, nitrogen, and sulfur dioxide. This gas is passed through a chromatogram, and the percent mass of each element is calculated. Elemental analysis data for the samples used in the surface and interface energy measurements is found in Table B.9.

B.12 Other Ligand Exchanges

Hydrofluoric Acid

Treatment with hydrofluoric acid was adapted from the procedure by Kim *et al.*[22] A stock solution of myristic acid capped quantum dots not prepared with a hydrogen atmosphere was diluted to 15 mL in hexanes to make a 20 μM solution. In a Teflon vessel, this solution was added with 15 mL of dimethyl sulfoxide and 52 μL of hydrofluoric acid. The vessel was sealed with a Teflon cap and a steel pressure vessel and shaken thoroughly for 1 minute. The vessel was then placed in a boiling water bath for 30 minutes, after which it was allowed to sit to cool to room temperature. The vessel was opened, and the contents transferred to a separatory funnel where the solution separated into two layers, a reddish layer on the bottom and a relatively clear layer on top. Additionally, a red mass formed at the interface of the two layers, which was attributed to be myristic acid contaminated with residual indium phosphide quantum dots. The lowest layer was drained and saved while the upper layer was discarded. The lower layer was placed back into the separatory funnel and 15 mL of hexanes was added. The funnel was capped and shaken, and the layers were allowed to separate. After this the process of washing with hexanes was repeated an additional four times.

Oleylamine

For the exchange, 1 mL of the stock solution of indium phosphide quantum dots capped with stearic acid synthesized in absence of a hydrogen atmosphere was treated with 20 µL of oleylamine that had been degassed at 90 °C for one hour. The quantum dots were then

Sample	C%	H%	N%	S%
InP 532	39.75	5.83	-	-
InP 554	34.92	5.38	-	-
InP 576	38.27	5.82	-	-
InP 585	33.93	5.03	-	-
InP 600	35.26	5.36	-	-
InP/ZnS 493	29.04	4.42	-	11.20
InP/ZnS 538	29.36	4.46	-	8.85
InP/ZnS 548	33.52	4.98	-	8.11
InP/ZnS 566	27.22	4.24	-	10.59
InP/ZnS 608	24.87	3.71	-	13.04
ZnS 253	52.46	8.15	-	6.77
ZnS 266	49.04	7.56	-	8.32
ZnS 274	48.96	7.57	-	9.09
ZnS 275	47.06	7.30	-	9.23
ZnS 282	43.02	6.64	-	11.02
CdS 358	47.64	7.30	-	5.12
CdS 363	47.63	7.38	-	5.48
CdS 369	46.36	7.07	-	5.67
CdS 384	44.26	6.76	-	6.35
CdS 393	42.34	6.54	-	6.98
PbS 787	32.35	4.96	-	5.11
PbS 896	29.77	4.56	-	5.84
PbS 1000	28.22	4.33	-	6.29
PbS 1271	22.78	3.60	-	7.66
PbS 1565	15.30	2.44	-	9.42
CdO 2.00:1	14.28	2.08	-	-
CdO 1.00:1	11.60	1.83	-	-
CdO 0.75:1	6.61	0.97	-	-
CdO 0.50:1	8.36	1.23	-	-
CdO 0.25:1	4.41	0.65	-	-

Table B.9: Elemental analysis of samples used in dissolution calorimetry experiments. Samples are given labels based on the wavelength in nanometers of the first exciton peak in the absorption spectrum except in the case of cadmium oxide nanocrystals, and instead the ratio of bis(trimethylsilyl)amine to cadmium acetylacetonate is used. Count refers to the number of nanocrystals whose area was measured. The results of the CHNS elemental analysis for each element is reported, with an assumed error of 0.3%. Note that the indium phosphide samples for shelling with zinc sulfide were not measured by CHNS elemental analysis.

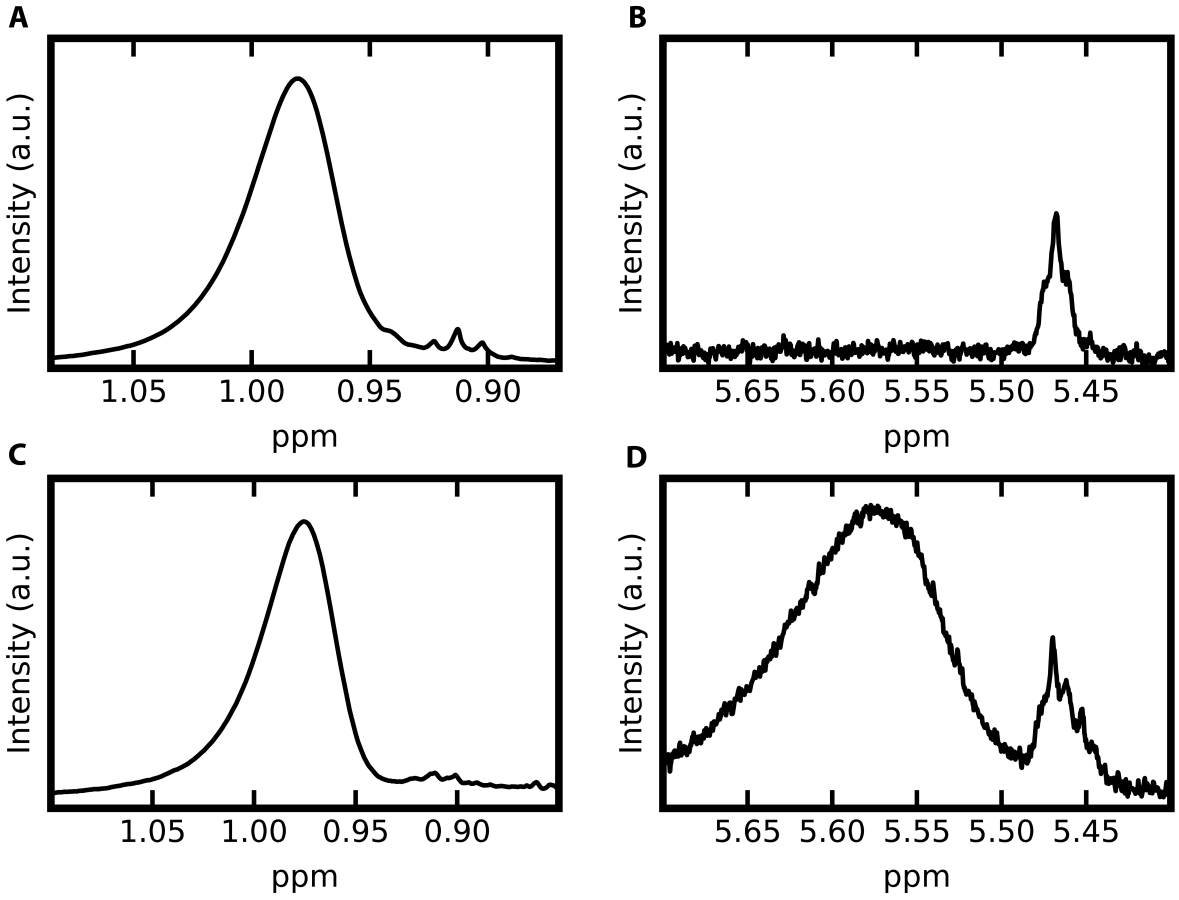


Figure B.4: ^{1}H NMR of indium phosphide quantum dots treated with oleylamine, taken in toluene-d_8. (A) Methyl peak showing little unbound ligand for native stearate capped indium phosphide quantum dots. (B) Vinyl peak region showing an impurity in the ^{1}H NMR spectra. (C) Methyl peak showing little unbound ligand for stearate capped indium phosphide quantum dots with 10% oleylamine exchanged. (D) Vinyl peak region showing bound oleylamine peak.

precipitated with 3 mL of acetone, and then resuspended in 1 mL of hexanes. An additional 20 µL of oleylamine was added and then the washing process was repeated 3 more times without the addition of any more oleylamine.

^{1}H NMR measurements of indium phosphide quantum dots capped with stearate ($C_{18}H_{35}O_2$) before and after they were washed with oleylamine ($C_{18}H_{37}N$) give insight to the extent of the ligand exchange (Figure B.4). The integrations of the areas beneath the peaks with the oleylamine exchange indicate that approximately 10% of the total ligand coverage is oleylamines, or bent ligands. This agrees nicely with the results by Balan *et al.*, which indicate that the phase transition between the more ordered and less ordered phase of ligands should be below room temperature for a 10% bent ligand shell, while for 100% straight ligand shell this transition should occur above room temperature.[42]

Appendix C

On the Use of Nanocrystal Size and Extinction Coefficient Calculators

C.1 Size and Extinction Coefficient Calculation Background

When working with colloidal nanocrystals, it is essential to know the size of the nanocrystals and the concentration of nanocrystals in a given solution for many applications. Unfortunately, these simple properties of a solution of nanocrystals are less straightforward than they initially would appear to be, as evidenced by the wide range of literature disputing methods of calculating them.[52,244–248] Perhaps the best method is take take a transmission electron microscope (TEM) image of the nanocrystals to calculate the size of the nanocrystals (for which there is invariable a size distribution rather than a uniform size), and then using quantitative inductively coupled plasma optical emission spectroscopy (ICP-OES) to determine the concentration of metal ions in a solution, and from the size measurements (with the density of the nanocrystal) it is possible to calculate the concentration of nanocrystals in solution. However, beyond the enormous amount of work this method is to calculate these properties for a single sample, there are significant errors with this method.

First, TEM imaging is not a trivial undertaking. Alignment of the TEM and proper calibration is crucial, and many images of particles should be taken. Unfortunately it is surprisingly easy to get a non-representative image of a sample (hopefully unintentionally rather than intentionally), and people have spent significant time attempting to create automated image acquisition and analysis of hundreds of particles to alleviate this problem.[249] Further, when working with small nanocrystals, particularly of those with low contrast such as indium phosphide, it can be difficult to determine the edges of the nanocrystal and the size might be calculated to be smaller than it is in actuality (due to lower density of atoms at the edges of a spherical particle). An excellent paper by Jasieniak *et al.* suggest that this error could be around 0.17 nm for cadmium selenide, and also discusses many of the other difficulties with determining sizing and extinction coefficients in nanocrystals.[244] Further, as

much as it is convenient to discuss particles as spheres, they are not perfect spheres. While some particles have better faceting than others,[29,32,36,81,182] and many particles can be approximated as spheres, this assumption is not strictly true, so defining a diameter or a radius also includes some ambiguity.

Beyond TEM imaging, ICP-OES is more straightforward in terms of measurement, but the interpretation and use of the data is still challenging in terms of calculating a concentration of nanoparticles, particularly when the nanocrystals are no longer stoichiometric. For II-VI and III-V quantum dots, such as cadmium chalcogenides and indium pnictides, they are often capped with ligands such as carboxylates (or, viewed differently, metal carboxylates) and thus the metal ion is in greater concentration than the chalcogenide or pnictide.[122] However, the spacing between atoms in a nanocrystal remain the same as bulk crystals,[250,251] and thus the density of the nanocrystal as a whole will be greater than that of the bulk material, assuming the metal ion is more massive than the chalconide or pnictide. This can potentially cause error in the determination of the mass of the nanocrystal from the volume calculated by TEM if the non-stoichiometry is not taken into account.[244] Additionally, samples must be significantly purified of excess ligand that is universally present in the crude synthesis of nanoparticles, as well as other byproducts,[233,246] else the mass calculations will be inaccurate, and if ligands such as metal carboxylates are present, the metal ion concentration will be artificially inflated.[156,244,246]

Due to these difficulties, for quantum dots, the most common method used is simply take an absorption spectrum of the nanocrystals and use a size and extinction coefficient calculator to determine the size and concentration of the nanocrystals. These calculators have been provided in the literature *ad nauseam*.[51,52,99,132,165,244–248,252–254] While it may seem that this wealth of data would be welcome, disagreement between the calculators are often significant[244–246,255] and it can become difficult to determine which should be used.

Herein lies a discussion and justification on indium phosphide size calculators and cadmium sulfide concentration calculators used which proved to be the most relevant for the work discussed.

C.2 Indium Phosphide Size Calculators

One of the most commonly used size calculators for indium phosphide is the one provided by Reiss *et al.*[99] In this review paper, size calculators are provided for cadmium sulfide, cadmium selenide, and cadmium telluride from data reported by Yu *et al.*,[51] and a size calculator for indium phosphide is provided referencing Dr. Dmitri V. Talapin's Ph.D. dissertation.[232] The indium phosphide sizing calculator is given as

$$D = (-3.7707 \times 10^{-12})\,\lambda^5 + (1.0262 \times 10^{-8})\,\lambda^4 - (1.0781 \times 10^{-5})\,\lambda^3 + (5.4550 \times 10^{-3})\,\lambda^2 - (1.3122)\lambda + 119.9$$

where D is the diameter of the nanocrystal and λ is the wavelength of the first exciton peak in nanometers, while the equation for the molar extinction coefficient is given as

$$\varepsilon = 3046.1(D)^3 - 76532(D)^2 + \left(5.5137 \times 10^5\right)(D) - \left(8.9839 \times 10^5\right)$$

where ε is the molar extinction coefficient. However, these equations are not found in Dr. Talapin's Ph.D. dissertation. Rather, there are two plots containing the molar extinction coefficient as a function of the wavelength of the first exciton peak and as a function of nanocrystal size.[232] A similar plot can be found in the data reported by Adam *et al.*,[83] and these values also appear to be reported by Talapin *et al.*[231] By extracting the data from these plots, a sizing curve can be constructed, but this does not match the sizing curve given by Reiss *et al.*[99] (Figure C.1).

From examining the reported data from multiple sources, including those extracted from this work (Appendix A.2), it is evident that there are large discrepancies in the reported data, sometimes by nearly doubling the nanocrystal size based on the wavelength. For this reason, selection of an appropriate sizing curve is a nontrivial task. As has been observed (Chapter 2), the ligands on the surface of the nanocrystal can shift the first exciton peak absorption wavelength, but likely only by a few nanometers. Additionally, not all sizing data also provide extinction coefficient data (Cho *et al.*,[254] Mićić *et al.*,[256] Guzelian *et al.*[257]), leaving fewer options. The calculator provided by Ministro[132] seemed to be the superior calculator as it was the most consistent with the compiled data (including size determination in this work), myristate was used as the capping ligand, it has been supported by other theoretical work,[248] and as it had both concentration and sizing information. The size calculator is

$$E_g = 1.35 + \frac{1}{(0.119 \pm 0.003)D^2}$$

where E_g is the energy of the first exciton peak absorption in eV, and D is the diameter of the quantum dots. The accompanying extinction coefficient calculated used was

$$\varepsilon_{410} = (1.29 \pm 0.06) \times 10^4 D^3$$

where ε_{410} is the extinction coefficient at 410 nm.

Unfortunately, the initial studies on the metal halide treatments with indium phosphide (Chapter 3) and the ligand length dependence of inter-ligand interactions (Chapter 4) used the calculator by Reiss *et al.*[99] as this discrepancy had not been detected before publication. As the work on the size of the nanocrystal influencing inter-ligand interactions (Chapter 4) and the surface and interface energy measurements (Chapter 6) had not been published, these studies used the calculator provided by Ministro.[132] Significant debate occurred regarding whether the analysis of the older works should be retroactively corrected for publication of this dissertation, which this author believes would be more correct but may lead to confusion as data presented would be different. As the XRD diffraction work only used the size in only one figure (Chapter 5) and the exact size was not a critical component (rather it was more of an empirical trend), this figure was corrected to reflect the preferred calculator. As a compromise for the other published work, the data from the original metal halide work was reanalyzed for the reaction of indium phosphide with zinc chloride. The Ising models was

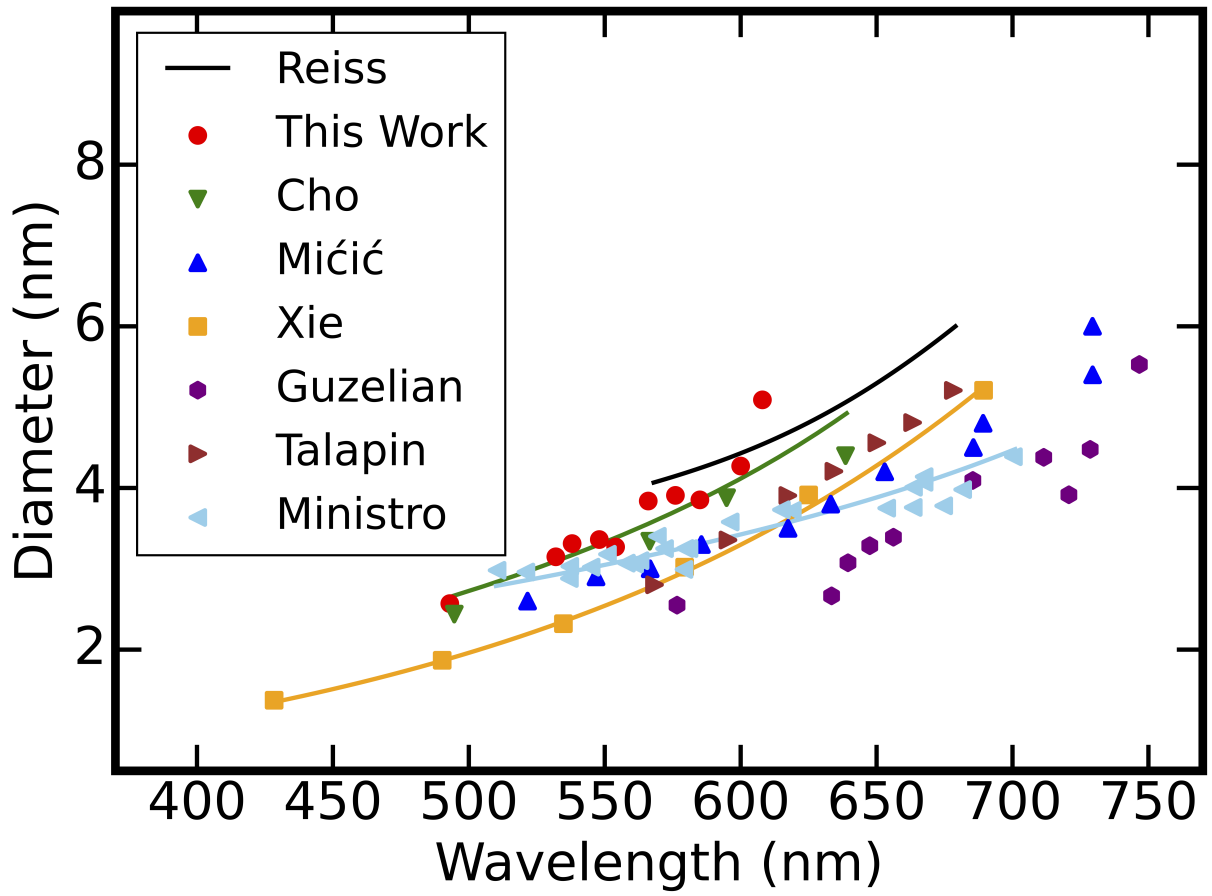


Figure C.1: Indium phosphide sizing data. The data points represent reported experimentally determined sizes by transmission electron microscope (TEM) or scanning tunneling electron microscope (STEM) imaging as a function of wavelength of the first exciton peak. Data reported by Cho *et al.*,[254] Xie *et al.*,[252] and Ministro[132] also provide fit equations for the data, while data sets extracted from Mićić *et al.*,[256] Guzelian *et al.*,[257] and Talapin[232] do not provide fit equations. The fit line provided by Reiss is also given.[99] Due to the nature of the empirical curve fitting, curves are not extrapolated past the experimentally provided data sets.

	ΔH_{head}	$\Delta H_{tail}AB$	$\Delta H_{tail}BB$	$T\Delta S_{head}$	$T\Delta S_{tail}AB$	$T\Delta S_{tail}BB$
Reiss *et al.*[99]	-40.18	13.06	22.78	-25.86	8.90	7.39
Ministro[132]	-40.46	13.81	22.76	-25.83	9.47	6.72

Table C.1: Comparison of Ising model parameters for different nanocrystal calculators. Energies given in kJ/mol.

the most critical thing that would change, although ligand coverages were also found to be fairly different although variable across syntheses (Chapter 4), and thus the difference in parameters of the Ising model using both calculators is given in Table C.1, and it is observed the the parameters are not strongly significantly different, so the original published work was not changed for this dissertation. Additionally, the calculated ligand coverage for the indium phosphide quantum dots used in Chapter 3 with the calculator from Reiss *et al.* was found to be 4.1 ± 1.1 indium myristates/nm^2, while the calculated ligand coverage from the same data using the calculator by Ministro was found to be 3.3 ± 1.0, so at least from an error standpoint these measurements agree with each other.

C.3 Cadmium Sulfide Concentration Calculators

Regarding the molar extinction coefficient of cadmium sulfide nanocrystals, there is some ambiguity in the exact value. Several concentration calculation curves have previously been published by Yu *et al.*,[51] Hamachi *et al.*,[245] and Li *et al.*[246] that yield different results, and it is difficult to know which is most accurate, particularly as there are significant discrepancies in the published works. For example, raw data published by Hamachi *et al.*[245] in the supplemental information did not match their initially published concentration calculation curve or the data presented graphically in the main text, however, a subsequent correction to the raw data does align with the presentation in the main text although no indication for why the original data was incorrect was given. However, it appears that the data may not be significantly different from each other, although with such few data points used the extinction coefficient fit varies significantly. Additionally, Hamachi *et al.*[245] assumed that 100% of the thiourea was converted to cadmium sulfide nanocrystals during synthesis to calculate their extinction coefficient, but if this conversion was less than 100%, more cadmium sulfide nanocrystals would be assumed than truly present. In the work by Li *et al.*,[246] rather than the absorption value at the first exciton peak, the integrated half peak area of the first exciton peak is used to account for differences in size distributions in the concentration calculator, making the comparison between the different concentration calculator curves difficult. However, presented data in the supplemental for the extinction coefficient as a function of wavelength was published, and these data points were converted to a function of size using their published size calculator. Unfortunately, from our absorption measurement of our particles (Chapter 3) and using the sizing calculator presented in Li *et al.*,[246] we

calculate a predicted diameter of 2.8 nm for particles whose first exciton peak corresponds to 428 nm, but this value is different from the ones previously predicted by Yu *et al.*[51] of 4.4 nm and similar previously measured values,[51,245] as well as TEM measurements of the particles synthesized in this work (Appendix A.3), which were measured to be on average 4.3 nm with a sample size of 47 particles. Due to this discrepancy, we chose not to use this concentration calculator. A complilation of data for calculating the extinction coefficient of cadmium sulfide nanocrystals can be found in Figure C.2.

Due to this significant uncertainty and comparing the different published results, we opted to use the sizing and concentration calculator determined by Yu *et al.*,[51] as we did not notice any significant errors in the presented data and the authors used many data points (eighteen) in determining the concentration curve rather than the five in the report by Hamachi *et al.*[245] The sizing correlation function is given as

$$D = (-6.6521 \times 10^{-8})\lambda^3 + (1.9557 \times 10^{-4})\lambda^2 - (9.2352 \times 10^{-2})\lambda + 13.29$$

where D is the diameter of the nanocrsytals and λ is the wavelength of the first exciton peak. The extinction coefficient calculator is given as

$$\varepsilon = 21536(D)^{2.3}$$

where ε is the extinction coefficient at the first exciton peak. However, we would like to emphasize once again the inherent uncertainty in the concentration of nanocrystal solutions, particularly with smaller quantum dots, and this uncertainty (10%) has been carried through in the calculations of the data in the main text.

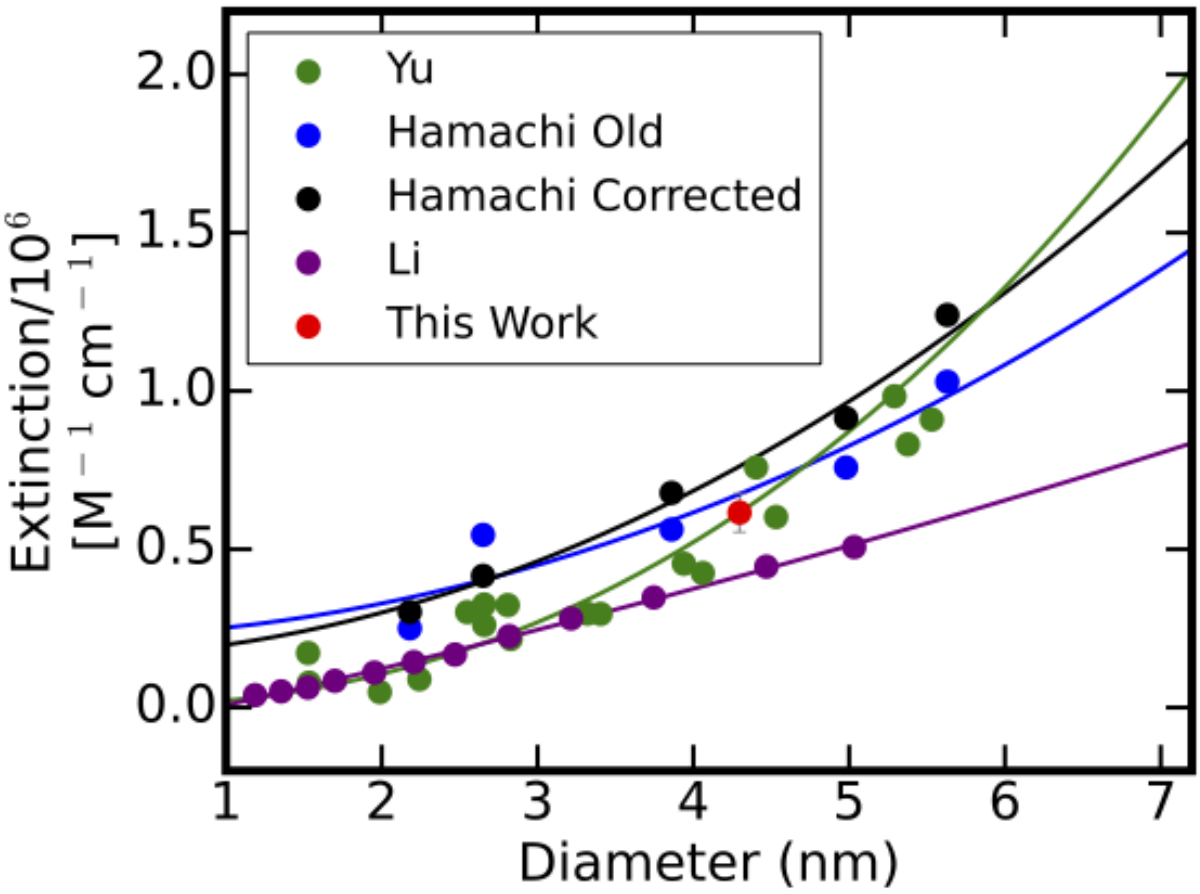


Figure C.2: Cadmium sulfide extinction coefficient data. This data was published by Yu *et al.*,[51] Hamachi *et al.*,[245] and Li *et al.*[246] and and included are the extinction coefficient curves published by Yu *et al.*,[51] Hamachi *et al.*,[245] and Li *et al.*[246] Additionally, the calculated extinction coefficient of the cadmium sulfide nanocrystals with a 10% error as presented in this work (Chapters 3 and 4) is included. Note that the original and corrected raw datasets published by Hamachi *et al.*[245] are included with similarly calculated fits, and that the concentration curve from Li *et al.*[246] were manipulated from data presented in the supplemental information with their published sizing calculator to be in the same format as the other data.

Appendix D

Theoretical and Computational Chemistry Methods

Reproduced in part with permission from Calvin, J. C.; Swabeck J. K.; Sedlak, A. B.; Kim, Y.; Jang, E.; Alivisatos, A. P. "Thermodynamic Investigation of Increased Luminescence in Indium Phosphide Quantum Dots by Treatment with Metal Halide Salts" *J. Am. Chem. Soc.* **2020**, *142*(44), 18897–18906. Copyright 2020 American Chemical Society.[71]

Reproduced in part with permission from Calvin, J. C.; O'Brien, E. A.; Sedlak, A. B.; Balan, A. D.; Alivisatos, A. P. "Thermodynamics of Composition Dependent Ligand Exchange on the Surfaces of Colloidal Indium Phosphide Quantum Dots" *ACS Nano* **2021**, *15*(1), 1407–1420. Copyright 2021 American Chemical Society.[121]

Reproduced in part with permission from Calvin, J. C.; Kaufman, T. M.; Sedlak, A. B.; Crook, M. F.; Alivisatos, A. P. "Observation of Ordered Organic Capping Ligands on Semiconducting Quantum Dots via Powder X-ray Diffraction" *Nat. Commun.* **2021**, *12*, 2663 under a Creative Commons license CC BY 4.0.[135]

D.1 Ising Model Simulations

Metal Halide Ligand Exchange

To simulate the ^{1}H NMR and isothermal titration calorimetry results, a modified Ising model was used.[10] For this model, the initial conditions were set so that every grid point was given an organic ligand designation, in a square or rectangular grid such that the number of sites was close to the number of sites determined by ^{1}H NMR, with a given number of organic ligands being designated as free also determined by the experimental ^{1}H NMR results. Periodic boundary conditions ensured that each lattice point had four nearest neighbors. Some amount of inorganic ligand was introduced to the system (e.g., 100 inorganic ligands),

and a random point on the grid was selected. After the point was selected, the ligand that the attempted exchange would occur with was selected randomly from the pool of free ligands. For a ligand exchange, the difference in ΔG was calculated as

$$\Delta G = \Delta H_{\text{head}} + \Delta H_{\text{tail}} + \Delta H_{\text{PT}} - T\Delta S_{\text{head}} - T\Delta S_{\text{tail}} - T\Delta S_{\text{PT}}$$

where ΔH_{head} was the difference in binding energy for the head group, ΔH_{tail} was the difference in nearest-neighbor interactions, $T\Delta S_{\text{head}}$ was the entropy gain from the organic ligand becoming free in solution, and $T\Delta S_{\text{tail}}$ was the difference in nearest-neighbor ordering. For the metal halide exchange with stearate capped indium phosphide nanocrystals, the phase transitions terms (ΔH_{PT} and $T\Delta S_{\text{PT}}$) were also included. The probability of a ligand exchange was given by

$$P = \mathrm{e}^{-\Delta G/k_{\text{B}}T}$$

if ΔG was positive. If ΔG was negative, the exchange was accepted. If the ligand at the grid point was identical with the attempted exchange (e.g., ΔG was zero), there was no change to the grid for that attempt. For each simulation, 10,000 ligand exchanges were attempted to simulate the system being at thermal equilibrium, and for each amount of inorganic ligand the simulation was run 100,000 times. After the simulation was run, the total enthalpy change was computed for the grid and then averaged across all grids run with the same amount of inorganic ligand. Next, the change in enthalpy between subsequent groups of grids was computed (e.g., the enthalpy change between the average of grids having 110 inorganic ligands and 100 inorganic ligands) to mimic isothermal titration calorimetry titrations. These enthalpy changes were then divided by the difference in amounts of inorganic ligands to compute the enthalpy measured in kJ/mol and plotted as a function of inorganic ligands/nanocrystal. The fraction of unbound organic ligand was found similarly, where the fraction of free organic ligands after the simulation was averaged across the 100000 runs.

Cadmium Oleate Ligand Addition

A modified Ising model simulation was used to fit thermodynamic parameters of the ligand addition. A 15x14 grid of lattice sites was used to represent the nanocrystal surface for a total of 210 lattice sites, similar to the maximum cadmium oleate ligand density calculated from ^{1}H NMR measurements of 211 $\pm$ 21 per quantum dot for the cadmium sulfide nanocrystals. Periodic boundary conditions ensured that each lattice point had four nearest neighbors. At the beginning of the simulation, each lattice point was designated to be empty, and a certain number of ligands was introduced to the system free pool, representing ligands free in solution. As the exchange continued, the concentration of free ligands decreased, and this was represented by replacing ligands in the free pool with empty values. A Monte Carlo algorithm was used to randomly select a lattice site on the grid and a random ligand from the free pool, and the Gibbs free energy of the addition (or removal) of the ligand was calculated. If a site on the nanocrystal was selected and the ligand from the free pool was

the same designation, no exchange occurred. If these values were different, the change in Gibbs free energy was computed by the following equation:

$$\Delta G = \Delta H_{\text{head}} + \Delta H_{\text{tail}} - T\Delta S_{\text{head}} - T\Delta S_{\text{tail}}$$

The values for ΔH_{head} and $T\Delta S_{\text{head}}$ are the change in the enthalpy and entropy for adsorption or removing a ligand, while the values of ΔH_{tail} and $T\Delta S_{\text{tail}}$ were computed from the local environment of four nearest neighbors and represent the inter-ligand interaction enthalpy and entropy. The probability of the ligand exchange happening is given by:

$$P = \mathrm{e}^{-\Delta G/k_{\mathrm{B}}T}$$

and after the exchange occurs or is rejected, another site is selected. Each nanocrystal surface was iterated over 10,000 times to simulate thermal equilibrium with a given number of ligands. At this point, the change in the enthalpy and Gibbs free energy of the surface with respect to the empty lattice was calculated, as well as the total number of adsorbed ligands. These calculations were then averaged 100,000 times for a given number of exchange ligands. To simulate the isothermal titration calorimetry data, the change in enthalpy between a given number of exchange ligands was calculated and plotted. The values for the thermodynamic parameters were optimized to match the observed isothermal titration calorimetry and ^{1}H NMR data.

Carboxylic Acid Exchanges

To model the surface of the nanocrystals to gain insight from the ^{1}H NMR and isothermal titration calorimetry measurements, a modified Ising simulation was used. For this simulation, a 20x20 grid was used with periodic boundary conditions to represent the surface of the nanocrystal, and for the simulations for the palmitate and myristate, each grid point was given the designation of having a straight-chain ligand bound to the surface. To simulate the lower ligand coverage for the quantum dots capped with stearate, 120 empty sites were randomly distributed to the grid, with the remaining sites designated as having a stearate bound to them. To match the NMR results, free straight-chain ligands were also added to the initial pool of free ligands and represent the bound/free equilibrium between indium carboxylates in solution and on the surface of the quantum dots. This number of initial free ligands was determined by the concentration of free ligands from the methyl peak of the ^{1}H NMR before any exchange ligands had been added. Because empty binding sites on the native stearate surface are filled via X-type binding, the number of free ligands was not allowed to drop below this minimum for the stearate simulation. For each simulation, a certain number of exchange ligands were introduced to the system (e.g. 100 free oleate ligands). Using a Monte Carlo algorithm, a random spot on the grid was selected as well as a random ligand from the pool of free ligands, accounting for back reactions as a straight-chain ligand could be selected. If the grid point selected and the free ligand selected had the same ligand, no reaction occurs. The Gibbs free energy change for the ligand exchange is given by

$$\Delta G = \Delta H_{\text{head}} + \Delta H_{\text{tail}} - T\Delta S_{\text{head}} - T\Delta S_{\text{tail}}$$

where ΔH_{head} is the difference in binding energies of the head groups, ΔH_{tail} is the difference in van der Waals interactions between the ligands, $T\Delta S_{\text{head}}$ is the difference in entropy of the head groups, and $T\Delta S_{\text{tail}}$ is the difference entropy caused by interactions between nearest neighbor ligands. The probability of the ligand exchange happening is given by

$$P = e^{-\Delta G/k_B T}$$

and the surface is iterated over 10,000 times to simulate the reaction being at equilibrium. After the surface is at equilibrium, the fraction of unbound ligands was calculated as well as the net change in energy from the natively passivated surface, and this process was averaged 100,000 times for a given number of exchange ligands. To simulate the data obtained from isothermal titration calorimetry, the difference in energy of averaged simulations for a given number of initial ligands was calculated and plotted to mimic titration measurements.

D.2 Restriction of Internal Rotations of Aliphatic Chains

From the Ising model simulations, it was evident that a entropic inter-ligand tail interaction was needed to effectively fit the model. The initial justification for this was that if the ligands on the surface were packed tightly then they would likely lose some entropy due to their motion being restricted. To test this hypothesis, structures were built in Gaussian 16. To simulate the close packing of ligands on a nanocrystal surface, a lattice of indium atoms was created and fixed in place. Three myristate ligands were bound to each indium atom, and the indium myristate structures were brought as close as possible together without overlapping bonds or atoms; then, the myristate ligands were placed parallel to each other.

Using Maestro, the indium myristate clusters were subjected to a conformational search using universal force field (UFF) while fixing the positions of the indium atoms. After the potential energy of the structure had been optimized to a minimum, the structure was imported back into Gaussian 16 for calculations. For the free ligand structure, the structure was optimized using the ωB97XD DFT method with def2-SVPP basis sets for the aliphatic carbons and hydrogens, def2-SVPD basis set for the carbons and oxygens in the carboxylate, and the def2-TZVP basis set with an effective core potential for the indium. For the clustered indium myristate, the indium atoms were fixed in place as well as all of the myristates except the central indium myristate structure (see Figure D.1 for images of structures). The structure of the central myristate was optimized using the same method and basis sets. From the optimized structures, the entropy of the structures was calculated by DFT vibrational analysis.

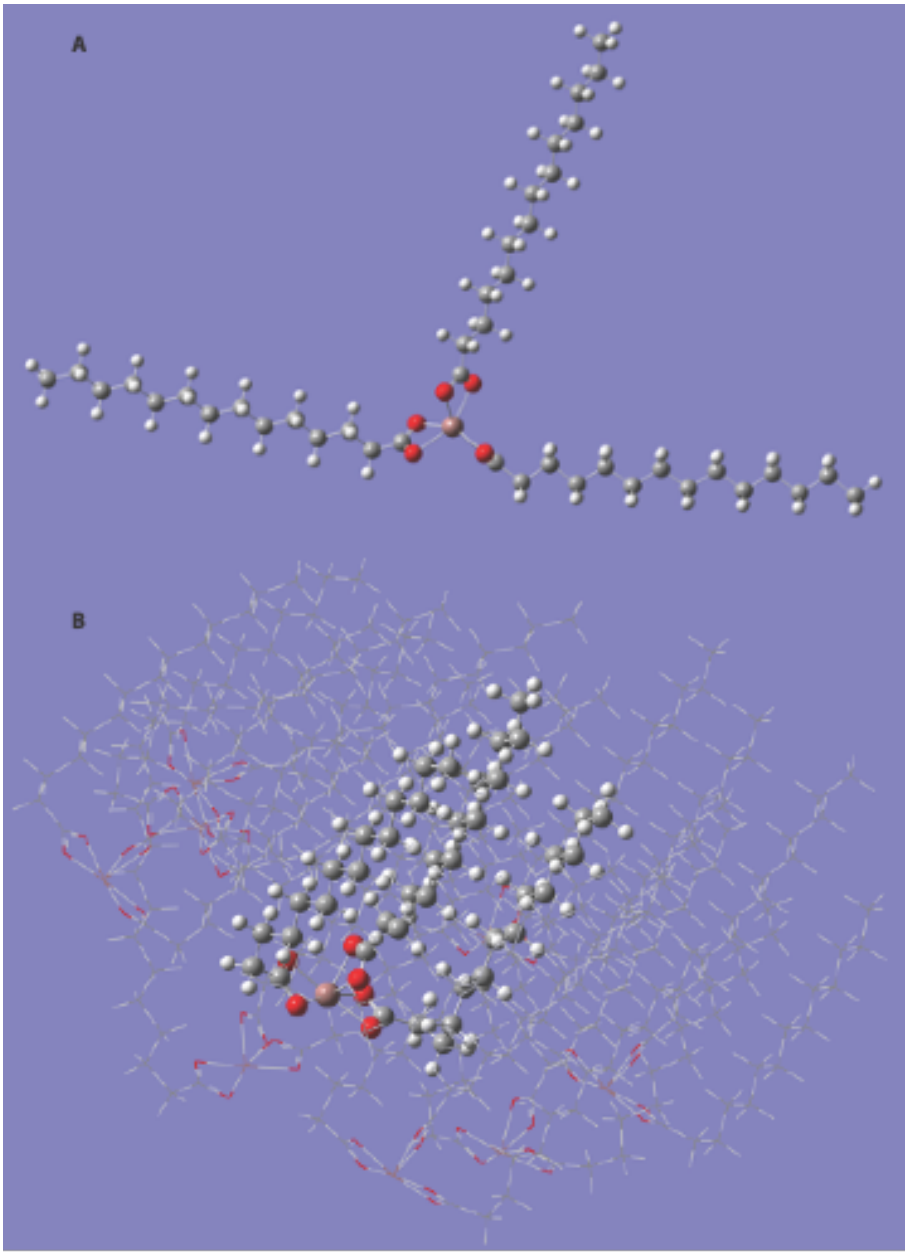


Figure D.1: Gaussian 16 images of indium myristate. (A) Free indium myristate and (B) constrained indium myristate.

D.3 Powder X-ray Diffraction Simulations

To test the hypothesis that the observed peak around 1.4 Å^{-1} in the powder X-ray diffraction data of the indium phosphide nanocrystals could be attributed to ordered ligands on the surface of the quantum dots, models of indium phosphide nanocrystals were built and their powder X-ray diffraction patterns simulated. First, the crystal structure of indium phosphide was downloaded (Crystallographic Information File, or CIF) from the Cambridge Crystallographic Data Centre (CCDC), although the Materials Project Database (MPD) was typically used to find the Inorganic Crystal Structure Database (ICSD) identification number. As a side note, the CIF can be directly downloaded from MPD quite easily, but this structure is *wrong*. It is wrong because the crystal structure is computed using DFT, but due to limitations with DFT, it does not accurately calculate the bond lengths, and while qualitatively the structure is correct, this inaccuracy will lead to a significant shift in the X-ray diffraction pattern.

This CIF file can be opened in a program like Visualization for Electronic and Structural Analysis (VESTA), and using boundary restrictions with cutoff planes for crystal indices, nanocrystals with faceted structures can be created of various sizes. For ease, tetrahedrons of indium phosphide were made, although from TEM and STEM images (Appendix A.2) they are obviously not perfect tetrahedrons. Once the structure was created, it was imported into Gaussian 16 where myristate ($C_{14}H_{27}O_2$) ligands could be arranged on its surface at a density of 8 myristates/nm^2 where the chains were straight and the ligands evenly spaced. This density of ligands created a peak around 1.4 Å^{-1}, and it had reasonable good agreement with the previously determined ligand coverage of 12.3 ± 3.3 myristates/nm^2 from ^{1}H NMR measurements in conjunction with sizing and extinction coefficient calculators. Of course, it was later determined that the sizing and extinction coefficient calculator used[99] was grossly incorrect (Appendix C.2), and it was rather found that the ligand coverage was closer to 9.9 ± 3.5 myristates/nm^2 using the the extinction coefficient and sizing calculator provided by Ministro,[132] and fortunately this makes the density of ligands that used for the X-ray diffraction simulations appear more reasonable.

Once this structure was made, it was saved as an XYZ type file and run in the Python program DebyeByPy written by Trigg and available on GitHub.[258] From there the structure could be modified and the impacts observed on the X-ray diffraction pattern. Intensities (I) as a function of the scattering length vector (q) in units of Å^{-1} were calculated using the Debye formula

$$I(q) = \sum_{\mathrm{i}} \sum_{\mathrm{j}} f_{\mathrm{i}}(q) f_{\mathrm{j}}(q) \frac{\sin\left(q r_{\mathrm{ij}}\right)}{q r_{\mathrm{ij}}}$$

where the sums are over all of the atoms, f is the angle-dependent scattering factor calculated by Hartree-Fock wavefunctions by Cromer and Mann, and r is the distance between atoms in Å.[142,250] The scattering length vector was converted to 2θ using the formula

$$2\theta = 2\arcsin\left(\frac{q\lambda}{4\pi}\right)$$

where λ is the wavelength of incident X-rays (1.541 Å) for plotting against experimental data. One note about the program is that the computational time scales exponentially with the number of atoms in the structure, as with each atom added the sum must contain N (where N was the original number of atoms) more terms, so larger structures will take considerably more time. Attempts were made to simulate powder X-ray diffraction patterns of larger nanocrystals as part of a project centered around determining shape distributions using X-ray diffraction simulations that was ultimately abandoned, and this was successfully done in a reasonable time frame by using a different program.[259]

D.4 Molecular Dynamics Simulations of Aliphatic Chains

Closely related to the powder X-ray diffraction simulations were the molecular dynamics simulations of the organic ligand shell. When the ligands were originally placed on the surface, they were perfectly ordered with uniform density. The molecular dynamics simulations attempted to determine if a more physically realistic system would also result in a simulated X-ray diffraction peak around 1.4 $Å^{-1}$. The structure was imported into Maestro using Desmond. Unfortunately, molecular dynamics simulations on the entire structure were unsuccessful, and this was attributed to the indium atoms and possibly the phosphorus atoms in the structure. The next attempt was to remove these atoms and lock the oxygen atoms in place and run molecular dynamics simulations, but this was also unsuccessful, attributed to the proximity of the oxygen atoms to each other and the unbalanced charges. The final and successful attempt involved removing all of the oxygens and replacing the carboxylate group with a methyl group, and then fixing those terminal carbon atoms in place. Under these conditions the molecular dynamics simulations could run, albeit only at certain temperatures, reasons for this being unknown.

Structures were prepared via the System Builder using the OPLS2005 force field. For the simulation, terminal methyl carbons near the interior of the structure were fixed with a force constant of 100 kcal mol^{-1} $Å^{-1}$. Simulation temperature was selected, and the simulation was run for 1.2 nanoseconds with a recording interval of 4.8 picoseconds. After simulation, the resulting structure was exported into Avogadro, the carboxylates were reinstated as well as the indium phosphide core for powder X-ray diffraction simulation.

D.5 Thermodynamics of Cadmium Complexes

Correcting the experimental isothermal titration calorimetry data to yield the binding enthalpy of cadmium oleate to the surface of cadmium sulfide quantum dots required the use

	TZ SCF	QZ SCF	Infinite SCF	TZ Corr.	QZ Corr.	Infinite Corr.	Total Energy
$CdOAc_2$	-623.928860	-624.146738	-624.176749	-2.351931	-2.545045	-2.688092	-626.864841
$CdOAc_2THF_2$	-1088.105863	-1088.454153	-1088.502126	-4.368026	-4.671497	-4.896290	-1093.398415
$CdOAc_2THF_4$	-1552.247743	-1552.725353	-1552.791138	-6.397799	-6.810832	-7.116783	-1559.907921
THF	-232.063247	-232.128922	-232.137968	-0.996088	-1.051048	-1.091758	-233.229726

Table D.1: Raw CCSD(T) energy calculations of metal complexes and THF used to calculate dative bond energies with the automatic extrapolation energies to an infinite basis set. Corr. stands for correlation. Energies in Hartrees.

of computational calculations. Molecules of cadmium oleate, cadmium acetate, cadmium acetate di-tetrahydrofuran, cadmium acetate tetra-tetrahydrofuran, and tetrahydrofuran were built in IQmol. The CCSD(T) (coupled cluster single-double and perturbative triple) computational method was selected to calculate the energies due to its high accuracy, but for the geometry optimization and cadmium oleate structure these methods were too time consuming, so structures were then geometrically optimized in ORCA using density functional theory (DFT) with the ωB97X-V functional, the def2-QZVPD basis set, and Grimme's empirical dispersion correction. Once the structures were optimized, separate CCSD(T) calculations were performed in ORCA on the structures, with the exception of cadmium oleate, using the def2-TZVPP and def2-QZVPP basis sets, and the results were automatically extrapolated to the basis set limit.[260,261] Raw energies of these calculations can be found in the Table D.1, and the error in these calculations is estimated to be less than 1 kcal/mol.[261,262]

While the algorithm to compute the energy of the complex is recorded in the ORCA program manual, it is repeated here. First, the infinite self-consistent field (SCF) energy is calculated by solving the system of equations

$$E_{\text{SCF}}^{(X)} = E_{\text{SCF}}^{(\infty)} + Ae^{(-\alpha\sqrt{X})}$$

where X is the cardinal number of the basis set calculated (TZ being 3 and QZ being 4). The value for α is provided in the ORCA manual based on basis sets used, and for def2 this value is 7.88 when using TZ and QZ. The unknowns that need to be solved are $E_{\text{SCF}}^{(\infty)}$ and A, hence two basis sets are needed to create a system of two equations.

To calculate the correlation energy for the infinite basis set, the equation

$$E_{\text{corr}}^{(\infty)} = \frac{X^\beta E_{\text{corr}}^{(X)} - Y^\beta E_{\text{corr}}^{(Y)}}{X^\beta - Y^\beta}$$

is used. X and Y are the cardinal number of the basis sets used (TZ being 3 and QZ being 4, respectively). The value of β is provided in the ORCA manual based on basis sets used, and for def2 this is 2.97 when using TZ and QZ. By adding the infinite basis set SCF and the infinite basis set correlation energy, the total energy of the structure is calculated.

Finally, these structures were transferred into Gaussian 16, and DFT frequency calculations were performed on these structures using the ωB97XD functional and the def2-SVPP basis set for the hydrogen atoms, the def2-SVPD basis set for the carbon and the oxygen

	Translational	Rotational	Vibrational	Total
$CdOA_2$	56.655	52.892	292.679	402.226
$CdOAc_2$	52.675	36.962	30.870	120.506
$CdOAc_2THF_2$	54.472	42.511	91.439	188.422
$CdOAc_2THF_4$	55.678	44.834	131.389	231.900
THF	48.328	31.032	13.050	92.409

Table D.2: Calculated entropies of metal complexes and tetrahydrofuran from Gaussian 16. Entropies given as TS at 298.15 K in kJ/mol.

atoms, and the def2-TZVP basis set with an effective core potential for the cadmium atoms. The resulting entropies can be found in Table D.2.

With sufficient thermochemical data, a correction to the gas phase entropies can be performed that result in the coordination entropies of ligands in solution.[114] First, the entropy of vaporization from the liquid phase to the gas phase must be known. For tetrahydrofuran this value is equal to 87.91 J mol^{-1} K^{-1} at 339.1 K, the boiling point of tetrahydrofuran.[263] Next, the entropy of cooling the liquid from the boiling point to 298.15 K must be known, and has been measured to be -16.1 J mol^{-1} K^{-1}.[264] Combining these two values together, the entropy change from going from the gas phase to the liquid phase at 298.15 K is -104.0 J mol^{-1} K^{-1}, or $T\Delta S$ of -31.01 kJ/mol at 298.15 K. This correction was then applied to the change in gas phase entropies calculated.

Appendix E

Ising Model Simulation Code

E.1 On the Ising Model Simulation

Included here is the Python code used to simulate the Ising model. This code was originally adapted from code from CHEM 220A "Thermodynamics and Statistical Mechanics" taught by Dr. David T. Limmer during the Fall 2018 semester at the University of California, Berkeley, and was based on the Ising model simulation described in "Introduction to Modern Statistical Mechanics" by Dr. David Chandler.[10] It was further modified to model nanocrystal surfaces in a variety of conditions, including free ligands, two different ligands, empty sites, and phase transitions in the ligand shell. Further, an optimization routine was added to the simulation to find fit parameters for the thermodynamic variables. The code included here has been compiled in an attempt to generalize the individual scripts for all code that was used to simulate the various experiments described.

While the Ising model has proven itself useful for understanding reactions on the surfaces of nanocrystals, it is certainly not correct. While efforts have been made to be rigorous, there are certainly approximations, assumptions, and compromises that have been made. In this section these shortcomings will be addressed.

First, periodic boundary conditions on the Ising model have been applied to the model. In many respects this approximation used to simulate infinite lattices is preferable for studying nanocrystals; the nanocrystal surface is not infinite. Further, if it is assumed that the nanocrystal is spherical, these periodic boundary conditions are almost certainly one of the best approximations for the surface of the nanocrystal. However, this model is likely not applicable to faceted nanocrystals, and this also assumes no clumping of ligands on the nanocrystal surface. Additionally, multiple types of sites were not incorporated in any model. The application of an Ising model for faceted surfaces should hopefully not be too challenging, but this has not been attempted here, and for all models described the assumption was made that the nanocrystal was spherical.

Next, nearest neighbor interactions were implemented on a square grid, assuming that each site had four nearest neighbors. This is almost certainly incorrect. While attempts

could have been made for other shapes of grid and different numbers of nearest neighbor interactions, it was not clear if any had more merit than the other, and implementation of a square grid was by far the simplest. For faceted nanoparticles such as cubes or tetrahedrons, the shape of the grid may become more important and significant care and effort will be needed to be made on the coding and implementation of a different shape to the grid. A rectangular grid was adopted for nanocrystal surfaces that had numbers of ligand sites that were not perfect squares, but even so exact numbers of ligand sites (to the nearest integer) were not possible, but rather the closest integer multiple between perfect squares was used (*e.g.* 8X8, 8X9, or 9X9).

Additionally, only nearest neighbor interactions were accounted for. It is reasonable to assume that next-nearest neighbor interactions could impact the surface of the nanocrystal, either through organic ligand chains or through "empty" space. Both of these types of next-nearest neighbor interactions are possible, and both would likely have to be accounted for separately. However, no implementation of this was done in the models used.

The implementation of empty sites on the nanocrystal is not rigorous. The presence of empty sites can be observed in isothermal titration calorimetry data from the reaction of oleic acid with indium phosphide nanocrystals capped with stearate (Chapter 4, Section 1). Note that the signal from the isothermal titration calorimetry is not monotonic but becomes more endothermic quickly before becoming subsequently less exothermic. This signal, combined with the increase in total ligand coverage observed from ^{1}H NMR, indicates that there were sites on the nanocrystal that ligands can add to rather than exchanging with native ligands on the surface. Implementing sites on the nanocrystal that are empty is easily achieved, but using them in the free ligand pool is less straightforward. An option would be to make it such that once the site is filled it can no longer be empty in the simulation, while another option would be to allow that empty site to be placed into the free ligand pool. In the original published model, these empty sites were simply placed into the free ligand pool. However, this decision is not wholly satisfactory. Additionally, there is no mechanism to decide if a ligand should simply pop off the surface of nanocrystal, without any exchange implemented. Further, in the simulation based on cadmium sulfide nanocrystals (Chapter 3, Section 2), the cadmium carboxylate crystals can "exchange" with empty sites, but the total number of empty sites is only the number of sites on the nanocrystal as determined from the full ligand coverage values.

Next, the phase transition aspect of the model is somewhat difficult to implement. From the powder X-ray diffraction data, we can see that an exchange to 10% of the organic ligands being eighteen-carbon bent chains from 100% eighteen-carbon straight chains induces a phase transition in the packing of ligands in the ligand shell (Chapter 5, Section 2), and this was also indicated from the model studying the temperature dependence of the phase transition using optical measurements.[42] However, with only four nearest neighbors, determining when a phase transition should happen is limited. The implementation was that when there are not four nearest eighteen-carbon straight chain ligands next to a site (so 75% or less of the nearest neighbors), there is a phase transition, because the only other option would have been even less nearest-neighbors to trigger the transition or no phase transitions at all.

Other things to discuss about the Ising model simulations are somewhat practical. In general, noise in the modeled results is worse for the isothermal titration calorimetry data than the ^{1}H NMR data, likely because the isothermal titration calorimetry data requires subtractions of the overall enthalpies from each other to build a titration curve. Averaging each simulation with a different number of exchange ligands is critically important, and usually at least 100 averages per number of exchange ligands is necessary to get usable data. For fine tuning the parameters and optimization, usually 10,000 averages were used, and for publication data, 100,000 averages provided nice smoothness to the isothermal titration calorimetry curves. However, with more averages the computational time increases significantly.

Other parameters that increased computational time was the number of grids needed to simulate. A significant time saver would be to not run the isothermal titration calorimetry simulations and ^{1}H NMR simulations separately, but rather to calculate both parameters for a given number of exchange ligands. The issue with this is that the mole ratio for the isothermal titration calorimetry data and the ^{1}H NMR data does not line up due to the overflow nature of the isothermal titration calorimetry (Chapter 2, Section 1). For optimizing the model, the mole ratio values need to align themselves, and so running separate grids for isothermal titration calorimetry data and ^{1}H NMR data was preferable. As a note, the mole ratio from the isothermal titration calorimetry or ^{1}H NMR will not be an integers, but for the simulation integer values for ligands are required.

Getting the model to thermal equilibrium is also less well defined. For all of the models reported, 10,000 random sites were selected for an attempted exchange, and this seemed to perform well for the models. However, changing this number can modify the results obtained. Performing more exchanges should get closer to thermal equilibrium, but will take more time, where computational time is linear with the number of attempted exchanges.

Significant time can be saved optimizing the model by allowing some parameters to not vary or only vary slightly. First, the zero point of the model should be defined as all the parameters are relative to each other. For example, it is possible to calculate thermodynamic parameters for all of the possible nearest neighbor interactions, however, the model will not change if all of those thermodynamic parameters are adjusted by a scalar addition. The same is true for the head binding enthalpies and entropies. Thus, in a two ligand system, only one head binding enthalpy, one head binding entropy, two nearest neighbor enthalpy terms, and two nearest neighbor entropy terms need to be optimized, as the other terms can be defined as zero. In the case that empty sites need to be used, the empty site values are considered the zero point values, and so 10 parameters need to be optimized rather than the 6 listed above. Note, however, that the optimization routine performs better for a two ligand system when the native ligands are defined as the zero point, rather than the exchange ligands, although it can be more informative to report the exchange ligands as the zero point (Chapter 4, Section 3).

For fine tuning the model and optimization, running high numbers of averages is helpful, but more so the variation in the parameters is critical. As the number of parameters increases and smaller changes are neccessary for the fitting, the varation in parameters should decrease. In general, $\pm$ 0.1 $k_{\mathrm{B}}T$ was effective at finding best fits for the range in parameters. For

the optimization routine, 100 attempts at optimization with 20 random guesses seemed to perform well. The sum of squares error was used to determine goodness of fit, but to optimize both the isothermal titration calorimetry and ^{1}H NMR data where the magnitude of these values was very different, each sum of squares error was divided by the variance in the experimental dataset to normalize the two residuals, and this was then added together to create the minimization parameter.

It is almost certainly true that this model can be improved significantly, not only in increasing the speed at which it runs but also in modifying it to better reflect reality. The experimental dataset and parameters for the initial measurements of the additional of zinc chloride to indium phosphide quantum dots were used in the provided code below, after the correction to the sizing and molar extinction coefficients was applied (Appendix C.2). Included are graphs of the experimental and simulated results as well as the map of the ligand shell generated from the code provided.

E.2 Python Script

```
#!/usr/bin/env python3
# -*- coding: utf-8 -*-
"""
Created on Wed Feb  2 09:26:17 2022

@author: jasoncalvin
"""

import numpy as np
import numba
from skopt import gp_minimize
import matplotlib.pyplot as plt
plt.style.use('classic')

# Ising model parameters
# Size of the lattice
Nx = 10
Ny = 9
N = Nx * Ny
# Temperature
kT = 1
# Initial thermodynamic parameters
# Assume for empty site models that vacuum parameters are zero
# If no empty sites, set zero point to the native ligand grid
optimize = False
iHA = 0
iHB = -16.32
iHAA = 0
iHAB = 5.52
iHBB = 9.18
```

```
iTSA = 0
iTSB = -10.42
iTSAA = 0
iTSAB = 3.79
iTSBB = 2.71
# Sign of phase transition term matters based on zero point energy
iPTH = 0
iPTTS = 0
# If running optimization, specify the variation on each parameter
VHA = 0.001
VHB = 0.1
VHAA = 0.001
VHAB = 0.1
VHBB = 0.1
VTSA = 0.001
VTSB = 0.1
VTSAA = 0.001
VTSAB = 0.1
VTSBB = 0.1
VPTH = 0.001
VPTTS = 0.001
# Determine total optimization call number and random call number
calls = 100
random_calls = 20
# Initial free ligand pool
IA = 12
IB = 0
empty_sites = 0
# Ligand B populations
# Add a zero value to the beginning of the ITC values
# Often first injection is disregarded, create another set of x-values
BITC = np.array
    ([0,4,9,13,18,23,27,32,37,42,47,52,57,62,67,72,77,82,88,93,98,
                  104,109,115])
BITC2 = np.array([9,13,18,23,27,32,37,42,47,52,57,62,67,72,77,82,88,93,98,
                  104,109,115])
BNMR = np.array
    ([0,4,7,11,14,18,21,25,28,32,35,39,43,46,50,53,57,60,64,67,71,
                  74,78,81])
# Fraction of free ligands measured
ANMR = np.array
    ([0.113365972,0.135959049,0.156215517,0.171891453,0.182991316,

    0.197485239,0.209202063,0.211083536,0.228212992,0.253100943,

    0.248019232,0.245877937,0.25573964,0.270196763,0.269933602,

    0.264020406,0.274845408,0.274463757,0.281595397,0.295057978,
                  0.290130163,0.28939703,0.288274268,0.293250229])
# Enthalpy measured
```

```
H = np.array([7.305680795,6.14815699,5.497401237,4.743350349,3.899592366,
    3.209654712,2.792299362,2.409014862,2.082214662,1.825116315,
    1.644341129,1.46762532,1.326554383,1.24433166,1.121890046,
    1.104998208,1.064707361,0.962262716,0.949990324,0.893206194,
                0.782429932,0.691143947])
# Determine number of exchange attempts to try
Nsweep = 10000
# Number of times to run each number of exchange ligands
M = 1000

# Randomly select a surface site and free ligand and attempt to exchange
# numba.jit helps the program run faster
@numba.jit(nopython=True)
def Monte_Carlo(sites, free_array, HA, HB, HAA, HAB, HBB, TSA, TSB, TSAA,
    TSAB,
                TSBB, PTH, PTTS):
    # Attempt Nsweep random exchanges
    for step in range(Nsweep):
        # Draw random site and free ligand
        ii=int(np.random.rand()*Nx)
        jj=int(np.random.rand()*Ny)
        kk=int(np.random.rand()*len(free_array))
        # Attempt to exchange
        # If there are no free ligands, no exchange is attempted
        if len(free_array !=0):
            Metropolis(sites,ii,jj,kk,free_array, HA, HB, HAA, HAB, HBB,
    TSA,
                       TSB, TSAA, TSAB, TSBB, PTH, PTTS)

# Determine if the ligands will exchange
# numba.jit helps the program run faster
@numba.jit(nopython=True)
def Metropolis(sites,ii,jj,kk,free_array, HA, HB, HAA, HAB, HBB, TSA, TSB,
               TSAA, TSAB, TSBB, PTH, PTTS):
    # Define 1 as ligand A, -1 as ligand B
    # Ligands must have different identities to exchange
    if sites[(ii),(jj)] != free_array[kk]:
        # Define the neighbors with periodic boundary conditions
        up = sites[(ii+1)%Nx][jj]
        down = sites[(ii-1)%Nx][jj]
        left = sites[ii][(jj-1)%Ny]
        right = sites[ii][(jj+1)%Ny]
        # Set initial conditions of the 5 squares
        dG = 0
        A = 0
        B = 0
        # Count the nearest neighbors
```

```
120         if up == 1:
121             A += 1
122         if up == -1:
123             B += 1
124         if down == 1:
125             A += 1
126         if down == -1:
127             B += 1
128         if left == 1:
129             A += 1
130         if left == -1:
131             B += 1
132         if right == 1:
133             A += 1
134         if right == -1:
135             B += 1
136         # Compute the energy of the exchange
137         if (sites[ii][jj] == 1 and free_array[kk] == -1):
138             dG = ((HB + (B * HBB) + (A * HAB) - HA - (A * HAA) - (B * HAB)
    ) -
139                   (TSB + (B * TSBB) + (A * TSAB) - TSA - (A * TSAA) -
140                    (B * TSAB)))
141         if (sites[ii][jj] == -1 and free_array[kk] == 1):
142             dG = ((HA + (A * HAA) + (B * HAB) - HB - (B * HBB) - (A * HAB)
    ) -
143                   (TSA + (A * TSAA) + (B * TSAB) - TSB - (B * TSBB) -
144                    (A * TSAB)))
145         if (sites[ii][jj] == 1 and free_array[kk] == 0):
146             dG = ((- HA - (A * HAA) - (B * HAB))- (- TSA - (A * TSAA) -
147                                                    (B * TSAB)))
148         if (sites[ii][jj] == -1 and free_array[kk] == 0):
149             dG = ((- HB - (B * HBB) - (A * HAB)) - (- TSB - (B * TSBB) -
150                                                     (A * TSAB)))
151         if (sites[ii][jj] == 0 and free_array[kk] == 1):
152             dG = (HA + (A * HAA) + (B * HAB)) - (TSA + (A * TSAA) + (B *
    TSAB))
153         if (sites[ii][jj] == 0 and free_array[kk] == -1):
154             dG = (HB + (B * HBB) + (A * HAB)) - (TSB + (B * TSBB) + (A *
    TSAB))
155         # Think carefully about this assignment based on PT sign
156         if (sites[ii][jj] == 1 and A == 4):
157             dG = dG + (PTH - PTTS)
158         if (free_array[kk] == 1 and A == 4):
159             dG = dG - (PTH - PTTS)
160         #Probability of accepting exchange
161         if dG < 0:
162             prob_accept = 1
163         else:
164             prob_accept = np.exp(-dG/kT)
165
```

```
166         # Counts number of non-empty site ligands
167         freeLigands = 0
168         i = 0
169         for i in range(len(free_array)):
170             if free_array[i] == 1:
171                 freeLigands +=1
172             if free_array[i] == -1:
173                 freeLigands += 1
174         # Determine if exchange is accepted, swap identities
175         # Maintains minimum number of free ligands
176         if (np.random.rand() < min(prob_accept,1) and freeLigands > IA +
    IB):
177             oldSite = sites[ii][jj]
178             sites[ii][jj] = free_array[kk]
179             free_array[kk] = oldSite
180 
181 # After simulation completes, calculate enthalpy change of the grid
182 def calculate_enthalpy(sites, HA, HB, HAA, HAB, HBB, TSA, TSB, TSAA, TSAB,
183                        TSBB, PTH, PTTS):
184     # Set starting enthalpy at zero
185     enthalpy_calc = 0
186     # Get enthalpy change for each grid site
187     for ii in range(Nx):
188         for jj in range(Ny):
189             A = 0
190             if sites[ii][jj] == 1:
191                 enthalpy_calc += HA
192                 # Calculate up and right to avoid double counting
193                 if sites[(ii+1)%Nx][jj] == 1:
194                     enthalpy_calc += HAA
195                     A += 1
196                 if sites[(ii+1)%Nx][jj] == -1:
197                     enthalpy_calc += HAB
198                 #right
199                 if sites[ii][(jj+1)%Ny] == 1:
200                     enthalpy_calc += HAA
201                     A += 1
202                 if sites[ii][(jj+1)%Ny] == -1:
203                     enthalpy_calc += HAB
204                 if sites[(ii-1)%Nx][jj] == 1:
205                     A += 1
206                 if sites[ii][(jj-1)%Ny] == 1:
207                     A += 1
208             if sites[ii][jj] == -1:
209                 enthalpy_calc += HB
210                 # Calculate up and right to avoid double counting
211                 if sites[(ii+1)%Nx][jj] == -1:
212                     enthalpy_calc += HBB
213                 if sites[(ii+1)%Nx][jj] == 1:
214                     enthalpy_calc += HAB
```

```
                #right
                if sites[ii][(jj+1)%Ny] == -1:
                    enthalpy_calc += HBB
                if sites[ii][(jj+1)%Ny] == 1:
                    enthalpy_calc += HAB
            if A != 4:
                enthalpy_calc += PTH
    return enthalpy_calc

# This function runs the simulation
def simulation_function(parameters):

    HA, HB, HAA, HAB, HBB, TSA, TSB, TSAA, TSAB, TSBB, PTH, PTTS =
   parameters

    # Arrays to save simulated data for each datapoint
    enthalpy=np.zeros(len(BITC))
    ligandsA=np.zeros(len(BNMR))
    ligandsB=np.zeros(len(BNMR))
    ligandsTotal=np.zeros(len(BNMR))
    fracligandsA=np.zeros(len(BNMR))

    # Simulation for different amounts of ligands for the ITC data
    for step in range(len(BITC)):
        step_enthalpy = np.zeros(M)
        for m in range(M):
            # Given initial conditions, add exchange ligands
            free_pool = np.array([IA,IB])
            free_pool[1] = free_pool[1] + BITC[step]
            # Initialize grid
            # This randomly assigns the empty sites to the surface
            sites = np.array([0,1])
            sites = np.repeat(sites, [empty_sites, N - empty_sites],axis
   =0)
            np.random.shuffle(sites)
            sites = sites.reshape([Nx,Ny])
            # We add all the free ligands into one array
            free_array = np.zeros([free_pool[0]+free_pool[1]]) - 1
            i = 0
            for i in range(free_pool[0]):
                free_array[i] = 1
                i += 1
            # Run the simulation
            Monte_Carlo(sites,free_array, HA, HB, HAA, HAB, HBB, TSA, TSB,
                        TSAA, TSAB, TSBB, PTH, PTTS)
            # Save the results
            step_enthalpy[m] = calculate_enthalpy(sites, HA, HB, HAA, HAB,
    HBB,
                                                  TSA, TSB, TSAA, TSAB,
   TSBB,
```

```
                                                    PTH, PTTS)
        # Average the results
        enthalpy[step] = step_enthalpy.mean()

    for step in range(len(BNMR)):
        step_sitesA = np.zeros(M)
        step_sitesB = np.zeros(M)
        step_sitesTotal = np.zeros(M)
        for m in range(M):
            # Given initial conditions, add exchange ligands
            free_pool = np.array([IA,IB])
            free_pool[1] = free_pool[1] + BNMR[step]
            # Initialize grid
            # This randomly assigns the empty sites to the surface
            sites = np.array([0,1])
            sites = np.repeat(sites, [empty_sites, N - empty_sites],axis
    =0)
            np.random.shuffle(sites)
            sites = sites.reshape([Nx,Ny])
            # We add all the free ligands into one array
            free_array = np.zeros([free_pool[0]+free_pool[1]]) - 1
            i = 0
            for i in range(free_pool[0]):
                free_array[i] = 1
                i += 1
            # Run the simulation
            Monte_Carlo(sites,free_array, HA, HB, HAA, HAB, HBB, TSA, TSB,
                        TSAA, TSAB, TSBB, PTH, PTTS)
            # Count number bound of each ligand and total ligand coverage
            boundA = 0
            boundB = 0
            for ii in range(Nx):
                for jj in range(Ny):
                    if sites[ii][jj] == 1:
                        boundA += 1
                    if sites[ii][jj] == -1:
                        boundB += 1
            boundLigands = boundA + boundB
            step_sitesA[m] = boundA
            step_sitesB[m] = boundB
            step_sitesTotal[m] = boundLigands
            # Average the results
        ligandsA[step] = step_sitesA.mean()
        ligandsB[step] = step_sitesB.mean()
        ligandsTotal[step] = step_sitesTotal.mean()
        # Calculate fraction free
        fracligandsA[step] = (N + IA - ligandsA[step])/(N + IA)

    # Construct enthalpy results into a titration and convert to kJ/mol
    enthalpy_results = np.zeros(len(enthalpy))
```

```
    for i in range(len(enthalpy)):
        # For the first injection calculate the initial enthalpy
        if i == 0:
            enthalpy_results[i] = (2.479*enthalpy[i])
        # Calculate the change in enthalpy with added ligands
        else:
            enthalpy_results[i] =(2.479*(enthalpy[i] -
                                        enthalpy[i-1]))/(BITC[i] - BITC[i
    -1])
    # Create a dataset to fit the ITC experimental results to
    enthalpy_results_fit = np.zeros(len(BITC2))
    enthalpy_results_fit[0] = enthalpy_results[0]
    for i in range(len(enthalpy_results_fit)):
        enthalpy_results_fit[i] = enthalpy_results[i+2]
    # Normalized error from simulation results compared to experimental
    ANMR_ss = (1/np.var(ANMR))*np.sum((fracligandsA - ANMR)**2)
    H_ss = (1/np.var(H))*np.sum((enthalpy_results_fit - H)**2)

    if optimize == False:
        # Plot the data on a single graph
        fig = plt.figure()
        ax1 = fig.add_subplot(1, 1, 1)
        ax2 = ax1.twinx()
        # Simulated results are dark colors
        ax1.scatter(BITC2,H, color='skyblue',label = "Exp ITC")
        ax1.scatter(BITC,enthalpy_results, color='b',label = "Sim ITC")
        ax2.scatter(BNMR,ANMR,color='pink', label = "Exp NMR")
        ax2.scatter(BNMR,fracligandsA, color = 'r', label = "Sim NMR")
        # Set limits of the graph to zoom in on regions
        ax1.set_ylim(-1,11)
        ax2.set_ylim(0.1,0.35)
        ax1.set_xlim(-3,118)
        # Set the ticks and labels for the graph
        ax1.tick_params(labelsize=24,length=12, width=2)
        ax2.tick_params(labelsize=24,length=12, width=2)
        ax1.set_xlabel('Mole Ratio (A ligands/NC)', size = 24)
        ax1.set_ylabel('Enthalpy (kJ/mol)', size = 24)
        ax2.set_ylabel('Fraction A Bound', size = 24)
        ax1.set_xticks([0,20,40,60,80,100])
        ax1.set_yticks([0,2,4,6,8,10])
        #ax2.set_yticks([0,20,40,60,80,100])
        # If you want a legend here is the code
        '''ax1.legend(loc='best', fontsize='20',prop={'size': 18},ncol=1,
                    scatterpoints=1)
        ax2.legend(loc='best', fontsize='20',prop={'size': 18},ncol=1,
                    scatterpoints=1)'''
        # Often convenient to plot the zero enthalpy line
        x = [-10,150]
        y = [0,0]
        ax1.plot(x,y, color ='gray', linewidth=4, linestyle = 'dashed')
```

```
359
360         # This helps your graph look nice
361         ax1.spines['right'].set_linewidth(4)
362         ax1.spines['left'].set_linewidth(4)
363         ax1.spines['top'].set_linewidth(4)
364         ax1.spines['bottom'].set_linewidth(4)
365         plt.tight_layout()
366
367         # This plots the surface map after the final simulation
368         fig2, ax = plt.subplots(1, 1,figsize=(6,6))
369         ax.set_aspect('equal')
370         ax.set_xlim(-.5, Nx-1/2.)
371         ax.set_ylim(-.5, Ny-1/2.)
372         plt.setp(ax, xticks=[], yticks=[])
373         img = ax.imshow(sites,cmap='winter',interpolation='None')
374         plt.draw()
375
376     # This is the error we would like to minimize
377     return ANMR_ss + H_ss
378
379 # This defines the function we want to minimize
380 def sim_wrapper(parameters):
381     HA, HB, HAA, HAB, HBB, TSA, TSB, TSAA, TSAB, TSBB, PTH, PTTS =
    parameters
382
383     result = simulation_function([HA, HB, HAA, HAB, HBB, TSA, TSB, TSAA,
    TSAB,
384                                   TSBB, PTH, PTTS])
385
386     # Returning error
387     return result
388
389 # This returns the results of the simulation for your initial parameters
390 print(simulation_function([iHA,iHB,iHAA,iHAB,iHBB,iTSA,iTSB,iTSAA,iTSAB,
    iTSBB,
391                            iPTH,iPTTS]))
392
393 if optimize == True:
394     # This optimizes your parameters based on your experimental data
395     res = gp_minimize(sim_wrapper,[(iHA-VHA,iHA+VHA),(iHB-VHB,iHB+VHB),
396                                    (iHAA-VHAA,iHAA+VHAA),(iHAB-VHAB,iHAB+
    VHAB),
397                                    (iHBB-VHBB,iHBB+VHBB),(iTSA-VTSA,iTSA+
    VTSA),
398                                    (iTSB-VTSB,iTSB+VTSB),
399                                    (iTSAA-VTSAA,iTSAA+VTSAA),
400                                    (iTSAB-VTSAB,iTSAB+VTSAB),
401                                    (iTSBB-VTSBB,iTSBB+VTSBB),
402                                    (iPTH-VPTH,iPTH+VPTH),
403                                    (iPTTS-VPTTS,iPTTS+VPTTS)],
```

```
404                         x0 = [iHA,iHB,iHAA,iHAB,iHBB,iTSA,iTSB,iTSAA,iTSAB,
    iTSBB,
405                               iPTH,iPTTS],n_calls=calls,
406                         n_random_starts=random_calls, verbose = True)
407
408     # This prints the optimized parameters
409     print(res.x)
```

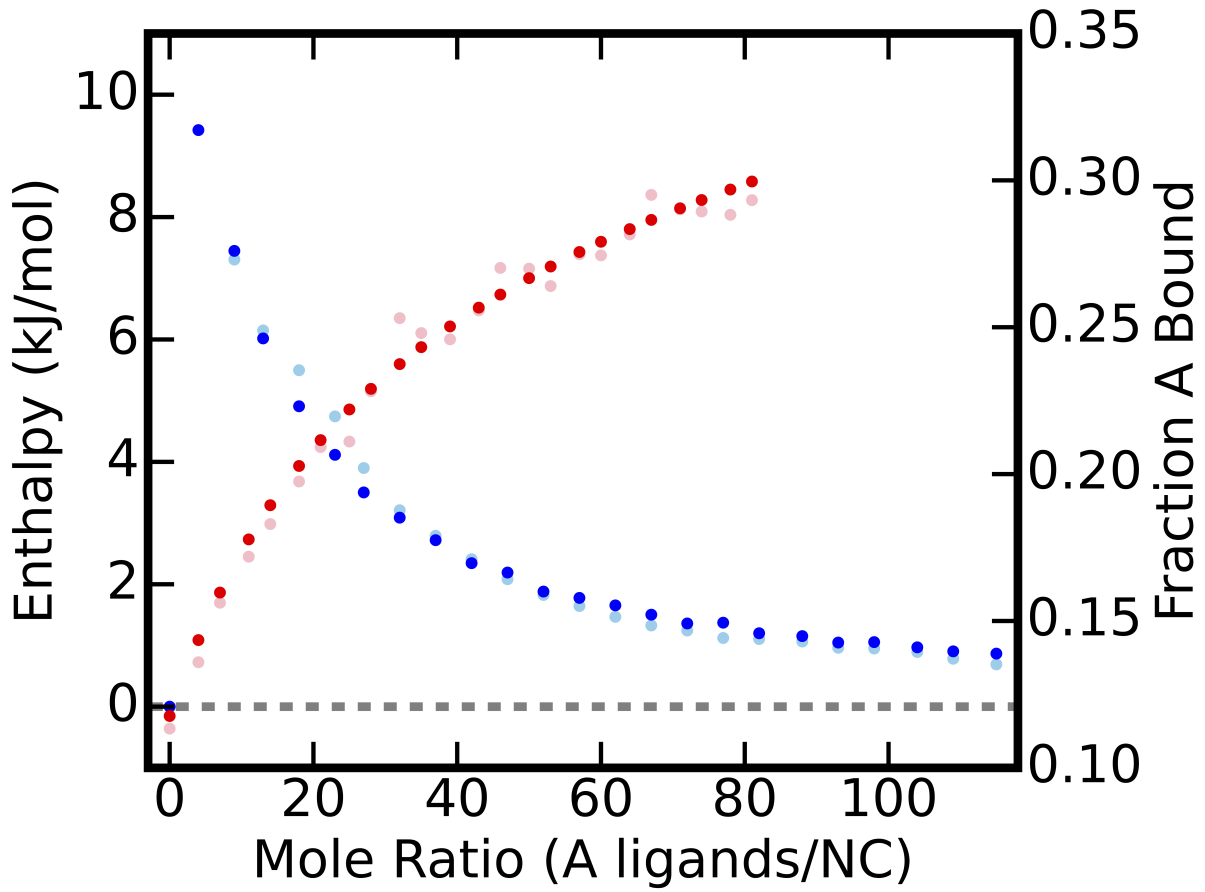


Figure E.1: Ising model simulation generated graph example. The simulation was done on data generated by titrating zinc chloride (B ligand) into a solution of indium phosphide quantum dots capped with indium myristate (A ligand). The pink data points represents the experimentally determined fraction of free A ligand, while the red data points represents the simulated fraction of free A ligand. The light blue data points represents the experimental isothermal titration calorimetry data while the blue data points represents the simulated data. The error reported for the fit from the Ising model was 0.69 units.

E.3 Ising Model Generated Graphs

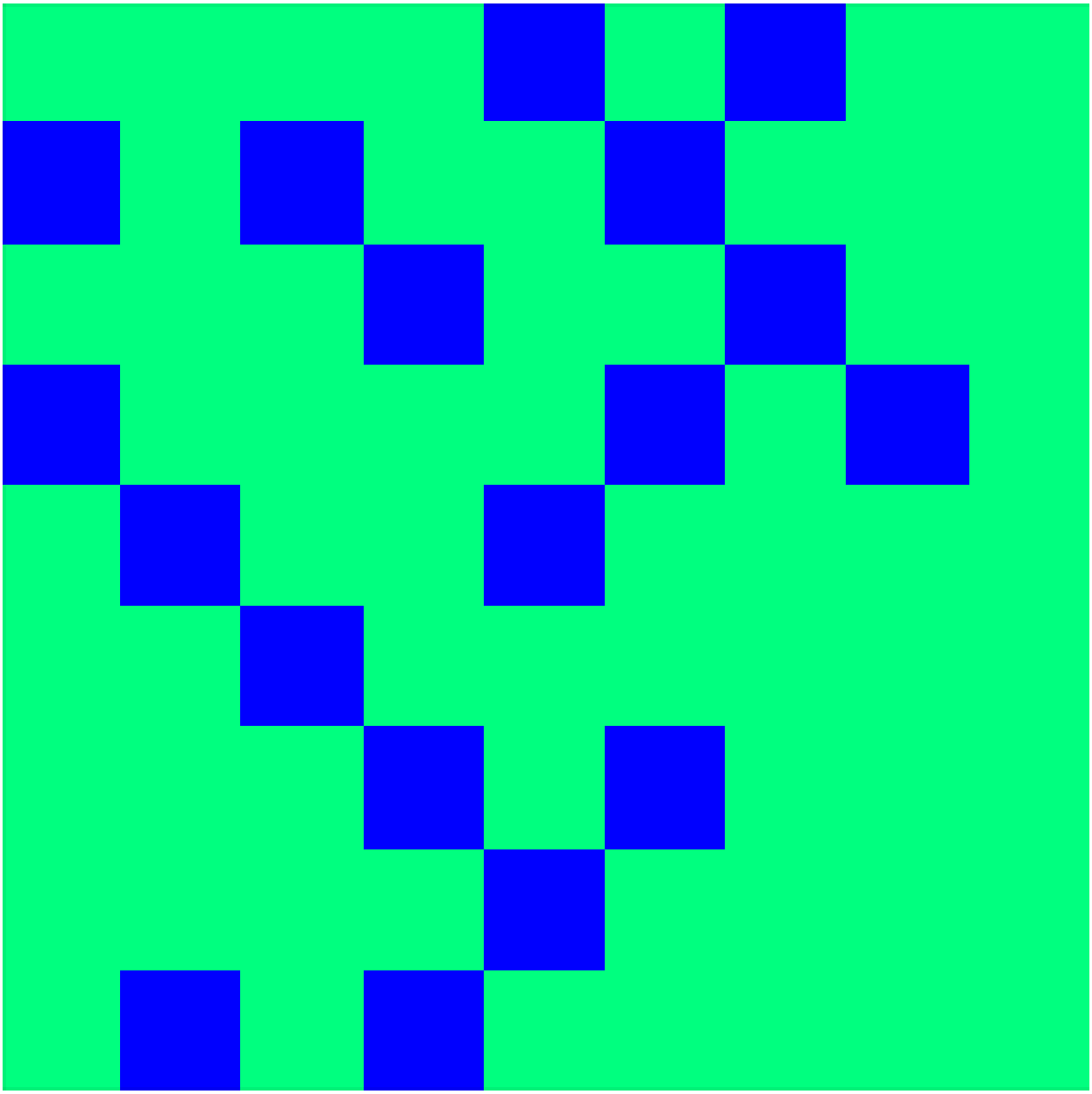


Figure E.2: Ising model simulation generated map example. Green squares represent the native indium myristate ligands (ligand A) while blue squares represent the zinc chloride exchange ligands (ligand B). Green squares represent organic indium myristates while blue squares represent inorganic metal halides. The coverage maps are representative of the surface of the nanocrystal where each individual square represents a binding site on the nanocrystal. Note that this simulation was done on a 10X9 grid, and thus the map is not square.